

**EFFECTS OF STRAIN RATE ON MECHANICAL PROPERTIES  
AND FRACTURE MECHANISMS IN DUAL PHASE STEELS.**

A Dissertation  
Presented to  
The Academic Faculty

By

Sukanya M. Sharma

In Partial Fulfillment  
of the Requirements for the Degree  
Doctor of Philosophy in the  
School of Materials Science and Engineering

Georgia Institute of Technology

August 2019

Copyright © Sukanya M. Sharma 2019

**EFFECTS OF STRAIN RATE ON MECHANICAL PROPERTIES  
AND FRACTURE MECHANISMS IN DUAL PHASE STEELS.**

Approved by:

Dr. Naresh Thadhani, Advisor  
School of Materials Science and  
Engineering  
*Georgia Institute of Technology*

Dr. Arun Gokhale, Advisor  
School of Materials Science and  
Engineering  
*Georgia Institute of Technology*

Dr. Shrikant Bhat, Advisor  
*ArcelorMittal, USA*

Dr. Preet Singh  
School of Materials Science and  
Engineering  
*Georgia Institute of Technology*

Dr. Kimberly Kurtis  
School of Civil and Environmen-  
tal Engineering  
*Georgia Institute of Technology*

Date Approved: July 23rd, 2019



For my grandparents and parents, giants upon whose shoulders I stand...

## ACKNOWLEDGEMENTS

The past five years have helped shape my personality not only as a researcher but also as a person. I have a number of people to thank, without whom this journey would not have been as enlightening and enjoyable as it was.

I would first like to thank the three people who helped shape this work and guided me every step of the way. I have had the privilege to be advised by three advisers, Dr. Naresh Thadhani, Dr. Arun Gokhale and Dr. Shrikant Bhat. I would like to sincerely thank Dr. Thadhani and Dr. Gokhale for providing all their guidance and for motivating me to delve deeper on every problem. They have championed me and guided me through both professional and personal struggles and I will always be indebted to them for that. Dr. Shrikant Bhat has always been a source of inspiration and a great mentor, and has maneuvered me to tackle some of the most perplexing concepts and problems. My discussions with him have been both informative and extremely enjoyable. I would also like to thank my committee members, Dr. Preet Singh and Dr. Kimberly Kurtis for all their support and encouragement.

Further, I would like to thank ArcelorMittal global R&D for sponsoring this work. They have been immensely helpful in not only providing the materials used in this work but also extending their cooperation and expertise. I would like to specifically thank Dr. Gang Huang and George Germin for taking the time to help perform and analyze experiments that were critical in shaping some important discussions. I would also like to thank Dr. Paul Allison, Dr. Wilburn Whittington and Omar Rodriguez for their help with the Hopkinson bar experiments.

I have been very fortunate to have the best lab-mates and mentors one could ask for. I would first like to thank Dr. Gregory Kennedy for being patient with me and making so many of my experiments a resounding success, and Mr. Gautam Patel for his expertise and help. I would also like to thank Drs. Rene Diaz, Alex Bryant, David

Scripka and Manny Gonzales for their friendship and constant encouragement. A big thank you to Travis Voorhees (thank you for being the best office mate!), Andrew Boddorff, Karla Wagner, Katie Koube, Kishlay Mishra and all the current and past members of the high strain rate and stereology lab that I had the privilege to share my journey with.

I am deeply indebted to my friends Vivek, Sanjana, Asmita, Madhusudan, Prachi, Manali, Abhinaya, Ananya, Dushhyanth, Kiran, Devan, Raphael, Coline, Tapan, Ajinkya, Brandon and many others who made the last five years the best of my life and graduate school the most memorable- I could not have done this without you guys. Thank you for being my home away from home and building a family I will always love and cherish. Rabi, Upasana and Shrinwanti, thank you for always supporting me and trusting in my abilities to pursue and complete a PhD.

I owe the successful completion of my PhD to my fantastic family. Thank you for making the entire journey worthwhile. I would like to thank my sister and brother-in-law, Lavania Sharma and Dr. Avinash Shanmugham for being there with me through the ups and downs and believing in me at all times. Didi, thank you for listening and always being by my side and being the best mentor and counsellor anyone could ask for. I don't have enough words to thank my parents who have shaped me to be who I am today and are the pillars of my strength. Thank you Ma and Dad for the great sacrifices you made so we could achieve and live our dreams. Thank you Dad for always encouraging and motivating me and teaching me to believe in myself. Ma, you are a role model, thank you for always encouraging my curiosity and showing the power of a kind heart and an open mind.

## TABLE OF CONTENTS

<b>Acknowledgments . . . . .</b>	<b>iv</b>
<b>List of Tables . . . . .</b>	<b>x</b>
<b>List of Figures . . . . .</b>	<b>xi</b>
<b>Chapter 1: Introduction and Problem Definition . . . . .</b>	<b>1</b>
<b>Chapter 2: Background . . . . .</b>	<b>4</b>
2.1 Dual Phase Steels . . . . .	4
2.1.1 Alloying elements and processing of Dual Phase steel . . . . .	5
2.2 Mechanical properties and fracture response of DP steels at Quasi-static strain rates. . . . .	11
2.2.1 Effects on Mechanical Properties . . . . .	11
2.2.2 Effect on deformation and fracture response . . . . .	18
2.2.3 Fracture surface response . . . . .	23
2.3 Mechanical properties and fracture response of DP steels at high strain rates. . . . .	27
2.3.1 Introduction to dynamic testing of sheet steels at Intermediate strain rates . . . . .	28
2.3.2 Strain rate sensitivity of DP steels . . . . .	30
2.3.3 Fracture at high strain rates . . . . .	36

2.3.4	Plate Impact Dynamic Tensile (Spallation) tests . . . . .	40
2.4	Protective coatings on steel . . . . .	48
2.5	Stereology for Microstructure Quantification . . . . .	49
2.6	Quantitative Fractography . . . . .	54
2.7	Summary . . . . .	62
<b>Chapter 3:</b>	<b>Experimental Work . . . . .</b>	<b>64</b>
3.1	Overview . . . . .	64
3.2	Material system and chemistry . . . . .	65
3.2.1	Ultrasonic Testing . . . . .	66
3.2.2	Density Measurements . . . . .	67
3.3	Microstructural characterization . . . . .	69
3.3.1	Metallography . . . . .	69
3.3.2	Quantitative Microscopy . . . . .	71
3.4	Mechanical Testing . . . . .	74
3.4.1	Sample geometries and machining . . . . .	74
3.4.2	Servo-hydraulic Testing . . . . .	76
3.4.3	Hopkinson Bar Testing . . . . .	77
3.4.4	Uniaxial strain plate impact experiments . . . . .	81
3.5	Fractography . . . . .	84
3.5.1	Profilometry . . . . .	84
3.5.2	Image based fractography . . . . .	88
<b>Chapter 4:</b>	<b>Results . . . . .</b>	<b>92</b>

4.1	Quantitative Characterization of Microstructures . . . . .	92
4.1.1	Qualitative observations from microstructures of as-received steels	92
4.1.2	Quantitative estimations of the microstructure . . . . .	96
4.1.3	Connectivity of martensite . . . . .	96
4.1.4	DP 980 GAD- Quantifying the gradient in the microstructure	97
4.1.5	Galvannealed Coating layer . . . . .	102
4.2	Mechanical Properties: Effect of strain rate and microstructure . . . .	102
4.2.1	DP 590 : Mechanical Properties . . . . .	103
4.2.2	DP 980 NC : Mechanical Properties . . . . .	104
4.2.3	DP 980 GAN and DP 980 GAD: Mechanical Properties . . . .	105
4.3	Fractography of Dual Phase Steels . . . . .	106
4.3.1	Qualitative Fractography . . . . .	106
4.3.2	Quantitative Fractography . . . . .	114
4.3.3	DP 590 . . . . .	114
4.4	Fracture profile and deformed microstructures . . . . .	117
4.4.1	DP 590 . . . . .	117
4.4.2	DP 980 NC . . . . .	118
4.4.3	DP 980 GAN . . . . .	122
4.4.4	DP 980 GAD . . . . .	122
4.5	Plate Impact Experiments- Spall Failure . . . . .	122
4.5.1	Overview . . . . .	122
4.5.2	Free Surface Velocity Traces . . . . .	125
4.5.3	Post-Mortem Fractography . . . . .	134

4.5.4	Incipient Spall-Deformed microstructure . . . . .	138
<b>Chapter 5:</b>	<b>Discussions . . . . .</b>	<b>146</b>
5.1	Effect of Volume fraction of martensite . . . . .	146
5.1.1	Comparing microstructures . . . . .	147
5.1.2	Quasi-static mechanical properties . . . . .	149
5.1.3	Effect of strain rate on mechanical properties . . . . .	151
5.1.4	Fracture response . . . . .	158
5.1.5	Fracture response of DP steels under dynamic tensile (spall) failure . . . . .	166
5.2	Effect of protective coating and decarburized layers . . . . .	170
5.2.1	Effect on mechanical properties . . . . .	171
5.2.2	Strain rate sensitivity . . . . .	171
5.2.3	Fracture surface response . . . . .	175
5.2.4	Comparing fracture mechanisms . . . . .	184
5.3	Effect of geometry on the stress-strain and fracture response . . . . .	189
<b>Chapter 6:</b>	<b>Conclusions and Proposed Future work . . . . .</b>	<b>192</b>
6.1	Research Outcomes . . . . .	192
6.2	Recommendations for future work . . . . .	196
<b>Appendix A</b>	<b>Effect of galvanized and decarburized layers . . . . .</b>	<b>199</b>
<b>Appendix B</b>	<b>Plate-Impact test configurations . . . . .</b>	<b>201</b>
<b>References</b>	<b>. . . . .</b>	<b>211</b>

## LIST OF TABLES

2.1	Function of typical alloying elements of DP steels [9] . . . . .	6
3.1	Nominal composition of as-received Dual Phase steels. . . . .	66
3.2	Sound speed and bulk properties of DP steels . . . . .	68
4.1	Quantitative Characterization of DP steels . . . . .	97
4.2	Quantitative Characterization of Banding of martensite . . . . .	97
4.3	Quantitative fractography of DP 590. . . . .	114
4.4	HEL and Spall strength of DP 590 . . . . .	126
4.5	HEL and Spall strength of DP 980 NC at different velocities . . . . .	130
4.6	HEL and Spall strength of DP 980 GAD . . . . .	132
5.1	Comparing mechanical properties of JIS and Miniature geometries . . . . .	191
5.2	Comparing aspect ratios of ferrite and martensite in the JIS and Miniature geometries . . . . .	191



## LIST OF FIGURES

2.1	Typical TTT diagram of a steel; red curves depict the superimposed quenching curves from above the $A_{c3}$ temperatures (completely austenised) or from the intercritical regime resulting in the formation of ferrite and martensite microstructure. [6] . . . . .	9
2.2	(a) Heat treatment of a typical galvanized DP steel, (b) Representative stress-strain curve of a galvanized DP steel showing continuous yielding with $\sim 20\%$ martensite [10], (c) Schematic layout of galvannealing line for producing coils [15] . . . . .	10
2.3	Plots showing the effect of increasing volume fraction of martensite ( $V_M$ ) (for a given composition of steel) on (a) carbon content of martensite and (b) UTS of the steel. Increasing the $V_M$ reduced the carbon in the martensite which in turn did not increase the UTS beyond a threshold of $V_M$ as the strength of the martensite is derived from the amount carbon partitioned in it [18] . . . . .	14
2.4	Plots showing that the (a) tensile strength and (b) yield strength depend only on the volume fraction of martensite and are independent of the carbon content in the DP steel. The open circles represent carbon levels of 0.07%, open triangles represent 0.10% and open squares represent 0.18%. The dashed lines correspond to the strength levels calculated by the authors using various models. [19] . . . . .	15
2.5	Plots showing the effect of increasing $V_M$ on the (a) increase in strength and (b) largely an increase in total elongation of DP steels. Excluding the 80% $V_M$ , higher $V_M$ resulted in a finer microstructure. [1], (c) Plots showing the effect of refining the microstructure on the strength and ductility of DP steels where $d_f$ is the average ferrite grain size. The Ultra Fine grained DP steel showed the highest strength [20] . . . . .	16

2.6	Strain hardening behavior using Hollomon analysis of DP steels as a function of volume fraction of martensite at (a) lower volume fraction and (b) higher volume fraction of martensite. The number of stages of strain hardening increase with an increase of volume fraction of martensite. Strain hardening behavior of DP steels using the Crussard-Jaoul analysis as a function of the morphology of martensite with (c) fibrous martensite and (d) blocky martensite [24] . . . . .	18
2.7	Plot showing the strain partitioning ratio as a function of the volume fraction of martensite with the higher volume fractions of martensite showing a higher ratio indicating a greater toughness and plasticity of the martensite phase [25]. . . . .	19
2.8	Equivalent strain maps and amount of strain partitioned into the ferrite and martensite phases at different strain levels for (a) dispersed martensite phase and (b) connected martensite phase. The connected martensite phase shows greater plasticity [26]. . . . .	20
2.9	Deformed microstructures and fracture profile deformation with different martensite distributions for (a) dispersed martensite showing greater fracture strain and (b) banded martensite showing a lower fracture strain. Irrespective of distribution, both steels showed fracture initiation by martensite cracking [3] . . . . .	21
2.10	Fracture initiation in DP steels as function of the volume fraction of martensite showing (a) interfacial decohesion at lower volume fraction of martensite (b) cracking of martensite bands at higher volume fractions of martensite [27]. . . . .	22
2.11	(a) Plot showing the distribution of voids as a function of volume fraction of martensite with lower volume fractions showing a larger area fraction and a linear dependence of voids as a function of true thickness strain, and a higher volume fraction of martensite showing fewer voids, (b) plot showing the strain in the martensitic phase as a function of the distribution of martensite. The red circles show a larger strain in the banded structure vs the equiaxed structure, (c) Fracture profile showing the distribution of voids in the steel with 17% martensite and banded structure,(d) fracture profile showing the distribution of voids with 41% martensite and banded structure. [29] . . . . .	24

2.12	(a) Low magnification fracture surface of a DP steel with an equiaxed martensite distribution showing considerable necking, (b) low magnification fracture surface of DP steel with a connected martensitic structure preventing substantial necking, (c) higher magnification image of (a) showing a ductile dimple fracture and (d) higher magnification image of (b) showing dimple ductile features. The authors qualitatively characterized the dimples in the connected martensite steel to be finer [26]. . . . .	25
2.13	(a) Fracture surface of DP steel showing a central crack running corresponding to the central band of martensite, (b) a high magnification fracture surface identifying ferrite and martensite, (c) Low magnification SEM images of the brittle regions highlighted by the white rectangles, (d) higher magnification images in the previously identified brittle regions showing the inclusions and the EDX map confirming the inclusions to be MnS [32]. . . . .	26
2.14	(a) Nominal setup of a Hopkinson Bar under compression. The figure also shows the different strains at the interface (b) The incident, transmitted and reflected waves generated in the bars. The stress-strain response can be captured using only the transmitted wave (blue- one wave analyses) or by incorporating all three waves (red- three wave analyses). [45] . . . . .	30
2.15	Quasi-Static and Dynamic tensile stress-strain response of DP steels. (a) quasi-static response of DP steels [53], Quasi and Intermediate strain rate response of (b) DP 600, (c) DP 800 and (d) DP 1000 with DP 600 showing the maximum positive strain rate sensitivity [4]. Effect of increasing temperature on DP 600 steels at strain rates of (e) $10^{-3}$ /s and (f) 1200/s strain rate [52] . . . . .	32
2.16	Effect of geometry on the ductility of DP steels. Stress-Strain curves at quasi-static and intermediate strain rates of (a) DP 600 and (b) DP 800 steels using the geometry depicted in (c) [5], (d) Stress-Strain curves reporting a drop in ductility at higher strain rates using a different geometries for quasi-static tests: (e), and dynamic tests: (f) [50]. . . . .	35
2.17	Fracture surfaces of Dual Phase steels at different strain rates, (a) DP 600- $10^{-3}$ /s, (b) DP 600 $10^3$ /s, (c) DP 1000 $10^{-3}$ /s, (d) DP 1000 $10^3$ /s. DP 600 showed reduced plasticity at higher strain rates whereas DP 1000 showed a more ductile dimpled region at higher rates indicating improved plasticity [4]. . . . .	37

2.18	(a) and (b) show the void network (yellow lines) and deeper dimples and facets (white arrows) in the steel with 67% martensite at $2.7 \times 10^{-4}/s$ and at 650/s strain rates respectively. (c) and (d) show the dimple size distribution in the same steel at $2.7 \times 10^{-4}/s$ and at 650/s strain rates respectively . . . . .	38
2.19	(a) and (b) show the void network (yellow lines) and deeper dimples and facets (white arrows) in the steel with 67% martensite at $2.7 \times 10^{-4}/s$ and at 650/s strain rates respectively. (c) and (d) show the dimple size distribution in the same steel at $2.7 \times 10^{-4}/s$ and at 650/s strain rates respectively . . . . .	39
2.20	Shock wave schematic depicting the original state of the material and the state after it is affected by the shock wave [59]. . . . .	41
2.21	(a) Ideal shock wave profile and (b) a representative real shock wave profile showing pressure and materials dependent characteristics such as HEL, spall strength etc. [59]. . . . .	43
2.22	(a) X-t plot showing the propagation and reflections of shock waves within a sample along with the stress profiles at different times and distances [59], (b) Free velocity curves at different strain rates showing different amounts of damage nucleated in a high specific strength steel [61], (c) Incipient and partial spall generated at different velocities in a mild steel [62]. . . . .	45
2.23	Plot showing the variation in the volume fraction of voids nucleated in copper at a pressure of 3.8 GPa as a function of the grain size and processing conditions [64, 59]. . . . .	46
2.24	Plot showing the variation in the volume fraction of voids nucleated in copper at a pressure of 3.8 GPa as a function of the grain size and processing conditions [66] . . . . .	47
2.25	Images depicting the Galvannealed layer as formed and after the application of load. (a) Different layers of the coating, 1- $\Gamma$ , 2- $\delta$ and 3- $\zeta$ , (b) cracks developed during compression, (c) cracks developed during tension [70], (d) galvannealed layer on DP steel with similar layers as seen in (a), (e) De-bonding of the galvannealed layer on DP steel under the application of a tensile load [71]. . . . .	50

2.26	Plots relating volume fraction of martensite to properties and damage mechanism of DP steels. (a) UTS as a function of $V_M$ discussed earlier by Bag et al [1]. (b) Plot of $V_M$ as a function of the ferrite grain size showing the predominant damage mechanism as martensite cracking for higher $V_M$ and moderate ferrite grain size [7, 6] . . . . .	52
2.27	(a) Vertical Sections with cycloids used to calculate $S_V$ for anisotropic microstructures, (b) Plot of $S_V$ of grains vs percent cold rolled reduction showing an increase in the grain boundary area with rolling [74].	53
2.28	(a) Use of unbiased frame for counting features in a 2-D sectioning plane, (b) Use of cycloidal area to estimate the anisotropic lineal features [74]. . . . .	55
2.29	Values of the fracture roughness profile parameter $R_L$ calculated on an Al-Li alloy on three vertical planes at (a) $0^\circ$ , (b) $120^\circ$ and (c) $240^\circ$ [81]	58
2.30	Fracture profile of DP steel with about 60% martensite. the red tracers show the fracture path lying in ferrite (bright regions) and the blue tracers show the fracture path lying in martensite (dark regions) [82] .	58
2.31	Quantitative fractography results performed on DP steel to understand the variation in ductility. (a) Direct co-relation of the dimpled region with increase in ductility confirming that the area fraction can be used a reliable technique to estimate the ductility of a material, (b) Inverse-correlation of the number density of pullouts with the ductility indicating the pull outs may be responsible for premature fracture. (c) Nominal fracture surface observed showing dimpled regions with the pull-outs that cause reduction in ductility [82]. . . . .	61
3.1	Representative etched optical micrographs showing the longitudinal sections of (a) DP 590, (b) DP 980 NC, (c) DP 980 GAN and (d) DP 980 GAD. Ferrite is the lighter phase while martensite is etched dark.	70
3.2	Representative SEM images showing the longitudinal sections of (a) DP 590, (b) DP 980 NC, (c) DP 980 GAN, and (d) DP 980 GAD. The harder phase can be identified as the phase with the relief. . . . .	71
3.3	Schematic and representative microstructure (DP 980 NC) illustrating the point counting method employed to estimate the volume fraction. Points lying in the harder phase were manually counted. If the point lay on the interface of the two phases, it was counted as 0.5 . . . . .	72

3.4	Schematic and representative SEM image (DP 980 NC) illustrating the method employed to determine the $S_V$ of the interfaces for the anisotropic sheet steels using cycloids. The number of intersections made by the interfaces with the cycloids was counted manually. . . .	73
3.5	Specimen geometries that were used to test DP 590 steel. (a) Japanese Industrial standard, used to establish the baseline for quasi-static strain rates, (b) modified miniature tensile geometry for Hopkinson bar tests, (c) modified miniature tensile geometry with extended grip sections for quasi-static strain rate tests. . . . .	75
3.6	(a) specimen geometry used for all the quasi-static and Hopkinson bar tests of DP 980 grade steels, (b) geometry used for intermediate strain rate testing at ArcelorMittal. Extended grip sections were added to improve gripping of sample. . . . .	76
3.7	(a) Schematic of the servo-hydraulic setup used for the quasi-static strain rates. High speed digital camera was used to conduct DIC, (b) Representative DIC images of the miniature tensile geometry of DP 590 showing the undeformed, completely deformed and before fracture and the fractured samples. The frame just before fracture was used to confirm the final strain in the sample . . . . .	78
3.8	(a) Tensile split Hopkinson bar setup at UA showing the striker tube and the input bar along with the pressure chamber used for firing, (b) Principle used by the tensile Hopkinson bar, (c) DP 590 sample mounted in the titanium grips developed by the UA group in house, (c) representative DIC image of DP 590 showing the frame used to compute the total strain, (d) representative DIC and strain map image showing the frame used to calculate the total strain in the DP 980 NC sample. . . . .	80
3.9	(a) Schematic showing the design and setup used for the plate impact experiments. All samples were 1 inch in diameter, (b) picture showing the target setup with VISAR probe mounted behind one sample and the two recovery samples, (c) picture showing the face that was impacted by the projectile. . . . .	83
3.10	(a) Unetched fracture profile showing the gage and grip sections along with a high magnification image of the fracture profile, (b) Etched fracture profile showing the deformed microstructures and the delamination voids. . . . .	86

3.11	Schematic showing the technique used to estimate the aspect ratio of the deformed phases in the microstructure of DP 590. The ratio $< P_L >$ along the horizontal and vertical directions gives the aspect ratio. . . . .	87
3.12	Schematic and representative low magnification fracture surface showing the central one-third area used to compute the area fraction and the systematic uniform sampling of the area to capture unbiased fields of view for the quantitative estimations. . . . .	88
3.13	Representative fracture surface showing the different features observed across all the DP steels. Dimpled regions are classified as ductile while the facets, secondary cracks and pullouts are classified as brittle. . . .	89
3.14	Representative fracture surface showing the different features observed across all the DP steels. Dimpled regions are classified as ductile while the facets, secondary cracks and pullouts are classified as brittle. . . .	90
3.15	(a) Representative fracture surface with superimposed grid used for the estimation of area fraction of different features observed. Examples of the points in the grid used to estimate each feature are also shown, (b) Representative fracture surface with an unbiased counting frame on a completely dimpled region to estimate the dimple size, (c) Low-magnification, high resolution image with an unbiased counting frame on the central one third of the fracture to estimate the number density and length of the secondary cracks. . . . .	91
4.1	The orthogonal views containing the short-transverse, transverse and longitudinal sections of (a) DP 590 and, (b) DP 980 NC. The white circles show the connectivity of the harder martensite phase. . . . .	94
4.2	The orthogonal views containing the short-transverse, transverse and longitudinal sections of (a) DP 980 GAN and, (b) DP 980 GAD steels. The white circles show the connectivity of the harder martensite phase. . . . .	95
4.3	Montages showing the extent of martensite banding along the longitudinal sections in (a) DP 980 NC and (b) DP 980 GAN . . . . .	98
4.4	SEM images showing the montage and the different sections along the thickness of the DP 980 GAD steel. The cross sections from the surface show the decarburized layer deprived of martensite. Cross sections from the center show a Dual Phase microstructure with some connectivity in martensite. . . . .	100

4.5	Variation of hardness in the longitudinal section of DP 980 GAD as function of distance from the edge. . . . .	101
4.6	Variation of (a) Volume fraction of martensite and (b) Surface area per unit volume of the harder and ferrite phase interface as a function of distance from the edge. . . . .	101
4.7	Longitudinal cross sections showing the (a) Galvannealed coating (b) magnified view of the coating on the galvannealed and decarburised steels . . . . .	102
4.8	Energy Dispersive Spectrography (EDS) peaks from three different parts of the coating and compared to the substrate. . . . .	103
4.9	Stress strain response of DP 590 steels at quasi-static and intermediate strain rates. . . . .	104
4.10	Stress strain response of DP 980 NC steels at quasi-static and intermediate strain rates. . . . .	106
4.11	Stress strain response of DP 980 GAN steels at quasi-static and intermediate strain rates. . . . .	107
4.12	Stress strain response of DP 980 GAD steels at quasi-static and intermediate strain rates. . . . .	108
4.13	SEM images of the fracture surface of DP 590 at low and high magnification at strain rates of (a) $10^{-4}/s$ , (b) $1/s$ , (c) $10/s$ and (d) $3 \times 10^3/s$	109
4.14	SEM images of the fracture surface of DP 980 NC at low and high magnification at strain rates of (a) $10^{-6}/s$ , (b) $10^{-4}/s$ , (c) $1/s$ , (d) $10/s$ , (e) $5 \times 10^2/s$ and (f) $2.5 \times 10^3/s$ . . . . .	111
4.15	SEM images of the fracture surface of DP 980 GAN at low and high magnification at strain rates of (a) $10^{-4}/s$ , (b) $1/s$ , (c) $5 \times 10^2/s$ and (d) $2.5 \times 10^3/s$ . . . . .	112
4.16	SEM images of the fracture surface of DP 980 GAD at low and high magnification at strain rates of (a) $10^{-4}/s$ , (b) $1/s$ , (c) $5 \times 10^2/s$ and (d) $2.5 \times 10^3/s$ . . . . .	113
4.17	Area fraction of Dimpled regions as a function of strain rate for DP 980 steels. . . . .	115



4.18	Area fraction of featureless faceted regions as a function of strain rate for DP 980 steels. . . . .	116
4.19	Area fraction of regions with secondary cracks as a function of strain rate for DP 980 steels. . . . .	117
4.20	Fracture profile and deformed microstructures of DP 590 NC at (a) $10^{-4}/s$ , (b) $1/s$ and (c) $3 * 10^3/s$ . Voids generated by the cracking of martensite an inter-facial fracture can be observed at all strain rates. . . . .	119
4.21	Plot showing the aspect ratio of the ferrite and martensite grains at different strain rates close to the fracture surface and away from it in the uniformly deformed region. High aspect ratio of ferrite and conversely low aspect ratio of martensite at the highest strain rate suggest a large portion of the strain was partitioned in ferrite at the highest strain rate. . . . .	120
4.22	Representative low and high magnification SEM images showing the fracture profiles of DP 980 NC at different strain rates. (a) fracture profile at $10^{-6}/s$ with a few circular voids showing delamination, (b) fracture profile at $10^{-4}/s$ showing the formation of cracks originating by martensite cracking, (c) substantially long delamination crack observed on the fracture profile at strain rate of $1/s$ , (d) Fracture profile at $2 * 10^3/s$ strain rate showing a significantly deformed microstructure and scattered elongated delamination voids. . . . .	121
4.23	Fracture profile of DP 980 GAN at strain rates of (a) $10^{-4}/s$ ; the profile shows the formation of a fissure and heavily deformed martensite bands indicating the plasticity of the phase, (b) fracture profile at $2 * 10^3/s$ showing scattered elongated voids and a few delamination voids along the banded regions of martensite . . . . .	123
4.24	Fracture profiles of DP 980 GAD at (a) $10^{-4}/s$ strain rate showing few circular delamination voids, (b) $2 * 10^3/s$ strain rate also showing largely circular voids. The elongated voids observed in the NC and GAN counterparts were not observed. . . . .	124
4.25	Representative schematic of (a) an x-t diagram for a symmetric impact experiment showing the interaction of the waves and the generation of the spall plane, (b) VISAR free surface velocity profile showing the HEL at $t_1$ , the pull back velocity and the spall signal. . . . .	125

4.26	(a) Full VISAR free surface velocity of the DP 590 tested at 600 m/s, (b) zoomed in plot to show the Hugoniot Elastic Limit (HEL), (c) zoomed in plot showing the pull-back velocity and recompression wave. Two different slopes were observed in the recompression wave. . . . .	127
4.27	(a) Full VISAR free surface velocity of the DP 980 NC tested at 600 m/s, (b) zoomed in plot to show the Hugoniot Elastic Limit (HEL), (c) zoomed in plot showing the pull-back velocity and recompression wave. Two different slopes were observed in the recompression wave. . . . .	129
4.28	(a) Full VISAR free surface velocity trace of the DP 980 NC experiment at 300m/s, (b) zoomed in plot showing the HEL, (c) zoomed in plot showing the pull back velocity and change in slope in the recompression wave. . . . .	131
4.29	(a) Full VISAR free surface velocity of the DP 980 GAD tested at 600 m/s, (b) zoomed in plot to show the Hugoniot Elastic Limit (HEL), (c) zoomed in plot showing the pull-back velocity and recompression wave. Two different slopes were observed in the recompression wave. . . . .	133
4.30	(a) Low magnification image of the spalled sample and showing the magnification at which the sample was investigated for quantitative fractography, (b) Representative SEM image of the quasi- cleavage fracture observed , (c) High magnification image of the quasi-cleavage brittle fracture in DP 590. . . . .	135
4.31	(a) Spalled sample generated from the 600m/s experiment, (b) Low magnification image of the mounted spalled sample and showing the region of the sample investigated for quantitative fractography, (c) Low magnification image of the race-track like striations seen on the fracture surface, indicated by white arrows, (d) Low magnification image of a largely brittle fracture observed. . . . .	136
4.32	Representative SEM images of DP 980 NC showing the heterogeneities in the fracture surface by highlighting the ductile (a) to (d) and brittle fracture features (e) to (h). (a) Racetrack like striations, (b) largely dimpled region, (c) region showing a mixture of the striations, dimples and a few brittle facets, (d) high magnification image of the striations showing the presence of dimples and flat featureless areas, (e) low magnification image showing brittle fracture, (f) large void observed in a brittle region, (g) facets showing brittle fracture and (h) high magnification image of the faceted region interspersed with a few voids. . . . .	137

4.33	(a) Low magnification image of the spalled sample of DP 980 GAN with a large area occupied by the long bands surrounded by dimples and a zoomed in image showing the magnification at which the sample was investigated for quantitative fractography, (b) Representative SEM image of the long bands parallel to the rolling direction, (c) High magnification image of the quasi-cleavage brittle fracture and (d) High magnification image of the flat bands with dimples. . . . .	139
4.34	(a) Low magnification image of the spalled sample of DP 980 GAD with a large area occupied by the long bands surrounded by dimples and a zoomed in image showing the magnification at which the sample was investigated for quantitative fractography and the area containing the flat bands and dimples, (b) Representative SEM image of the long bands parallel to the rolling direction and a corresponding high magnification image of the flat bands with dimples. . . . .	140
4.35	(a) Optical unetched montage of the incipient spall sample showing large voids, (b) elongated voids observed on the center of the sample, (c) large coalesced voids (d) collection of smaller connected voids . .	141
4.36	(a) optical microstructure showing the deformed martensite bands around large voids, (b) shows significant rotation of the phases near a void, (c) shows bending and rotation of the phases close to the void, (d) SEM image showing a deformation band linking two separated voids, (e) high magnification image of the heavily deformed and rotated martensite, (f) interfacial delamination cracks observed on the center of the specimen.	143
4.37	(a) Vertical deformation band connecting two cracked regions, (b) horizontal deformation band connecting cracks to a network of voids, (c) deformed and rotated martensite between two interfacial delaminated cracks. . . . .	145
5.1	Representative SEM images of the different AHSS steels with different volume fractions of martensite. (a) HSLA-completely ferritic with dispersed carbides [85], (b) DP 590-with 30% martensite and ferrite matrix, (c) DP 980 NC-with 70% martensite and dispersed ferrite islands, (d) USIBOR-100% martensitic microstructure. . . . .	148
5.2	Quasi-static stress-strain response at strain rate of $10^{-4}/s$ of HSLA (blue), DP 590 (red), DP 980 NC (black) and USIBOR (yellow). Miniature geometry used for HSLA 590 and DP 590 and REL geometry used for DP 980 NC and USIBOR 1500. . . . .	150

5.3	Plot showing the intermediate strain rate stress-strain response at the highest strain rates the AHSS steels were tested for. (a) HSLA and (b) DP 590, both at $3 * 10^3/s$ , (c) DP 980 NC at $2.5 * 10^3/s$ and (d) USIBOR at $10^3/s$ strain rate. All the steels showed an intital peak in stress arising due to mechanical instabilities. . . . .	152
5.4	Plot showing the variation of the UTS of the AHSS steels as a function of strain rate. Two different regimes in the strain rate sensitivity were observed. . . . .	154
5.5	Plot showing the change in the UTS of the four steels from the lowest to the highest strain rate . . . . .	155
5.6	Plot showing the strain rate sensitivity of the total elongation of the AHSS steels. All steels showed an increased elongation at intermediate strain rates that could be attributed partially to adiabatic heating. .	157
5.7	Plots showing the change in the (a)total elongation and (b) Post-Uniform Elongation(PUS) of the four steels from the lowest to the highest strain rate . . . . .	158
5.8	Representative SEM images of the fracture surfaces at the lowest strain rate and the highest strain rate achieved using the hopkinson bar for (a) HSLA, (b) DP 590, (c) DP 980 NC and (d) USIBOR. The secondary cracks were observed the most in the DP steels which had a connected martensitic phase. . . . .	160
5.9	Representative low magnification SEM images of the fracture surfaces for (a) DP 590, and (b) HSLA 590. HSLA 590 shows a considerable necked region compared to DP 590 . . . . .	161
5.10	Plot showing the area fraction of dimples in the four steels as function of strain rate. DP 980 NC shows the highest sensitivity to strain rate.	164
5.11	Representative SEM images showing the spalled fracture surfaces of (a) DP 590 and (b) DP 980 NC. . . . .	167
5.12	Plot showing the time and velocity adjusted recompression curves of DP 590 and DP 980 NC. DP 590 shows a longer void nucleation region.	168
5.13	Quasi-static stress strain response of the three DP 980 grade steels. The increase in strength can be attributed to a finer microstructure in the case of DP 980 GAN and GAD. This refinement did not affect the total elongation of the steels at this strain rate. . . . .	172

5.14	Intermediate stress strain response of the three DP 980 grade steels. No difference in strength was observed at these strain rates, however, the elongation in DP 980 NC was the highest. . . . .	173
5.15	Plot showing the variation of UTS with the logarithm of strain rate for DP 980 NC, GAN and GAD. DP 980 NC shows the highest increase in strength as a function of strain rate. . . . .	174
5.16	Plot showing the variation of total elongation with the logarithm of strain rate for DP 980 NC, GAN and GAD. DP 980 NC shows the highest increase in elongation as a function of strain rate, while GAN and GAD remain largely insensitive. . . . .	176
5.17	Schematic of the hypothesis for the fracture and formation of fracture surface features of DP 980 NC at different strain rates. The increase in the local stress leads to the formation of higher area fraction of voids at higher strain rates. The lowest strain rates are dominated by the presence of the facets while dimples dominate at the higher strain rates. Thus, there is a change in the dominant operative fracture mechanism with an increase in strain rate. . . . .	178
5.18	Schematic of the void formation and coalescence in DP 980 NC at different strain rates. At lower strain rates, the threshold for void nucleation is not reached at multiple locations, while at higher strain rates, a large number of voids are nucleated, especially along the interfaces. . . . .	179
5.19	Schematic showing the fracture mechanism hypothesis for DP 980 GAN at different strain rates. The presence of a higher degree of banding along with an increase in the interfacial area leads to higher local stresses that increases the area fraction of voids. The higher area fraction of secondary cracks in the fracture surface is attributed to the higher degree of harder phase banding in these steels and increased interfacial surface area. . . . .	181
5.20	Schematic of the void formation and coalescence in DP 980 GAN at different strain rates. At lower strain rates the threshold for void nucleation is not reached at multiple locations, while at higher strain rates, a large number of voids are nucleated, especially along the interfaces. . . . .	182
5.21	Schematic showing the fracture mechanism for DP 980 GAD steels at different strain rates. With a highly dispersed harder phase (compared to GAN), the void initiation sites in GAD steels is increased, leading to the high area fraction of dimples in this steel. The presence of secondary cracks and a connected harder phase only in the center of steel also indicates that these cracks are formed due to decohesion. . . . .	183

5.22	Schematic of the void formation and coalescence in DP 980 GAD at different strain rates. At lower strain rates the threshold for void nucleation is not reached at multiple locations, while at higher strain rates, a large number of voids are nucleated, especially along the interfaces.	184
5.23	Plot showing the time and velocity adjusted recompression curves of DP 980 NC and DP 980 GAD. DP 980 GAD shows a longer void nucleation region.	185
5.24	High magnification SEM images from the center of the short transverse direction of (a) GAN and (b) GAD steel.	186
5.25	(a) Low magnification SEM image of the fracture surface before and after the partial polishing to reveal the deformed microstructure that participated in the fracture, (b) formation of a secondary crack by the linking of voids and decohesion of the ferrite and harder phase, (c) image showing the blunting of a cracks by a large harder phase island and interfacial decohesion along a long crack, (d) and (e) high magnification images of the microstructure consisting of the secondary cracks showing interfacial decohesion between the ferrite and harder phase.	188
5.26	Stress-Strain response of the JIS and miniature tensile geometry at strain rates of $10^{-4}/s$ and $1/s$ . The effect of forced elongated on the miniature samples is observed clearly at both strain rates.	190
A.1	Schematic showing the fracture mechanism for DP 980 GAD steels at different strain rates. With a highly dispersed harder phase (compared to GAN), the void initiation sites in GAD steels is increased leading to the high area fraction of dimples in this steel. The presence of secondary cracks and a connected harder phase only in the center of steel also indicates that these cracks are formed due to decohesion.	200
A.2	Schematic of the void formation and coalescence in DP 980 GAD at different strain rates. At lower strain rates the threshold for void nucleation is not reached at multiple locations, while at higher strain rates, a large number of voids are nucleated, especially along the interfaces.	200

## Abstract

Dual Phase (DP) steels are a class of Advanced High Strength Sheet (AHSS) steels which are used as structural components of an automobile body. They possess a good combination of strength and formability coupled with crashworthiness. The microstructure of DP steels consists largely of ferrite and martensite. These commercial grade steels may also contain a coating layer to protect the steel against atmospheric corrosion. These steels are exposed to strain rates of the order of  $10 - 10^2/s$  during sheet metal forming operations, and strain rates of the order of  $10^2 - 10^4/s$  can be reached under an automotive crash condition. The fracture mechanisms of these DP steels at slow strain rates are well understood; however, these may not be representative of the material's fracture response under dynamic or high strain rate loading conditions. The mechanical behavior of DP steels under dynamic rates ( $10^2 - 10^4/s$ ) has been studied in the past but there are no conclusive results on the operative fracture mechanisms. Another important aspect currently lacking is the effect of the protective coating under dynamic rates. Hence, to address these critical gaps, an understanding of the role of all microstructural features (substrate and coating) on the fracture response of DP steels under varying strain rates is required. Thus, the objective of this work is to investigate and quantitatively characterize the fracture surfaces of DP steels generated under a wide range of strain rates and gain an understanding on the microstructure-based fracture mechanisms. Four DP steels, of two nominal strength levels (590 MPa and 980 MPa) are subjected to strain rates spanning twelve orders of magnitude ( $10^{-6}$  to  $10^6/s$ ).

Three kinds of 980 MPa DP steels with and without protective coatings are investigated. While DP 590 and DP 980 contained different amounts, all three DP 980 steels contained similar volume fractions of martensite. The differences in the volume fractions and connectivity of the martensite in the different DP steels are

estimated using quantitative characterization of microstructures. The mechanical properties are measured for strain rates spanning twelve orders of magnitude from  $10^{-6}$ /s (quasi-static strain rate) to  $10^6$ /s (dynamic strain rates). Servo-hydraulic machines, Hopkinson bar and plate impact gas gun experiments are used to generate the different magnitudes of stresses and strain rates. An important aspect of the work performed in this study is that all of the quasi-static and intermediate strain rate experiments on the four DP steels are conducted with the same specimen geometry to eliminate the effects of post-uniform elongation and allow valid comparisons of ductility across different magnitudes of strain rates.

The effect of the volume fraction of martensite is discussed both in terms of its effect on the mechanical properties and on the fracture response. Discussions on the effects of adding protective coating layers and the resulting microstructure of the three DP 980 steels are provided to understand the differences in the mechanical properties and fracture response of these steels at both quasi-static and dynamic strain rates. The strain rate sensitivity of both the mechanical properties and fracture response as a function of the underlying microstructure is also explored. The main thrust of the current work is to employ quantitative fractography, a stereological technique, to understand the effects of the quantity, distribution and morphology of the various microstructural constituents of the substrate and coating on the operative fracture mechanisms of DP steels under varying strain rates. For this purpose, the area fractions of various features observed on the fracture surfaces are estimated. Ultimately, hypotheses for the fracture mechanisms of these steels as a function of strain rate are presented. The significance of this study is to help gain a deeper understanding on the differences in microstructure obtained in DP steels of similar nominal strength levels when processed to contain protective coatings, and the effects of these differences on the mechanical properties and fracture response under strain rates representative of automotive crash. The results of the current work will help design better grades for



improved forming and higher crash-resistant automobile parts.

# CHAPTER 1

## INTRODUCTION AND PROBLEM DEFINITION

The development of Advanced High Strength Sheet (AHSS) Steels was a major technological and scientific breakthrough for the steel industry. AHSS steels were developed in response to the strong demands of the automotive industry which were largely two fold, first an increased demand for passenger safety, and second, an increase in the fuel efficiency of the automobile by reducing its weight. The AHSS developed proved to be a great match to satisfy both these demands as they are designed to have high-strengths coupled with moderate ductility and improved crash-resistance which is ideal for increased passenger safety. They also have a high strength to weight ratio reducing the weight of the automobile and increasing fuel efficiency. Dual Phase steels are a class of AHSS Steels that were among the first type of AHSS to be incorporated in the weight reduced automotive parts. The nominal microstructure of these steels largely consists of a soft and tough ferrite phase with a stronger and harder martensite. The morphology and distribution of these phases determine the mechanical properties of these steels. For corrosion protection DP steels can be galvanized or galvanized among various possible alternatives. The adherent coatings applied have a distinct microstructure and fracture behavior which is different from the substrate. The coating layers are generally brittle and reduce the bendability of the underlying steel substrate. In order to enhance the bendability, galvanized DP steels have been manufactured with a decarburised layer (surface depleted of Carbon) to produce a graded microstructure with improved bendability and corrosion protection.

In order to understand and improve the crash-worthiness of DP steels, an in depth understanding of their fracture behavior is necessary. This understanding can

be largely divided into (a) capturing the operative fracture mechanisms of the DP steels, (b) understanding the change in the mechanisms with the presence of a microstructural gradient, and (c) evaluating the fracture mechanisms of the protective coating layers under quasi-static and dynamic strain rates. In the past, various authors [1, 2, 3] have attempted to understand a microstructure based fracture response of DP steels, albeit at low strain rates. In order to understand the crashworthiness of DP steels, they need to be subjected to stresses and strains under dynamic loading conditions. Various authors [4, 5] have investigated the mechanical response of DP steels under dynamic conditions but not a holistic fracture response. Any material derives its properties from its microstructure. As the processing conditions of the steels studied and reported vary considerably in the literature, the resulting microstructures are also a variable for every study conducted. Hence, a detailed quantitative analysis of the microstructure is required to gain a complete understanding of the properties. Another important feature affecting the mechanical properties, specifically the elongation at fracture is dependant on the geometry of the specimen tested. The deformation of a material under dynamic rates is often a highly localized phenomenon, and hence a geometry dependent aspect. Thus, the elongation at fracture of a material tested under quasi-static and dynamic strain rates with different geometries cannot be compared. Furthermore, capturing the fracture response of the protective coating is significant in order to gain a complete understanding of the fracture response of commercial DP steel. Galvannealed protective coatings on steels are brittle and may possess cracks even in the absence of load. Investigating the response of these cracks and those generated during loading is therefore required. Quantitative Fractography is an essential tool that can be incorporated to gain a complete understanding of the operative fracture mechanisms under varying strain rates. Thus, the *motivation* for the proposed work is to employ quantitative fractography and conduct an extensive study of the microstructure based fracture response of DP steels under quasi-static

*and* dynamic strain rates.

The goals of the proposed work are to expand the existing knowledge of the dynamic behavior of DP steels and to validate and provide a comprehensive analysis of the fracture mechanisms under dynamic conditions to design DP steels which can ultimately improve passenger safety and reduce the weight of the automobile. Thus, to meet these goals, the objectives of the proposed research are:

- To characterize the strain rate dependence of the mechanical response of four varieties of a DP steel , (i) DP 590: with lower volume fraction of the harder martensite phase and 590 MPa nominal strength at quasi-static strain rates, (ii) Three kinds of DP 980, which contain higher volume fractions of the harder phase: one non-coated labelled DP 980 NC, second with a galvanized surface coating labelled DP 980 GAN, and the third with a galvanized surface coating and decarburised layer labelled DP 980 GAD. Specimen geometry of samples using servo hydraulic and Hopkinson bar test equipment were maintained identical to eliminate the effects associated with sample geometry.
- To quantitatively characterize three dimensional microstructure of the tested specimens via unbiased stereology and quantitative fractography.
- To utilize experimental data from mechanical testing and microstructural quantification to establish quantitative relationships concerning effects of bulk microstructure, microstructural gradient due to decarburized layer, and galvanized surface coating on the strain rate dependence of mechanical properties and fracture micro-mechanisms in the DP steels

## **CHAPTER 2**

### **BACKGROUND**

The current work is focused on understanding the microstructure-driven fracture micro-mechanisms and mechanical properties of Dual Phase (DP) steels as a function of strain rate. Further, the addition of protective coatings such as galvanized steels, as well as those with a microstructural gradient is also investigated. Stereology and quantitative measurements conducted on the microstructures and fracture surfaces are used to hypothesize the operating fracture mechanisms and sensitivity of the mechanisms to the strain rates the steels are exposed to, and their underlying microstructures. The following sections contain a brief background on Dual Phase steels, its processing, and, the effects of different microstructural features and strain rate on the mechanical properties, in addition to a detailed description of the fracture mechanisms of DP steels at different strain rate regimes. Background information on the use of stereology and quantitative fractographic analysis techniques is also presented.

#### **2.1 Dual Phase Steels**

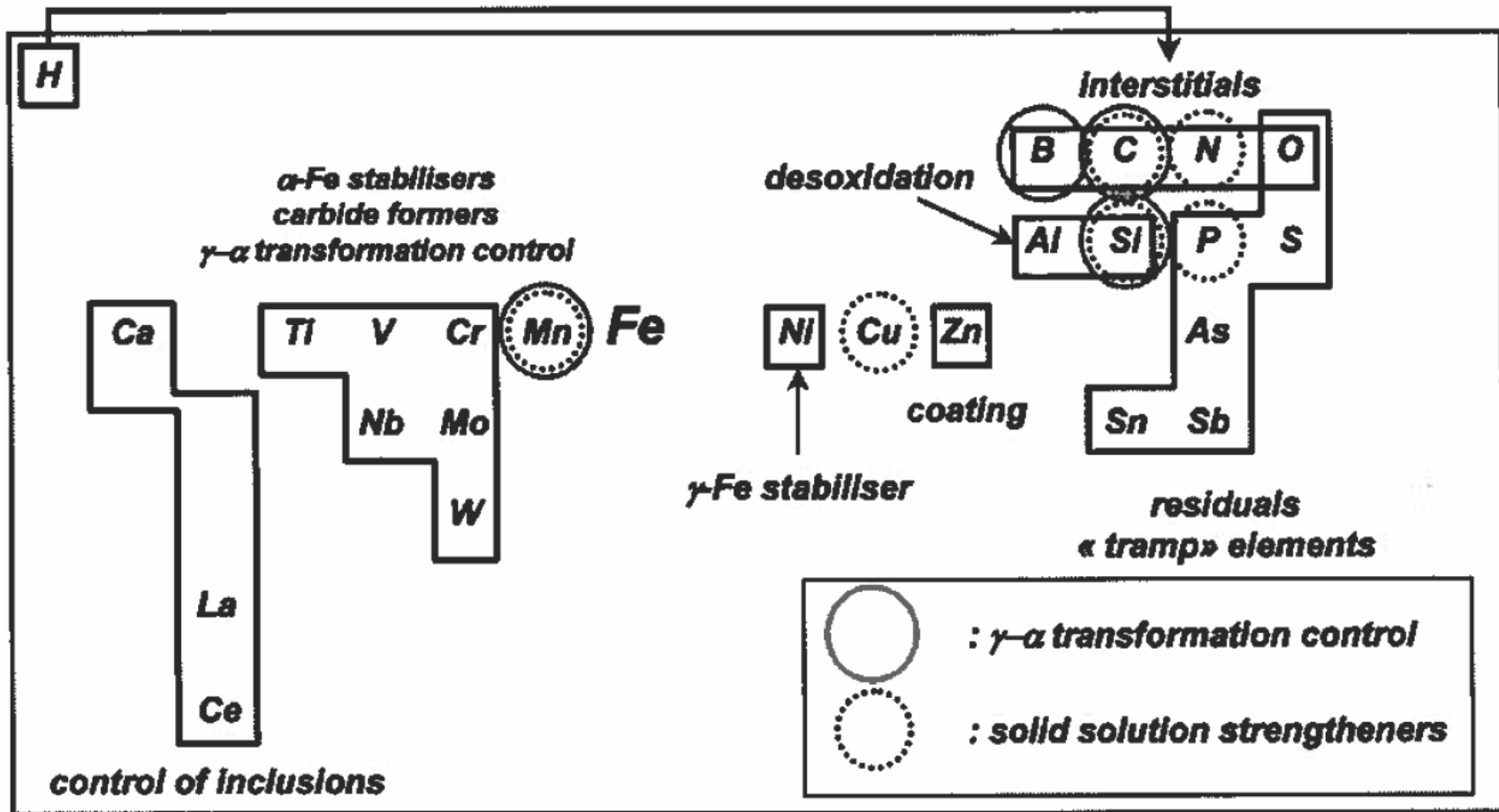
The term Dual Phase steels, or DP steels, refers to the class of Advanced High Strength Sheet (AHSS) steels that is predominantly composed of two microstructural constituents : a soft ferrite phase and a hard martensite phase. However, based on the processing route taken, trace amounts of bainite and retained austenite can also be present. An additional microstructural feature present in these commercial sheet steels is a protective coating to ensure better corrosion resistance. Dual Phase Steels were developed in response to the increased demand by the automotive industry for passenger safety against crashes and vehicle weight reduction [6, 7]. These steels

are designed to have a combination of high strength and energy absorption against crashes, coupled with moderate ductility. The DP are mainly used in the structural components such as B-pillars and side impact beams of an automobile [6, 7, 8]. The chemical composition and processing of different grades of DP steels vary considerably resulting in a variety of microstructures. The addition of protective coatings may also necessitate changes in the alloying composition depending on the specifics of the manufacturing methods. The following sub-sections discuss the nominal composition and generic processing routes for DP steels without any coatings, and how the changes in the composition and processing conditions to manufacture coated DP steels influence the microstructure.

#### 2.1.1 Alloying elements and processing of Dual Phase steel

A typical DP steel consists of low carbon content ( $< 0.2\%C$ ) with Mn in the range of 0.5 – 1.5%, and micro alloying elements such as Nb, Mo, Cr, Ni, Ti and V, to name a few. The effects of some of the alloying elements are given in table 2.1 [9]. The alloying elements influence the stability and the rates of phase transformations. Thus, they play an important role in determining the resulting microstructure which ultimately controls the fracture mechanism.

Table 2.1: Function of typical alloying elements of DP steels [9]



Another factor which influences the microstructure and fracture mechanism is the thermo-mechanical processing of DP steels. A DP microstructure is attained by a continuous annealing process. The cold-rolled steel with a ferrite-pearlite or ferrite-bainite structure is heated to either the inter-critical temperature (between  $A_1$  and  $A_3$  temperatures) or austenitized completely. This is followed by rapid quenching to convert the austenite completely into martensite (in case of inter-critical annealing), or intersect the C-curve to partially transform the austenite to ferrite and quench the remaining to martensite. Figure 2.1 illustrates the TTT diagram and superimposed quenching curves (red curves on the TTT diagram) showing both the processing routes [6]. Based on the processing route followed, the DP steel may contain some trace amounts of retained austenite and/or bainite, which are undesirable as they are not as strong as martensite. The amount of martensite formed is dependent on three major factors: the alloying elements present, the quenching rate, and the inter-critical annealing temperature. While the inter-critical temperature and holding time control the nucleation and growth of austenite formed and hence the resulting martensite, the quenching rate controls the residual stresses. A slow cooling to the quench temperature followed by rapid quenching results in lower residual stresses and better overall mechanical properties [6].

The aforementioned processing technique is suitable for a cold-rolled DP steel without any coatings. However, protective coatings are an important part of commercial DP steels, as they protect the steel substrate from corrosion. The processing technique employed to obtain a galvanized DP steel is discussed ahead.

**Galvanized DP steels:** The processing of the galvanized layer begins by immersing a clean, oxide free sheet steel in a molten zinc bath. The zinc adheres to the sheet metal and the excess molten zinc is removed. The zinc bath contains small amounts of Al added to: (i) improve the reflectivity of the coating, (ii) reduce the ox-



idation of zinc in the bath and (iii) improve the ductility and adhesion of the coating by preventing the formation of brittle Zn-Fe phases. Hot dip galvanizing is followed by annealing the sheet in the temperature range of  $500^{\circ} - 565^{\circ}C$  to promote the diffusion of zinc and iron to form alloy layers within the coating. The galvannealing process also has an unintentional effect of auto-tempering the martensite. Additionally, since the cooling rate of the coated steel is typically slower compared to its uncoated counterpart, the hardenability of galvannealed steels needs to be designed carefully. To accommodate these process changes, the alloy composition may need to be altered from the nominal uncoated, faster cooled DP steels. Two important parameters to be considered when altering or choosing the alloying elements for galvannealed steels are that they need to improve the hardenability and at the same time not impede the wettability of the coating layer to the substrate. A number of studies have discussed the particular elements that can be used to obtain a galvannealed steel with a dual phase core [10, 11, 12, 13, 14]. Figure 2.2 (a) shows the schematic of a nominal galvannealing heat treatment process resulting in a dual phase microstructure. Since the galvannealing process can result in the auto-tempering of martensite in addition to slower cooling rates, it is important to ensure that the yield point elongation (YPE) phenomenon does not reappear. Figure 2.2 (b) shows the stress-strain behavior of a galvannealed steel confirming the absence of YPE and continuous yielding, indicating the presence of sufficient amount of martensite. Figure 2.2(c) shows the schematic of a typical galvannealing process during the production of steel coils.

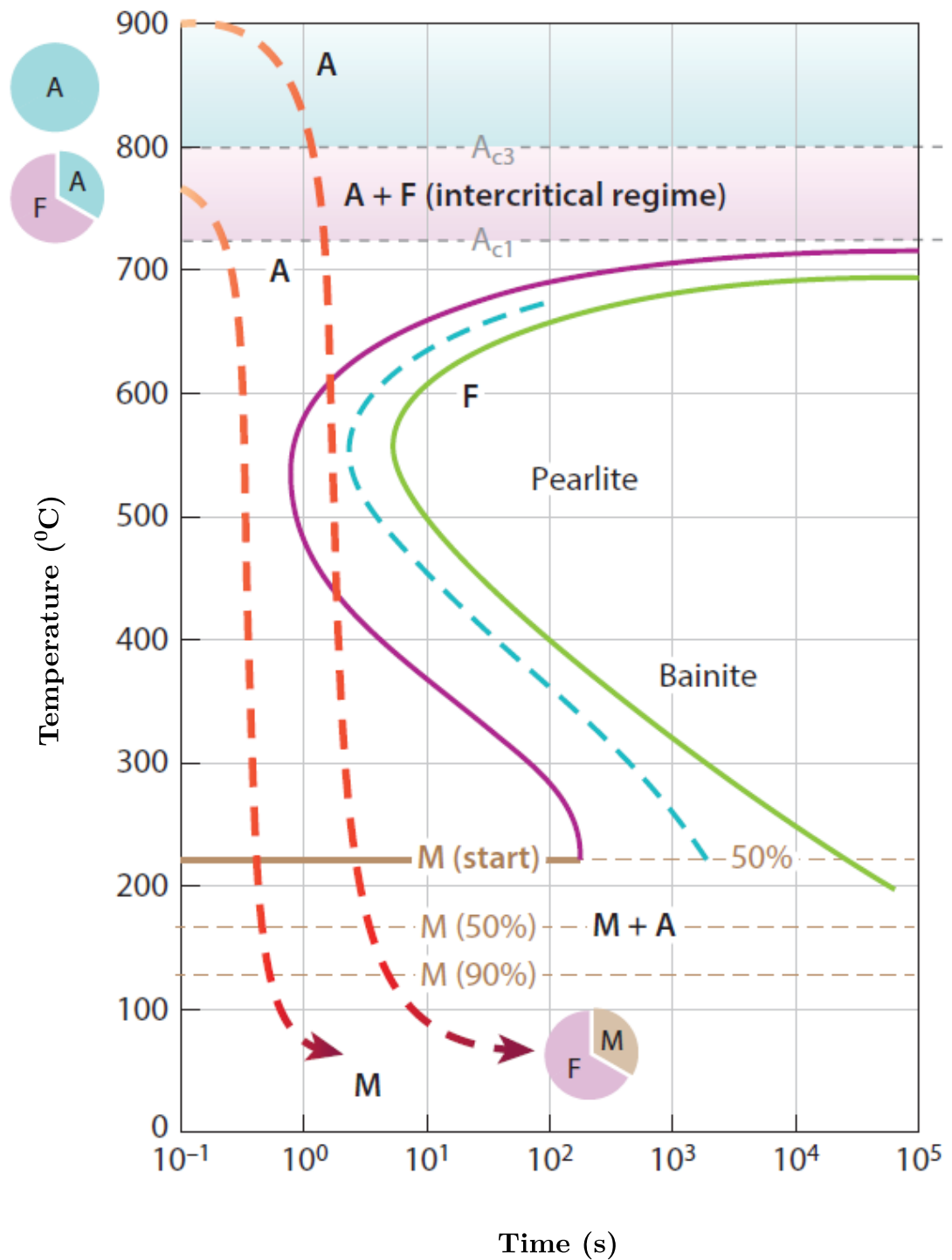


Figure 2.1: Typical TTT diagram of a steel; red curves depict the superimposed quenching curves from above the  $A_{c3}$  temperatures (completely austenised) or from the intercritical regime resulting in the formation of ferrite and martensite microstructure. [6]

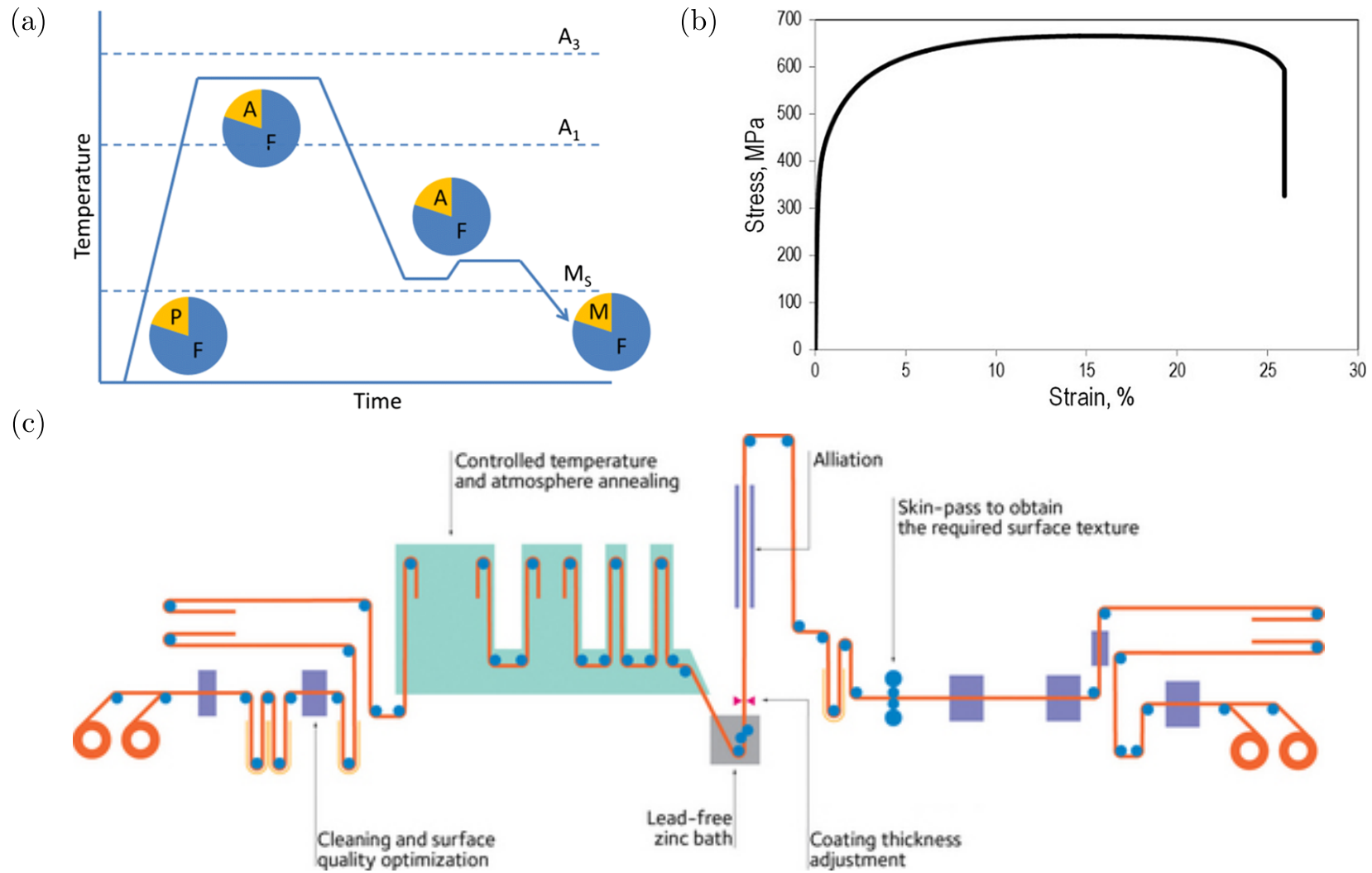


Figure 2.2: (a) Heat treatment of a typical galvanized DP steel, (b) Representative stress-strain curve of a galvanized DP steel showing continuous yielding with ~ 20% martensite [10], (c) Schematic layout of galvannealing line for producing coils [15]

Although the galvanized layer enhances the corrosion performance of DP steels, it reduces the bendability of the steel which is important for the production of commercial parts.

As a method to improve the bendability of High Strength Steels, ArcelorMittal has designed a novel method of decarburizing the surface of dual phase steels which results in a gradient in the final microstructure. The decarburizing is obtained by introducing an oxidizing atmosphere and controlling the depletion of carbon from the steel surface. This results in a steel with a graded microstructure with a depleted carbon surface and a dual phase core.

The microstructures of DP steels can have a lot of variables such as the volume fraction, distribution and size of phases, coating layers and microstructural gradients. This has a direct impact on the mechanical properties and the fracture mechanisms. A detailed discussion is provided ahead.

## **2.2 Mechanical properties and fracture response of DP steels at Quasi-static strain rates.**

The microstructural features of DP steels are largely responsible for the resulting mechanical properties and fracture response. The following sub-sections discuss these effects in the case of the steels tested at quasi-static strain rates ( $10^{-4}$  to  $10^0/s$ ).

### 2.2.1 Effects on Mechanical Properties

DP steels consist of a composite structure composed of a soft and ductile ferrite along with a harder, stronger martensite. Previous studies have shown that the tensile strength of DP steels increases *linearly* with an increase in the volume fraction of martensite and can be determined using a simple rule of mixtures, given in equation

1 [16, 17].

$$\sigma_{DP} = \sigma_{\alpha}(1 - V_M) + \sigma_M V_M \quad (1)$$

where,  $\sigma_{DP}$  is the strength of the DP steel,  $\sigma_{\alpha}$  and  $\sigma_M$  are the strengths of ferrite and martensite phases respectively, and  $V_M$  is the volume fraction of martensite. However, a study conducted by Birgani et al. [18] demonstrates that the rule of mixtures does not apply in all circumstances. The study investigated the effect of increasing volume fraction of martensite ( $V_M$ ) by keeping the bulk carbon in the steel the same. As a result, as  $V_M$  increases, the carbon partitioned in the martensite phase reduces. Thus, at higher  $V_M$ , deviation from the rule of mixtures is observed as the strength of the steel is shown to be dependent on not only the volume fraction of martensite but the carbon partitioned in it. Figure 2.3 (a) plots the carbon partitioned in the steel as a function of  $V_M$ , and figure 2.3(b) shows the effect of the same on the tensile strength of the steel.

On the contrary, studies conducted by Fonstein et al. [19] conclude that the tensile strength and the yield strength are both independent of the carbon content in the steel. Steels with varying carbon content in the bulk steel but similar  $V_M$  were prepared such that the carbon partitioned in the martensite phase for a given  $V_M$  would be different. As shown in figure 2.4 (a) and (b), steels with different bulk carbon but similar  $V_M$  shows a similar response for tensile and yield strengths. While the insensitivity of YS can be attributed to elastic deformation of martensite at low strains, the tensile strength behavior is more complicated and is controlled by additional microstructural features, such as the connectivity of the ferrite and martensite phases.

As discussed in previous sections, processing conditions play an important role in determining the microstructures of DP steels. Based on the size of the resulting ferrite and martensite phases, they can be classified as coarse or fine-grained DP steels. The distribution of martensite within the microstructure can be classified as

banded or uniformly distributed equiaxed. Banding of martensite is a common phenomenon observed in these microstructures and is largely attributed to the presence of alloying elements such as manganese and silicon that promote the segregation of carbides leading to preferential martensite formation (usually along the center of the steel thickness). A review of the literature [20, 1, 6] has shown that a fine, equiaxed ferrite grain structure with uniformly distributed martensite results in the best combinations of strength and ductility. Although the volume fraction of martensite is expected to be inversely related to the total elongation, the latter is a function of how voids nucleate and coalesce in the steel and, thus, is influenced more by the strength and distribution of the phases, than by the volume fraction alone.

Bag et al. [1] conducted a series of tensile tests on DP steels with varying volume fraction of martensite ( $V_M$ ). Steels with lower  $V_M$  had a coarse ferrite grain structure with carbides and martensite, while they obtained a finer ferrite grain structure with martensite and carbides at higher  $V_M$ . The highest  $V_M$  of 80% showed blocks of martensite and ferrite. As illustrated in Figure 2.5 (a) and (b) the tensile test results illustrate an increase in the strength *and* total elongation of DP steels with an increase in  $V_M$ . The increase in strength due to high martensite content is expected while the increase in elongation is due to a finer microstructure. The elongation drops with the highest  $V_M$  which has a coarse microstructure. The behavior of DP steels also follows the Hall-Petch relationship with a finer microstructure resulting in a higher strength, as shown by Calcagnotto et.al [20] and illustrated in figure 2.5 (c).

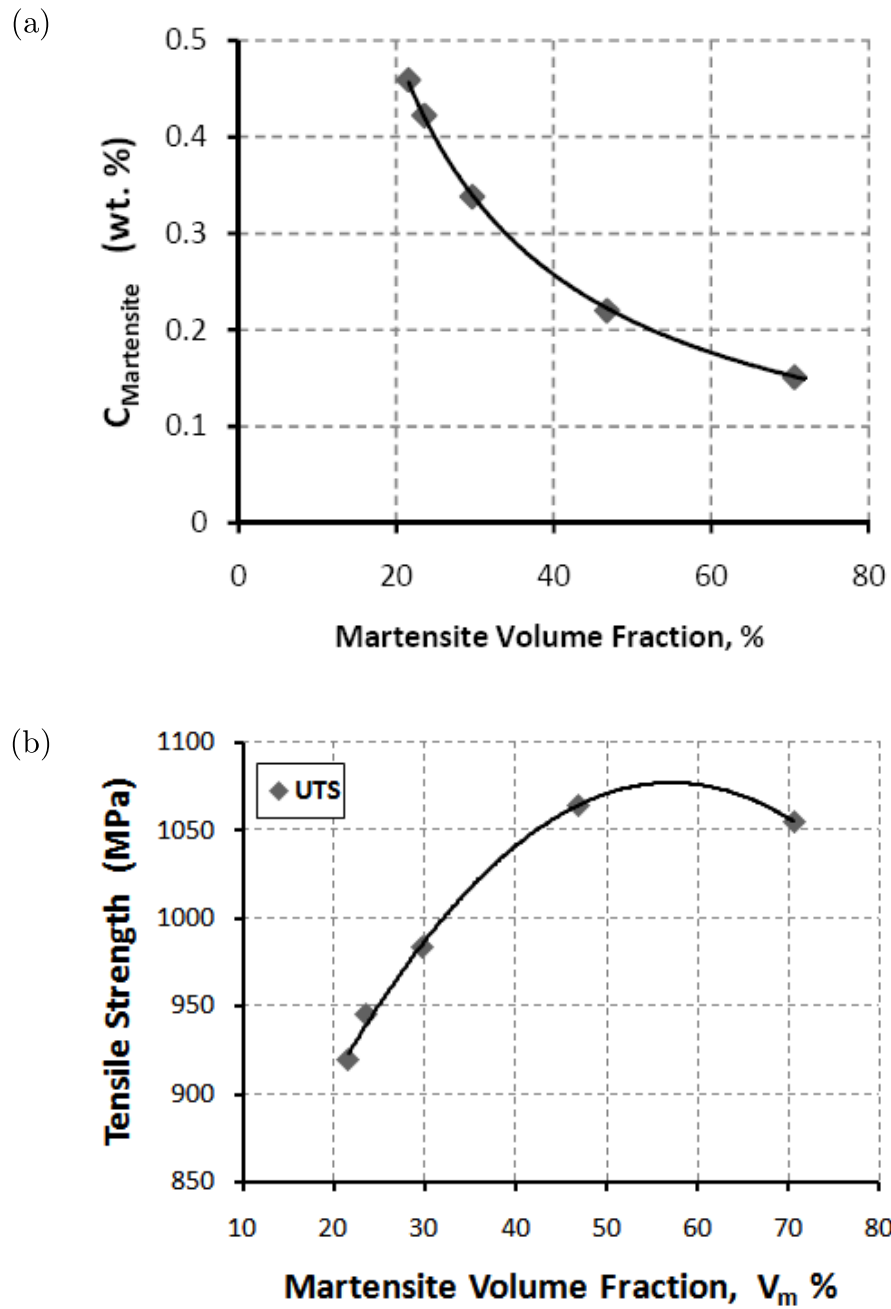


Figure 2.3: Plots showing the effect of increasing volume fraction of martensite ( $V_M$ ) (for a given composition of steel) on (a) carbon content of martensite and (b) UTS of the steel. Increasing the  $V_M$  reduced the carbon in the martensite which in turn did not increase the UTS beyond a threshold of  $V_M$  as the strength of the martensite is derived from the amount carbon partitioned in it [18]

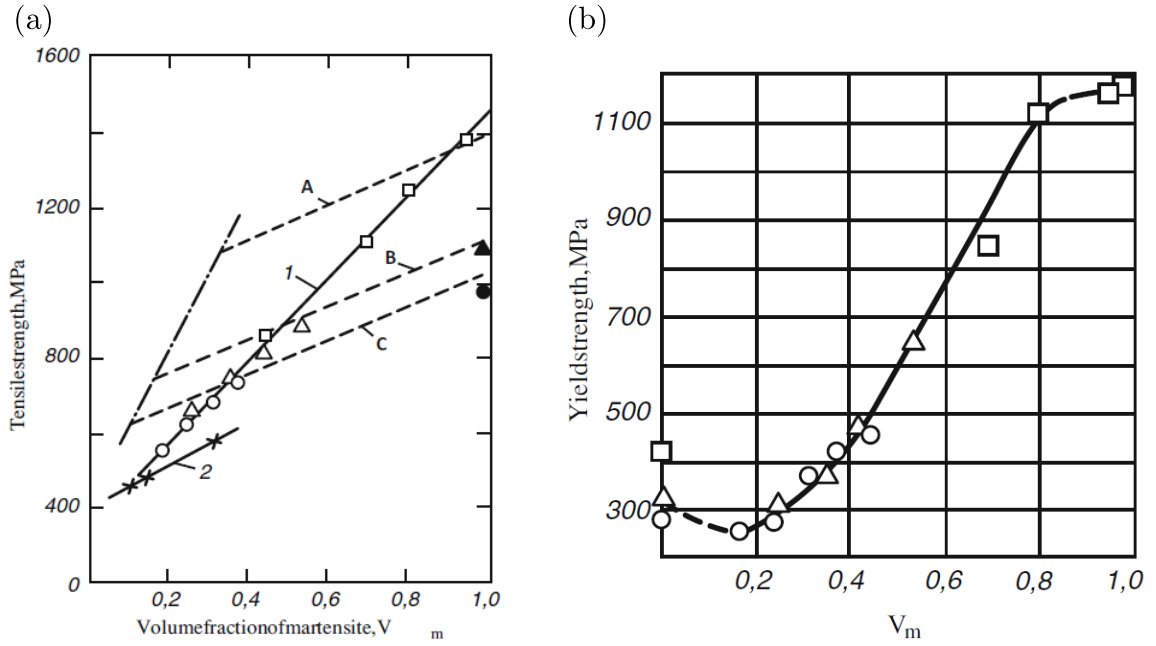


Figure 2.4: Plots showing that the (a) tensile strength and (b) yield strength depend only on the volume fraction of martensite and are independent of the carbon content in the DP steel. The open circles represent carbon levels of 0.07%, open triangles represent 0.10% and open squares represent 0.18%. The dashed lines correspond to the strength levels calculated by the authors using various models. [19]



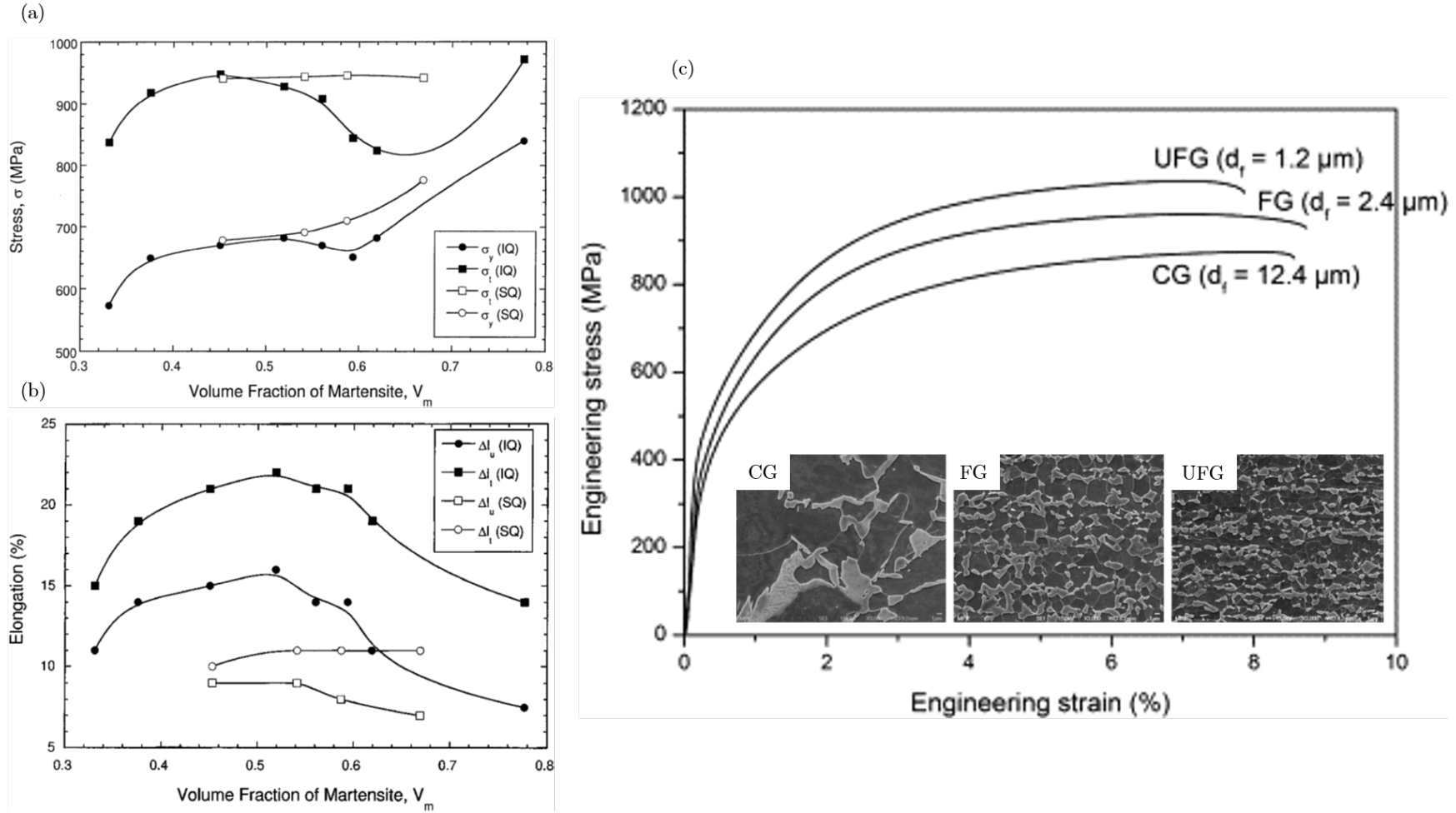


Figure 2.5: Plots showing the effect of increasing  $V_M$  on the (a) increase in strength and (b) largely an increase in total elongation of DP steels. Excluding the 80%  $V_M$ , higher  $V_M$  resulted in a finer microstructure. [1], (c) Plots showing the effect of refining the microstructure on the strength and ductility of DP steels where  $d_f$  is the average ferrite grain size. The Ultra Fine grained DP steel showed the highest strength [20]

Dual Phase steels show continuous yielding and high initial strain hardening. The continuous yielding phenomenon is attributed to the presence of mobile dislocations. The absence of the yield point elongation is attributed to the presence of a certain amount of martensite, and processing conditions imposed on it [19]. The strain hardening behavior of DP steels has also been widely studied and different stages within the hardening curve have been identified. A number of models including the Hollomon [21], Pickering [22] and Bergstrom[23] model have been used to capture the stress-strain response of the DP steels. Birgani et al. [18] studied the influence of martensite volume fraction on the work hardening behavior of DP steels and observed that steels with a volume fraction of greater than 70% showed a two-stage hardening process. Figure 2.6 (a) and (b) show the strain hardening behavior for DP steels with different volume fractions of martensite. While a lower volume fraction shows single stage hardening, higher volume fraction shows two stages. A different result was observed by Zhang et al. [24] by varying the morphology, connectivity, and volume fraction of the martensite phase and using a Crusard-Jaoul (CJ) model. A multi-stage hardening behavior is converted to a single stage as the volume fraction of martensite is increased. The different stages included, first, the deformation of ferrite and the movement of Geometrically Necessary Dislocations (GNDs) at the ferrite-martensite interface. The second stage involved predominantly the deformation of ferrite and the third stage involved the deformation of both the phases. The morphology of martensite was also observed to influence the strain hardening behaviour. Blocky martensite showed a lower strain hardening than fibrous martensite for similar volume fractions as shown in Figure 2.6 (c) and (d). The deformation and fracture behavior of DP steels will be discussed in detail in the sections ahead.

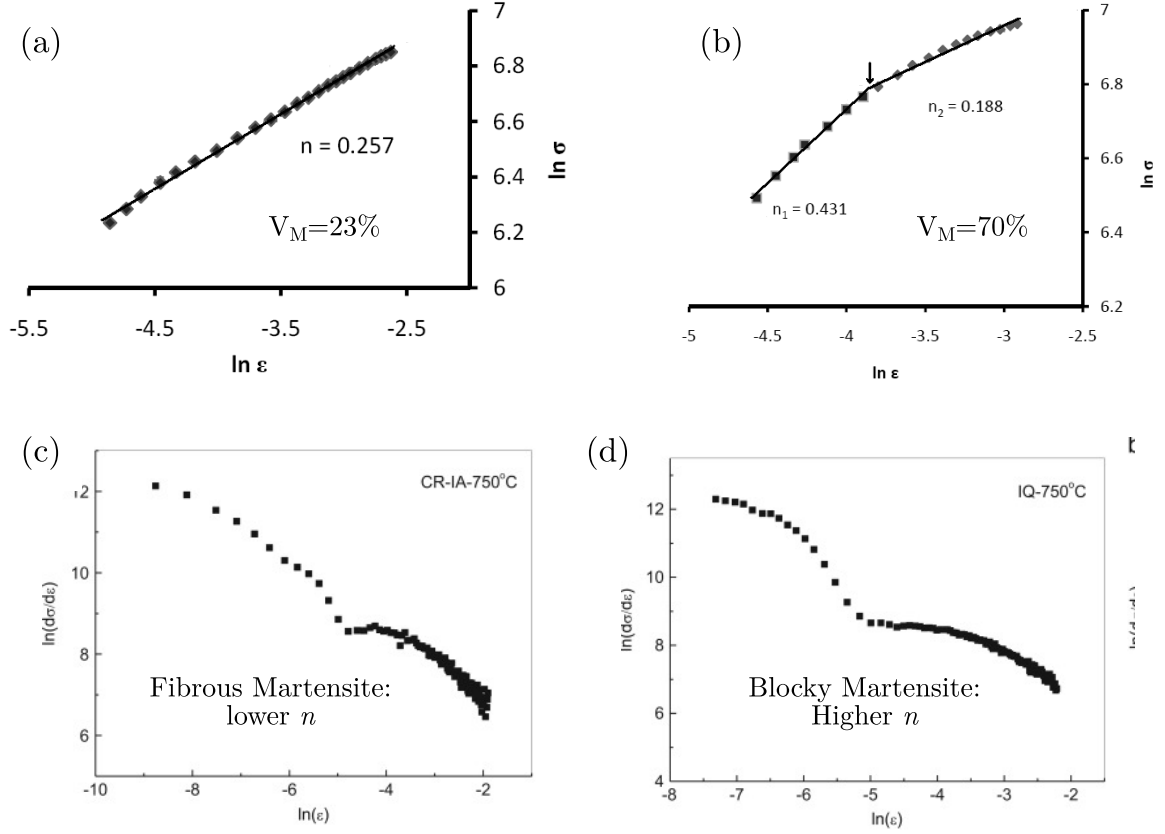


Figure 2.6: Strain hardening behavior using Hollomon analysis of DP steels as a function of volume fraction of martensite at (a) lower volume fraction and (b) higher volume fraction of martensite. The number of stages of strain hardening increase with an increase of volume fraction of martensite. Strain hardening behavior of DP steels using the Crussard-Jaoul analysis as a function of the morphology of martensite with (c) fibrous martensite and (d) blocky martensite [24]

### 2.2.2 Effect on deformation and fracture response

The following discussion has been subdivided to discuss the deformation of DP steels and crack initiation followed by the fracture surfaces resulting from uniaxial tensile tests.

**Deformation and strain partitioning in DP steels:** Since DP steels consist of a composite structure with the phases having starkly different plasticity, the global strains in the steel are not partitioned equally between the ferrite and martensite phases. This in-homogeneous deformation can be classified into three stages: the

first stage is when both phases deform elastically; the second stage is when ferrite deforms plastically but martensite remains elastic; and the third stage is when both phases deform plastically [24, 25]. The partitioning ratio has also been observed to be a function of the volume fraction of martensite. For steels with a similar bulk carbon, a higher martensite volume fraction can lead to a tougher martensite which can deform to a greater extent when compared to the same steel quenched to have a lower volume fraction of martensite. Figure 2.7 shows the strain partitioning ratio between the two phases at different volume fractions of martensite [25].

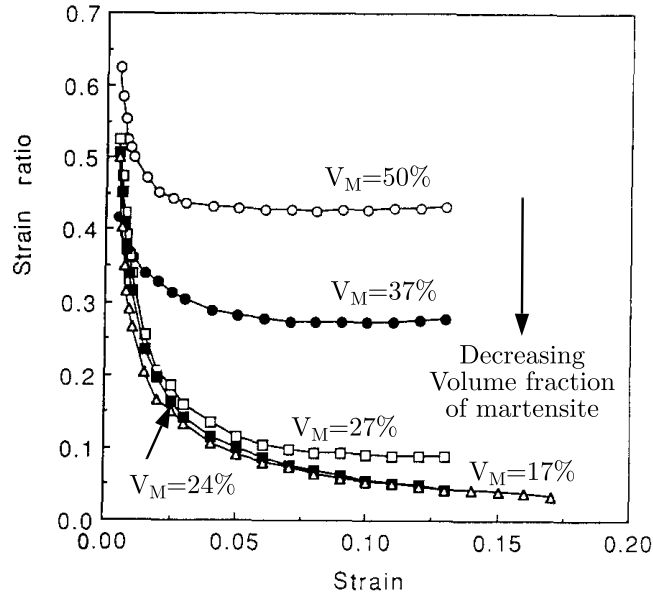


Figure 2.7: Plot showing the strain partitioning ratio as a function of the volume fraction of martensite with the higher volume fractions of martensite showing a higher ratio indicating a greater toughness and plasticity of the martensite phase [25].

Another important microstructural feature which controls deformation and strain partitioning is the connectivity and distribution of the phases. Park et al. [26] studied this phenomenon by using four DP steels with similar volume fractions of martensite ( $\sim 30\%$ ) but varying size of the phases and connectivity. They found that the connectivity of martensite leads to an increase in the deformation of the phase and a reduction in the extent of strain partitioning between the phases. Dispersed islands

of martensite mean a continuous ferrite matrix enabling the deformation by slip to continue by propagating through ferrite grain boundaries. On the other hand, in a connected martensite network, this deformation is restricted and enables the stress being partitioned into the harder phase, thus showing greater martensite plasticity. This is illustrated on the equivalent strain maps of the different DP steels in Figure 2.8.

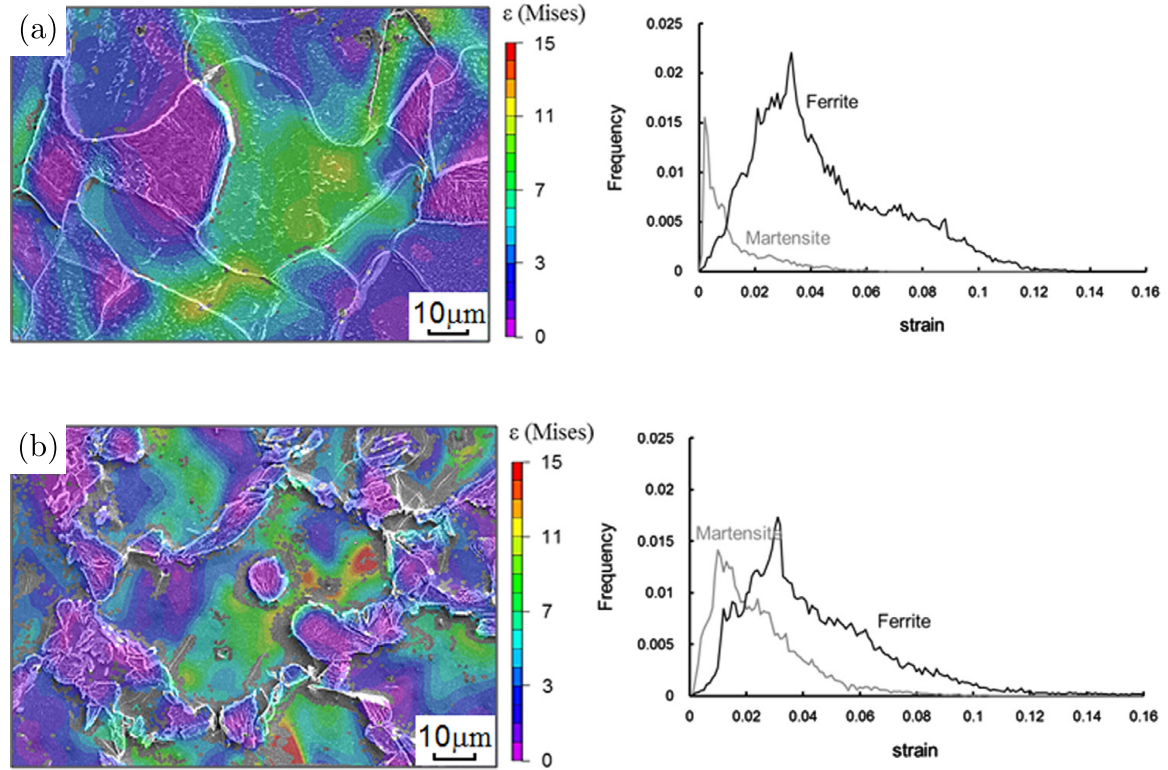


Figure 2.8: Equivalent strain maps and amount of strain partitioned into the ferrite and martensite phases at different strain levels for (a) dispersed martensite phase and (b) connected martensite phase. The connected martensite phase shows greater plasticity [26].

**Void Nucleation and growth** The fracture mechanisms of DP steels are largely governed by void nucleation, growth, and coalescence [6, 1, 5]. As elucidated in the works by Cingara et al. [2], Bag et al. [1] and Ramazani et al. [3], the failure of DP steels is initiated by martensite cracking. Ramazani et al. [3] reported that

martensite cracking is initiated at a comparatively lower plastic strain in steels in banded and coarse microstructures, in comparison to steels with fine and evenly distributed martensitic structures. Owing to the crack initiating at a lower threshold of strain, the crack propagates earlier and leads to premature fracture and low ductility. Figure 2.9 comprises the cracking of martensite under plastic strain for (a) banded microstructure and (b) equiaxed microstructure. Hence, even microstructures with a higher  $V_M$  but a finer grain structure of ferrite and evenly distributed martensite can lead to higher ductility as observed by Bag et al. [1].

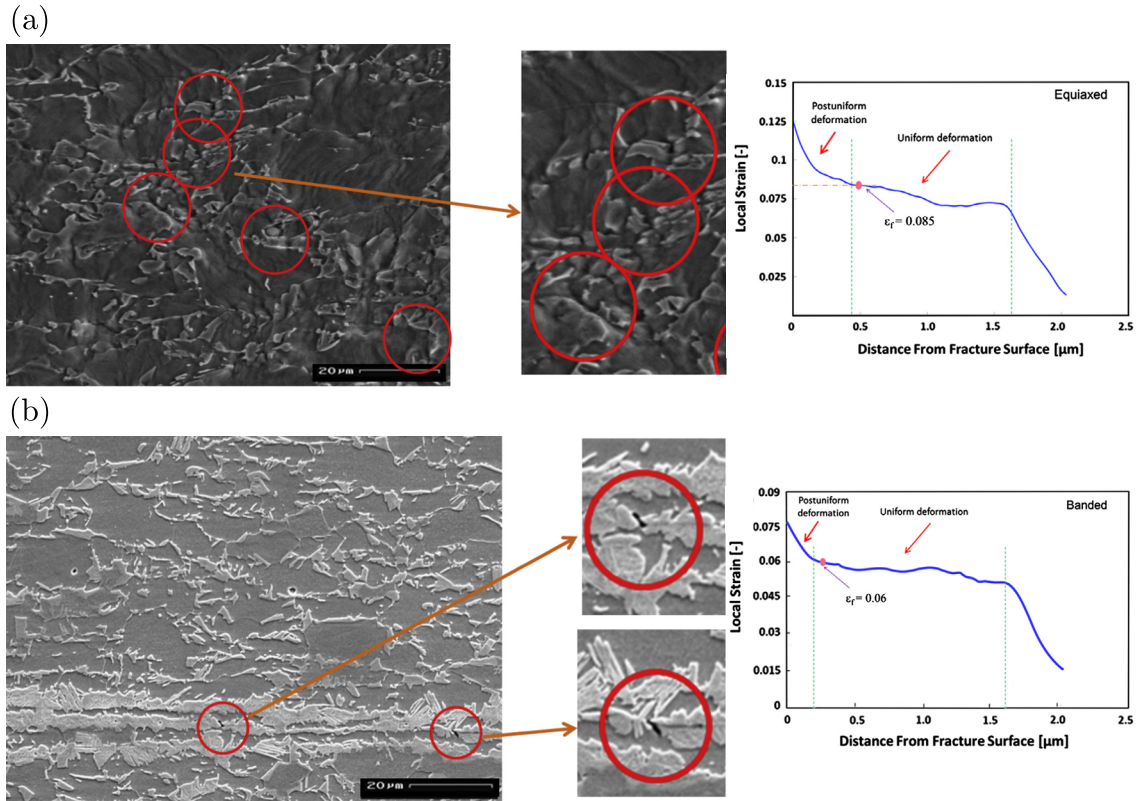


Figure 2.9: Deformed microstructures and fracture profile deformation with different martensite distributions for (a) dispersed martensite showing greater fracture strain and (b) banded martensite showing a lower fracture strain. Irrespective of distribution, both steels showed fracture initiation by martensite cracking [3]

Initiation of voids on inclusions and decohesion at the ferrite-martensite phases are also important damage mechanisms. Lai et. al [27] observed a change in dominant crack initiation mechanism to be a function of the volume fraction of martensite.

While at higher volume fractions of martensite, the cracking of the phase (especially in the connected martensitic bands) was observed to be dominant, with a decrease in the volume fraction, interfacial decohesion can become the prominent method of damage initiation. This can be attributed to a more strained interface with a lower volume fraction of the harder martensite since it has higher carbon partitioned in it. Figure 2.10 shows the dominant damage initiation mechanism at different volume fractions of martensite.

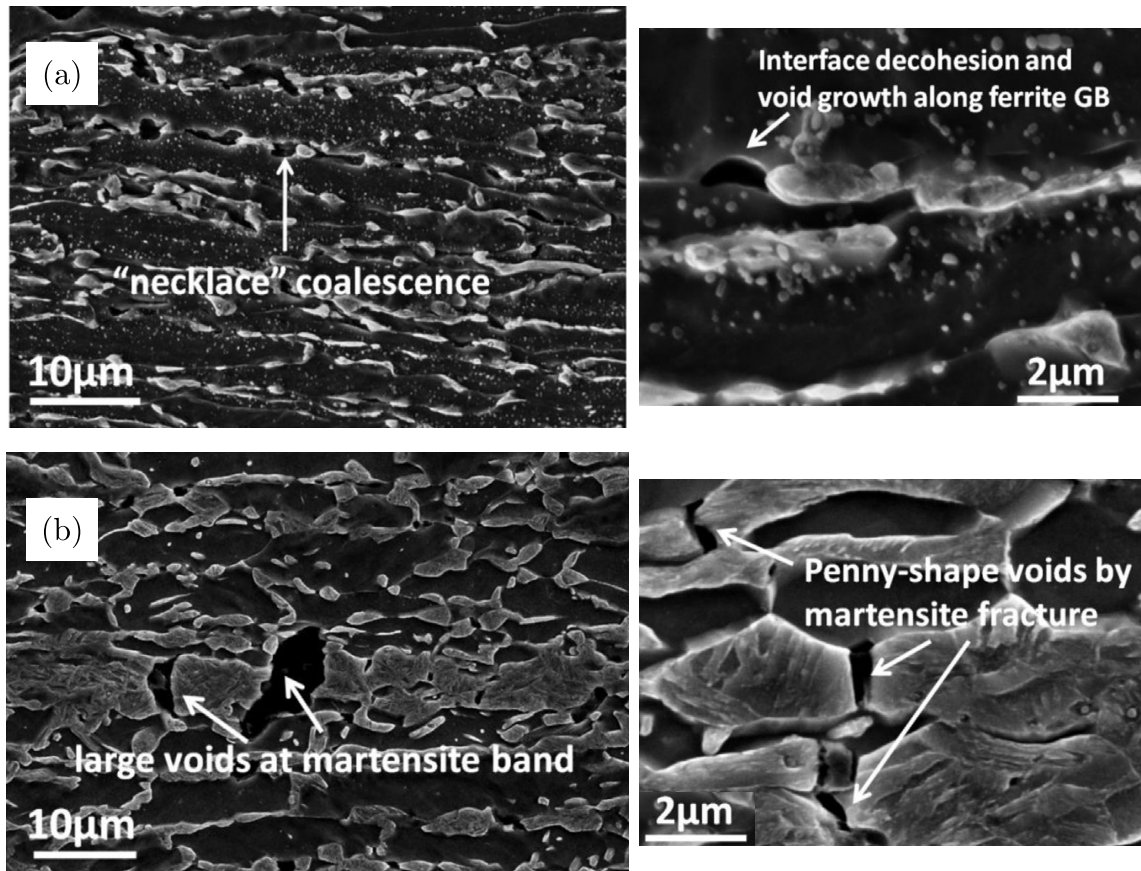


Figure 2.10: Fracture initiation in DP steels as function of the volume fraction of martensite showing (a) interfacial decohesion at lower volume fraction of martensite (b) cracking of martensite bands at higher volume fractions of martensite [27].

Voids nucleated during the deformation process have been quantified by using X-Ray microtomography [28], and void counting [29, 30] techniques. The size and distribution of voids are also observed to be a function of both the volume fraction and

distribution of martensite. Mazinani et. al [29] observed a decrease in the number and area fraction of voids as the volume fraction of martensite increased. This is attributed to the increased plasticity of martensite at higher volume fractions with the same carbon content as the lower volume fractions. In addition, while void nucleation shows a linear behavior with the far field thickness strain at lower volume fractions of martensite, the higher volume fraction of martensite shows a non-linear response as shown in figure 2.11 (a). A connected and banded martensitic structure displayed a greater plasticity compared to an equiaxed martensitic structure, as depicted by the red circles in figure 2.11 (b). Figure 2.11 (c) and (d) show the variation in the distribution of voids in DP steels as a function of the volume fraction and far field thickness strains.

Additional information regarding the mode and mechanism of fracture can be obtained by observing the characteristics of the fracture surface

### 2.2.3 Fracture surface response

The fracture surfaces of DP steels are largely ductile and dominated by dimples at all volume fractions of martensite. However, a relationship between the fracture features and the microstructural features has been observed. Lai et al. [27] observed a qualitative increase in the formation of brittle facets in the fracture surface at higher volume fractions of martensite. Park et al. [26] found that a connected martensitic structure prevented substantial necking of the specimen and also led to the formation of qualitatively finer dimples. Figure 2.12 shows the fracture surfaces of DP steels with different martensite connectivity.

Cingara et al [31] attempted to identify ferrite and martensite on the fracture surface, figure 2.13 (b). Features which have been described as larger and deeper dimples along the center line of a sample have been reported to occur due to central band of the martensite phase as shown in figure 2.13(a). A few studies [32, 33] have



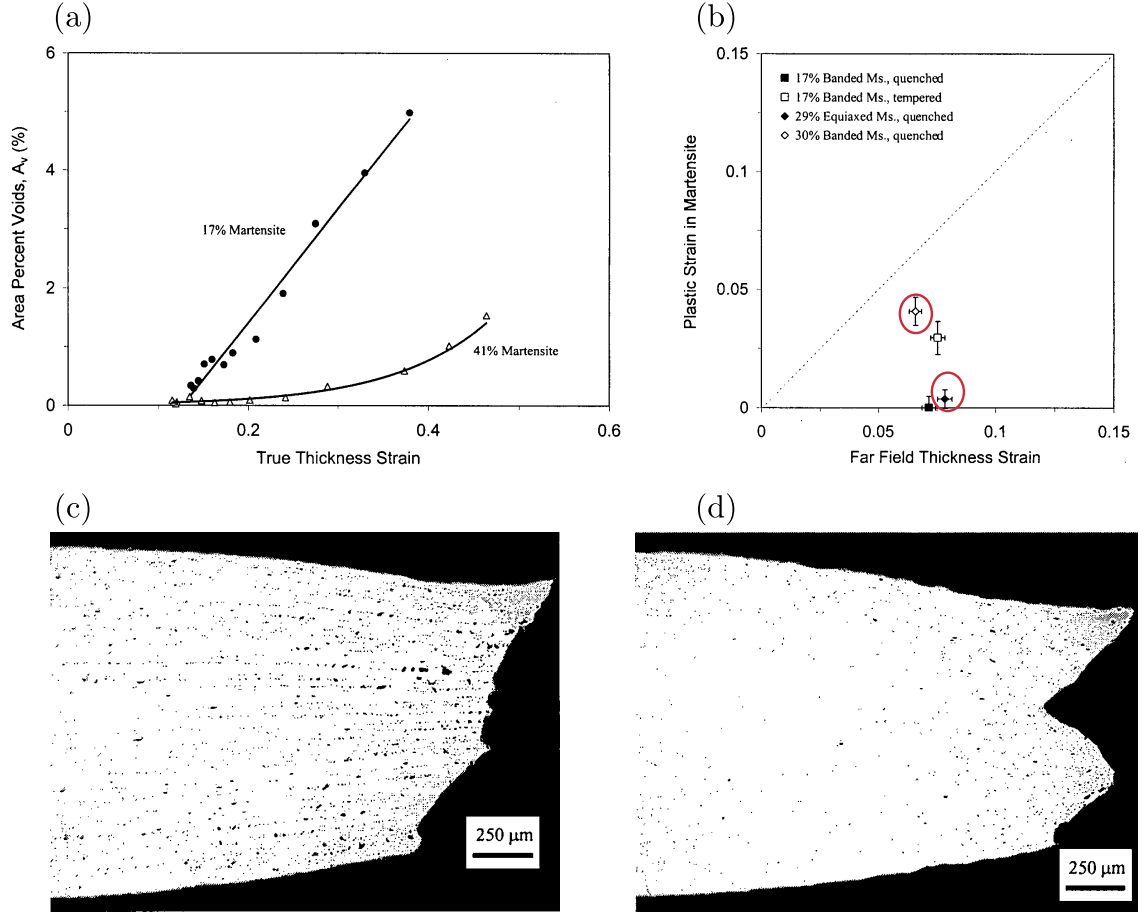


Figure 2.11: (a) Plot showing the distribution of voids as a function of volume fraction of martensite with lower volume fractions showing a larger area fraction and a linear dependence of voids as a function of true thickness strain, and a higher volume fraction of martensite showing fewer voids, (b) plot showing the strain in the martensitic phase as a function of the distribution of martensite. The red circles show a larger strain in the banded structure vs the equiaxed structure, (c) Fracture profile showing the distribution of voids in the steel with 17% martensite and banded structure, (d) fracture profile showing the distribution of voids with 41% martensite and banded structure. [29]

identified brittle features observed in the center of the steel, and have associated their origin to manganese sulphide (MnS) inclusions along the martensite segregated central line. Similar features have also been observed in TRIP steels with a central harder phase band in the microstructures [34]. Figure 2.13 (c) and (d) show the features identified and the EDX map confirming the presence of MnS inclusions.

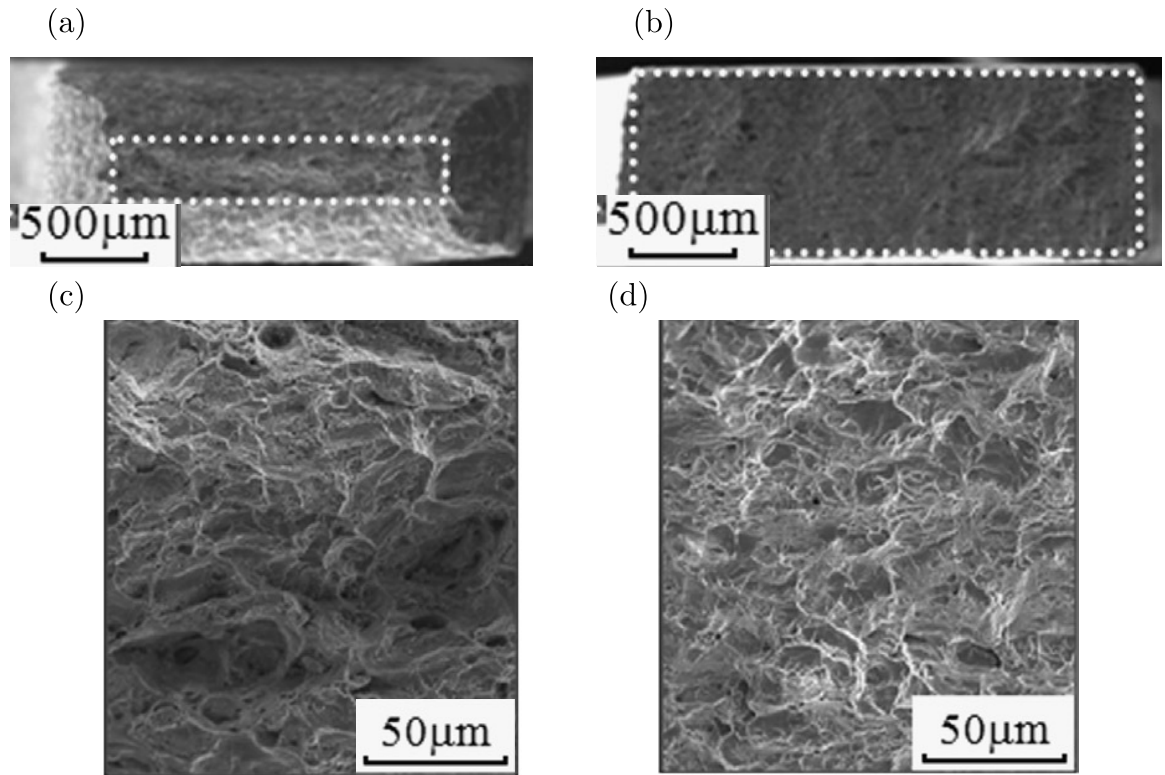


Figure 2.12: (a) Low magnification fracture surface of a DP steel with an equiaxed martensite distribution showing considerable necking, (b) low magnification fracture surface of DP steel with a connected martensitic structure preventing substantial necking, (c) higher magnification image of (a) showing a ductile dimple fracture and (d) higher magnification image of (b) showing dimple ductile features. The authors qualitatively characterized the dimples in the connected martensite steel to be finer [26].

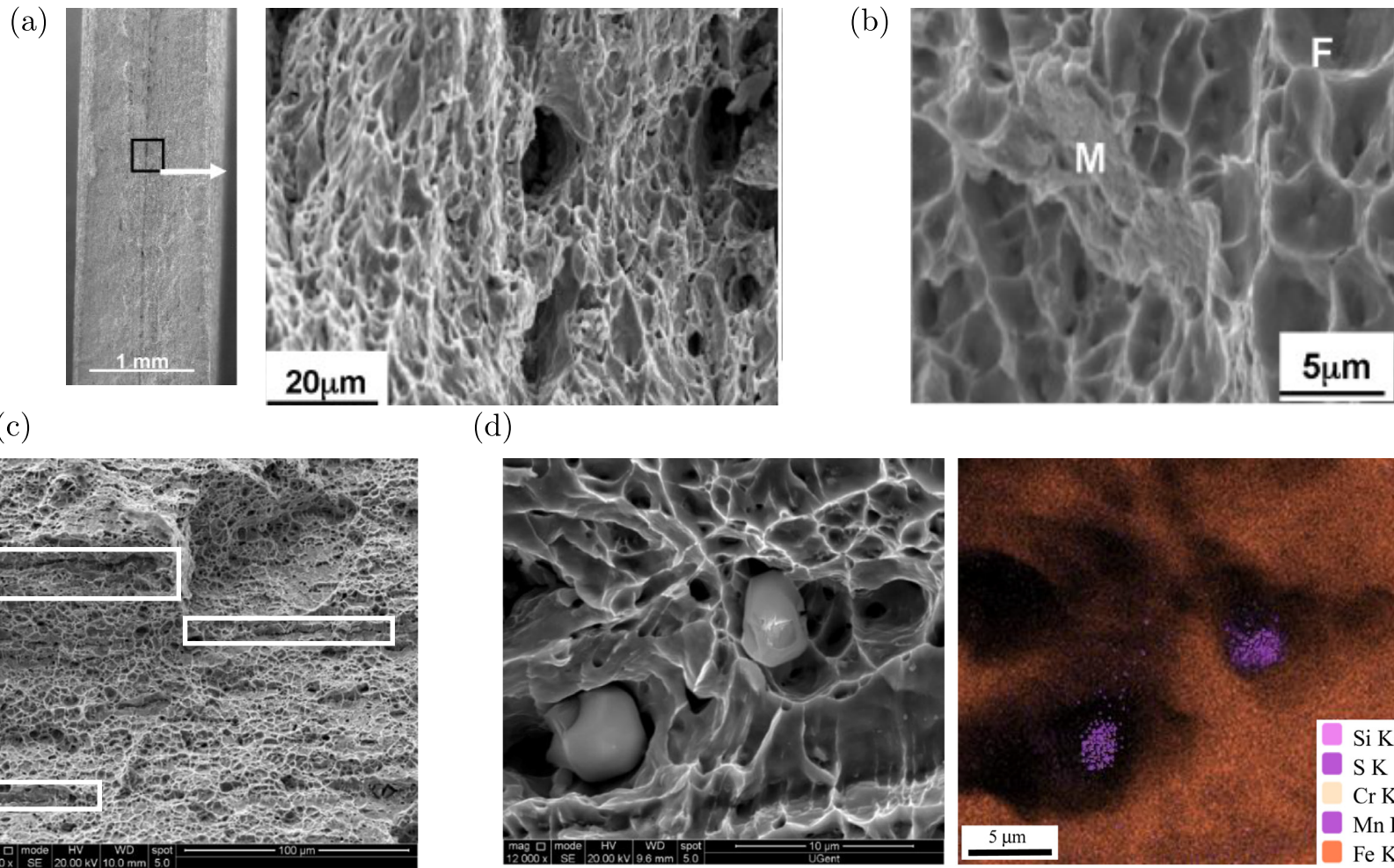


Figure 2.13: (a) Fracture surface of DP steel showing a central crack running corresponding to the central band of martensite, (b) a high magnification fracture surface identifying ferrite and martensite, (c) Low magnification SEM images of the brittle regions highlighted by the white rectangles, (d) higher magnification images in the previously identified brittle regions showing the inclusions and the EDX map confirming the inclusions to be MnS [32].

### **2.3 Mechanical properties and fracture response of DP steels at high strain rates.**

As previously discussed, DP steels are used as the structural components of an automobile, thus demanding characteristics such as high formability during manufacturing and crash worthiness during use are requirements. Forming operations subject a material to strain rates of the order of  $10^2/\text{s}$  to  $10^2/\text{s}$ , while crash worthiness testing involves strain rates of the order of  $10^2/\text{s}$  to  $10^4/\text{s}$ . Hence, in order to comprehensively determine the mechanical response of Dual Phase steels, a detailed understanding of its behavior as a function of these higher strain rates is required. This section reviews the understanding by considering the following aspects:

- (a) Introduction to dynamic testing of sheet steels
- (b) Strain rate sensitivity of DP steels: dynamic strain rate tensile tests.
- (c) Fracture response under dynamic strain rates.
- (d) Plate Impact dynamic tensile (spall) tests

Varying the strain rate of a material during testing provides two important pieces of information: First, it determines if the deformation is occurring under isothermal or adiabatic conditions based on the speed of the test [35]. Second, it determines the strain rate sensitivity of the material based on the hardening response of the material. [36, 37, 38]. Under quasi-static conditions, once a material is deformed plastically, work hardening occurs due to interlocking of dislocations. Under high strain rates, an opposing effect of work-hardening and work-softening can occur due to adiabatic heating and insufficient time for dissipation of heat generated due to plastic deformation[4]. Mason et al. [39] have reported that about 80-90% of the energy is converted to heat during dynamic testing of aluminum and steel.

### 2.3.1 Introduction to dynamic testing of sheet steels at Intermediate strain rates

The uniaxial tensile properties of Dual phase steels under quasi-static strain rates have been well documented in the literature. In order to subject the material to dynamic rates, experiments such as the Hopkinson bar test (also known as the Kolsky bar) have been conducted. Bertram Hopkinson in 1914 [40] developed a novel method of subjecting a metal bar to dynamic strain rates and measuring the stress pulse propagating through it. Kolsky and Davis [41, 42] improved the method by using two bars and incorporating electrical condensers and cathode ray oscilloscopes to record the stress pulse. Though these experiments were originally designed to subject the specimen under compression, with further advancement of the field, tension and torsion testing methods have also been developed[43, 44].

Figure 2.14(a) illustrates the basic working principle of the Hopkinson bar [45]. As the striker impacts the incident bar, a compressive stress wave is propagated along the bar. Upon reaching the transmitted bar-specimen interface, part of the wave is reflected and part is transmitted through the specimen. The transmitted wave propagates through the specimen and enters the transmitted bar. Strain gauges mounted on the incident and transmitted bar capture the real time stress pulses propagating through them. Under the safe assumption that the bars remain elastic and wave dispersion being minimal, the measured stress pulses can be attributed to the response of the specimen alone. The equations below relate the strains obtained from the strain gauges attached to the bars, to the stress-strain response of the specimen [46]. In order to obtain the strain rate ( $\dot{\epsilon}$ ), the following equation is used:

$$\dot{\epsilon} = \frac{2C_0\epsilon_R}{l_i} \quad (2)$$

where  $\epsilon_R$  represents the reflected strain pulse measured,  $C_0$  is the bulk sound speed of the bars, and  $l_i$  is the length of the specimen. The strain is found by the direct

integration of the above equation:

$$\epsilon(t) = \int \dot{\epsilon}(\tau) d\tau \quad (3)$$

The stress in the specimen can be computed using only the transmitted stress wave (one-wave analysis) or by averaging over all three incident, transmitted and reflected waves. The one wave stress analysis is given by:

$$\sigma_s(t) = \frac{A_b E \epsilon_t(t)}{A_s} \quad (4)$$

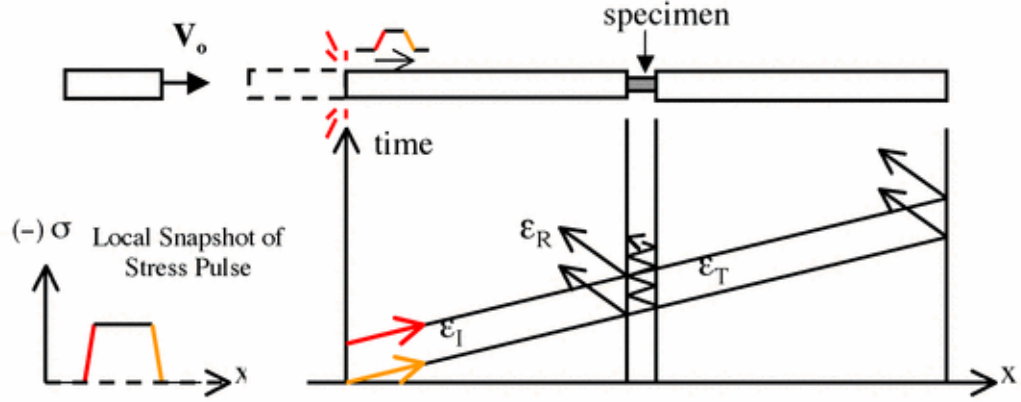
The three wave stress analysis is given by the equation:

$$\sigma_s(t) = \frac{A_b E \epsilon_t(t)}{2A_s} (\epsilon_I + \epsilon_R + \epsilon_T) \quad (5)$$

where  $A_b$  and  $A_s$  represent the cross-sectional areas of the bar and the specimen respectively. Further,  $\epsilon_I, \epsilon_R$  and  $\epsilon_T$  represent the strains generated by the incident, reflected and transmitted waves respectively. Figure 2.14(b) illustrates the voltage time traces and the resulting stress-strain response developed using a one-wave or a three-wave stress analysis [45, 46].

The above equations capture the deformation under compression. The equation for deformation under tension is not significantly different. The real challenge until recent years has been to incorporate sheet metals in the Hopkinson bar testing which were initially designed and optimized for cylindrical specimens [47, 48, 49]. The literature describes various routes taken by authors with regards to the challenge and some of the dynamic behavior captured by them in DP steels [50, 47, 4, 51] has been discussed further.

(a)



(b)

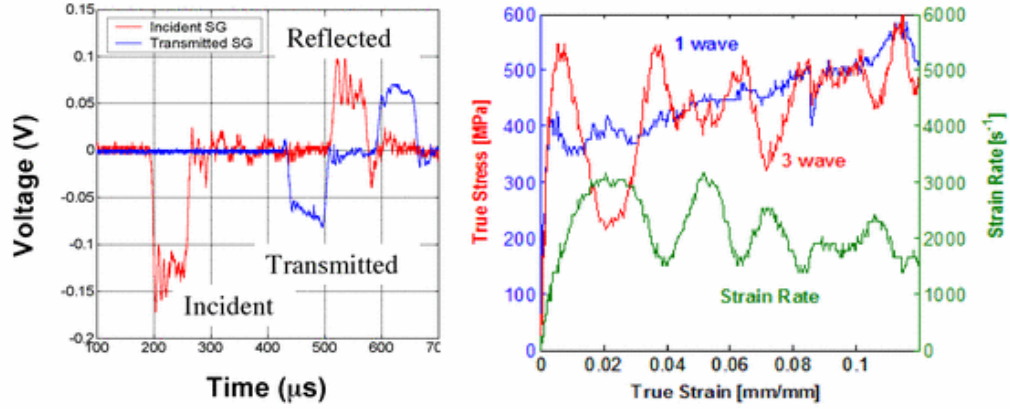


Figure 2.14: (a) Nominal setup of a Hopkinson Bar under compression. The figure also shows the different strains at the interface (b) The incident, transmitted and reflected waves generated in the bars. The stress-strain response can be captured using only the transmitted wave (blue- one wave analyses) or by incorporating all three waves (red- three wave analyses). [45]

### 2.3.2 Strain rate sensitivity of DP steels

Dual Phase steels have been observed to show positive strain rate sensitivity as the flow stress increases with an increase in strain rate. The ductility of the steels nominally decreases with an increase in the strain rate. Wang et al. [4] studied the effect of increasing the martensite content on the dynamic behavior of Dual Phase Steels. Figure 2.15 (b)-(d) depict the mechanical properties for three steels: DP 600, DP 800 and DP 1000 with increasing content of martensite respectively. DP 1000 con-

tained more than 70% martensite. The figures illustrate an increase in the tensile strength and decrease in the total elongation of DP steels at dynamic rates. They further observed that the steels with the least content of martensite (DP 600) exhibit a higher increase in strength with an increase in strain rate (positive strain rate sensitivity), while DP steels with more than 70% martensite (DP 1000) show little to no effect with an increase in strain rate. This result was attributed to high plasticity of ferrite and that steels with a higher amount of ferrite would show a higher strain rate sensitivity. A similar effect can be observed as the test temperature is increased. Curtze et al. [52] tested DP steels with varying volume fraction of martensite under dynamic rates and at high temperatures. The steels did not show a large variation in mechanical properties with increase in temperature at quasi-static strain rates but showed a substantial difference at dynamic rates. As illustrated in figure 2.15 (e) and (f), the DP steels are more sensitive to strain rate than temperature, a property typical of metals that deform by dislocation glide and interactions [52, 8, 23].



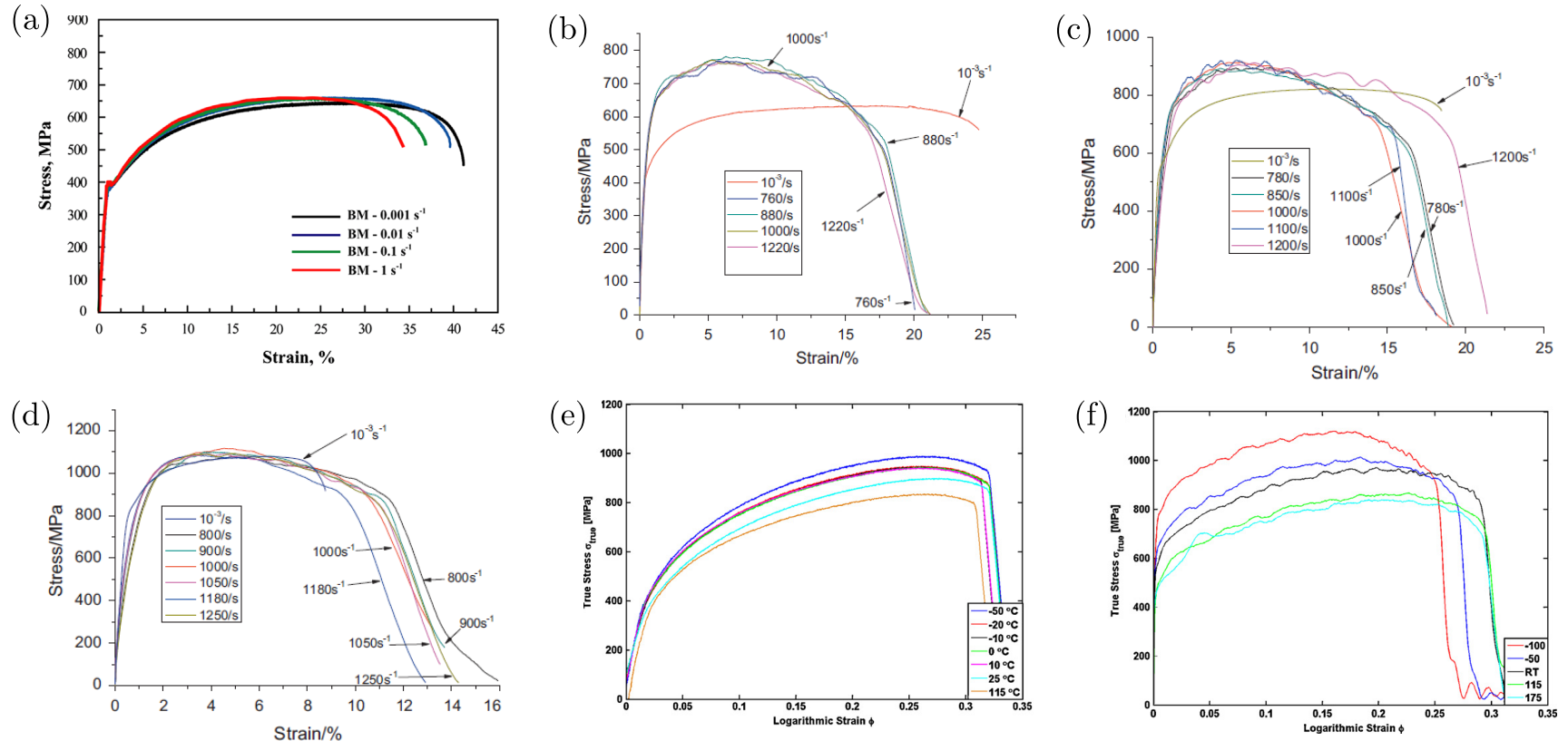


Figure 2.15: Quasi-Static and Dynamic tensile stress-strain response of DP steels. (a) quasi-static response of DP steels [53], Quasi and Intermediate strain rate response of (b) DP 600, (c) DP 800 and (d) DP 1000 with DP 600 showing the maximum positive strain rate sensitivity [4]. Effect of increasing temperature on DP 600 steels at strain rates of (e)  $10^{-3}/\text{s}$  and (f) 1200/s strain rate [52]

The ductility of a sheet steel when subjected to high velocity forming is significantly different from that seen under quasi-static conditions [54, 55, 56]. The post-uniform elongation is greatly affected by the strain rate. Seth et al. [57] conducted formability experiments using a punch on cold rolled sheet steels and reported that at high forming rates, fracture elongation increased. Thus, at high strain rates, the fracture elongation is a geometry dependent local phenomenon and materials exhibiting low quasi-static ductilities can report high ductilities under increased forming velocities [57, 4].

Singh et al. [58] studied the mechanical properties and the deformation and fracture surfaces of DP steels with different volume fractions ( 19% and 67% ) and spatial distributions of martensite, at quasi-static and dynamic strain rates. DP steels with the highest volume fraction of martensite showed the lowest strain rate sensitivity in strength. An interesting result was the increase in uniform and total elongation in the steel with a higher volume fraction of martensite, and a reverse trend in the steels containing lower volume fractions. The phenomenon was attributed to the low strain rate sensitivity of martensite to strain hardening, causing a minimal change in stress, but at the same time, a high susceptibility to adiabatic heating induced softening, leading to an increase in uniform and total elongation. The deformed microstructures with higher volume fraction of martensite showed significant martensite deformation along with crack tip blunting and crack bifurcation upon encountering the ferrite phases. These were the effects that were cited in aiding the increase in ductility at higher strain rates.

After a review of the literature, an important observation regarding the specimen geometries used for dynamic testing deserves mention. Due to the absence of a standard specimen geometry for dynamic tensile testing, various authors have used different geometries for conducting dynamic tensile tests on materials. The ductility and final fracture strain of a material are geometry dependent properties. Figure 2.16

illustrates the differences observed in the final strain of similar Dual Phase steels with different specimen geometries. Figure 2.16 (a) and(b) depict the results obtained by Huh et al. [5] who tested DP steels with the same specimen geometry (Figure 2.16 (c)) in the strain rate range of  $10^{-3}/s$  to  $10^2/s$  and did not observe a drop in final strain, while Figure 2.16 (d) illustrates the results obtained by Yu et al. [50] who used different specimen geometries for quasi-static (Figure 2.16(e)) and intermediate strain rates(Figure 2.16(f)) that resulted in a reduction in final strain. Though the strain values reported by Huh et al. [5] are engineering strain, a safe assumption that the true strain will follow the same trend can be made. According to a study conducted by Verleysen et al. [49, 47], that tested seven specimen geometries at various strain rates, they observed that at higher values of strain, the strain field is non uniform in the gage length of the sample. By changing the gage length, width and radius of the samples, the study concluded that the stress strain behavior of the same material with different geometries should not be compared as the distribution of deformation is strongly affected by specimen geometry. The tests were performed on Transformation Induced Plasticity (TRIP) steels, however, the general results can be extended on all ductile materials.

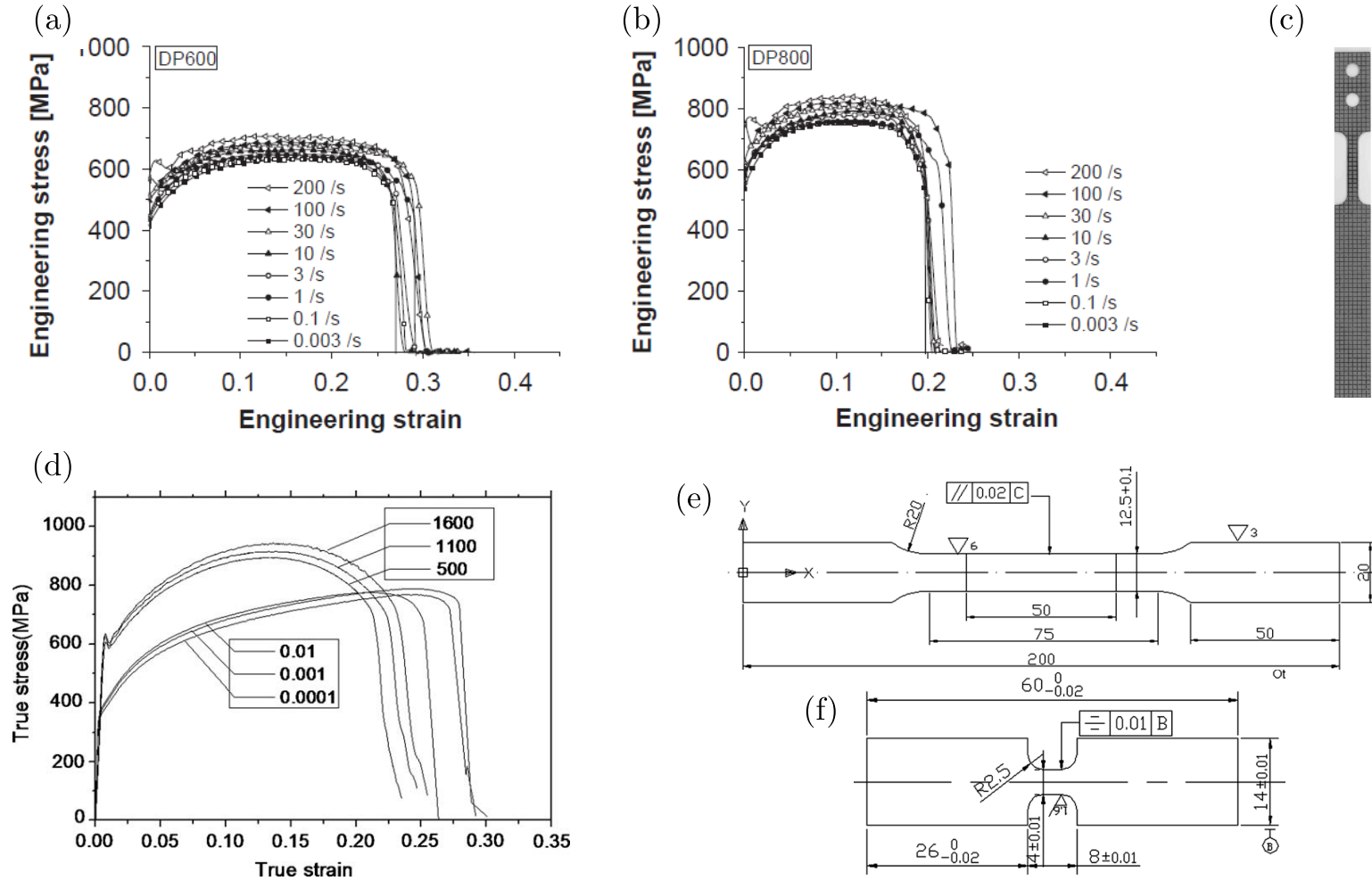


Figure 2.16: Effect of geometry on the ductility of DP steels. Stress-Strain curves at quasi-static and intermediate strain rates of (a) DP 600 and (b) DP 800 steels using the geometry depicted in (c) [5], (d) Stress-Strain curves reporting a drop in ductility at higher strain rates using a different geometries for quasi-static tests:(e), and dynamic tests:(f) [50].

### 2.3.3 Fracture at high strain rates

As discussed earlier, fracture surface can be affected by the microstructure and strain rate. Effects of microstructure on the fracture path and fracture surface were discussed in the previous section. Effects of strain rate on the fracture surface geometry of Dual Phase steels are discussed next.

The fracture surface of DP steels even under high strain rates of  $10^3/s$  has been observed to have a dimpled morphology [5, 4, 50]. Wang et al. [4] conducted high strain rate experiments on Dual Phase steels with increasing percentages of martensite. The fracture surfaces in these steels appear to have lower extent of dimpled fracture at high martensite volume fraction. Dual Phase steels with about 65% martensite (DP 1000) showed predominantly quasi-cleavage fracture morphology indicating brittle behavior at lower strain rates and a more dimpled appearance at a higher strain rates. This was also in tandem with the elongation observed in the specimens which increased with an increase in strain rate for specimens with higher volume fraction of martensite and was attributed to a softening effect due to adiabatic heating. Figure 2.17 shows the fracture surfaces of Dual phase steels. Figure 2.17 (a) and (b) show the fracture surface of DP600 steel under strain rates of  $10^{-3}/s$  and  $10^3/s$  respectively, and (c) and (d) depict the fracture surface of DP 1000 Steel under strain rates of  $10^{-3}/s$  and  $10^3/s$  respectively.

Furthermore, Singh et al. [58] observed the fracture features of DP steel with 67% martensite and showed that they contained a greater amount of shear like faceted fracture accompanied by void networks as shown in figures 2.18 (a) and (b). The dimple sizes at quasi-static and dynamic strain rates were measured and larger dimples at higher strain rates were observed. The larger dimples were attributed to enhanced plasticity hindering the void nucleation at higher strain rates. Figures 2.18 (c) and (d) show the dimple size distribution for strain rates of  $2.7 \times 10^{-4}/s$  and  $650/s$ , respectively.

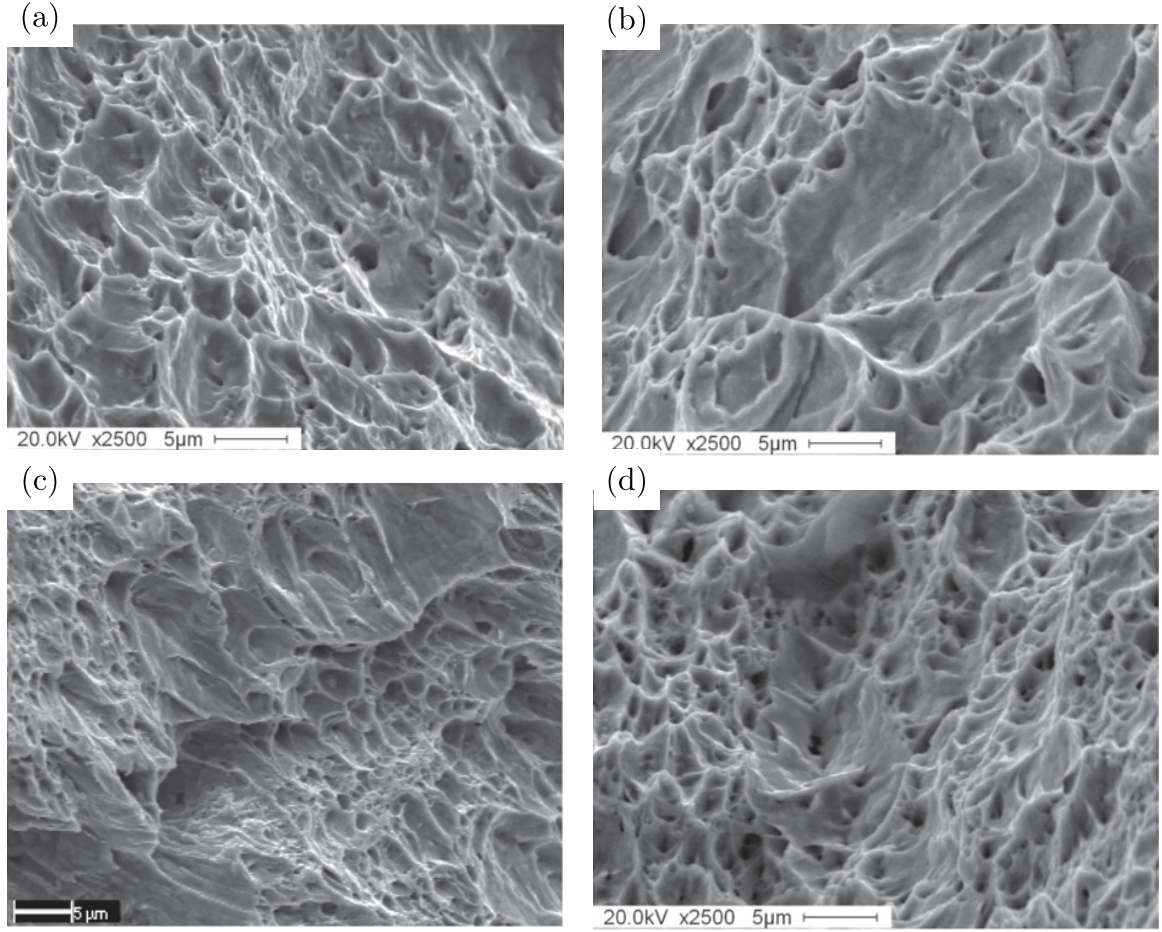


Figure 2.17: Fracture surfaces of Dual Phase steels at different strain rates, (a) DP 600-  $10^{-3}$ /s, (b) DP 600  $10^3$ /s, (c) DP 1000  $10^{-3}$ /s, (d) DP 1000  $10^3$ /s. DP 600 showed reduced plasticity at higher strain rates whereas DP 1000 showed a more ductile dimpled region at higher rates indicating improved plasticity [4].

Das et. al [51] investigated the dynamic behavior and fracture response of DP 600 and DP 800, with DP 600 having a lower volume fraction of martensite and a larger ferrite grain size and DP 800 having a larger volume fraction of martensite and smaller ferrite grain size. The strength of DP 600 showed a greater strain rate sensitivity compared to DP 800, however, no significant increase in ductility was observed in either steels. With observations made on the fracture surfaces coupled with TEM studies, the primary failure mechanism observed in DP600 was interface decohesion at all strain rates. However, in DP 800 steels, while martensite cracking

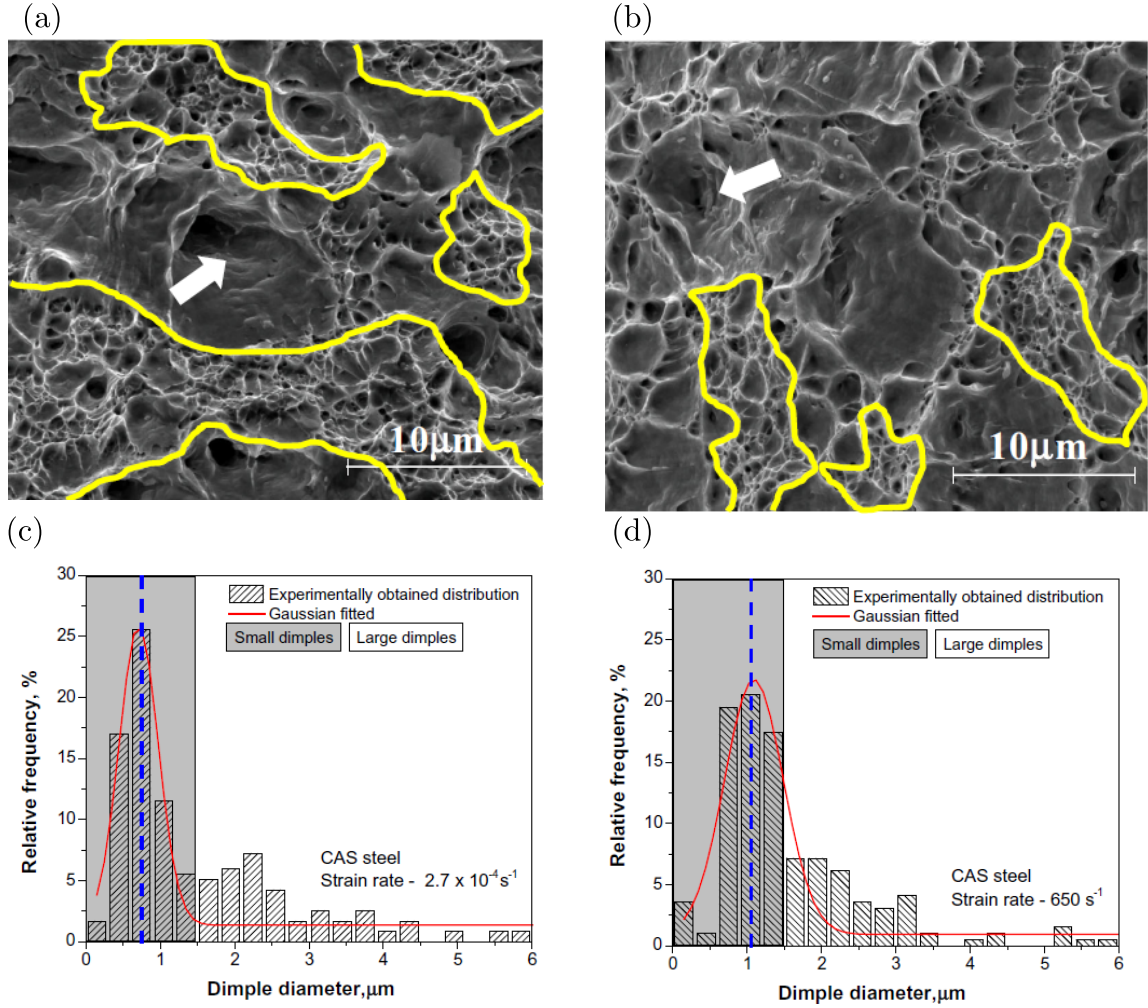


Figure 2.18: (a) and (b) show the void network (yellow lines) and deeper dimples and facets (white arrows) in the steel with 67% martensite at  $2.7 \times 10^{-4} \text{ s}^{-1}$  and at  $650 \text{ s}^{-1}$  strain rates respectively. (c) and (d) show the dimple size distribution in the same steel at  $2.7 \times 10^{-4} \text{ s}^{-1}$  and at  $650 \text{ s}^{-1}$  strain rates respectively

was deemed to be the primary mode of failure at quasi-static strain rates, it switched to interface decohesion at higher strain rates. Additionally, the TEM studies showed that while DP 600 formed finer dislocation cells at higher strain rates, DP 800 did not show dislocation cells at lower strain rates but rather martensite fragmentation at higher strain rates. Figure 2.19 shows the TEM images for DP 600 and DP 800 at the low and high strain rates.

An important point to consider regarding the previous studies is the use of different geometries at quasi-static and dynamic strain rates. As discussed before, the geometry



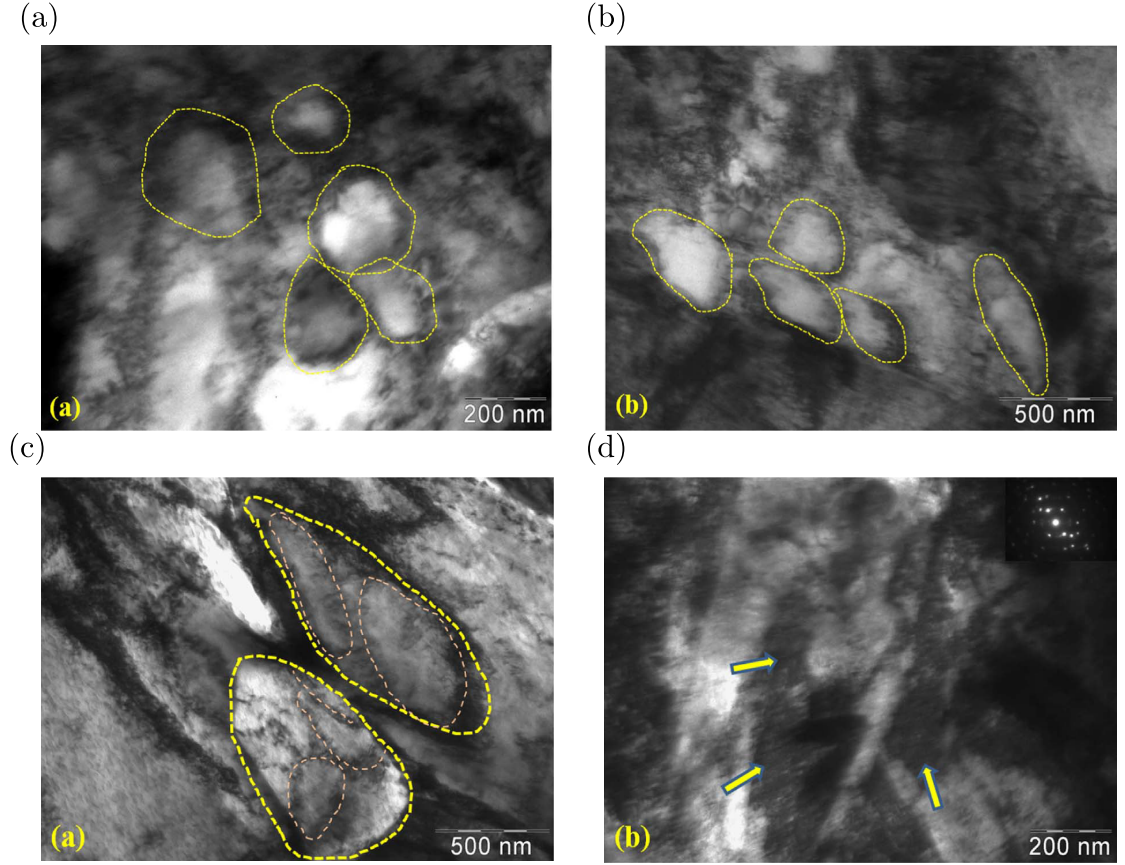


Figure 2.19: (a) and (b) show the void network (yellow lines) and deeper dimples and facets (white arrows) in the steel with 67% martensite at  $2.7 \times 10^{-4}/s$  and at 650/s strain rates respectively. (c) and (d) show the dimple size distribution in the same steel at  $2.7 \times 10^{-4}/s$  and at 650/s strain rates respectively

can play a significant role in determining both the uniform and total elongations. Hence, one has to be careful when comparing the elongations at different strain rates obtained from different geometries and correlating the fracture mechanisms to the observed mechanical response.

Additionally, although there are a number of studies that have quantified and discussed the number and sizes of dimples and voids in the fracture surfaces of DP steels, little to no studies exist that systematically classify and quantify all the features observed in the fracture surfaces spanning a range of strain rates. The dynamic response of DP steels under strain rates of  $10^4/s$  and higher has also not been investigated. A brief introduction and the procedures employed to test materials under such high



strain rates is presented ahead.

#### 2.3.4 Plate Impact Dynamic Tensile (Spallation) tests

Dynamic mechanical properties of materials at strain rates of higher than  $10^4/s$  can be achieved by using a plate-on plate-impact test method. The plate impact test is a technique used to probe the dynamic mechanical properties that generates a uniaxial strain within the targeted material. The uniaxial strain is induced by propagation of planar, parallel shock waves generated upon impact [59]. A comprehensive understanding of the interaction of shock waves and microstructure, nucleation and growth of damage can be achieved using these tests. In this section, a brief overview of the fundamentals of shock wave propagation, calculation and determination of the spall strength and Hugoniot Elastic Limit (HEL) and an over view of dynamic fracture is presented.

##### *Overview on shock propagation*

A discontinuity in density, pressure or internal energy can be defined as a shock wave. The current study focuses on the shock waves generated during a planar impact, although, shock waves can be generated using other techniques such as high energy lasers or by detonating explosives. A shock wave occurs when the hydrostatic stress component exceeds the dynamic flow stress and can be characterized as having a steep front generating a uniaxial strain loading condition, leading to an increase in the hydrostatic stress levels. Figure 2.20 shows a schematic representing a shock front.

The shock wave parameters can be determined by using the Rankine Hugoniot conservation equations [60, 59]. The parameters are computed by using the mass,

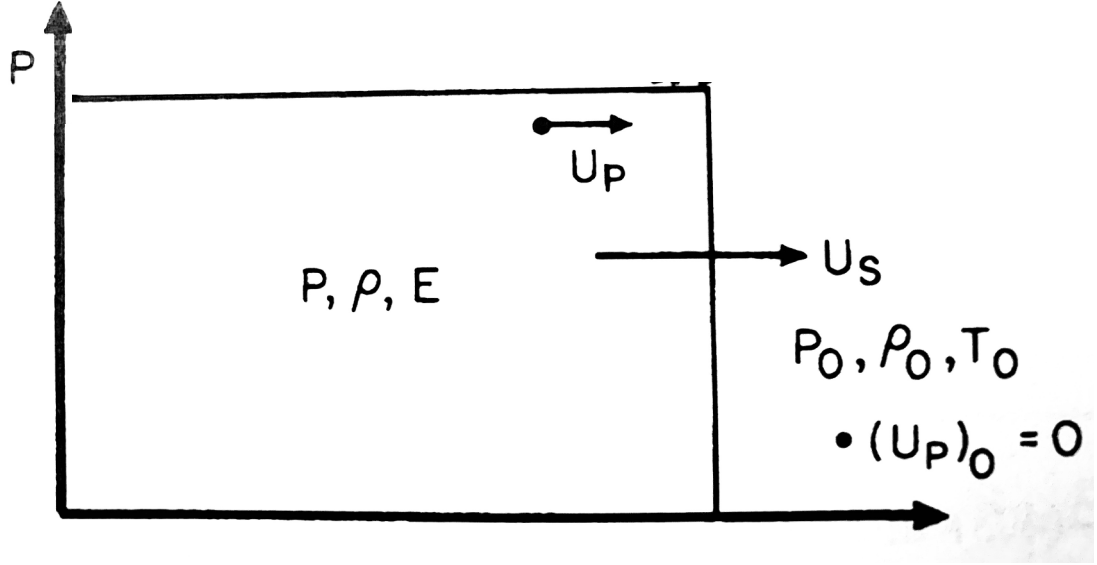


Figure 2.20: Shock wave schematic depicting the original state of the material and the state after it is affected by the shock wave [59].

momentum and energy conservation equations and are shown below:

*Conservation of Mass*

$$\rho_0 U_S = \rho(U_S - U_P) \quad (6)$$

where  $\rho_0$  is the "shock impedance"

*Conservation of Momentum*

$$(P - P_0) = \rho_0 U_S U_P \quad (7)$$

*Conservation of Energy*

$$E - E_0 = \frac{1}{2}(P + P_0)(V_0 - V) \quad (8)$$

where  $\rho_0$  is the initial density,  $U_S$  is the shock wave speed,  $U_P$  is the particle velocity,  $P$  and  $E$  are the pressure and energy behind the shock front, and  $V$  is the specific volume. The derivation of these equations is provided elsewhere [59].

### *Propagation of shock waves*

Figure 2.21 (a) shows a schematic of an ideal shock wave comprising a discontinuous front, peak pressure for a certain duration indicated by a flat top and a release that brings the pressure gradually to zero. However, the shock waves encountered in real materials have many different characteristics that are a function of the material and the pressure they are subjected to. Figure 2.21 (b) shows the schematic representing a real shock wave along with events that represent the shock wave interactions within the material. The arrival of a steep rise in pressure marks the elastic wave. The Hugoniot Elastic Limit (HEL) marks the material reaching its elastic limit and transitioning to the plastic phase. The pressure rises to the peak state after the HEL and the rate of this rise is a function of the constitutive properties of the material. Peak pressure reached can have a flat top (indicating a plate impact test) or a triangular peak (indicating detonating explosives or a pulsed laser). The arrival of the plastic wave is marked by the plastic modulus. After the flat top, the shock wave is reflected from the back of the sample and the material enters a state of tension by unloading due to decompression. If there is no fracture in the material, the wave velocity profiles would return to zero, however as seen in Figure 2.21 (b), a characteristic pull-back in the wave profile is observed indicating spallation. The spall cusp is used to calculate the dynamic tensile (spall) strength of the material. The wave profiles can be measured with the help of Photon Doppler Velocimetry (PDV) or Velocity Interferometer System for Any Reflector (VISAR). The phenomenon of spalling and the resulting fracture is discussed ahead.

### *Spalling*

Plate impact tests can be designed to induce a state of dynamic tension in the sample leading to spall. A dynamic tensile failure generated by the interaction of two rarefaction or release waves is termed as spalling. Figure 2.22 (a) shows a schematic

of the propagation of the compressive and tensile waves that result in a spall surface. The test setup consists of a target (or sample) plate that is impacted by a flyer plate. Upon impact, compressive waves travel in both the flyer and the target. The wave reflected from the back surface of the flyer, enters the target. In the meantime the compressive wave is also reflected off the back of the target. The interaction of these reflected release (unloading) waves results in a tensile stress in the sample. Spalling is a function of both the amplitude and duration of the tensile pulse. If the magnitude

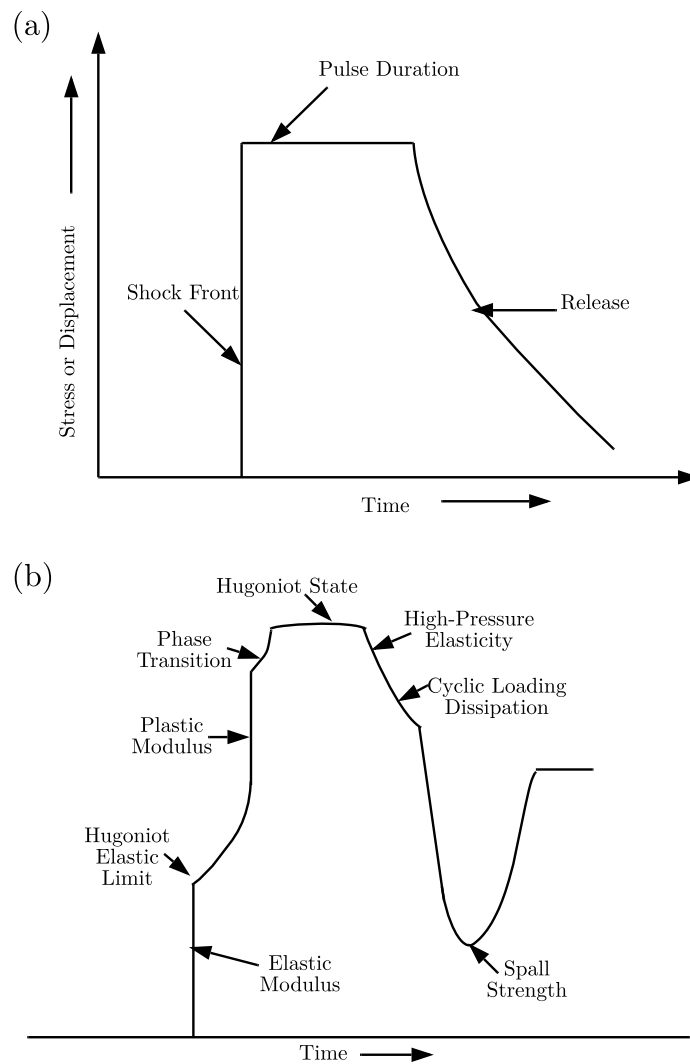


Figure 2.21: (a) Ideal shock wave profile and (b) a representative real shock wave profile showing pressure and materials dependent characteristics such as HEL, spall strength etc. [59].

of the tensile stress generated is greater than spall strength of the material, spalling will occur and the sample fractures. The damage and subsequent spallation in the sample can be controlled by varying the impact velocities and resulting pressure. Figure 2.22 (b) shows the free velocity traces generated at different strain rates resulting in different amounts of spall as a function of the sample thickness and strain rate in a high specific strength steel [61]. Figure 2.22 (c) shows the free velocity traces at different velocities and thus, different impact pressures resulting in incipient and partial spall in a mild carbon steel [62].

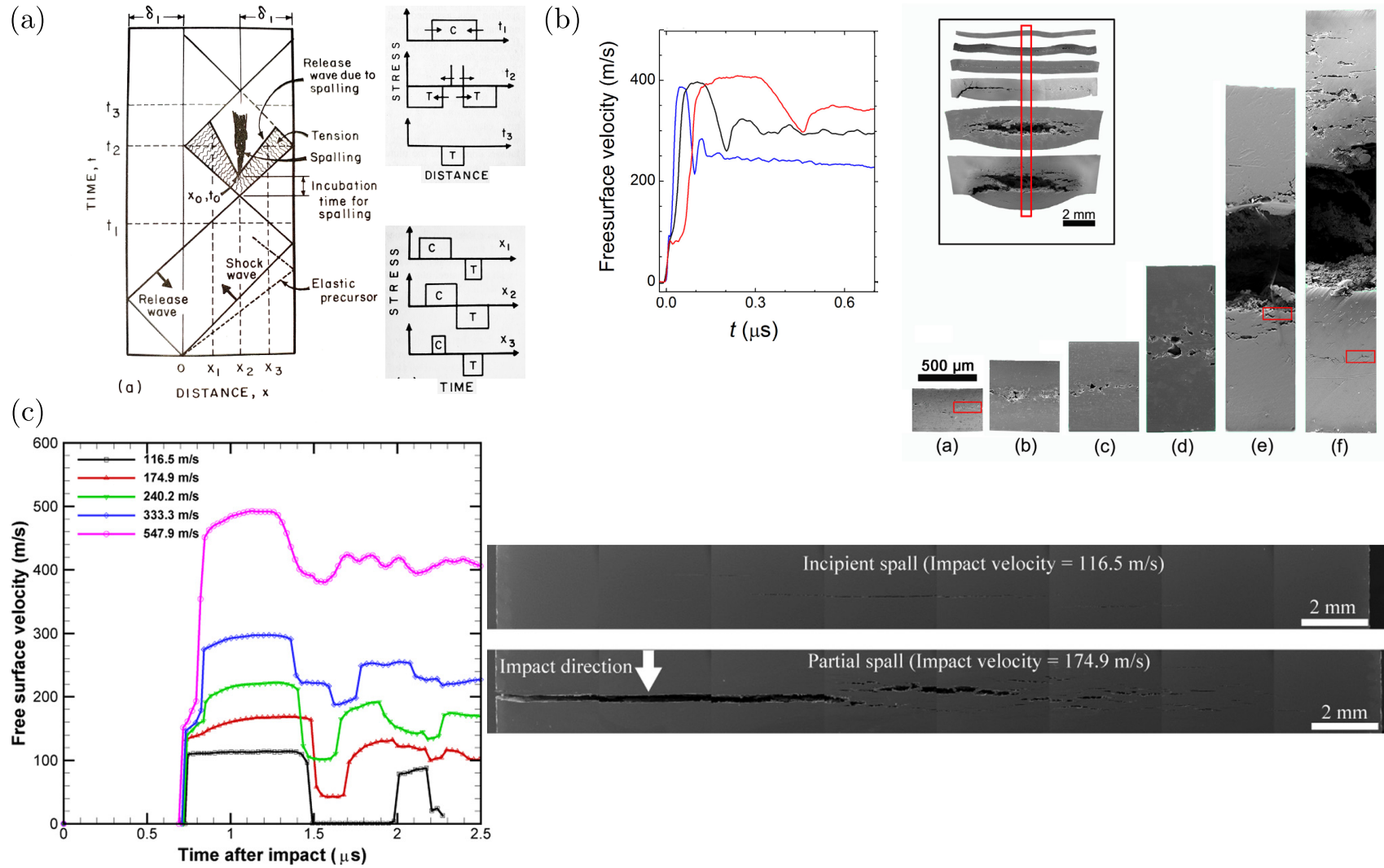


Figure 2.22: (a) X-t plot showing the propagation and reflections of shock waves within a sample along with the stress profiles at different times and distances [59], (b) Free velocity curves at different strain rates showing different amounts of damage nucleated in a high specific strength steel [61], (c) Incipient and partial spall generated at different velocities in a mild steel [62].

The spall strength of the material can be influenced by microstructural attributes, such as, grain size, secondary phase particles and inclusions [59, 63]. The extent of damage can be quantified by estimating the volume fraction of voids observed on the damaged samples. Figure 2.23 shows the extent of spall fracture at a given stress for different copper microstructures. The specimen with high impurity levels had a greater number of void initiation sites and displayed a lower spall strength.

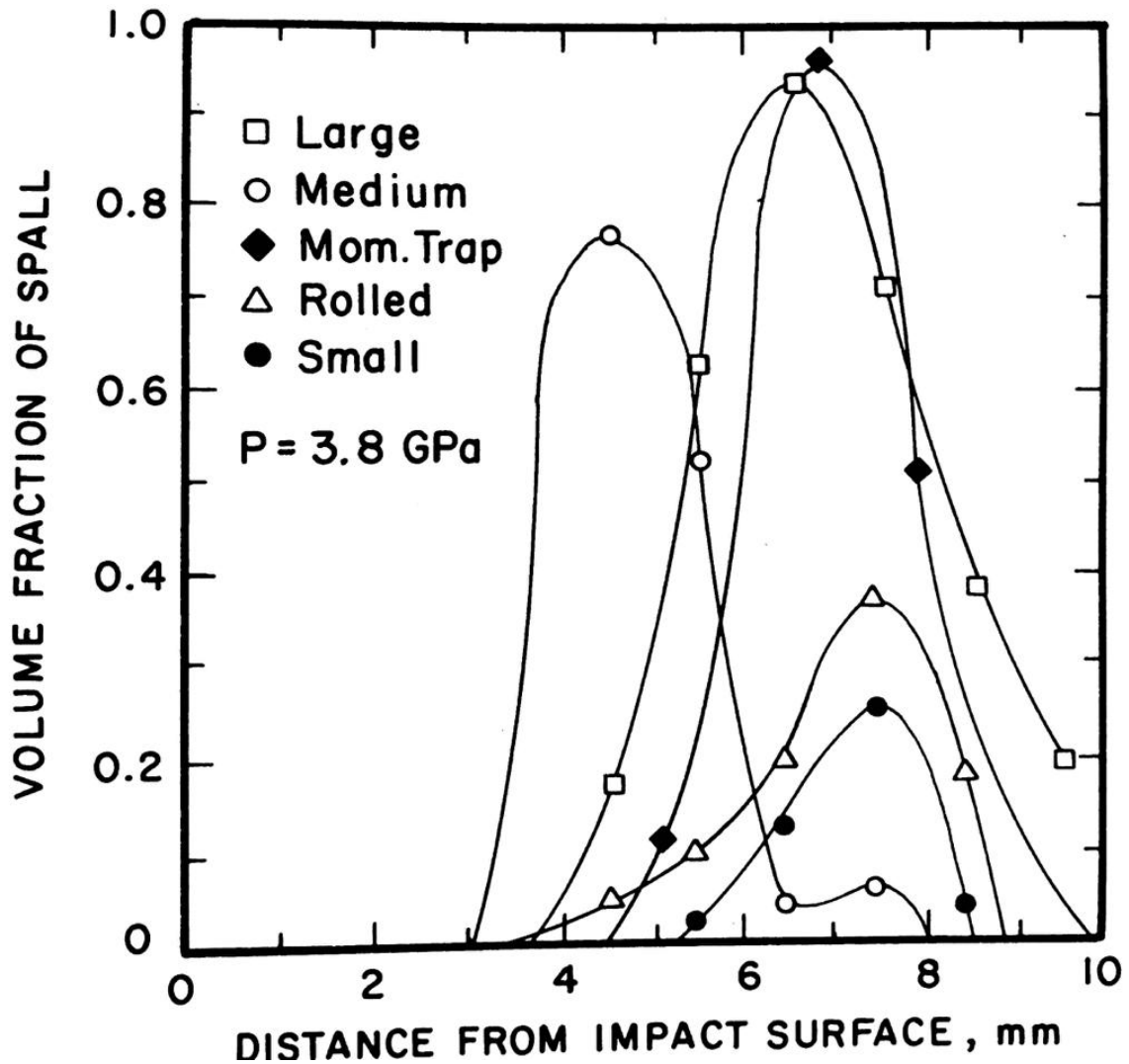


Figure 2.23: Plot showing the variation in the volume fraction of voids nucleated in copper at a pressure of 3.8 GPa as a function of the grain size and processing conditions [64, 59].

The presence of spall in a sample is characterized by the pull-back from the re-

compression wave as a result of the rarefaction wave triggered during fracture. The dynamic fracture mechanisms have been obtained from the velocity gradients of the pull-back curves [65, 66, 67, 68]. The initial rise in the pull-back is associated with the nucleation of voids and the change in the slope of the recompression wave indicates a change in fracture mechanism to growth or coalescence. Figure 2.24 (a) shows the time and velocity shifted superimposed recompression waves of OFHC copper with different grain sizes, impacted at the same velocity. The samples with the smallest and largest grain sizes ( $30\mu m$  and  $200\mu m$ ) show a more nucleation driven fracture and also show a corresponding higher area fraction of voids, as shown in figure 2.24 (b). The change in the mechanisms have been observed to be a function of the inherent microstructure of the sample and the peak impact pressures the materials are subjected to [66, 68].

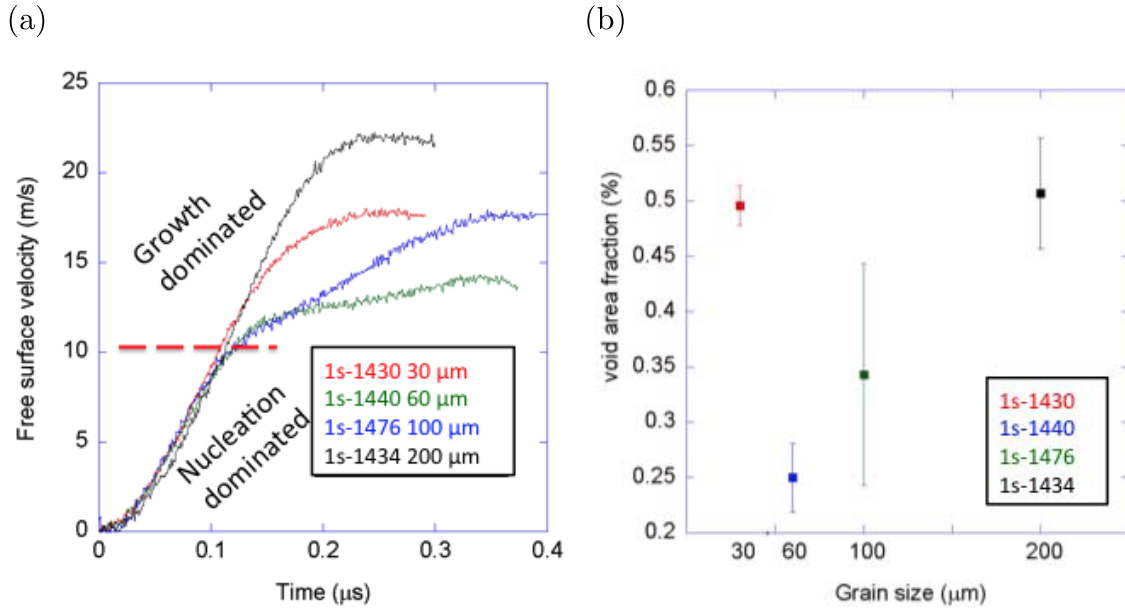


Figure 2.24: Plot showing the variation in the volume fraction of voids nucleated in copper at a pressure of 3.8 GPa as a function of the grain size and processing conditions [66]

To the best of the author's knowledge, the spall and failure of DP steels have not been investigated at strain rates of greater than  $10^4/s$ . Additionally, the effect of



processing conditions on the damage accumulation and spall behavior has also not been investigated. The current work is expected to provide a better understanding of the sensitivity of spall strength on the martensite content and morphology in DP steels.

Processing conditions play a significant role in determining the properties of individual phases and the overall bulk properties of DP steels. Thus, it is important to understand the effects of these processes on the fracture mechanisms. The steels can also be processed to leverage a double benefit of improving the corrosion protection by adding a protective coating and at the same time improving the mechanical properties of the underlying steel. The microstructure of the coating layers is discussed in the subsequent section.

## 2.4 Protective coatings on steel

Atmospheric corrosion can lead to the degradation of steels. In order to protect them from rusting, automotive steels are largely protected by the application of coatings. Metallic coatings on steels can be applied using the following methods: Hot dip galvanizing or aluminizing, thermal spraying, electroplating and sheardizing. Hot dip galvanizing, a process used to generate galvanized steels, is a popular technique and more relevant for the current work. Hot-dip galvanizing is a coating method employed where the steel sheet is dipped in a molten zinc bath to make a thin layer of zinc adhere on to the surface. The coating layer thickness on the steel can be controlled using various processing methods [69]. A galvanized layer is produced when the galvanized steel sheet is annealed. Due to diffusion at elevated temperatures, phases or layers of iron-zinc inter-metallic are formed and are largely classified as the Gamma( $\Gamma$ ), delta ( $\delta$ ) and zeta( $\zeta$ ) layers [69, 70].

The Gamma ( $\Gamma$ ) phase has been largely depicted as  $Fe_3Zn_{10}$ . It forms the first layer on the steel substrate and contains about 23-28 wt. % iron with a BCC structure.

The delta( $\delta$ ) phase depicted as  $FeZn_{10}$  has about 7-10 wt. % iron and a hexagonal structure. The outermost phase, zeta ( $\zeta$ ) depicted by  $FeZn_{13}$  contains about 5-6 wt % iron and has a monoclinic structure. Figure 2.25(a) depicts these phases. An important aspect of the galvanized coating is that there may be inherent cracks in the layer even without the application of load[70]. Understanding the generation and propagation of new cracks and propagation of the existing cracks under loading plays an important role.

According to the study conducted by Nunomura et al [70], the galvanized layer behaves differently under tension and compression. Figure 2.25 (b) illustrates the cracks found under compression and figure 2.25 (c) shows cracks under tension. In both cases, the cracks are generated in the  $\delta$  layer which propagate toward the substrate coating interface and subsequently along the interface resulting in de-bonding. In tension the cracks are observed to propagate along a straight line whereas under compression, the cracks propagate at an angle. The behavior of the coating is not very different when the substrate is DP steel as shown in figure 2.25 (d). Song et al [71] reported the cracking behavior of the galvanized layer on a DP steel and observed that the cracks propagate along the coating-substrate interface. Figure 2.25 (e) illustrates the crack propagation and de-bonding of the galvanized layer on DP steel.

## 2.5 Stereology for Microstructure Quantification

Stereology is the science of quantifying features of interest in a microstructure. Stereological techniques involve sampling of a three-dimensional (3-D) microstructure by lower dimensional geometric probes such as test planes, test lines, or test points. Estimating the 3-D features involves using unbiased, unambiguous, and assumption-free stereological equations to relate the measurements performed on 2-D planes to correspond to 3-D attributes. The current work extensively applies stereology to quantify

microstructure characteristics and fracture surface features and correlate these. The main stereological techniques are discussed next.

### Volume Fraction estimation

The volume fraction of a phase or a microstructural constituent  $V_V$ , is the fraction of microstructural space occupied by that constituent in 3-D space. Some advantages of stereological techniques for estimation of  $V_V$  are as follows:

1. It is independent of shape, size or spatial orientation of the feature of interest
2. It is not necessary to know the magnification of the image being used in the analyses.

The volume fraction can be obtained by areal analysis or by a point counting method.

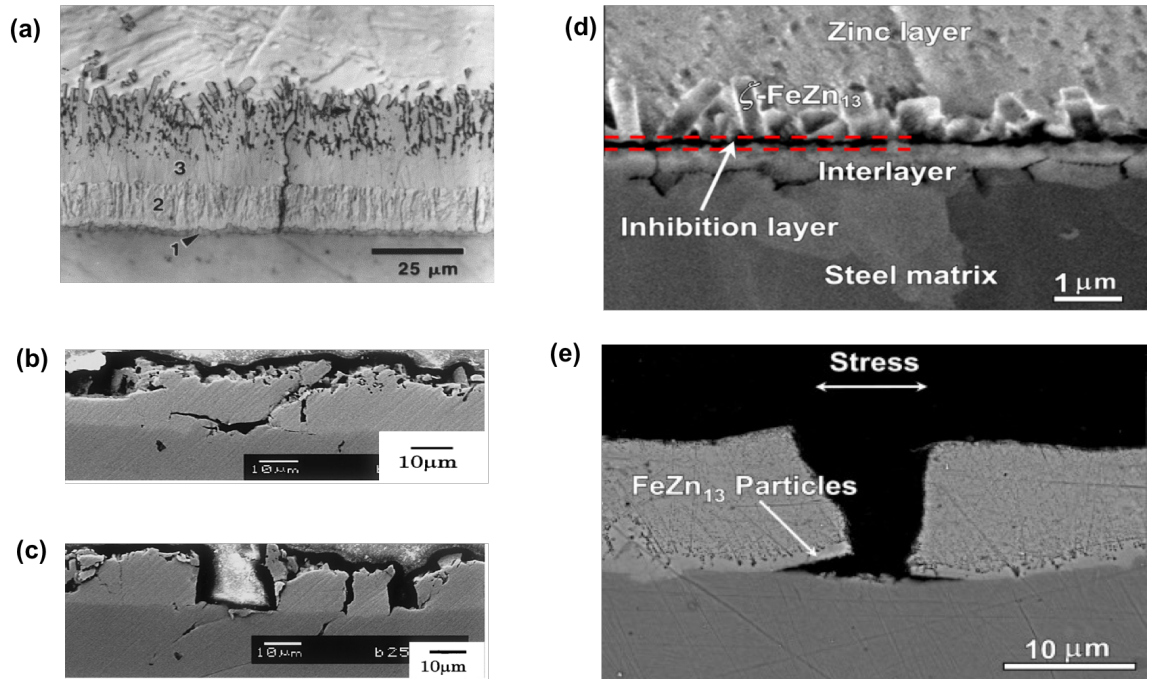


Figure 2.25: Images depicting the Galvannealed layer as formed and after the application of load. (a) Different layers of the coating, 1-  $\Gamma$ , 2-  $\delta$  and 3-  $\zeta$ , (b) cracks developed during compression, (c) cracks developed during tension [70], (d) galvannealed layer on DP steel with similar layers as seen in (a), (e) De-bonding of the galvannealed layer on DP steel under the application of a tensile load [71].

**Areal Analysis** involves measuring the area fraction of the phase of interest in a representative 2-D section. The population average value  $\langle A_A \rangle$  of the area fraction  $A_A$  is equal to the volume fraction of the constituent in 3-D [72, 73].

$$V_V = \langle A_A \rangle \quad (9)$$

Measurement of areal fraction requires image segmentation which can sometimes prove to be challenging. **Point Counting** is a faster and easier approach for images that are difficult to segment. In this method, test points are placed at random locations in the image of the microstructure and the number of points in the phase of interest are calculated :  $P_P$ . Now the population average of these points :  $\langle P_P \rangle$  is equal to the Volume fraction of the phase of interest [74, 73, 72]. The two methods used to achieve  $P_P$  are: a) Systematic uniform point counting, and b) independent uniform point counting; it can be proved that systematic point counting is more *efficient* than independent random point counting [75].

$$V_V = \langle P_P \rangle \quad (10)$$

Volume fraction can be used to correlate a variety of microstructural features to mechanical properties [74]. Figure 2.15 illustrates some examples. Figure 2.26 (a) depicts the variation of Ultimate Tensile Strength as a function of the Volume Fraction of martensite in a Dual Phase steel [1]. Figure 2.26 (b) depicts the damage mechanism as a function of martensite volume fraction ( $V_M$ ) and ferrite grain size ( $S_F$ ) in Dual Phase Steels [6]. For a smaller ferrite grain size, and a higher volume fraction of martensite, the cracking of martensite is deemed as the damage mechanism. The damage mechanism described in figure 2.26 (b) appear to be independent of the type of deformation that the material is subjected to (tension, compression, torsion etc.). The image depicts the mechanisms only as a function of the volume martensite and

the ferrite grain size, and a more comprehensive picture can be obtained by taking into account other microstructural features as well. This emphasizes the use of other techniques described ahead to capture all aspects of the microstructure influencing a material's property.

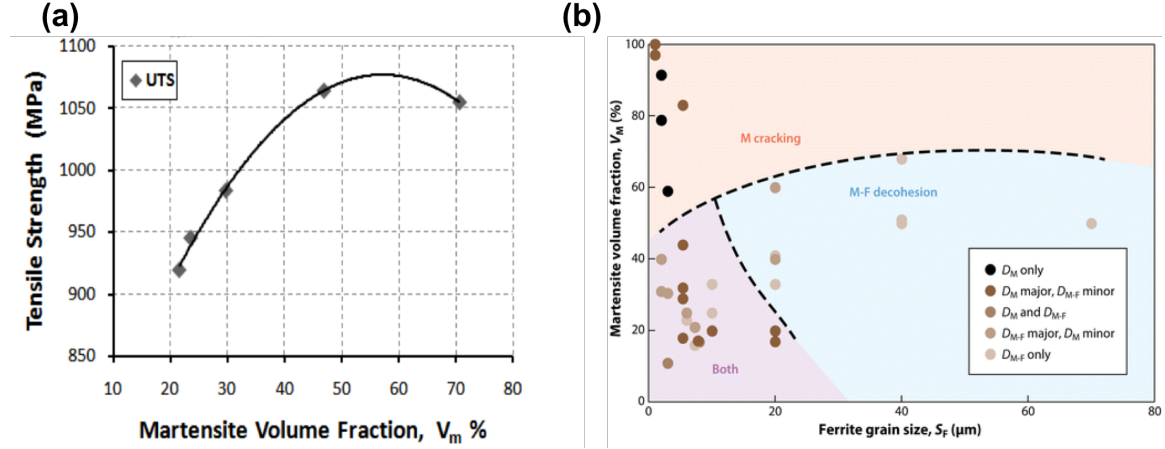


Figure 2.26: Plots relating volume fraction of martensite to properties and damage mechanism of DP steels. (a) UTS as a function of  $V_M$  discussed earlier by Bag et al [1]. (b) Plot of  $V_M$  as a function of the ferrite grain size showing the predominant damage mechanism as martensite cracking for higher  $V_M$  and moderate ferrite grain size [7, 6]

### Surface Area per unit volume

Microstructural features such as grain boundaries, matrix-precipitate interfaces, surfaces of internal voids/cavities, etc. can be represented by total area of the feature of interest per unit volume  $S_V$ . The stereological estimation of the total surface area of the features of interest is made by using the line intersection counting method. In this method, the test probe is a line. The number of intersections of the features of interest with the test line is measured, let's say (P). By dividing this number with the total test line length (length of each test line multiplied by no. of test lines)  $P_L$  is obtained. This is related to the total surface area  $S_V$  according to the following

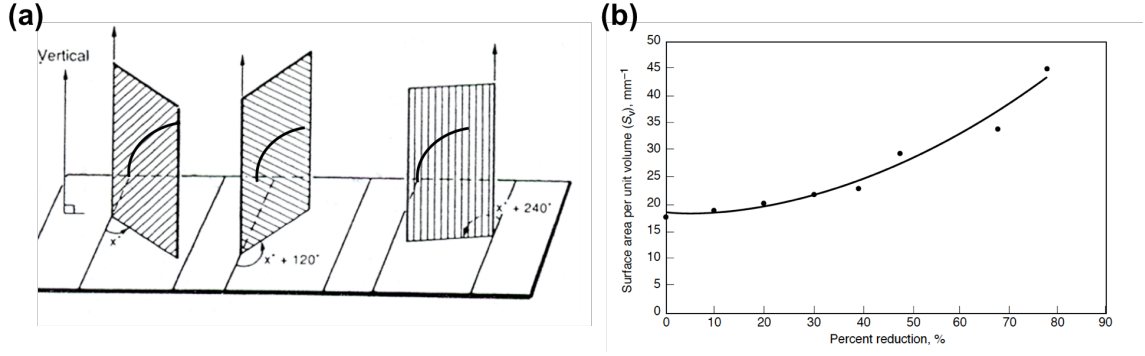


Figure 2.27: (a) Vertical Sections with cycloids used to calculate  $S_V$  for anisotropic microstructures, (b) Plot of  $S_V$  of grains vs percent cold rolled reduction showing an increase in the grain boundary area with rolling [74].

relationship[75]:

$$S_V = 2 \langle P_L \rangle \quad (11)$$

where  $\langle P_L \rangle$  denotes the population average value of the number of intersections per unit test line length. The above equation is applicable to both isotropic and anisotropic microstructures. For anisotropic microstructures, however, measurements on planes of many orientations need to be performed and then averaged over these orientations [74, 76]. This method of estimation is tedious and can be overcome by performing measurements using a vertical section approach and cycloid shaped test lines with minor axis parallel to the vertical axis as illustrated in Figure 2.27(a).  $S_V$  can be used to determine how fine or coarse the microstructure of the material is [74]. For a given volume fraction, a phase with a higher  $S_V$  would denote a finer dispersion. Figure 2.27(b) illustrates the  $S_V$  of grain boundaries versus the amount of cold work on a cold rolled extra low carbon steel. The plot shows that cold work results in an increase in the grain boundary area and the creation of new grain boundary surfaces.[74]

### Length Density per unit volume

In microstructures, features such as grain edges, needle shaped precipitates, fibers etc. can be treated as 1-D features in the 3-D space. Length density  $L_V$  is an important attribute of such lineal features.

The stereological estimation of lineal features can be made using sectioning planes or 3-D volumes. The lineal features are seen as points in a 2-D sectioning plane. If the number of intersections of these features with a random 2-D section is  $(Q)$ , then dividing  $Q$  by the area of the plane gives the number density of the lineal features:  $Q_A$ . This is related to the length density  $L_V$  as per the following relation [76, 75]:

$$L_V = 2 < Q_A > \quad (12)$$

where  $< Q_A >$  denotes the population average value of the number of intersections per unit area. For the valid application of the result, unbiased sampling is required. The unbiased sampling frame as illustrated in the figure 2.28 (a) consists of two permissible and two forbidden edges [77]. Any feature lying even partially on the forbidden edge is not counted, and, similarly, any feature lying even partially on the permissible edge is counted as a whole. In order to estimate anisotropic lineal features, the estimation across all orientations becomes necessary. Another method to perform the same on anisotropic features is by using cycloid surfaces with vertical sections as illustrated in figure 2.28 (b).

## **2.6 Quantitative Fractography**

Fractography is the study and analysis of fracture surfaces to gather information regarding the failure of the material. Fracture surface of any material holds key information regarding its fracture mechanisms. It represents a biased view, since the fracture path often follows the weak links. Quantitative fractography is a stereological

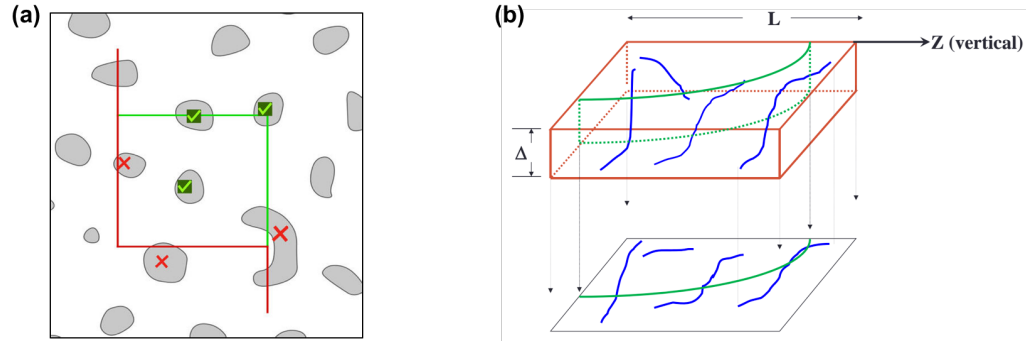


Figure 2.28: (a) Use of unbiased frame for counting features in a 2-D sectioning plane, (b) Use of cycloidal area to estimate the anisotropic lineal features [74].

tool used to quantify the features observed on the fracture surface and link them to the microstructure of the material to arrive at statistically viable fracture mechanisms [78, 79]. This section deals with the factors affecting the fracture surfaces and the different ways to quantify them. The two major methods to quantify the fracture surfaces are:

- (a) Profilometry of fracture surfaces
- (b) Quantitative fractography conducted on SEM images.

The geometry and topography of fracture surfaces are predominantly governed by the underlying microstructure and the strain rates subjected on the samples. A qualitative analysis of the fracture surface provides information on the global and local modes of fracture. These could be ductile or brittle depending on the fracture mechanism of the material. A ductile fracture surface is identified by the presence of dimples and voids, whereas a brittle fracture is usually identified by cleavage on the fracture surface. Though qualitative fractography can help determine the macroscopic fracture mode, a more detailed understanding of the mechanism can be determined by quantitative fractography.



## Profilometry Based Quantitative Fractography

A fracture profile is often seen as a tortuous line obtained by the intersection of a fracture surface with a 2D sectioning plane. Profilometry plays an important role for estimation of global fracture parameters. The surface topography yields important information on the global fracture. It is important to measure it in terms of parameters that are physically meaningful and can be correlated to the dominant failure mechanisms, microstructure and material properties. Gokhale et al.[80, 81] proposed fracture surface analysis using an important global attributes of the fracture surface namely the fracture roughness parameter ( $R_S$ ). It is defined as the ratio of the true area of fracture surface, S and its apparent projected area, A:

$$R_S = \frac{S}{A} \quad (13)$$

$R_S$  can be estimated from the measurements performed on fracture profiles generated by intersections of fracture surface with planes. The fracture *profile* roughness parameter  $R_L$  is equal to the ratio of the true profile length  $\lambda_0$  and the apparent profile length  $L$ .

$$R_L = \frac{\lambda_0}{L} \quad (14)$$

$R_L$  can be estimated from the vertical section planes similar to those discussed for microstructures. The surface roughness parameter  $R_S$  can be estimated from the experimentally measured profile roughness parameter,  $R_L$  by using the following equation developed by Gokhale and Underwood[80].

$$R_S = \langle \Psi \cdot R_L \rangle \quad (15)$$

where,

$$\Psi = \int_0^\pi [\sin\alpha + (\frac{\pi}{2} - \alpha)\cos\alpha] f(\alpha).d\alpha \quad (16)$$

$\Psi$  is called profile structure factor, and  $f(\alpha)$  is the orientation function of the fracture profile and is defined such that  $f(\alpha)d\alpha$  is the fraction of the profile length in the orientation range  $\alpha$  to  $(\alpha + d\alpha)$ , where  $0 < \alpha < \pi$ . Here  $\alpha$  is the angle between a line element in the vertical section fracture profile and the vertical axis.

The experimental values of  $R_L$  reported for many materials lie between 1-2.3. An example is presented in the works of Gokhale and Drury [81] where they calculated the value of  $R_L$  by performing measurements on vertical sections at mutually  $120^\circ$  on the fracture profile of an Al-Li alloy. The microstructure of the material consisted of unidirectional alumina fibers in the Al-Li alloy and tested under tension perpendicular to the fiber orientation introducing anisotropy in the microstructure. Figure 2.29 illustrates the value of  $R_L$ , distribution of the orientation of the fracture profile  $f_\alpha$  and the profile structure factor  $\Psi$  on the three different vertical sections. The values vary with the orientation of the vertical sectioning plane as expected.

Jamwal et al.[82] used the fracture profilometry to quantify the fracture path of Dual Phase steel under Quasi-static tension to understand the variability observed in the ductility of the specimens. They observed that the fraction of the fracture path passing through ferrite was the maximum and remained unchanged with the change in ductility, while, the fraction of the path passing through the ferrite-martensite interfaces increased with a decrease in ductility. Figure 2.30 depicts an optical micrograph of the Dual Phase steel with red tracers indicating the path lying on ferrite and the blue tracer indicating the path lying on martensite. Thus, the profilometry helped to understand the global fracture mechanism by establishing that ferrite facilitates fracture while martensite resists it. Another efficient way of determining the fracture mechanism is by performing image-based Quantitative fractography.

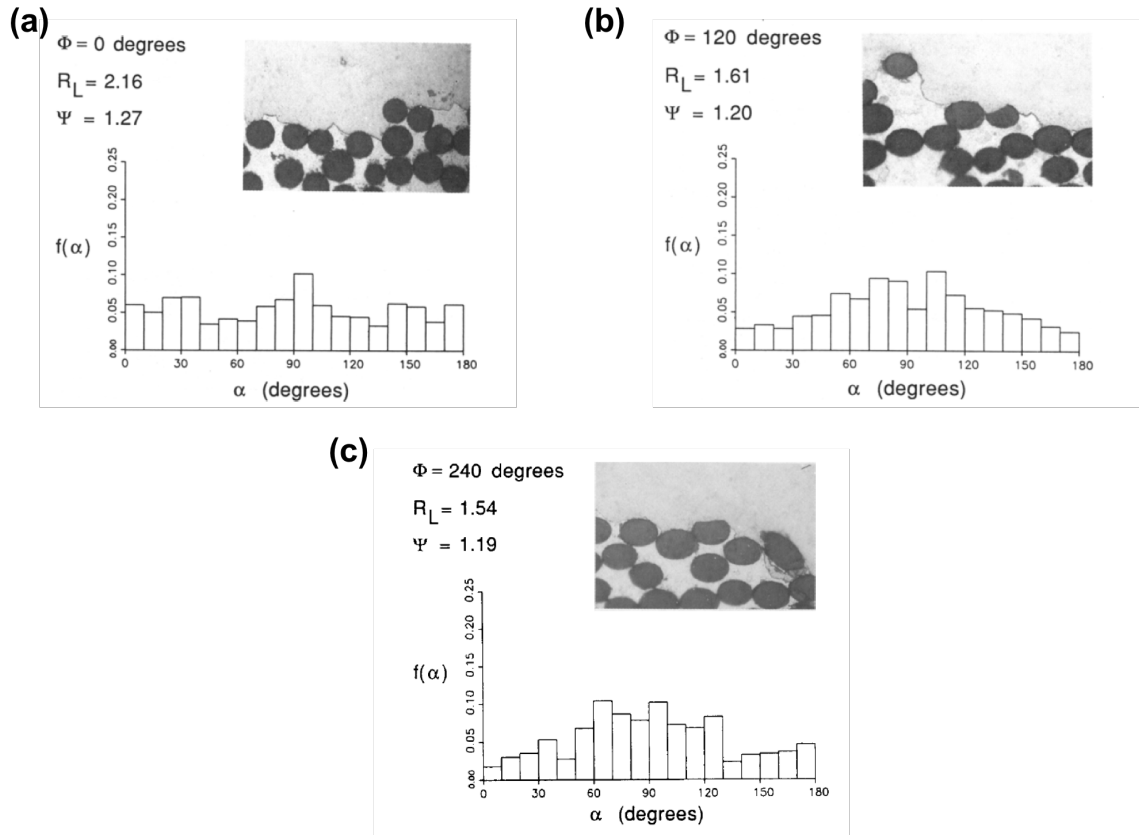


Figure 2.29: Values of the fracture roughness profile parameter  $R_L$  calculated on an Al-Li alloy on three vertical planes at (a)  $0^\circ$ , (b)  $120^\circ$  and (c)  $240^\circ$  [81]

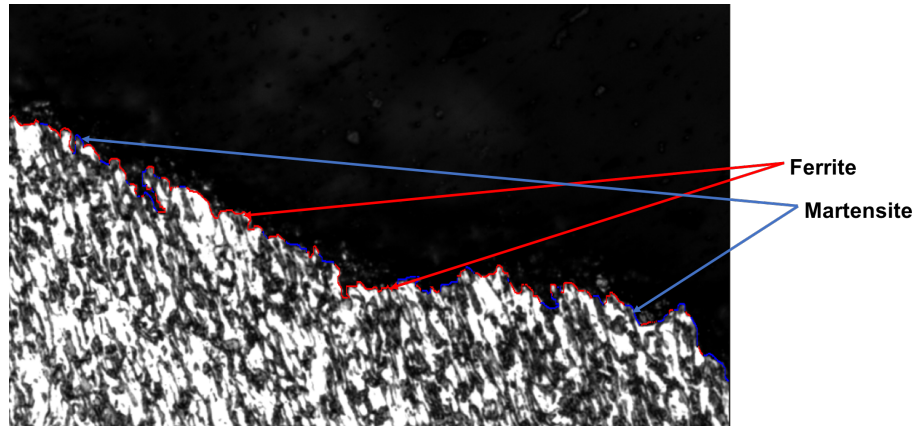


Figure 2.30: Fracture profile of DP steel with about 60% martensite. the red tracers show the fracture path lying in ferrite(bright regions) and the blue tracers show the fracture path lying in martensite(dark regions)[82]

### SEM image based fractography

SEM based fractography employs stereological techniques for qualitative and quantitative examination of fracture surfaces. It is useful for quantitative characterization

of specific features observed in the fracture surface[2]. These features can be quantified using number density, average size, orientations etc, of the feature of interest [80]. Estimation of the area fractions on the fracture surface corresponding to failure mechanisms like dimple fracture, cleavage fracture or quasi-cleavage fracture can be performed with accuracy and ease. Although, the dominant fracture mechanism can be obtained by a qualitative analysis of the fractographs, a quantitative analysis involving area fraction by point counting can lead to an estimation of the contribution of different mechanisms. Ductile regions correspond to dimpled surfaces, and cleavage and quasi-cleavage surfaces correspond to brittle surface. The area fraction of the region of interest can be obtained by the following equation[80, 74]:

$$P_P(\text{feature of interest}) = A_A(\text{dominant fracture mechanism}) \quad (17)$$

The quantity  $A_A$  is termed as the area fraction of the SEM image of the feature of interest. This area fraction is termed as the projected area fraction. The effect of projection in the SEM images can be accounted for by computing the true area fraction 'F' using the following equation[80]:

$$F = \left[ \frac{R_S}{(R_S)_\beta} \right] A_A \quad (18)$$

where  $R_S$  represents the fracture roughness parameter obtained using profilometry and is used to correct the effects of the projection in SEM images.

The number per unit area of a feature of interest in an SEM image,  $N_S$  can also be obtained by using unbiased sampling. The method employed is similar to  $N_A$  discussed earlier.  $N_S$  is calculated using the equation below[80]:

$$N_S = \frac{\langle N \rangle}{\frac{A}{M^2}} \quad (19)$$

where  $\langle N \rangle$  is the average of the number of features observed in an area  $A$  of the unbiased frame at magnification  $M$ . This can also be corrected for projection to obtain the true number density  $N_f$  using the following equation[80]:

$$N_f = \frac{N_s}{R_s} \quad (20)$$

The average size of the dimples can also be estimated from the SEM fractographs. The true area fraction divided by the true number density of dimples results in the true average dimple size given by  $\Omega$ . By incorporating the true values, the effects of projection can be eliminated[80, 76]:

$$\Omega = \frac{F}{N_f} \quad (21)$$

These features give important information on operative fracture mechanisms that generate the fracture surface. The number density and dimple sizes can provide information on the growth and coalescence mechanism of voids. Jamwal et al. [82] used the aforementioned techniques to understand the fracture mechanisms and variation in ductility in a Dual Phase steel containing about 60% martensite. Figure 2.20 illustrates some of the results from the work. The area fraction of the ductile regions has a direct correlation with an increase in ductility, whereas number density of pullouts shows an inverse correlation with the ductility. These data led to the conclusion that the pullouts were responsible for the fracture. The average size of the dimples was not affected by the ductility concluding that the variation in ductility resulted from processes occurring after the onset of necking. Figure 2.31 (c) illustrates a nominal fracture surface of the Dual Phase steel used in the study and the features measured using quantitative fractography.

The aforementioned techniques will be employed in the proposed research to determine the fracture mechanisms of DP steels at different strain rates.

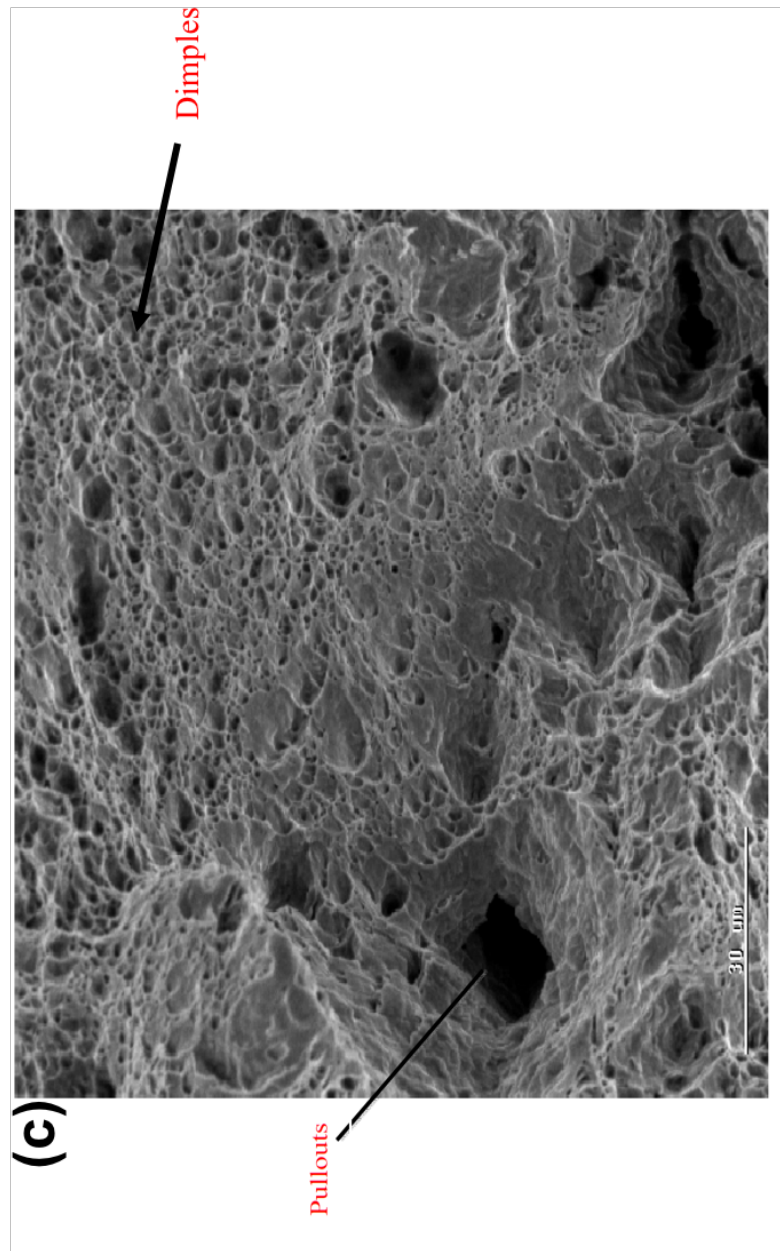
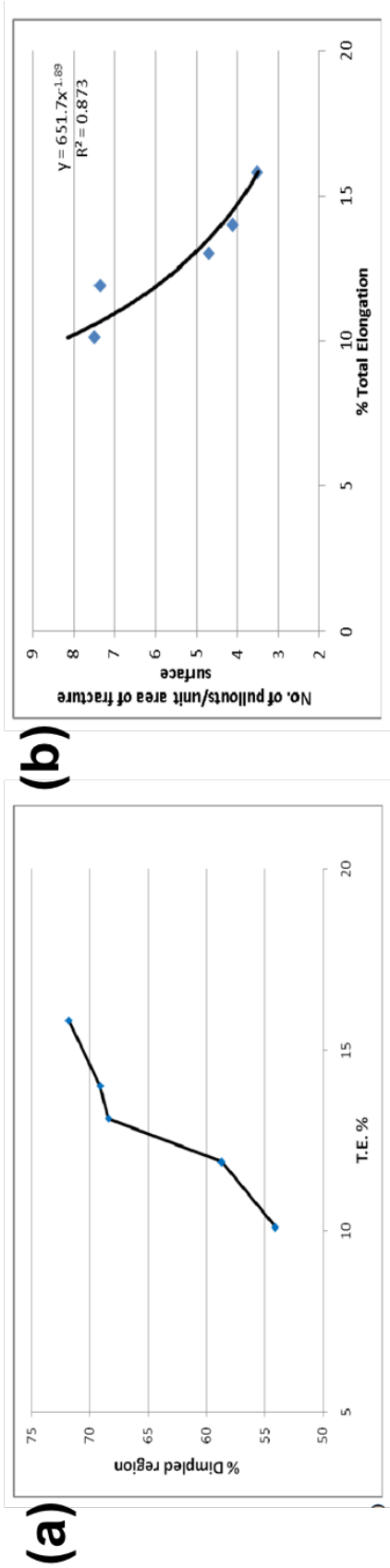


Figure 2.31: Quantitative fractography results performed on DP steel to understand the variation in ductility. (a) Direct correlation of the dimpled region with increase in ductility confirming that the area fraction can be used a reliable technique to estimate the ductility of a material, (b) Inverse-correlation of the number density of pullouts with the ductility indicating the pull outs may be responsible for premature fracture. (c) Nominal fracture surface observed showing dimpled regions with the pull-outs that cause reduction in ductility[82].

## 2.7 Summary

A review of the literature as discussed in this chapter reveals the following key aspects that are missing in the literature and are crucial to capture and understand the fracture mechanisms of DP steels :

- Although the microstructural features have been quantified, little to no studies exist that identify, classify and quantify all the fracture surface features as a function of the martensite volume fraction and morphology
- A systematic study on the effects of strain rate on the fracture features of DP steels with different martensite volume fraction and morphology does not exist
- No quantitative characterization and mechanical testing of DP steels with galvanized coating layers or a graded microstructure (eg: with decarburised layer) and their behavior under dynamic strain rates has been performed.
- Although, the effect of geometry on ductility is widely researched, no standard geometry exists for the testing of sheet materials under dynamic rates. Additionally, no studies exist on DP steels which capture the effect of strain rate on the mechanical properties independent of geometry.
- No studies have been conducted in the high strain rate regime associated with plate-on-plate impact experiments to observe the fracture and understand the operating fracture mechanisms in the DP steels under dynamic tensile (spall) loading conditions.

The current work aims to bridge the gap by conducting quantitative fractography on DP steels with and without a gradient, to establish microstructure-based operative fracture mechanisms under a wide range of strain rates including quasi-static and dynamic strain rates. The tests performed under quasi-static and intermediate strain

rates will be conducted using the same geometry to maintain uniformity and make a valid comparison between mechanical properties.



## CHAPTER 3

### EXPERIMENTAL WORK

This chapter provides a detailed description of the materials employed in the current study, the methods employed to characterize and quantify the microstructure, the procedures used to execute quasi-static and intermediate strain rate tensile tests, the design of uniaxial-strain plate impact tests and the methods employed for the holistic characterization and quantification of fracture surfaces.

#### 3.1 Overview

The research performed in this work addresses the following objectives:

- (a) capture and quantify the effects of microstructure and strain rate dependence of mechanical properties and fracture mechanisms in the different grades of DP steel.
- (b) understand if the failure mechanisms of the coating layers change as a function of strain rate, and if these mechanisms influence the failure mechanisms of the underlying steel substrate.
- (c) understand and compare the behavior of a graded microstructure (DP steel with decarburized layer) as a function of strain rate to that of a nominal DP steel.
- (d) investigate the effect of specimen geometry on the deformation behavior and ductility of the DP steel specimens.
- (e) subject the materials to high strain rates generated via plate impact tests and compare the properties and fracture mechanisms under uniaxial-strain loading with uniaxial stress loading achieved with quasi-static and intermediate strain rate regimes

Central to the above objectives is the notion that since the ductility is known to be dependent on the specimen geometry, the tensile testing sample geometry is kept constant across strain rates for  $10^{-6}$  to  $10^3/s$  to make a valid comparison of the

deformation and fracture response of the material.

For this purpose, experimental work has been performed on four commercial Dual Phase steels to understand the role played by (a) the volume fraction of martensite, (b) the processing conditions employed during manufacturing of the DP steels, (c) the addition of protective coatings, and (d) presence of a gradient in the microstructure. All of the steels used in the work were provided by ArcelorMittal Global R&D in East Chicago. The following sections contain details about the materials used, metallographic preparation of specimens for microscopy, quantitative characterization of the observed microstructures, quasi static and dynamic tensile tests, and plate on plate impact tests, and quantitative fractography and profilometry.

### **3.2 Material system and chemistry**

The following commercial DP steels are used in the experiments performed in this work:

- DP 590: with about 25% martensite and no protective coating. This steel serves as the baseline for establishing mechanical properties and operative fracture mechanisms at varying strain rates. Two thicknesses of 1.2mm and 2mm of sheet steel are used in the current work.
- DP 980 : with about 65% martensite and no coating or gradient. This has been used as a comparison to understand the differences in properties with the addition of protective coating layers and decarburized surface layers. This sheet steel will henceforward be referred to as DP 980 NC and has a thickness of 2mm.
- DP 980 GA : With volume fraction of phases similar to DP 980 NC. This steel is used to understand the differences obtained in microstructure and mechanical properties due to the addition of a galvanized coating layer. This sheet steel

Table 3.1: Nominal composition of as-received Dual Phase steels.

	<b>C(%)</b>	<b>Mn(%)</b>	<b>Si(%)</b>	<b>Mo(%)</b>	<b>Cr(%)</b>	<b>Al(%)</b>
<b>DP 590</b>	0.08	0.99	0.27	0.007	0.03	0.04
<b>DP 980 NC</b>	0.09	2.02	0.62	0.06	0.05	0.03
<b>DP 980 GAN</b>	0.08	2.29	0.29	0.29	0.27	0.064
<b>DP 980 GAD</b>	0.09	2.1	0.28	0.27	0.19	0.052

will henceforward be referred to as DP 980 GAN and it also has a thickness of 2mm.

- DP 980 GA decarburized : Steel with a graded microstructure and protective coating. The surface layers of the steel are intentionally decarburized to enhance bendability. The bulk material is similar to the DP 980 GA steel. The effects of both the gradient and the protective coating are studied. This sheet also has a thickness of 2mm and is hereby referred to as DP 980 GAD.

The nominal compositions of the four steels described above are presented in Table 3.1.

### 3.2.1 Ultrasonic Testing

The longitudinal and shear sound speeds are important characteristics of the material that are used in determining the Hugoniot Elastic Limit (HEL) and the spall strength of the material. Sound speed measurements were made on all steels using the Olympus 5072PR pulse/receiver in the pulse-echo configuration. The Ultrason VSP-200 transducer was used to measure the longitudinal sound speed and the SRD50-0 transducer was used to measure the shear wave velocity. Data was recorded using the Tektronix DPO 5104 1 GHz oscilloscope. Table 3.2 shows the measured values of the longitudinal ( $C_L$ ), shear ( $C_S$ ), and bulk ( $C_B$ ) sound speeds of the different steels. For the coated steels, the properties would be that of the composite structure. The bulk sound speed, computed using the longitudinal and shear sound speeds, is based

on the following equation (19).

$$C_B = \sqrt{C_L^2 + \frac{4}{3}C_S^2} \quad (22)$$

The elastic constants such as the Young's modulus (E) (eqn 20), the shear modulus (G) (eqn 21), the bulk modulus (K) (eqn 22), and the Poisson's ratio ( $\nu$ ) (eqn 23) were also computed using the longitudinal and shear sound speeds.

$$E = \rho C_L^2 \frac{(1 + \nu)(1 - 2\nu)}{(1 - \nu)} \quad (23)$$

$$G = \rho C_S^2 \quad (24)$$

$$K = \rho C_B^2 \quad (25)$$

$$\nu = \frac{1 - 2(\frac{C_S}{C_L})^2}{2 - 2(\frac{C_S}{C_L})^2} \quad (26)$$

### 3.2.2 Density Measurements

The density  $\rho_0$  of the steels was measured by using the Archimedes method. The specimens were weighed in air and then weighed when completely submerged in water at a known temperature. The density was calculated using equation (24). The density of the steels is also presented in table 3.2.

$$\rho_0 = \rho_{water} \frac{m_{dry}}{m_{dry} - m_{wet}} \quad (27)$$

Each measurement was repeated at-least three times for each specimen. When measuring the density of the specimens to be used for the plate-impact tests, the specimens were measured before and after lapping of the samples.

Table 3.2: Sound speed and bulk properties of DP steels

Material	Density	Sound Speed Measurements			Elastic Constants			
	$\rho_0(g/cm^3)$	$C_L(mm/s)$	$C_S(mm/s)$	$C_B(mm/s)$	$E(GPa)$	$G(GPa)$	$K(GPa)$	$\nu$
<b>DP 590</b>	$7.82 \pm 0.03$	$6.31 \pm 0.11$	$3.34 \pm 0.05$	$4.98 \pm 0.15$	$228 \pm 6$	$87.5 \pm 2.7$	$195 \pm 11$	$0.30 \pm 0.01$
<b>DP 980 NC</b>	$7.80 \pm 0.02$	$5.99 \pm 0.06$	$3.23 \pm 0.04$	$4.68 \pm 0.07$	$211 \pm 14$	$81.8 \pm 2.3$	$171 \pm 4.4$	$0.29 \pm 0.006$
<b>DP 980 GAN</b>	$7.84 \pm 0.04$	$5.88 \pm 0.05$	$3.19 \pm 0.04$	$4.57 \pm 0.05$	$205 \pm 5.4$	$79.8 \pm 2.4$	$164 \pm 3.8$	$0.29 \pm 0.006$
<b>DP 980 GAD</b>	$7.85 \pm 0.003$	$5.84 \pm 0.03$	$4.54 \pm 0.06$	$4.54 \pm 0.04$	$204 \pm 3.5$	$79.2 \pm 1.6$	$161 \pm 2.8$	$0.29 \pm 0.005$

### 3.3 Microstructural characterization

To characterize the as received steels, metallography along with a detailed quantitative analysis of the microstructures was performed. The methods employed are discussed ahead.

#### 3.3.1 Metallography

Metallography was performed on sections obtained from all three orthogonal planes of the rolled sheet steels. DP 590 and DP 980 NC, which did not have any coating, were mounted in conducting epoxy. For DP 980 GAN and GAD, however, an acrylic mount with a greater edge retention was used so as to observe the surface coatings with minimum damage. The sectioned and mounted specimens were subjected to wet grinding first, starting from a coarse 320 grit silicon carbide paper followed by 400, 600, 800, 1000, and finally finished with 1200 grit paper. Grinding was followed by polishing the sample with  $3\mu\text{m}$  and  $1\mu\text{m}$  aqueous-based diamond solutions. The final polishing step was performed by using a  $0.05\mu\text{m}$  colloidal silica solution to remove all scratches. Thorough cleaning of the sample in an ultrasonic bath was followed by etching to reveal the microstructures. A two-step etching procedure was followed to reveal all the present phases with clarity. A 2% Nital (Nitric Acid+Ethanol) solution to etch for grain boundaries followed by a 10% aqueous sodium metabisulphide solution to etch the harder phase was used in the current study for all steels.

*As reviewed in the background chapter, the processing conditions for manufacturing DP 980 GAN and GAD led to differences in the resulting microstructure such that instead of a low temperature tempered martensite, as in the case of DP 980 NC, a mixture of auto-tempered martensite, bainite and retained austenite may be contained in the harder phase of both GAN and GAD. However, for the ease of discussion, this phase will be referred to as 'martensite' for all the four DP steels henceforth.*

Optical microscopy images were taken using the Carl Ziess Microscope and the images were analyzed using Axio vision version 8. In the optical micrographs, the ferrite phase appeared as the lighter phase while the harder martensite phase was etched dark. Figure 3.1 shows the optical microstructures of (a) DP 590, (b) DP 980 NC, (c) DP 980 GAN and, (d) DP 980 GAD.

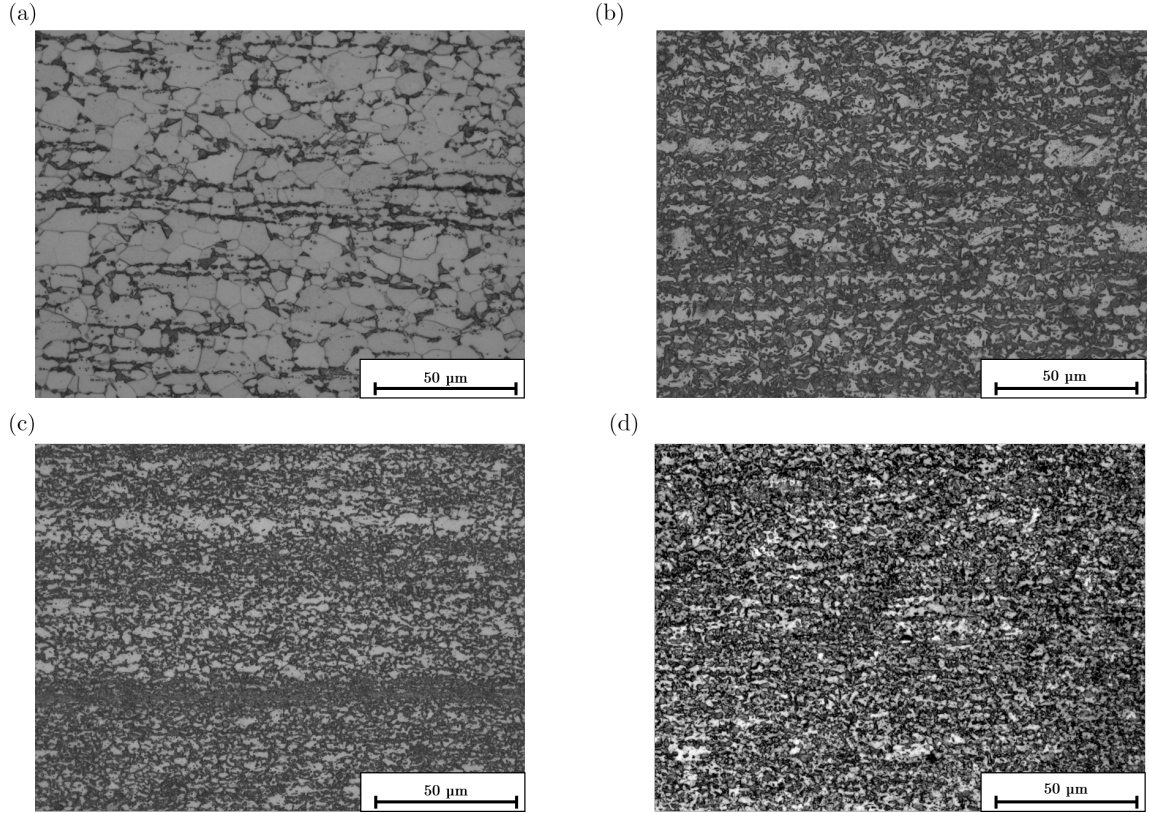


Figure 3.1: Representative etched optical micrographs showing the longitudinal sections of (a) DP 590, (b) DP 980 NC, (c) DP 980 GAN and (d) DP 980 GAD. Ferrite is the lighter phase while martensite is etched dark.

Scanning Electron Microscopy (SEM) images were captured using LEO 1530 and Hitachi SU-8030 SEMs. Figure 3.2 shows representative SEM images of (a) DP 590, (b) DP 980 NC, (c) DP 980 GAN and (d) DP 980 GAD steels. The harder martensite phase can be recognized as the one with the topological relief. Significant difference between the microstructures of the DP 590 grade and 980 grade can be observed, particularly in the volume fraction of martensite. Energy Dispersive X-

Ray Spectroscopy (EDX) was also used to characterize and observe the chemical composition of the galvanized coating layer and the decarburized layer of the GAN and GAD steels.

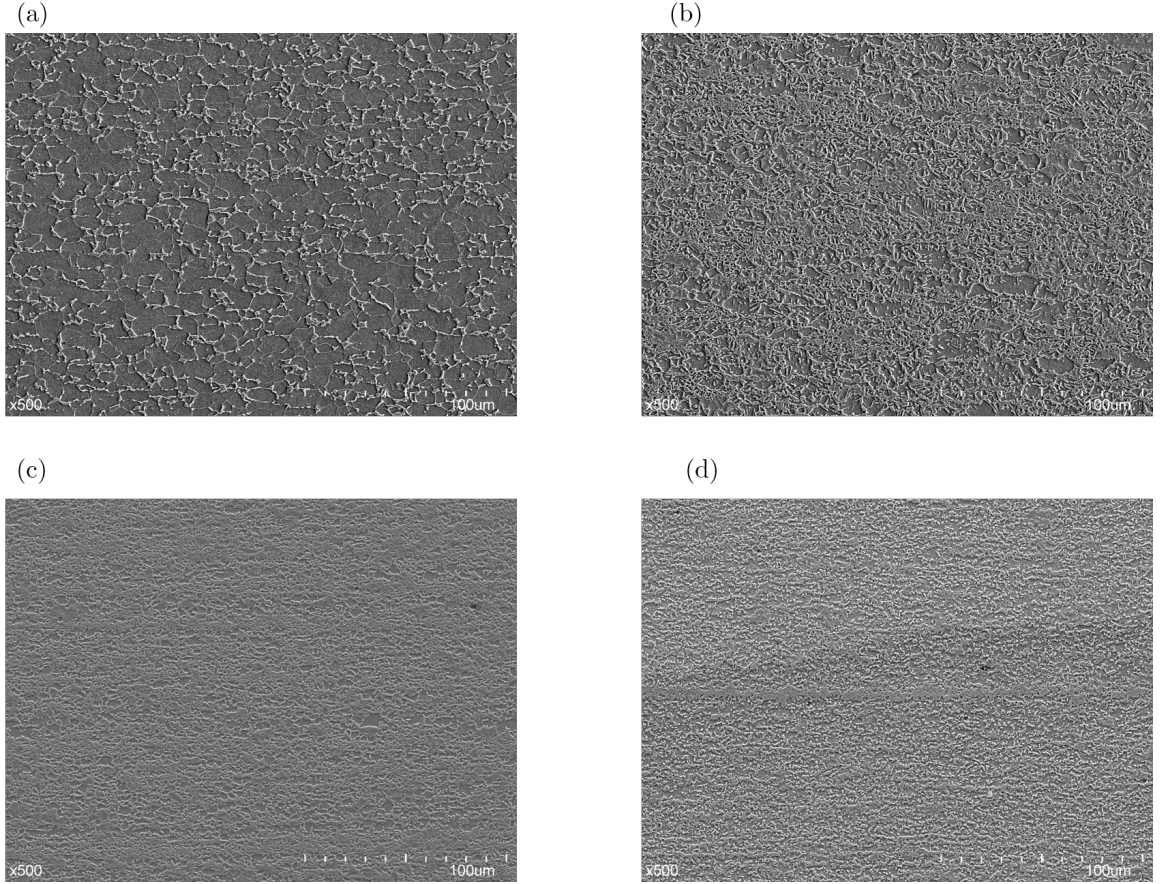


Figure 3.2: Representative SEM images showing the longitudinal sections of (a) DP 590, (b) DP 980 NC, (c) DP 980 GAN, and (d) DP 980 GAD. The harder phase can be identified as the phase with the relief.

### 3.3.2 Quantitative Microscopy

#### *Estimating Volume Fraction*

The volume fraction of the phases present was estimated by using systematic point counting technique. A grid containing 150 points was placed on each SEM micrograph,  $P_T = 150$ . The points that fell on the harder martensite phase were manually counted, ( $P^H$ ). Points that landed on the two-phase interface were counted as 0.5.



Thus, if we consider the total number of images sampled as  $N$ , the volume fraction of martensite, ( $V_V^M$ ), derived from the point fraction is estimated using equation (25):

$$V_V^M = \langle P_P^H \rangle = \left[ \frac{\langle P^M \rangle}{P_T} \right] = \left[ \frac{P^M}{P_T} \right] \pm \left[ \frac{1.96}{P_t} \right] \sqrt{\frac{s^2}{N}} \quad (28)$$

where  $s^2$  is the sample variance and is given by equation (26):

$$s^2 = \sum_{i=1}^N \frac{[(P^H) - (P^H)_i]^2}{(N - 1)} \quad (29)$$

Figure 3.3 shows an example of the point counting technique used. A representative image with points superimposed depicts how the counting was performed.

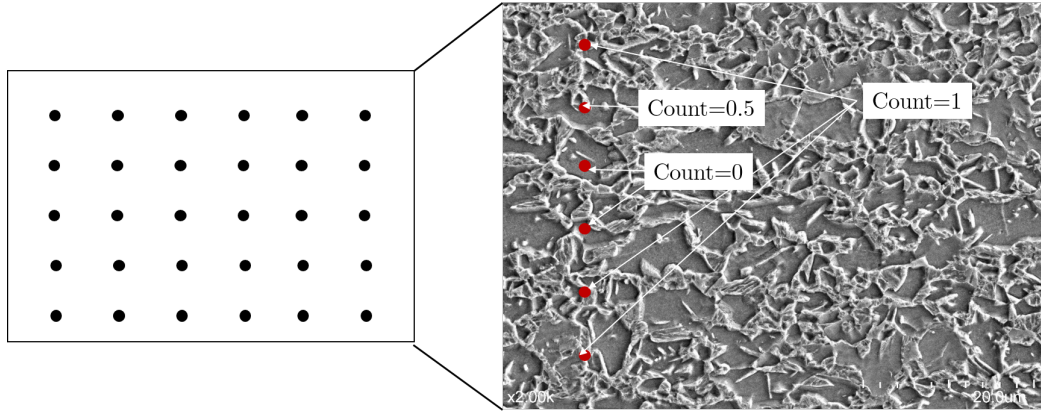


Figure 3.3: Schematic and representative microstructure (DP 980 NC) illustrating the point counting method employed to estimate the volume fraction. Points lying in the harder phase were manually counted. If the point lay on the interface of the two phases, it was counted as 0.5

Since all the sheet steels were rolled and have anisotropic microstructures, the surface area per unit volume of the interfaces ( $S_V$ ) was estimated using vertical sections and cycloids. The vertical direction was the normal direction and, thus, the longitudinal and transverse sections were the vertical sections for the measurements. A set of cycloids was superimposed on the images in a grid and the number of points lying on the interfaces was counted manually [ $P_i$ ]. The length of the cycloids was calculated and is denoted as  $L_i$ . The Surface area per unit volume was estimated using equation

(30):

$$S_V = 2[P_L]^C$$

where, (30)

$$[P_L]^C = \frac{\sum P_i}{\sum L_i}$$

A representative image identifying the vertical axis and vertical sections along with superimposed cycloids is shown in figure 3.4.

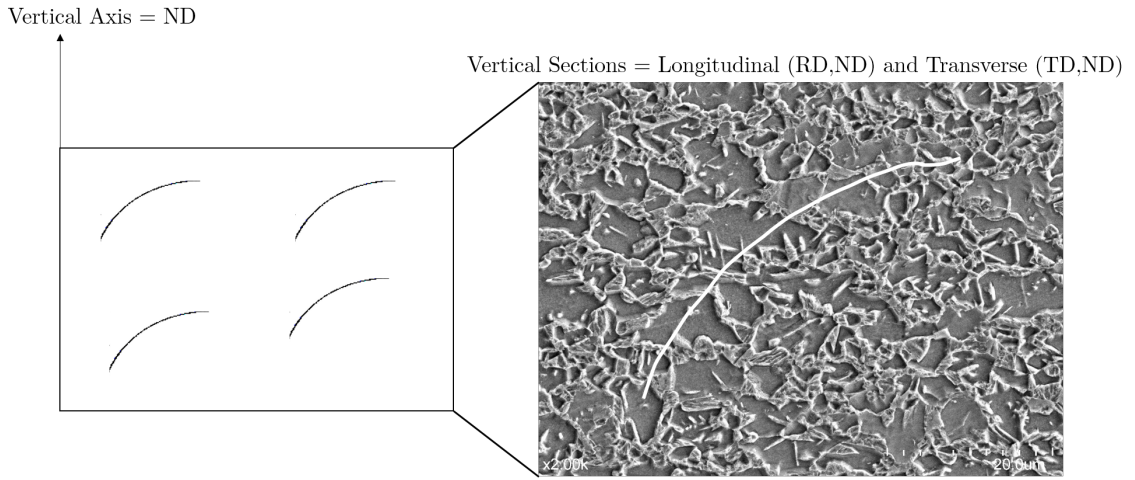


Figure 3.4: Schematic and representative SEM image (DP 980 NC) illustrating the method employed to determine the  $S_V$  of the interfaces for the anisotropic sheet steels using cycloids. The number of intersections made by the interfaces with the cycloids was counted manually.

The mean free path through the matrix phase ( $\lambda$ ) was thus calculated using equation (28). The matrix for the DP 590 steel was ferrite and for all the DP 980 grade steels was the harder phase. :

$$\lambda = \frac{4(1 - V_v)}{S_V} \quad (31)$$

### 3.4 Mechanical Testing

The mechanical properties have been characterized under three strain rate regimes - Quasi static, Intermediate and high strain rate. The specimen geometries used, machining of the samples, and the design of the tests at each strain rate regime are discussed ahead.

#### 3.4.1 Sample geometries and machining

The specimen geometry for the tensile tests for a given steel was kept constant across the quasi-static and intermediate strain rate regimes. This was done to ensure a true comparison of final elongation across all strain rates, since the post-uniform elongation and resulting final elongation are sensitive to the specimen geometry. The geometries that can be used for tensile tests at all strain rates are limited by those that can be successfully implemented at intermediate strain rates achieved using the Hopkinson bar. The current study utilized two Hopkinson bar systems, one for DP 590 and the other to test all the DP 980 grades. The details on the methods of testing are discussed later in this section.

To capture and understand the effect of geometry on the deformation behavior, DP 590 steel was tested using specimens of two different geometries: a Japanese Industrial Standard (JIS) geometry to establish a base line for mechanical properties and is shown in figure 3.5 (a), and a miniature tensile geometry that was compatible with the Hopkinson bar and could be used for both the quasi-static and intermediate strain rates.

The miniature tensile geometry that was employed in the current work was first tested by Sun et al [83] for TRIP steels under quasi-static and intermediate strain rates. They observed that the sample geometry showed a uniform strain distribution within the gage section and the grips underwent complete elastic deformation. The

geometry adopted from the study was modified slightly to reduce the energy required to fracture the sample under intermediate strain rates using the Hopkinson bar as shown in figure 3.5(b). The grip section of the geometry was doubled to ensure a better grip when testing the specimen under quasi-static strain rates. The modified geometry with the extended grip sections is shown in figure 3.5 (c). All dimensions are in mm.

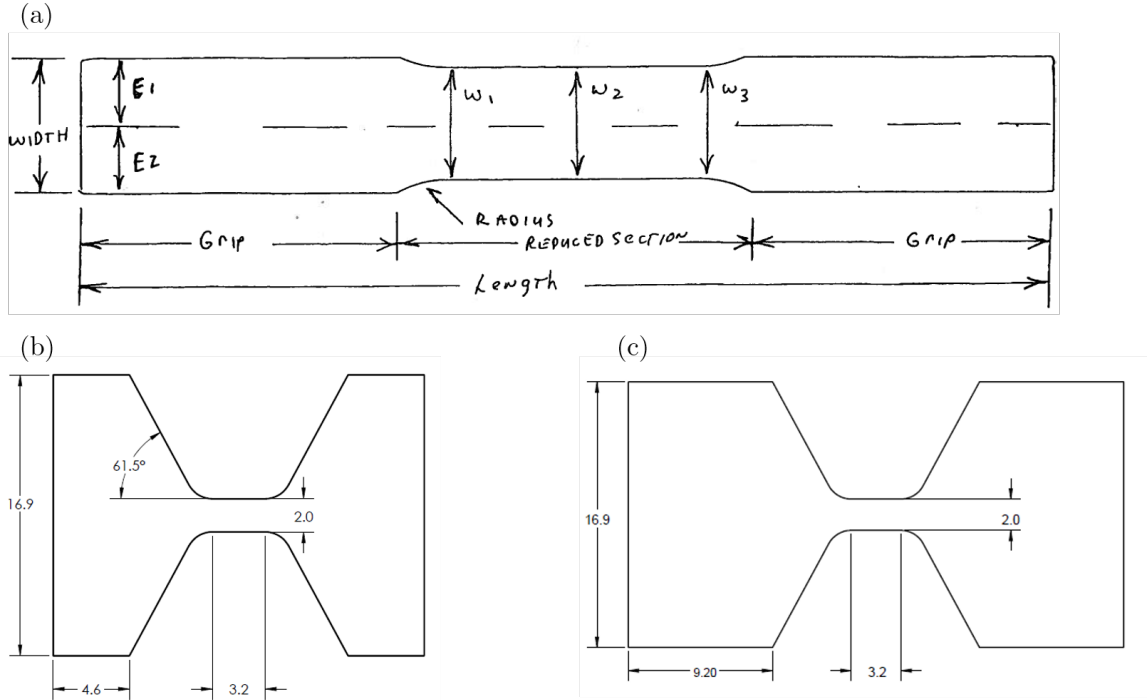
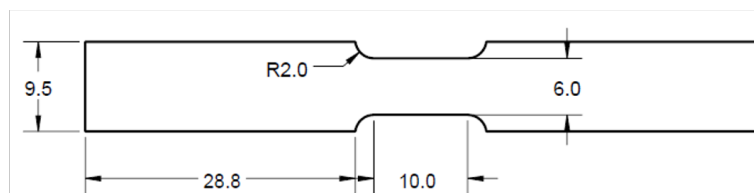


Figure 3.5: Specimen geometries that were used to test DP 590 steel. (a) Japanese Industrial standard, used to establish the baseline for quasi-static strain rates, (b) modified miniature tensile geometry for Hopkinson bar tests, (c) modified miniature tensile geometry with extended grip sections for quasi-static strain rate tests.

The intermediate strain rate tests for the DP 980 grade steels were conducted using the Hopkinson bar at REL Inc. The geometry used for all the tests for these steels was one that was compatible with the Hopkinson bar at REL Inc. and is shown in figure 3.6(a). Some intermediate strain rates that were too slow for the Hopkinson bar were conducted using the servo-hydraulic tensile tester at ArcelorMittal. To ensure better gripping, the grip regions of the geometry were extended. The modified

geometry is shown in figure 3.6 (b). No changes were made to the gage section of the geometry.

(a)



(b)

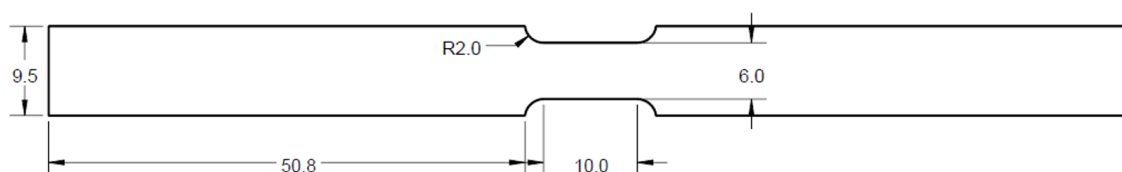


Figure 3.6: (a) specimen geometry used for all the quasi-static and Hopkinson bar tests of DP 980 grade steels, (b) geometry used for intermediate strain rate testing at ArcelorMittal. Extended grip sections were added to improve gripping of sample.

The JIS specimens used to test the DP 590 steels were provided by ArcelorMittal. The miniature tensile specimens and the REL geometry specimens were machined at Georgia Tech using the water jet equipment that enables machining without heating of specimens. All specimens were machined such that the loading direction during the test was along the transverse direction of the sheet steel. All specimens were also de-burred prior to testing to eliminate sharp edges created during machining.

### 3.4.2 Servo-hydraulic Testing

All quasi-static and a few intermediate strain rate tests were conducted using servo-hydraulic systems. The quasi-static strain rate tests from  $10^{-6}/s$  to  $1/s$  were performed on the MTS servo-hydraulic equipment in the Material Properties Research Laboratory (MPRL) at Georgia Tech. Strain rates of  $10^2/s$  were tested using the servo-hydraulic systems at ArcelorMittal Global R&D facility.

The raw data from the tensile tests consisted of load-displacement curves. The engineering stress was calculated by dividing the load obtained from a calibrated load cell by the measured undeformed area of the specimen. Both the elastic and plastic strains were captured. An accurate measure of the elastic strain was obtained by using precisely calibrated strain gauges for the REL and miniature geometries and an extensometer for the JIS geometry. The plastic strain was determined from the calibrated displacement cylinder of the servo-hydraulic machines.

Additionally, to capture the deformation of the miniature sample geometry, Digital Image Correlation (DIC) was used. To accomplish DIC, a high speed camera (NAC GX) was setup to capture the deformation. The images obtained served two main purposes: (i) to accurately measure the total strain and (ii) to map the real time deformation and necking of the specimen. Figure 3.7 (a) shows a schematic of the servo-hydraulic setup with a high speed camera for DIC, and (b) shows representative images taken of the miniature geometry to observe the deformation and capture the total strain in the sample using DIC.

### 3.4.3 Hopkinson Bar Testing

The uniaxial tensile tests at intermediate strain rates of the order of  $10^2/s$  to  $10^3/s$  were conducted using the Hopkinson bar at the University of Alabama (UA) Tuscaloosa and REL Inc. on DP 590 steel specimens and DP 980 steel specimens respectively. Figure 3.8(a) shows a picture of the pressure system and striker bar connections of the UA Hopkinson Bar, and 3.8 (b) shows the working principle of a tensile split Hopkinson bar.

As mentioned in the previous chapter, the incorporation of sheet materials in Hopkinson bar tested is a fairly recent development and is still being modified. One challenge is to grip the sheet specimens and connect them to the cylindrical bars. While the DP 980 grade steel specimens were tested using the REL grips, the grips

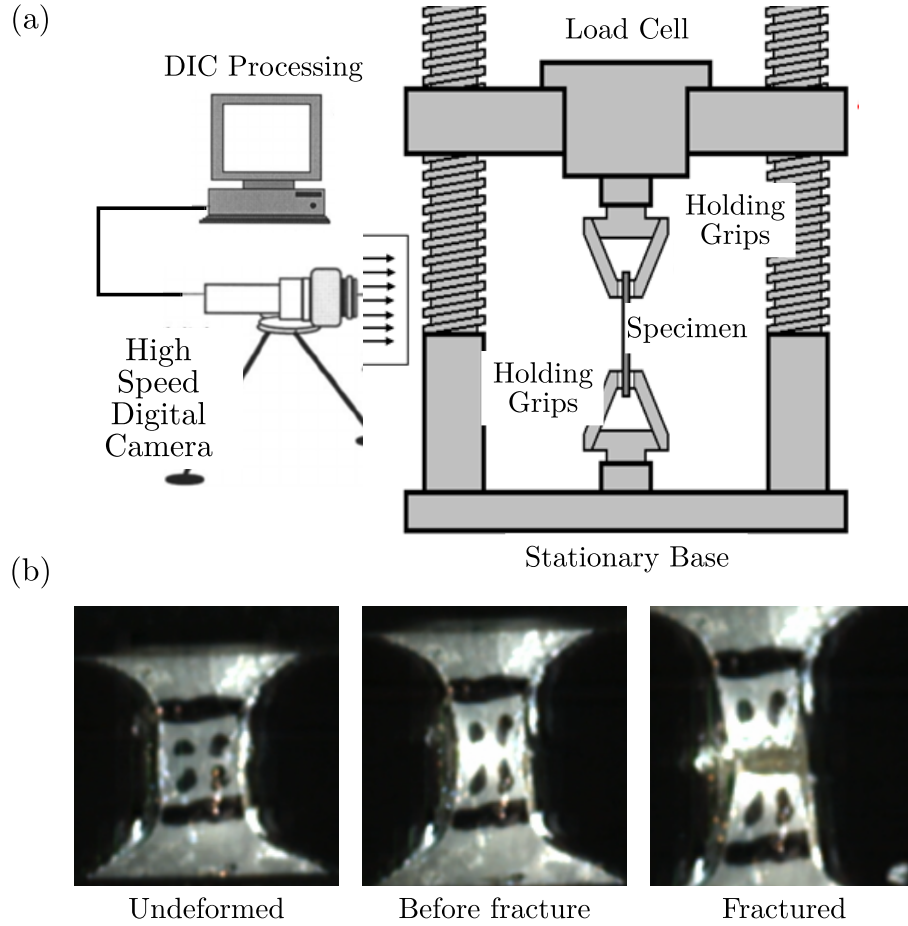


Figure 3.7: (a) Schematic of the servo-hydraulic setup used for the quasi-static strain rates. High speed digital camera was used to conduct DIC, (b) Representative DIC images of the miniature tensile geometry of DP 590 showing the undeformed, completely deformed and before fracture and the fractured samples. The frame just before fracture was used to confirm the final strain in the sample

used for the DP 590 steel specimens at UA were developed in-house by the UA group. The DP 590 sheet specimens were mounted using grips having a flat end on one side to hold the specimen, and a threaded cylindrical end on the other to make contact with the bars. Figure 3.8 (c) shows an image of the miniature geometry used for the tests at UA in the grips designed for these specimens. The material of the grips was

impedance-matched to the specimen to avoid noise in the data and was made of a high strength titanium alloy to facilitate all plastic deformation in the gage section of the mounted specimen.

Strain gauges mounted on the incident and transmitted bars of the Hopkinson bar setup were used to monitor the stress pulses going through. The voltage output from the strain gauges was converted into the stress-strain response of the material using the equations described in the previous chapter.

The strain in the specimen is further monitored by a high-speed camera. This setup, (which resembles the quasi-static setup) was also used to capture real time deformation and necking. Figure 3.8(d) and (e) show representative images taken using the high speed cameras for the miniature specimens and REL specimens respectively.



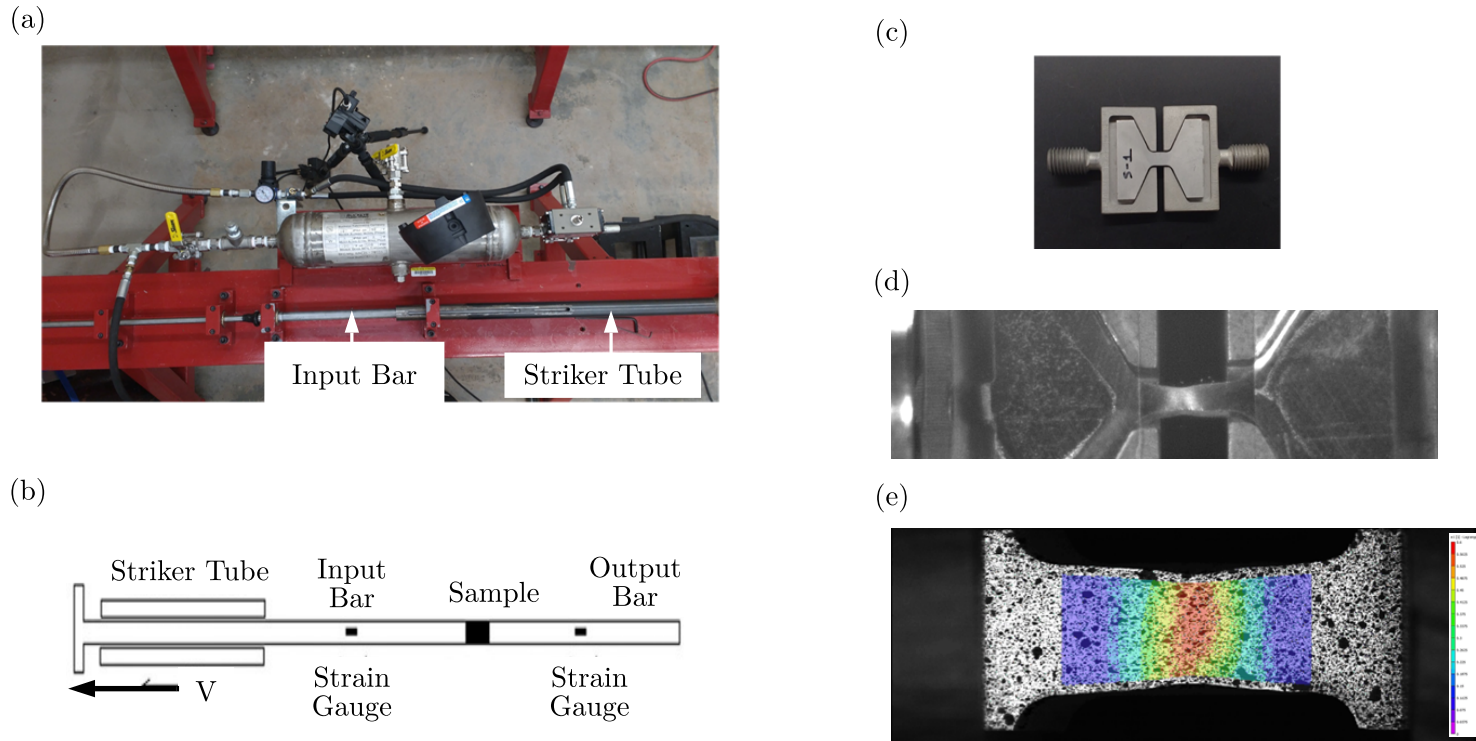


Figure 3.8: (a) Tensile split Hopkinson bar setup at UA showing the striker tube and the input bar along with the pressure chamber used for firing, (b) Principle used by the tensile Hopkinson bar, (c) DP 590 sample mounted in the titanium grips developed by the UA group in house, (c) representative DIC image of DP 590 showing the frame used to compute the total strain, (d) representative DIC and strain map image showing the frame used to calculate the total strain in the DP 980 NC sample.

#### 3.4.4 Uniaxial strain plate impact experiments

Dynamic strain rates of the order of  $10^4/s$  to  $10^6/s$  can be achieved via uniaxial strain plate impact experiments. In the present work, these experiments have been conducted using the 80 mm diameter, 7.6 m long single stage gas gun at Georgia Tech. Figure 3.9 (a) shows a schematic of the experimental design. Each experiment had three samples mounted in a stainless steel target holder with a slip fit. One sample was probed using VISAR to obtain the free surface velocity and the other two samples were recovered for post-mortem fractography. The target holder was mounted on a PMMA ring which upon impact can undergo brittle fracture and shatter. A polycarbonate backer plate was mounted behind the PMMA ring to allow the samples to pass through for soft recovery while restricting the target holder and projectile, thus, minimizing secondary collisions with the sample and causing further damage. An aluminum sabot was used as the projectile. DP 590 sheet steel with a thickness of 1.2 mm was used as the flyer plate. The DP 590 flyer was lapped to ensure a flat surface and the final thickness was controlled at 1mm. The flyer plate was maintained at half the thickness of the samples and the surrounding holder to allow the release waves from the rear surfaces of the target and flyer plates to interact along the mid-plane of the target plate. This interaction of release waves generates tension and consequent spallation. The decompression strain rate was used as an equivalent parameter for strain rate. Flyer plate material, velocity of the projectile and target thickness control the decompression strain rate of the specimen. Figures 3.9 (b) and (c) show representative pictures of the setup depicting the probing side and the impact side, respectively.

In the present work, the mechanical response of DP steels of interest has been characterized as a function of strain rate in a range spanning twelve orders of magnitude. In order to gain an understanding on the operative fracture mechanisms under this wide strain rate range, fractography based measurements were performed which

is discussed next.

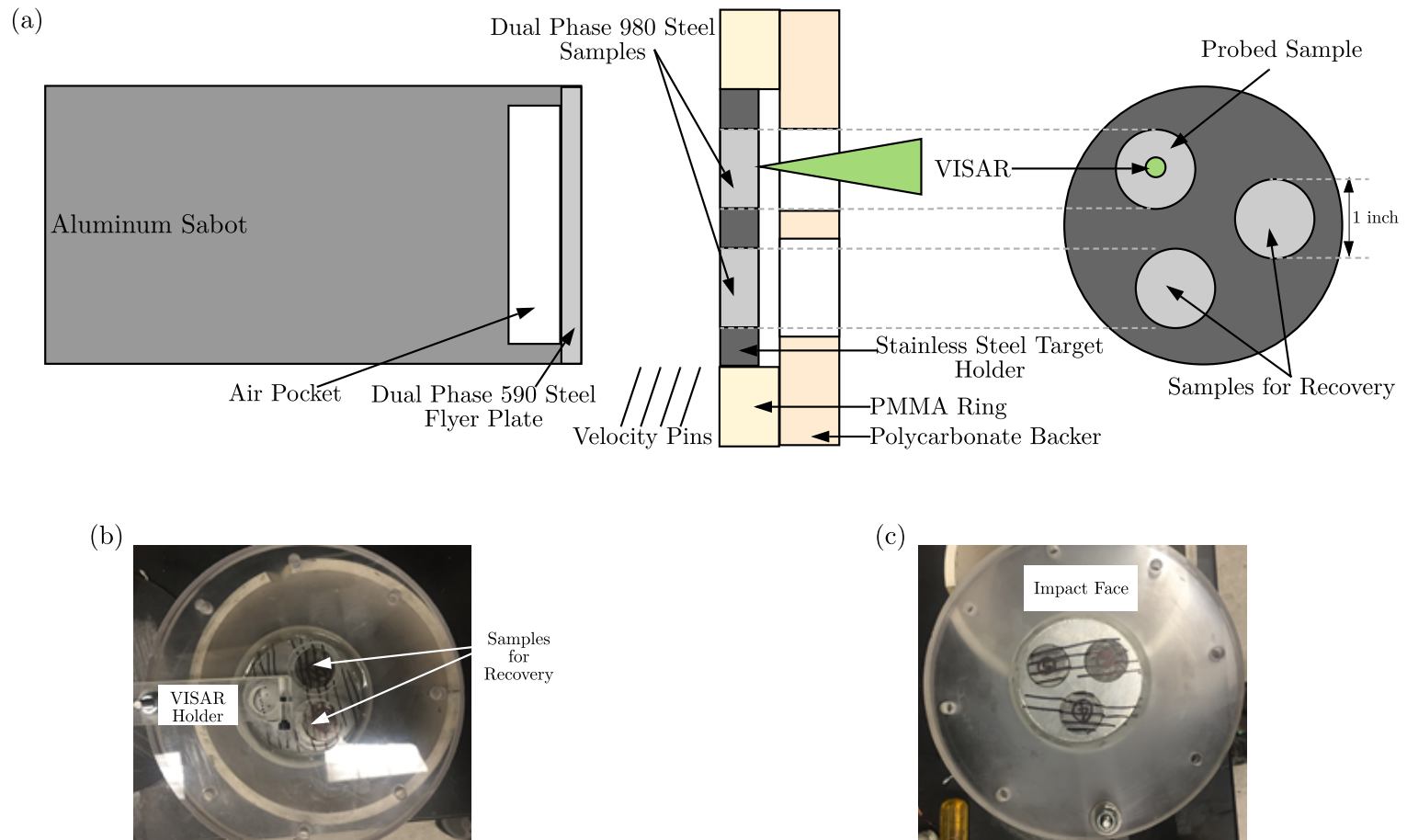


Figure 3.9: (a) Schematic showing the design and setup used for the plate impact experiments. All samples were 1 inch in diameter, (b) picture showing the target setup with VISAR probe mounted behind one sample and the two recovery samples, (c) picture showing the face that was impacted by the projectile.

### 3.5 Fractography

The fracture surface of a material is the most biased sample of the 3-D microstructure as it preferentially captures the features that are actively involved in determining the fracture response of the material. In other words, the fracture surface is a biased sectional view containing information on most of the weak links of the microstructural attributes. SEM based as well as profilometry based quantitative fractographic measurements were performed.

#### 3.5.1 Profilometry

The fracture profile along with the deformed microstructure capture three main attributes: (i) voids formed during tensile testing, (ii) plastic deformation of different phases and relative strain % partitioned in each phase, and, (iii) fracture path through different microstructural constituents. Figure 3.10(a) shows a representative fracture profile in the unetched condition showing the fractured edge at increasing magnifications, necked region, and the undeformed grip sections of a DP 590 miniature specimen.

The fracture profile specimens were prepared by carefully sectioning the fractured half that is to be observed and mounting the sectioned sample in an acrylic mount to ensure good retention with the fractured edge. In the current study, Struers Duro Cit-3 acrylic mount was used. For all profilometry studies, the section containing the transverse and thickness planes was mounted. The width and thickness of the necked regions were measured carefully before sectioning and mounting the samples. The mounted sample was ground to remove enough material such that the fracture profile being observed would lie in the central one-third of the entire width of the necked region. Optical images of the polished and unetched fractured edges and the deformed regions of the specimen were taken to observe the voids formed during the

tensile test. The prepared samples were then etched using 2% Nital and 10% sodium metabisulphide solutions, similar to the bulk microstructure. Figure 3.10 (b) shows representative etched optical micrographs with the fractured edge for the same DP 590 miniature sample as 3.10 (a). Micrographs of the etched sample were captured systematically as a function of the distance from the fractured edge to observe the deformation occurring in the necked region versus the uniformly deformed region and qualitatively differentiate the deformation in the different DP steels.

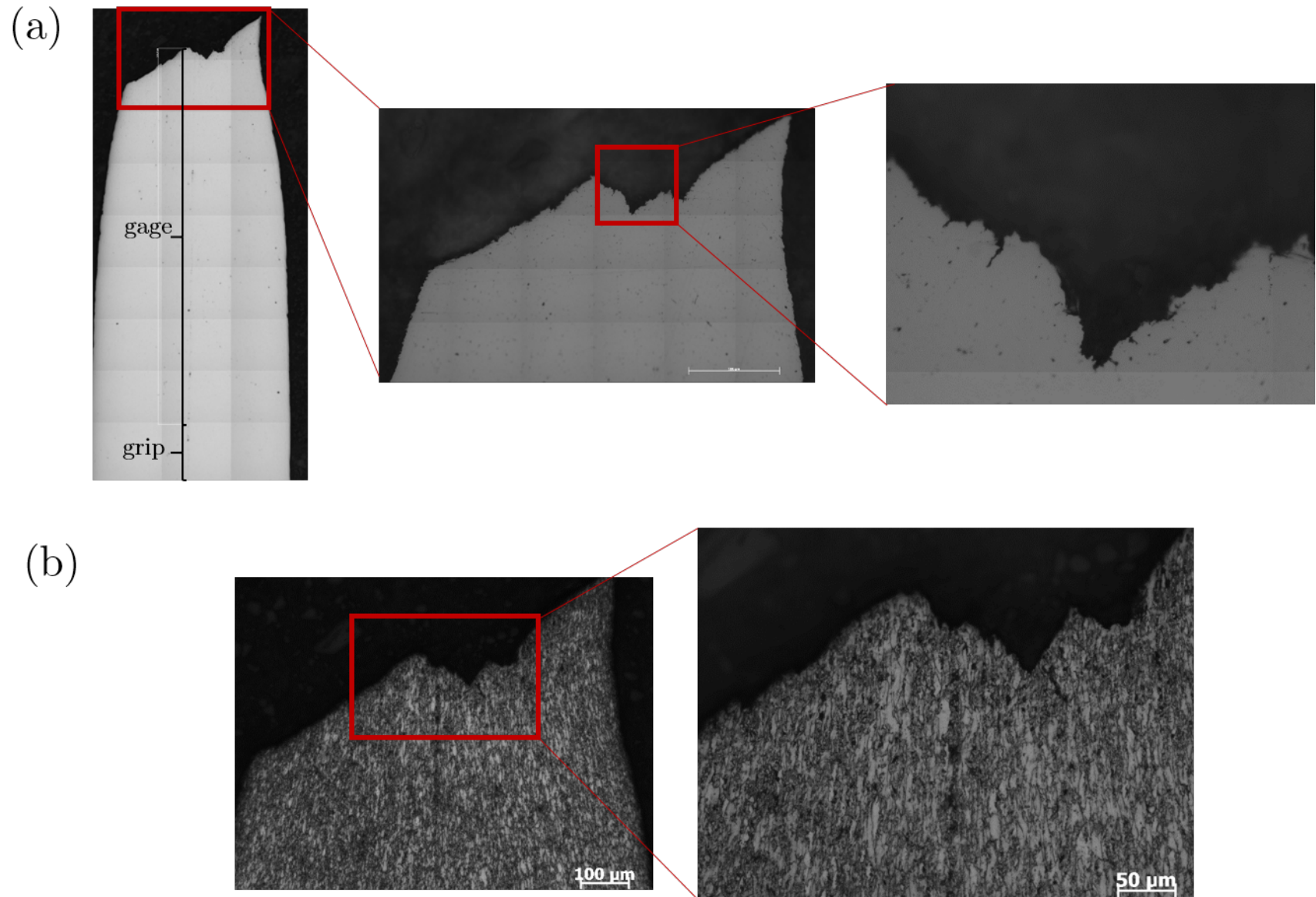


Figure 3.10: (a) Unetched fracture profile showing the gage and grip sections along with a high magnification image of the fracture profile, (b) Etched fracture profile showing the deformed microstructures and the delamination voids.

SEM images of the fractured edge and deformed regions were also captured to further attempt to quantify the strain and deformation partitioned in each phase of the Dual phase steels. This method was only used in the DP 590 steels, since the phase boundaries in all the deformed microstructure DP 980 steels could not be determined accurately.

To measure the deformation of the phases in DP 590 as a function of strain rate, the aspect ratio of the phases was estimated close to and away from (but still in the gage region) the fractured edge. A set of vertical and horizontal lines were superimposed on the images and the number of intersections of the lines made with each individual phase was recorded. Assuming the phase makes  $N$  intersections with the horizontal lines, and  $M$  intersections with the vertical lines, if the total lengths of the horizontal and vertical lines are  $H$  and  $V$ , respectively, then the  $P_L$  along the horizontal and vertical directions can be given as  $P_H = \frac{N}{H}$  and  $P_V = \frac{M}{V}$ , respectively. Thus, the aspect ratio is given by:  $P_H/P_V$ . If the aspect ratio is greater than one, a significant deformation along the loading direction has occurred. Figure 3.11 shows a representative deformed SEM image of DP 590 and a schematic illustrating the method employed to determine the aspect ratios.

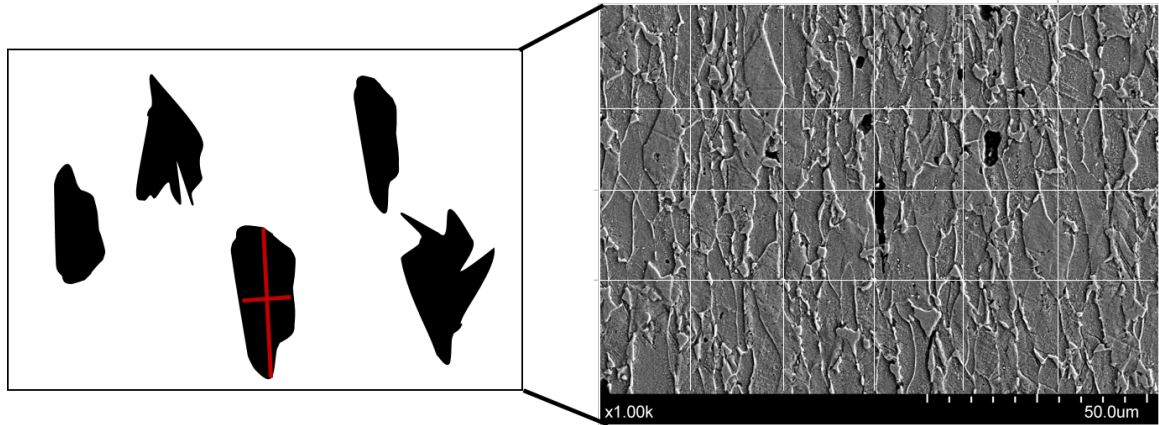


Figure 3.11: Schematic showing the technique used to estimate the aspect ratio of the deformed phases in the microstructure of DP 590. The ratio  $\langle P_L \rangle$  along the horizontal and vertical directions gives the aspect ratio.



### 3.5.2 Image based fractography

Image based SEM fractography can be used to understand the role of various microstructural features in the operative fracture mechanisms as a function of strain rate. Only the central one-third of the fractured surface area was captured for subsequent quantification to ensure that there is no influence of fast fracture that occurs near the edge of the samples. Atleast ten images were captured from each fractured sample. Figure 3.12 shows a schematic and a representative low magnification fracture surface image showing the method employed in capturing the images used for quantitative fractography.

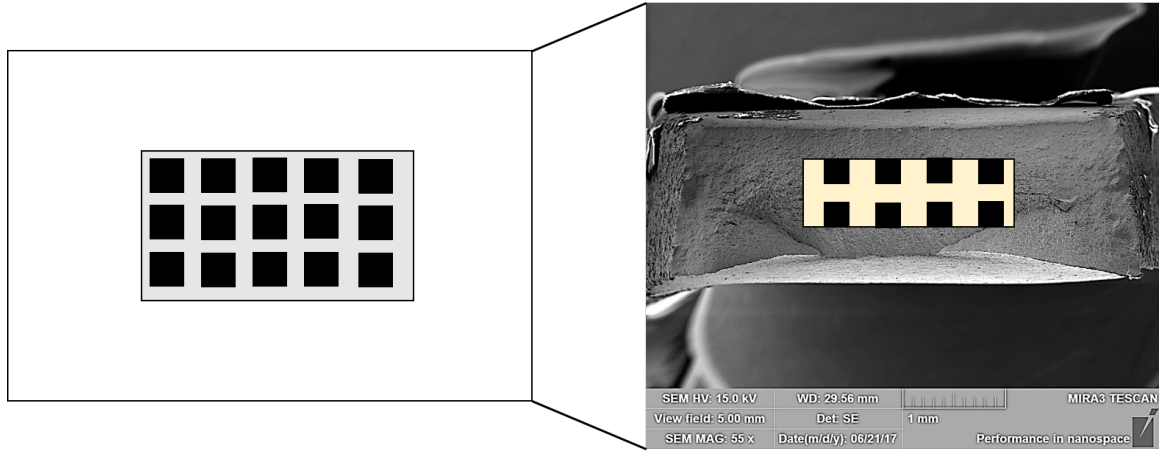


Figure 3.12: Schematic and representative low magnification fracture surface showing the central one-third area used to compute the area fraction and the systematic uniform sampling of the area to capture unbiased fields of view for the quantitative estimations.

The fracture surfaces of DP steels across the strain rates in the quasi-static and intermediate strain rates ( $10^{-6}$  to  $10^3/s$ ) consisted of largely three distinct features: (i) dimples, (ii) flat featureless regions or facets and (iii) secondary cracks surrounded by facets. Figure 3.13 shows a representative image identifying the different features.

At high strain rates obtained from the plate-on-plate impact tests resulting in spall, the features observed in the fracture surface were slightly different from those discussed above. Although, the ductile regions consisted of dimples, the brittle regions

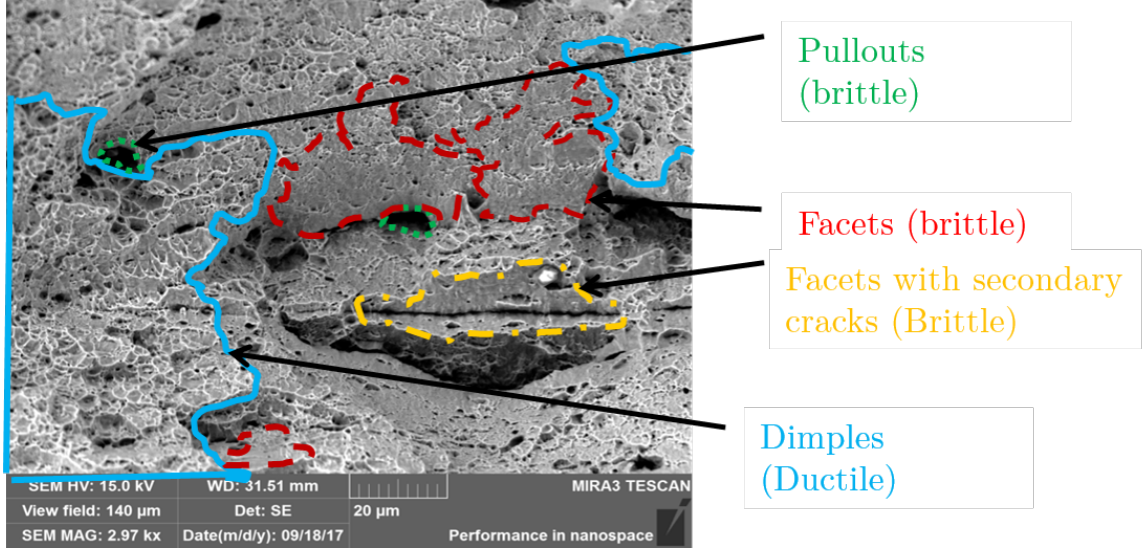


Figure 3.13: Representative fracture surface showing the different features observed across all the DP steels. Dimpled regions are classified as ductile while the facets, secondary cracks and pullouts are classified as brittle.

were comprised of quasi-cleavage fracture and long flat featureless bands in all the DP spall fracture surfaces. Figure 3.14 shows the representative spall fracture surface identifying the different features.

Although the features observed in all the DP steels and at the different strain rates were similar, the amount and distribution of each feature was a function of microstructure and strain rate. This was estimated by determining the area fraction of each feature by using systematic point counting technique, similar to the estimation of volume fraction of phases in the bulk microstructure. Figure 3.15 (a) shows a representative fracture surface superimposed with a grid showing the estimation of the area fraction of the different features. The dimple size was estimated by placing an unbiased counting frame in a completely dimpled region. The number density of dimples ( $N_A$ ) was estimated by manual counting and the dimple diameter ( $d$ ) was given by  $d = \sqrt{\frac{4}{\pi N_A}}$ . Figure 3.15 (b) shows the unbiased frame superimposed on the fracture surface image to estimate the dimple size. Since the length scale of the secondary cracks was substantially large, its length could not be estimated by using

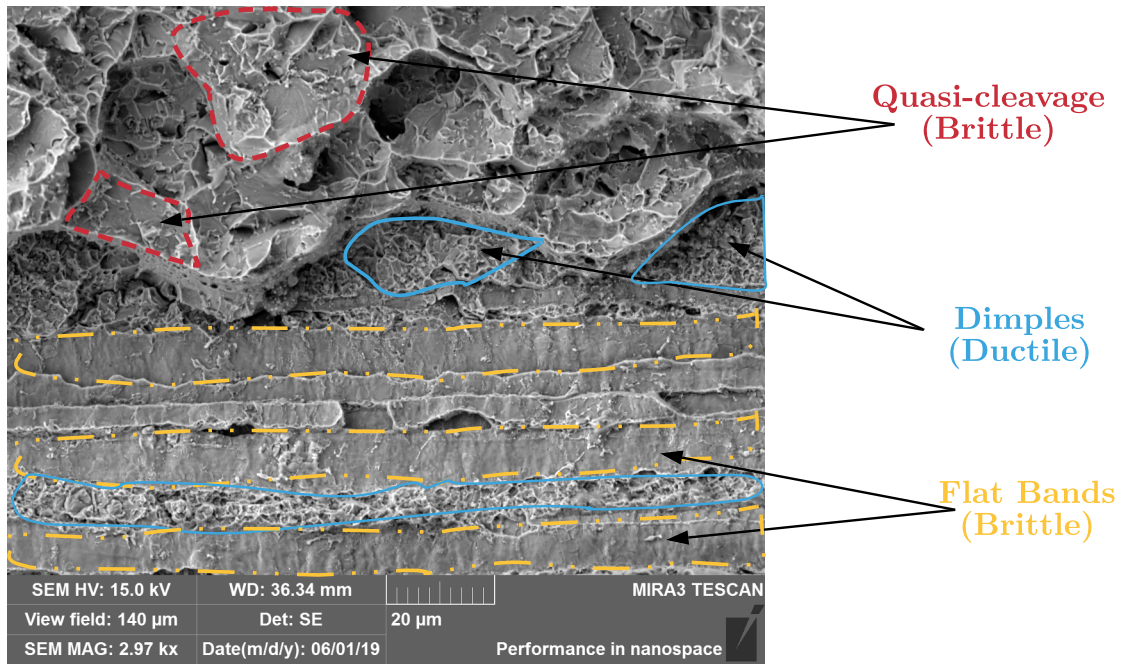


Figure 3.14: Representative fracture surface showing the different features observed across all the DP steels. Dimpled regions are classified as ductile while the facets, secondary cracks and pullouts are classified as brittle.

the field of view that was used to estimate the area fractions and the dimple sizes. Low magnification, high resolution images of the central third of the fracture surface were captured. The number density of the secondary cracks was then estimated by superimposing an unbiased frame on the center of the image. The length of each individual secondary crack that lay completely inside the unbiased frame or crossed the green lines was measured. The cracks touching the red lines were disregarded for both number density and length measurements. Figure 3.15 (c) shows a representative low magnification image superimposed with an unbiased frame and the secondary cracks that were identified and counted. All stereological estimations were performed with the aid of Image J, an interactive image software.

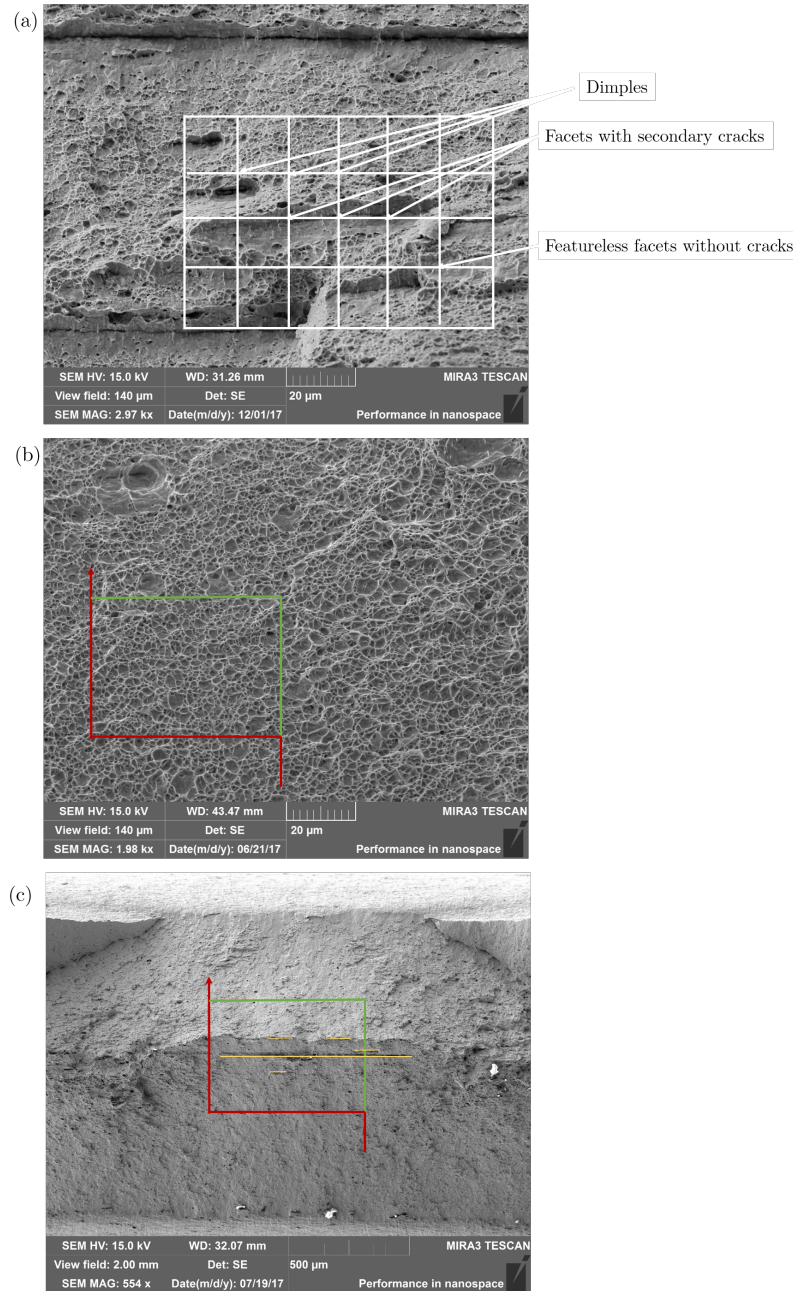


Figure 3.15: (a) Representative fracture surface with superimposed grid used for the estimation of area fraction of different features observed. Examples of the points in the grid used to estimate each feature are also shown, (b) Representative fracture surface with an unbiased counting frame on a completely dimpled region to estimate the dimple size, (c) Low-magnification, high resolution image with an unbiased counting frame on the central one third of the fracture to estimate the number density and length of the secondary cracks.

## CHAPTER 4

### RESULTS

This chapter will present the results of the quantitative characterization of microstructures of as-received materials, the quasi-static to intermediate strain rate tensile tests and the high strain rate uniaxial strain plate impact tests, along with the qualitative and quantitative fractography of all the Dual Phase steels tested. The discussion of the results as a function of different attributes of the microstructure, geometry of the specimen and strain rate of the test, will be presented in the next chapter.

#### 4.1 Quantitative Characterization of Microstructures

##### 4.1.1 Qualitative observations from microstructures of as-received steels

Figure 4.1 shows representative micrographs of (a) DP 590 and (b) DP 980 NC, and figure 4.2 shows the representative micrographs of (a) DP 980 GAN and (b) DP 980 GAD steels in the short-transverse (containing the rolling and transverse directions), the longitudinal section (containing the rolling and normal directions) and the transverse planes (containing the transverse and normal directions). The lower volume fraction of martensite is evident from the micrographs in DP 590, when compared to the DP 980 grades. Large ferrite grains form the matrix of DP 590 while the matrix of DP 980 NC and GAN is formed by a largely continuous and connected martensitic phase. DP 980 GAD has a dispersed martensite phase and co-continuous microstructure. The anisotropy and connectivity of martensite is more evident in the longitudinal and transverse sections of the steels. While DP 980 GAN qualitatively shows a higher degree of martensite banding compared to DP 980 NC; the DP 980 GAD steel shows a co-continuous microstructure with a highly dispersed martensite

with some connectivity and banding towards the center of the steel. The longer bands of the martensite phase are highlighted by the white ovals in the micrographs. As mentioned in the literature review chapter, DP 980 GAD has a microstructure gradient which will be discussed in detail later in this section. Another qualitative observation from Figure 4.1 is how the microstructure becomes finer from DP 980 NC to GAN to GAD. Details on the quantitative estimations are provided next.



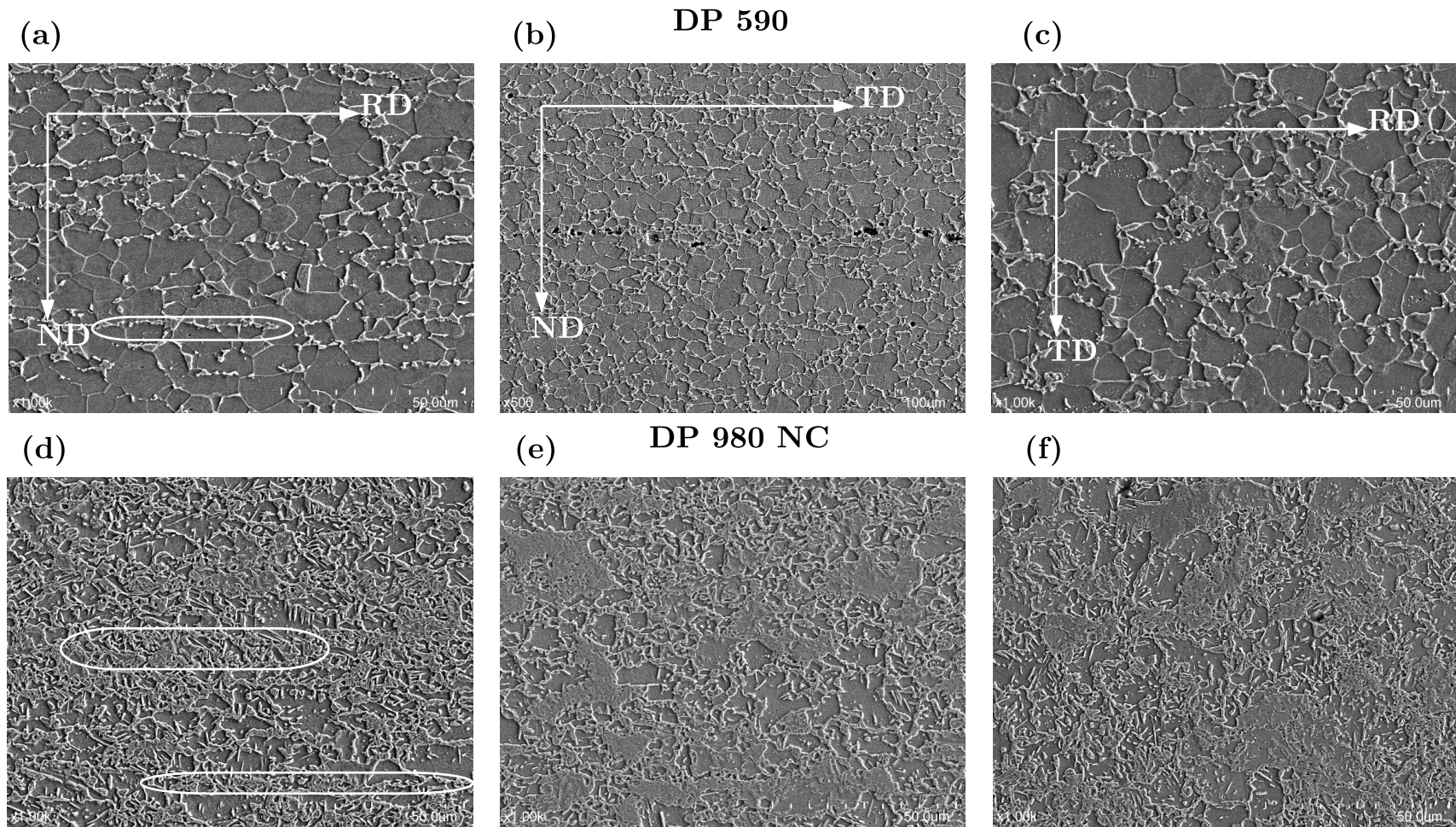


Figure 4.1: The orthogonal views containing the short-transverse, transverse and longitudinal sections of (a) DP 590 and, (b) DP 980 NC. The white circles show the connectivity of the harder martensite phase.

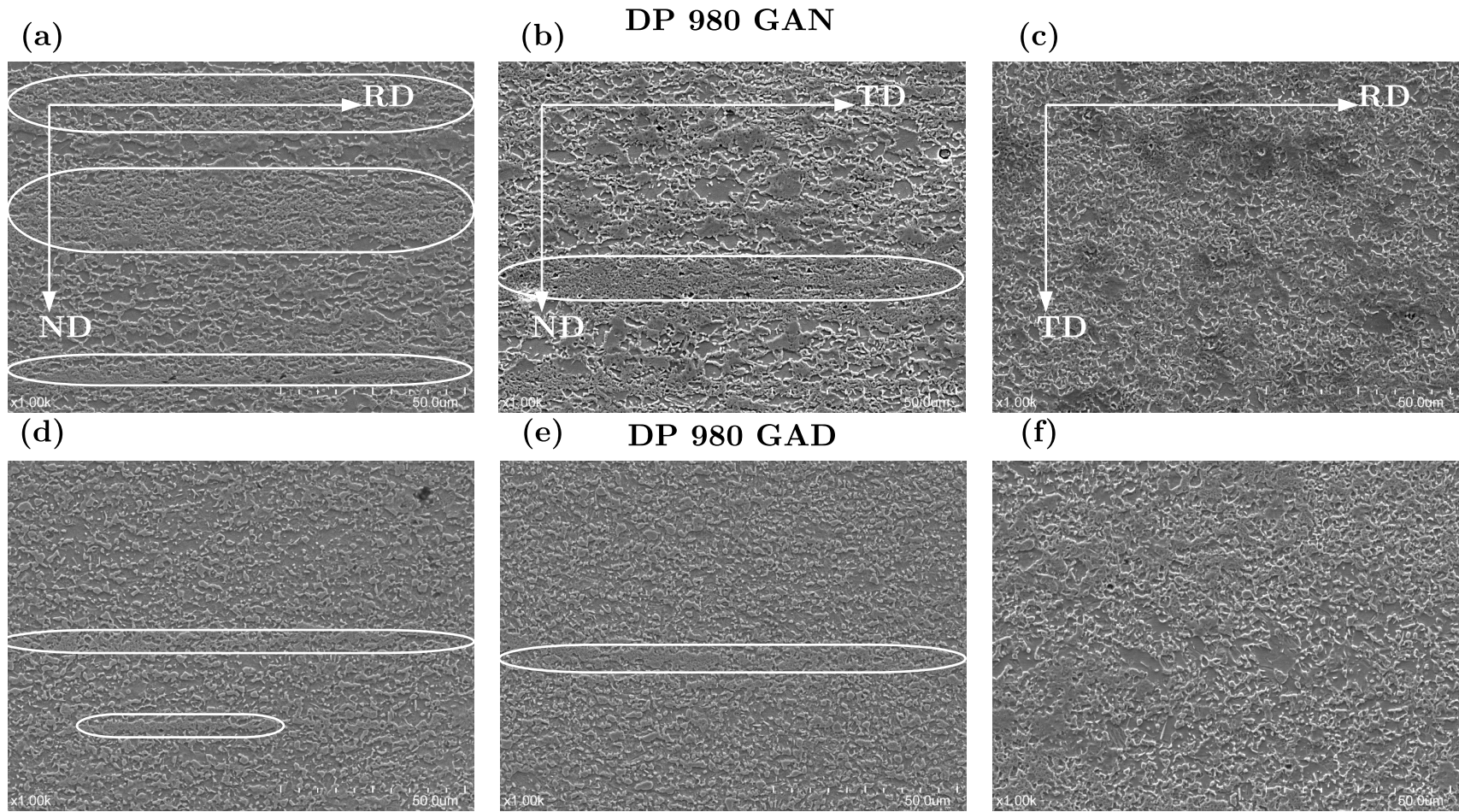


Figure 4.2: The orthogonal views containing the short-transverse, transverse and longitudinal sections of (a) DP 980 GAN and, (b) DP 980 GAD steels. The white circles show the connectivity of the harder martensite phase.



#### 4.1.2 Quantitative estimations of the microstructure

Table 4.1 shows the stereological estimations made on the DP steels. Since DP 980 GAD has a microstructure gradient, only the estimations performed in the central one third section comprising the bulk microstructure are presented in the table. The volume fraction of martensite (averaged over all three orthogonal planes) is  $\sim 30\%$  for DP 590 and  $\sim 70\%$  for the DP 980 steels grades. Hence, strictly in volume fraction terms, ferrite and martensite fractions are reversed in the DP 590 and DP 980 grades. The number per unit area of the dispersed phase islands (martensite in DP 590 and ferrite in DP 980 NC and GAN) are similar in DP 590 and DP 980 thereby implying a reversal in the matrix phase. The number density of the ferrite islands is higher in DP 980 GAN compared to the NC counterpart indicating a finer microstructure. Since GAD has a co-continuous microstructure, the number density of islands could not be estimated. Since all the steels possess anisotropy, the surface area per unit volume of the ferrite and martensite interfaces is estimated on the planes containing the thickness direction (i.e the longitudinal and transverse sections). These estimations clearly illustrate that the microstructure gets finer from DP 980 NC to GAN, and is the finest in GAD steels. The mean free path describes the free path in the dominant phase of the respective DP steels. The mean free path also indicates that the microstructures of GAN and GAD steels are finer. Apart from the refinement, the connectivity of martensite and gradient of microstructures have also been estimated and are discussed next.

#### 4.1.3 Connectivity of martensite

From Figure 4.1 (b) and (c), a qualitative observation that the connectivity of martensite and subsequent banding is higher in DP 980 GAN compared to NC can be made. Figure 4.3 shows low magnification optical montages depicting the phenomenon in greater clarity. In order to quantitatively estimate the banding differences in the two

Table 4.1: Quantitative Characterization of DP steels

	DP 590	DP 980 NC	DP 980 GAN	DP 980 GAD
Volume Fraction of martensite	$29 \pm 5$	$68 \pm 1.8$	$73.7 \pm 1.7$	$65.7 \pm 4.2$
Number per unit area of Islands ( $/mm^2$ ), (Martensite in DP590 and Ferrite in DP 980)	$9600 \pm 437$	$8070 \pm 1120$	$12406 \pm 2018$	Co-continuous microstructure
Surface area per unit volume( $/mm$ )	$292 \pm 23$	$710 \pm 55$	$1008 \pm 91$	$966 \pm 31$
Mean Free Path ( $4V_V/S_V$ )	3.9	3.8	2.8	2.7

steels, the surface area per unit volume of the banded regions using cycloids and vertical lines were obtained. They were estimated by performing measurements on the longitudinal section which is expected to have the maximum anisotropy. While the surface area, estimated using cycloids, is similar to the interfacial area between the phases, the surface area estimated using the vertical lines provides information on the surface area of the banded regions when projected along the longitudinal section. DP 980 GAN shows a higher surface area when estimated using both cycloids and vertical lines indicating a greater degree of banding in these steels and a higher interfacial area between the phases. The results are shown in Table 4.2.

Table 4.2: Quantitative Characterization of Banding of martensite

	$S_V$ (cycloids)( $/mm$ ) (interfaces of the bands)	$S_V$ (Vertical lines)( $/mm$ ) (interface projected on the rolling direction)	$S_V$ (cycloids)( $/mm$ ) (interfaces averaged over longitudinal and transverse sections)
DP 980 NC	$730 \pm 84$	$435 \pm 34$	$710 \pm 55$
DP 980 GAN	$981 \pm 80$	$650 \pm 89$	$1008 \pm 91$

#### 4.1.4 DP 980 GAD- Quantifying the gradient in the microstructure

As discussed earlier in the Background (chapter 2), the DP 980 GAD steels are manufactured with a decarburized layer to enhance the bendability of the galvanized DP steels. The introduction of the decarburized layer introduces a gradient in the microstructure where the surface is devoid of carbon and martensite and the bulk

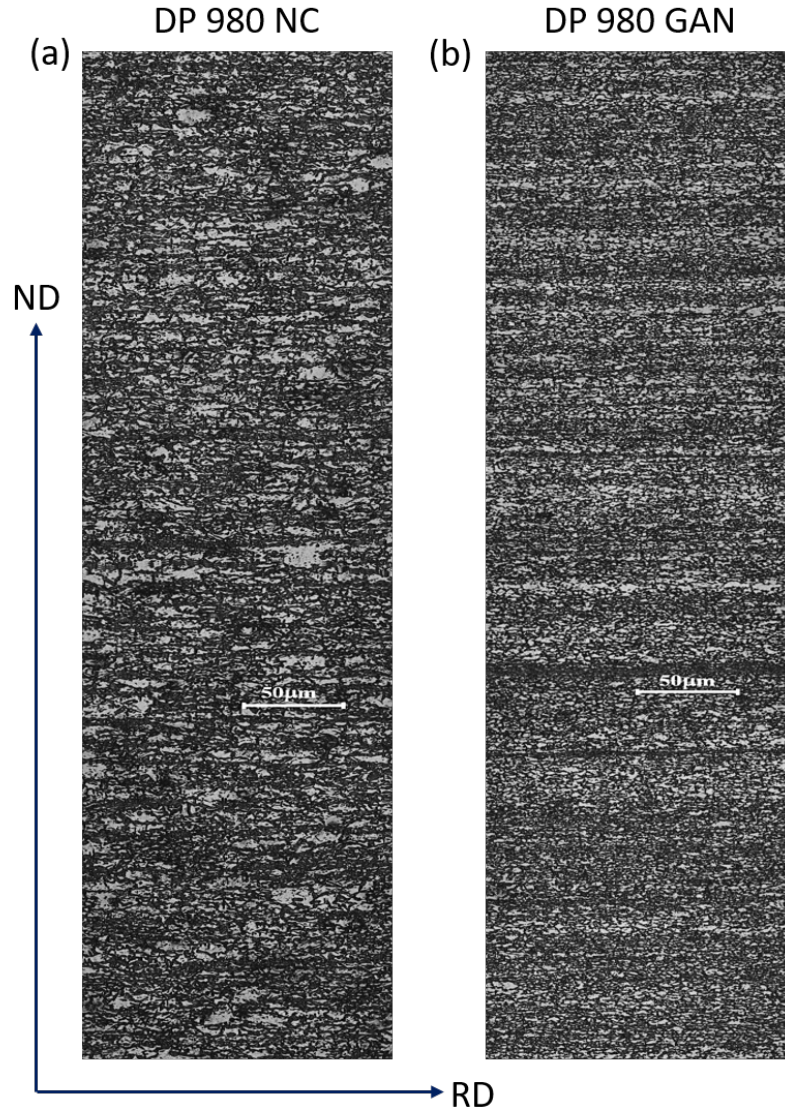


Figure 4.3: Montages showing the extent of martensite banding along the longitudinal sections in (a) DP 980 NC and (b) DP 980 GAN

comprises of a Dual Phase structure similar to its galvanized counterpart. Figure 4.4 shows representative micrographs from the surface and the bulk of the steel. The gradient captured using micro-hardness indents is shown in Figure 4.4. The increase in hardness going away from the edge greatly helps in identifying the decarburized layer on the surface. Various techniques can be used to define the thickness of the decarburized layer. One method can be to attribute the thickness to be the distance from the surface at which the steel attains the average hardness between the

bulk and the decarburized layer. It can also be defined to be the thickness at which an estimated microstructural parameter becomes constant. The volume fraction of martensite and surface area per unit volume of interfaces between ferrite and martensite were computed as a function of distance from the edge, as shown in figure 4.6. Figure 4.6 (a) shows the variation of volume fraction moving closer to the center of the steel. The error bars are significantly large in this estimation. This is primarily due to the small size of the dispersed martensite and the point counting technique used in the estimation of volume fraction. Due to the small size, the probability of the points landing on the dispersed phase was reduced that led to the larger error bars. Images with a higher magnification also did not greatly improve the result. The surface area per unit volume measurement however, was observed to be much more reliable and followed a trend similar to that of the hardness. Thus, from these results, it can be concluded that the surface area per unit volume is a better tool to characterize the decarburized thickness in a gradient microstructure compared to the volume fraction. The thickness was estimated to be  $\sim 60\mu m$  on either side of the steel.

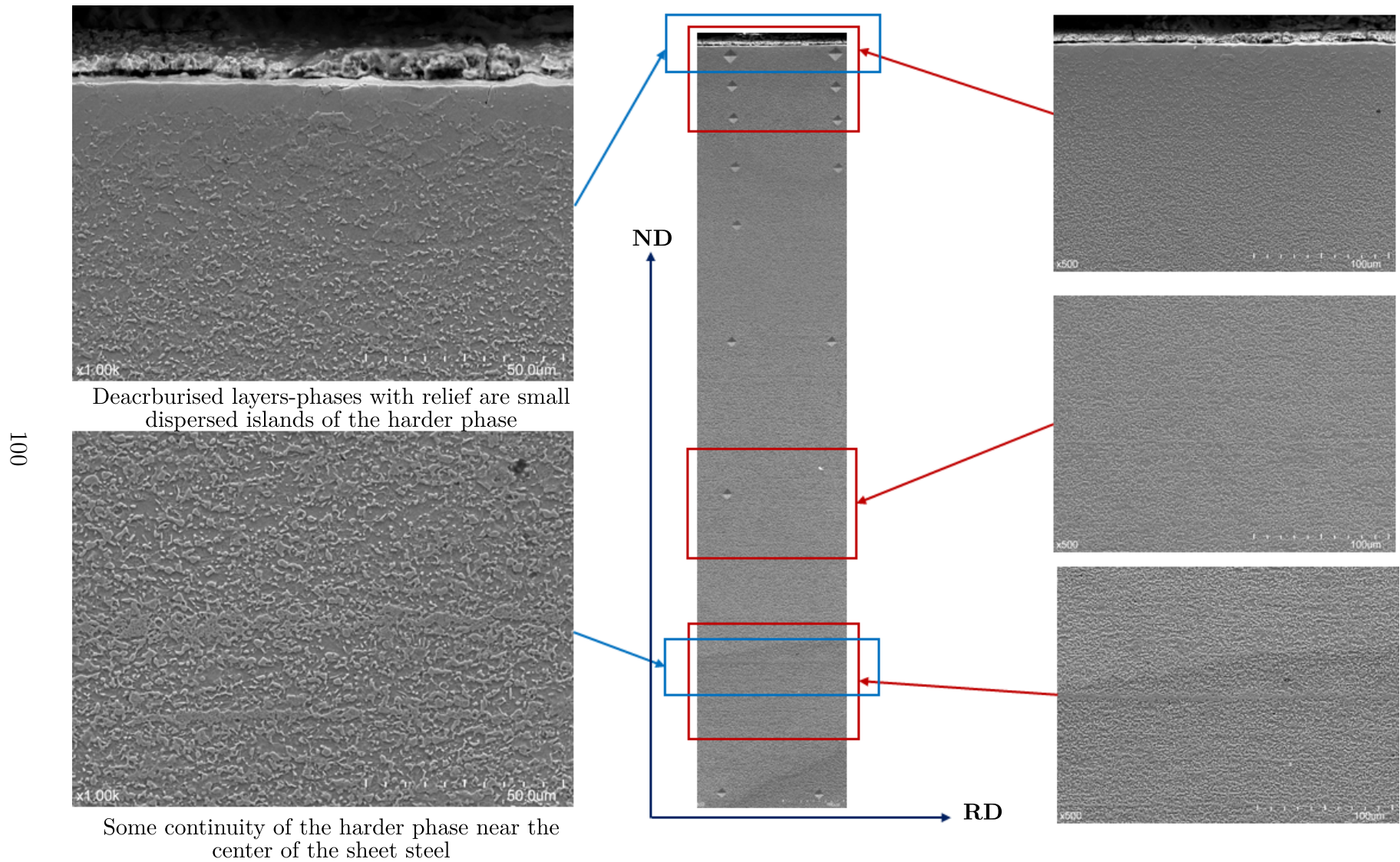


Figure 4.4: SEM images showing the montage and the different sections along the thickness of the DP 980 GAD steel. The cross sections from the surface show the decarburized layer deprived of martensite. Cross sections from the center show a Dual Phase microstructure with some connectivity in martensite.



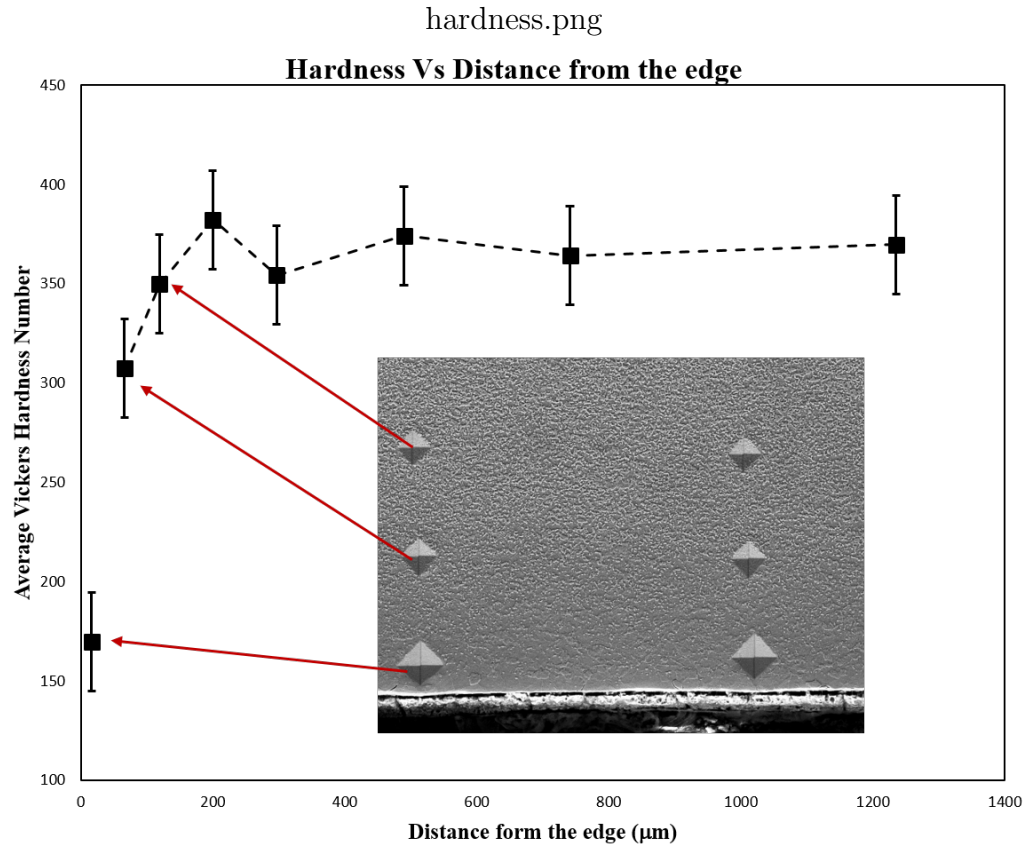


Figure 4.5: Variation of hardness in the longitudinal section of DP 980 GAD as function of distance from the edge.

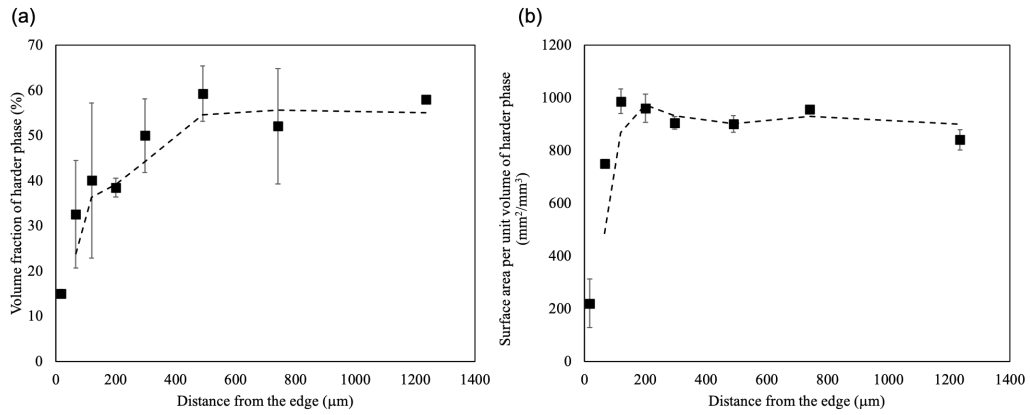


Figure 4.6: Variation of (a) Volume fraction of martensite and (b) Surface area per unit volume of the harder and ferrite phase interface as a function of distance from the edge.

#### 4.1.5 Galvannealed Coating layer

Figure 4.7 shows a representative micrograph of the galvannealed coating present in the DP 980 GAN and DP 980 GAD steels. Although figure 4.7 (b) shows some contrast within the galvannealed layers, the individual sub-layers within the coating could not be clearly identified. The thickness of the coating has been estimated to be  $10.5 \mu\text{m}$ . Figure 4.8 Pt-s 1 through 3 show the EDS spectra of the coating at three different locations along the thickness of the coating. Pt-4 lies on the substrate. No substantial differences in coating chemistry were found at the three locations probed on the coating.

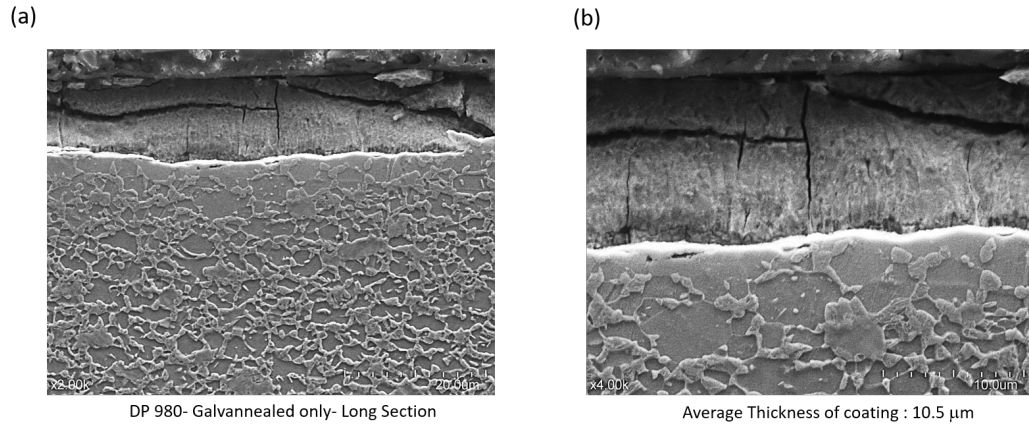


Figure 4.7: Longitudinal cross sections showing the (a) Galvannealed coating (b) magnified view of the coating on the galvannealed and decarburised steels

## 4.2 Mechanical Properties: Effect of strain rate and microstructure

Uniaxial Tensile tests were conducted on the DP steels spanning a strain rate range of  $10^{-6}/s$  to  $10^3/s$ . The mechanical properties measured are presented in the section ahead.

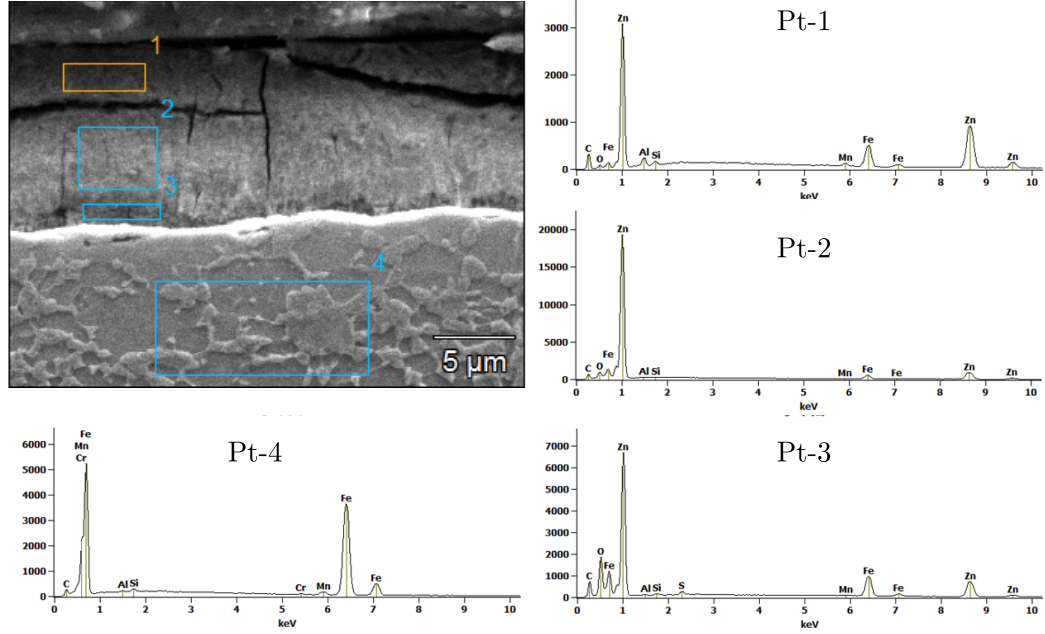


Figure 4.8: Energy Dispersive Spectroscopy (EDS) peaks from three different parts of the coating and compared to the substrate.

#### 4.2.1 DP 590 : Mechanical Properties

Figure 4.9 shows the stress-strain response of DP 590 steel using the miniature tensile sample geometry. Continuous yielding with substantial initial strain hardening can be observed at strain rates of  $10^{-4}/s$  through  $10/s$ . At the strain rate of  $3 \times 10^3/s$ , a peak at very low strains is observed. This is attributed to mechanical instabilities arising during the Hopkinson Bar test. These instabilities could not be controlled and arise due to the nature of the intermediate strain rate test using the Hopkinson bar. Since this peak leads to ambiguities when computing the Ultimate Tensile Strength (UTS), the UTS was computed from the High Speed camera images by determining the stress corresponding to the strain at which necking initiates. In the quasi-static regime the strength of DP 590 is seen to increase marginally while the fracture strain does not show any clear trend. However, at the intermediate strain rates, both the strength and fracture strain are seen to increase substantially.



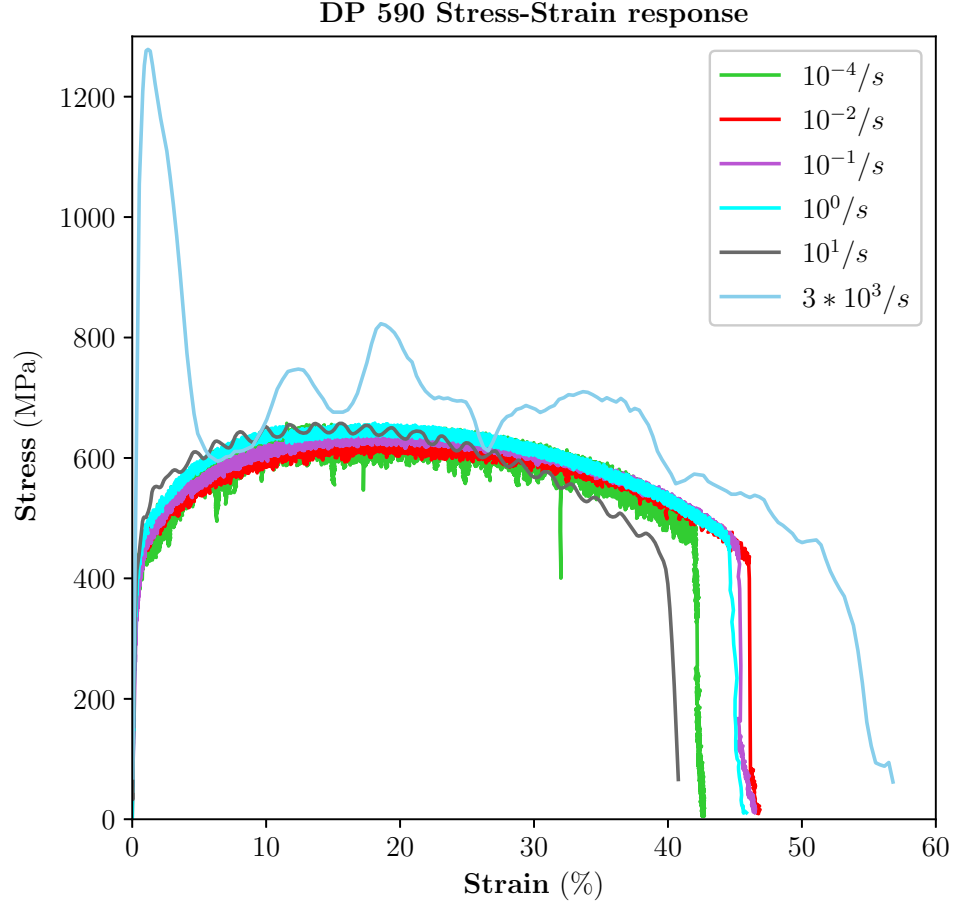


Figure 4.9: Stress strain response of DP 590 steels at quasi-static and intermediate strain rates.

#### 4.2.2 DP 980 NC : Mechanical Properties

The stress-strain response as a function of strain rate spanning nine orders of magnitude for DP 980 NC is shown in figure 4.10. Similar to DP 590, DP 980 NC also shows continuous yielding and initial strain hardening at quasi-static strain rates. At strain rates higher than  $10/s$ , disturbances arising due to load-cell oscillations result in a noisy stress-strain response. At strain rates of  $500/s$  and  $2500/s$ , a peak at low strains similar to DP 590 is observed that is attributed to the mechanical instabilities arising due to the nature of the Hopkinson bar tests. Further, the strain at these

strain rates was measured using digital image correlation which failed at high strains. The actual fracture strain was hence computed using images which showed complete fracture of the specimen and just before the two halves separated. The dotted lines depict the extrapolation of the strain to the actual measured fracture strain. Although the actual values of the fracture strain are accurate, the *shape* of the curve is approximated.

The strength of DP 980 NC appears to show two different regimes as a function of strain rate. In the quasi-static strain rate regime, the strength does not vary appreciably, however, at strain rates greater than 1/s, a substantial increase in strength is observed. As for the ductility, no significant trend is observed, although it is substantially higher at the intermediate strain rates compared to the quasi-static strain rates.

#### 4.2.3 DP 980 GAN and DP 980 GAD: Mechanical Properties

Figures 4.11 and 4.12 show the stress-strain response of DP 980 GAN and DP 980 GAD respectively, as a function of strain rate spanning seven orders of magnitude. Both GAN and GAD also show continuous yielding and initial strain hardening. The response in strength as a function of strain rate is not very different when compared to DP 980 NC. A prominent difference between the DP 980 NC and GAN and GAD is that at the intermediate strain rates, the strain in DP 980 NC is observed to increase significantly whereas in both GAN and GAD, the effect is not observed. The results illustrate the effects of microstructure on the fracture strain at higher strain rates. This could also indicate that the fracture mechanism of these steels may be significantly affected by the different microstructures, although their strengths remain largely unaffected. Fracture surfaces observed at all the aforementioned strain rates along with a quantification of the features observed are presented in the next section.

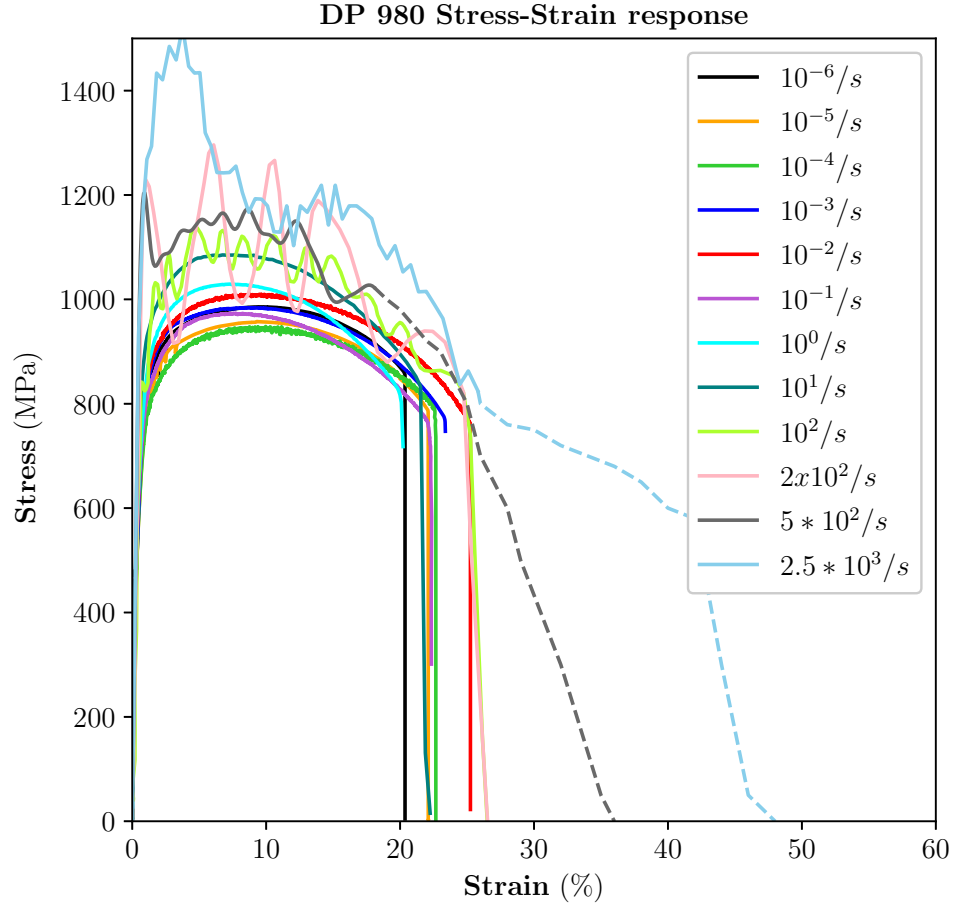


Figure 4.10: Stress strain response of DP 980 NC steels at quasi-static and intermediate strain rates.

### 4.3 Fractography of Dual Phase Steels

#### 4.3.1 Qualitative Fractography

The following subsection discusses the fractography of the DP steels and the quantification of the features observed in the fracture surface.

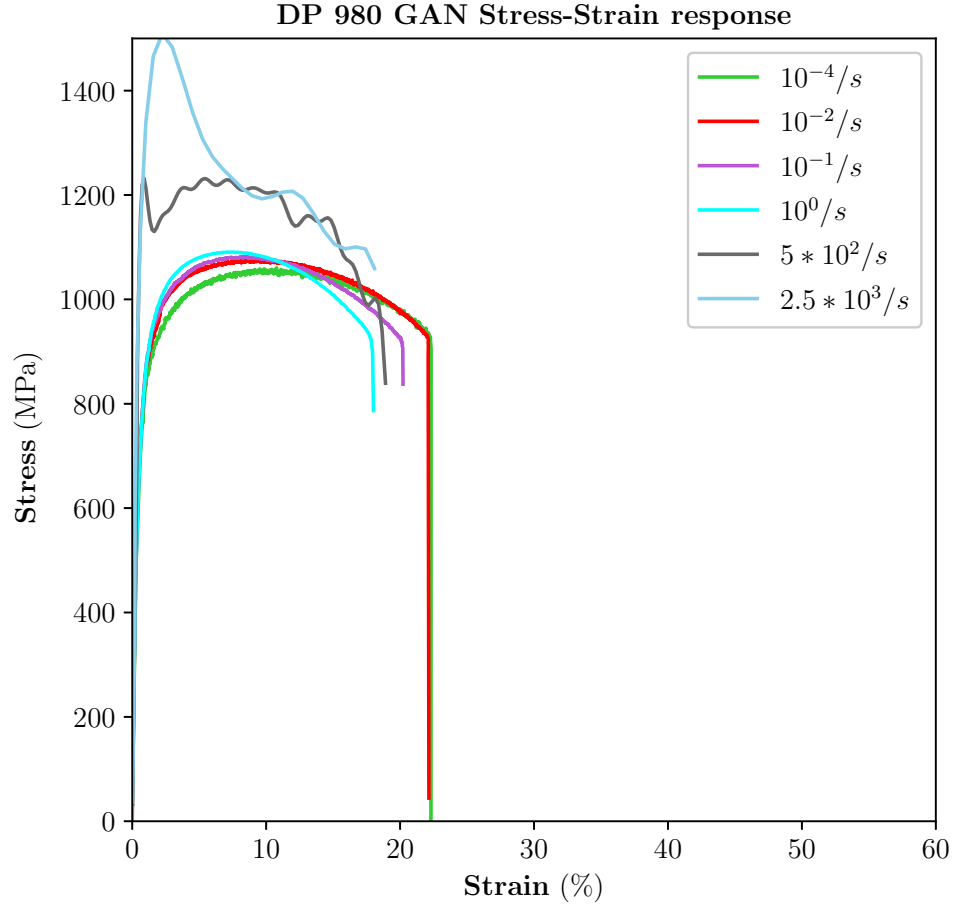


Figure 4.11: Stress strain response of DP 980 GAN steels at quasi-static and intermediate strain rates.

#### *Fractography of DP 590*

Figure 4.13 depicts the fracture surfaces of DP 590 at low and high magnifications at different strain rates. DP 590 shows a largely dimpled fracture surface at all strain rates. Some secondary cracks are also seen at all strain rates. While a dimpled fracture surface is attributed to plasticity, the secondary cracks surrounded by featureless regions are classified as brittle.

Qualitatively, the fracture surfaces do not appear to change significantly with an increase in strain rate.

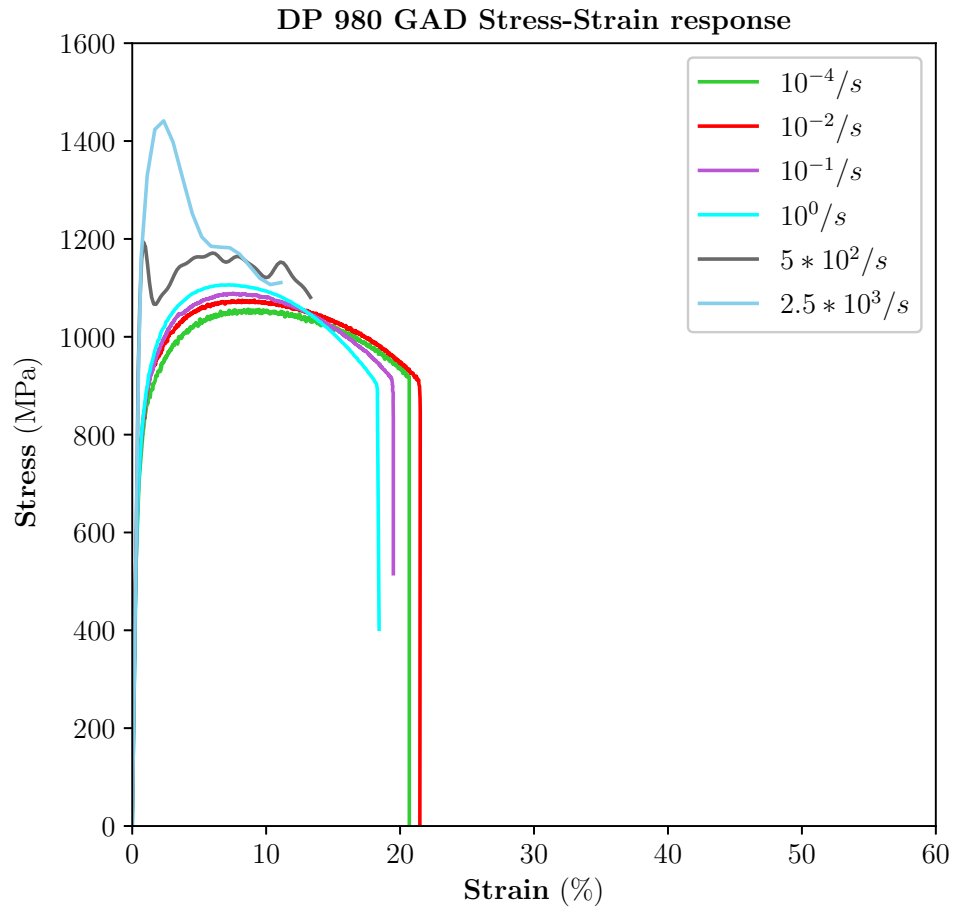


Figure 4.12: Stress strain response of DP 980 GAD steels at quasi-static and intermediate strain rates.

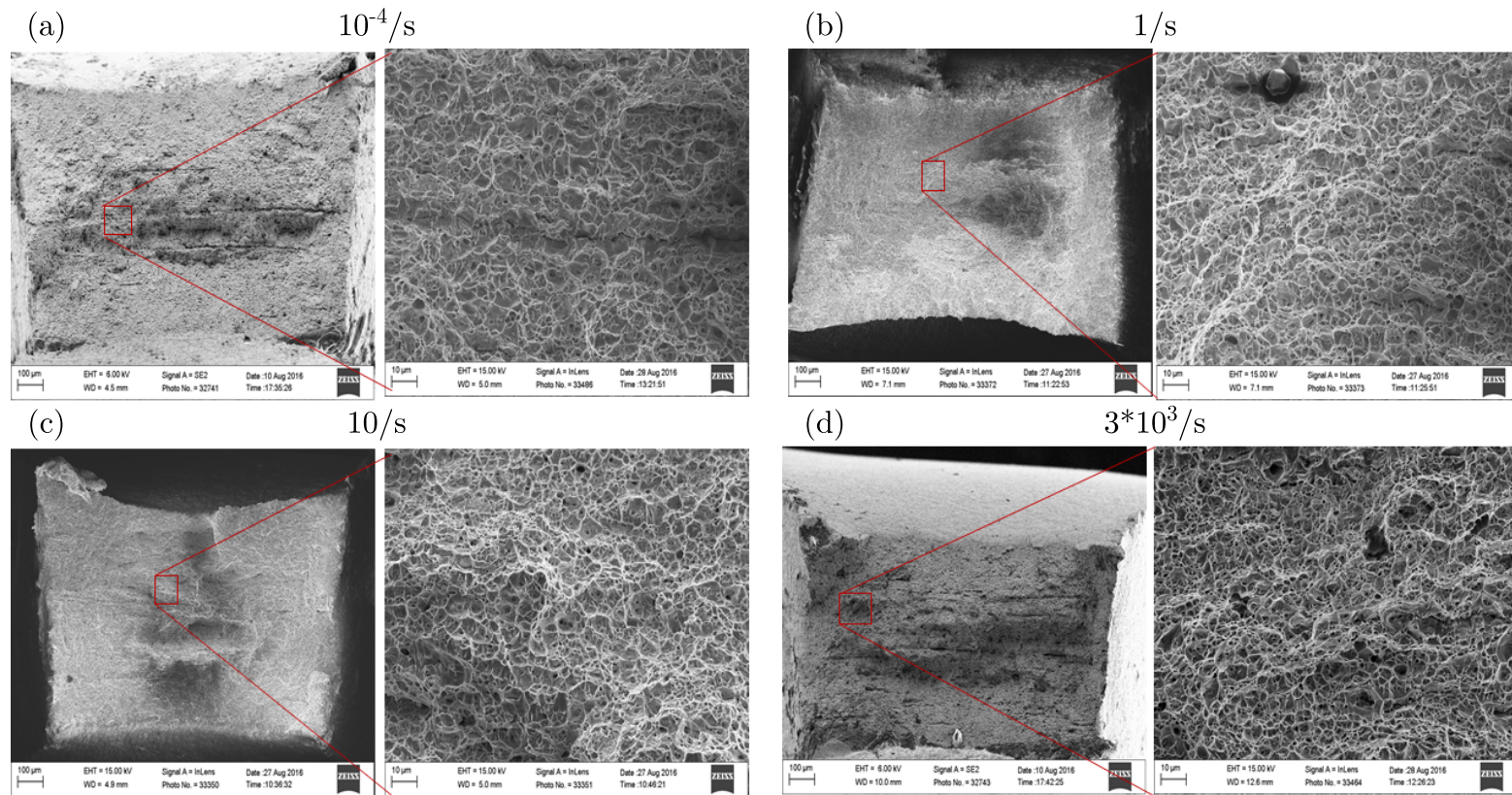


Figure 4.13: SEM images of the fracture surface of DP 590 at low and high magnification at strain rates of (a)  $10^{-4}/s$ , (b)  $1/s$ , (c)  $10/s$  and (d)  $3 \times 10^3/s$

### *Fractography of DP 980*

Figure 4.14 shows the fracture surfaces of DP 980 NC (at low and high magnifications) at different strain rates. DP 980 NC also depicts largely dimpled fracture surfaces. Large areas of featureless flat regions are also seen at all strain rates along with secondary cracks surrounded by featureless regions. Qualitatively, as the strain rate is increased, the areas of flat featureless regions reduce and the fracture surfaces take on a more dimpled appearance. Thus, the observations indicate that the fracture surface of DP 980 NC is strain rate sensitive.

Figure 4.15 shows the fracture surfaces (at low and high magnifications) of DP 980 GAN at different strain rates. Although the fracture surface is also largely dimpled, a large part of the fracture surface is occupied by the facets with secondary cracks. Qualitatively, the amount of facets with secondary cracks appear to be larger than DP 980 NC.

Similarly, Figure 4.16 shows the fracture surfaces at low and high magnifications of DP 980 GAD at different strain rates. In contrast to DP 980 NC and GAN, the fracture surfaces of GAD show larger amount of dimpled regions.

An important point to note is that the features observed in the fracture surface are similar in all the DP steels, although, the extent of the distribution of these features is a function of both the underlying microstructure and the strain rate.



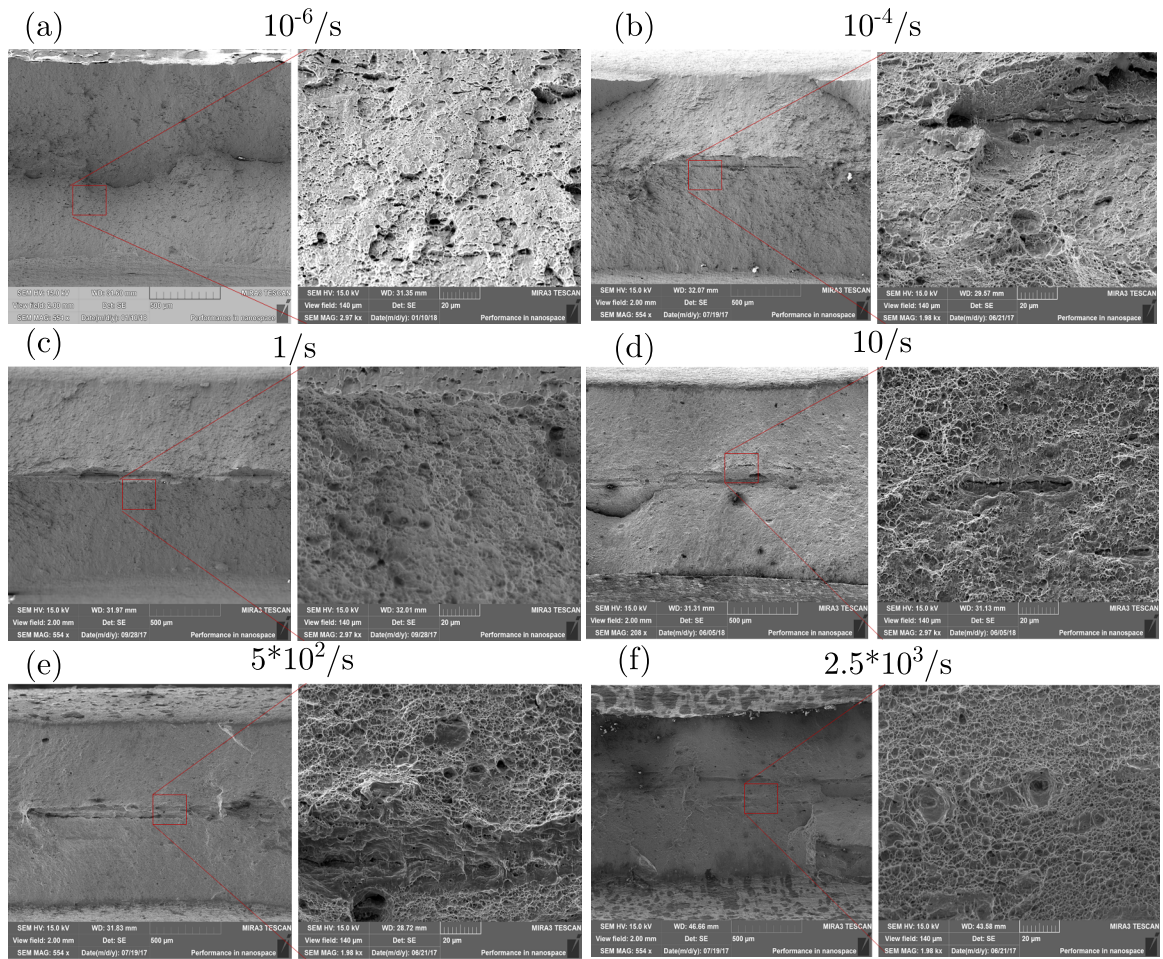


Figure 4.14: SEM images of the fracture surface of DP 980 NC at low and high magnification at strain rates of (a)  $10^{-6}/s$ , (b)  $10^{-4}/s$ , (c)  $1/s$ , (d)  $10/s$ , (e)  $5 \times 10^2/s$  and (f)  $2.5 \times 10^3/s$



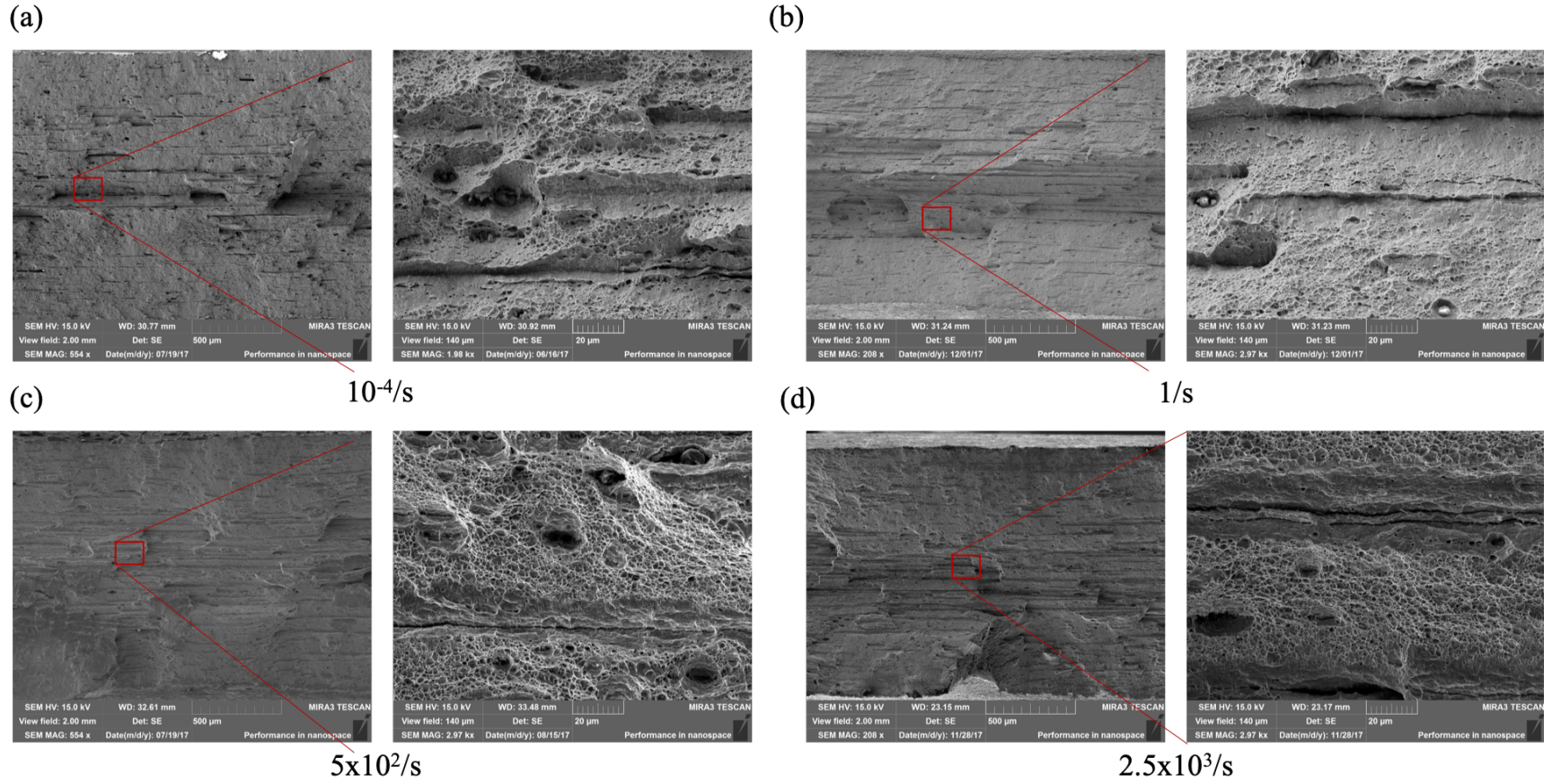


Figure 4.15: SEM images of the fracture surface of DP 980 GAN at low and high magnification at strain rates of (a)  $10^{-4}/s$ , (b)  $1/s$ , (c)  $5 \times 10^2/s$  and (d)  $2.5 \times 10^3/s$

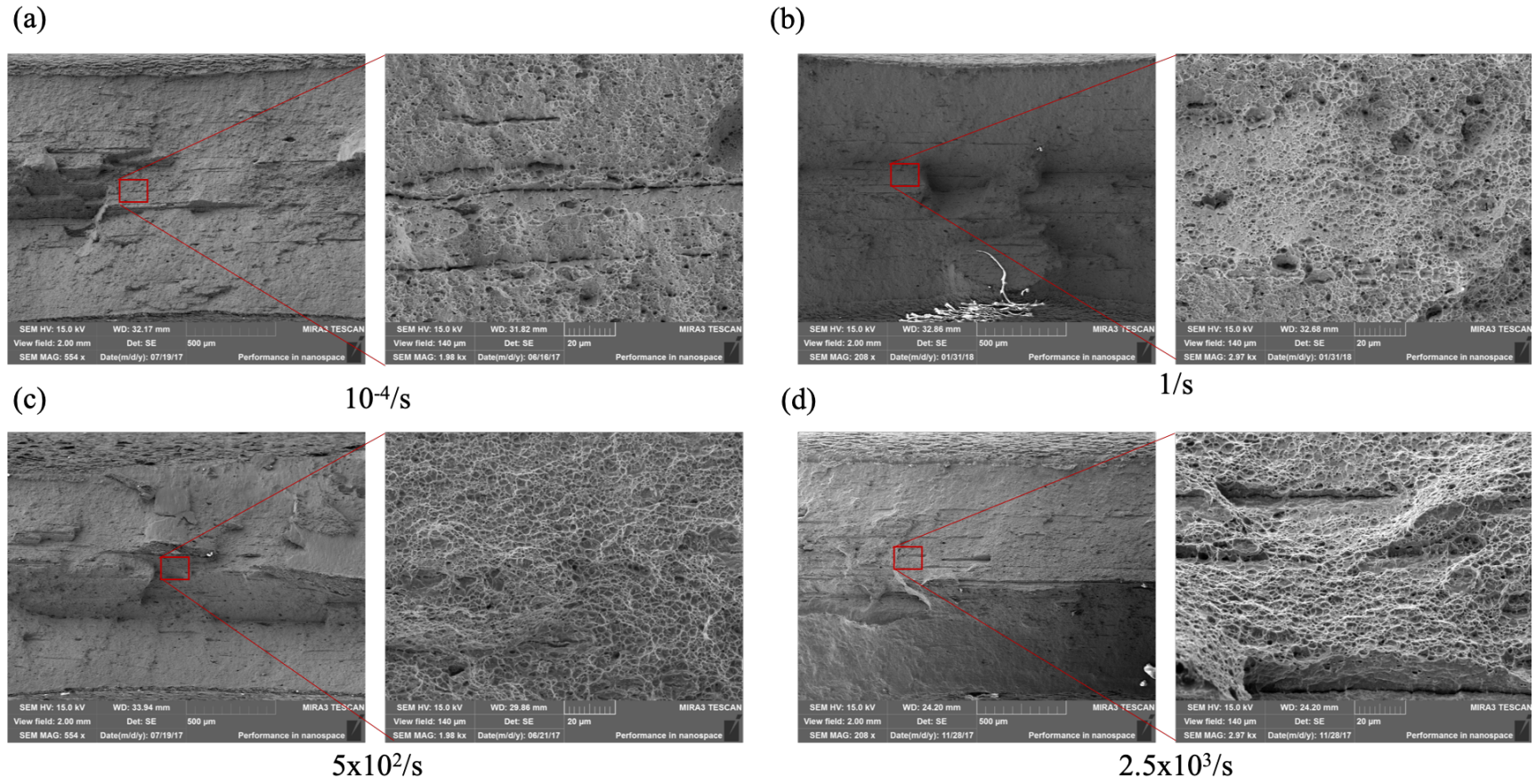


Figure 4.16: SEM images of the fracture surface of DP 980 GAD at low and high magnification at strain rates of (a)  $10^{-4}/s$ , (b)  $1/s$ , (c)  $5 \times 10^2/s$  and (d)  $2.5 \times 10^3/s$

### 4.3.2 Quantitative Fractography

#### 4.3.3 DP 590

The predominantly dimpled fracture surface of DP 590 is attributed to ductile mechanisms, whereas, the secondary cracks comprise the bulk of the brittle features observed in these steels. Table 4.3 shows the area fraction of dimpled regions and the dimple size as a function of strain rate. Both these features do not change appreciably with strain rate and thus are insensitive to the increase in strain rate.

Table 4.3: Quantitative fractography of DP 590.

Strain Rate	Area Fraction of Dimpled regions	Dimple Size
$10^{-4}/s$	$91.1 \pm 1.8$	$2.8 \pm 0.1$
$10^{-2}/s$	$89.6 \pm 2.3$	$2.7 \pm 0.2$
$10^{-1}/s$	$86.7 \pm 1.4$	$2.5 \pm 0.3$
$10^0/s$	$85 \pm 1.4$	$2.8 \pm 0.1$
$10^1/s$	$86.3 \pm 1.4$	$2.6 \pm 0.2$
$3 * 10^3/s$	$88.2 \pm 1.3$	$2.5 \pm 0.1$

#### *DP 980 steels*

As discussed previously, the fracture surfaces of the DP 980 steels are largely comprised of three main features: (a) dimples, (b) facets without cracks and (c) secondary cracks with facets. Figure 4.17 shows the area fraction of dimpled regions as a function of strain rate. DP 980 NC shows an increase in the area fraction of dimples with strain rates, however, at higher rates it plateaus. The area fractions of both DP 980 GAN and GAD are largely insensitive to strain rate depicted by the flat linear trends observed in these steels. Additionally, the area fraction of dimpled regions in DP 980 GAD is higher than in the GAN and NC counterparts at all strain rates. All these observations indicate that the mechanisms that control the plasticity of the steels are a function of both the microstructure and the strain rate.

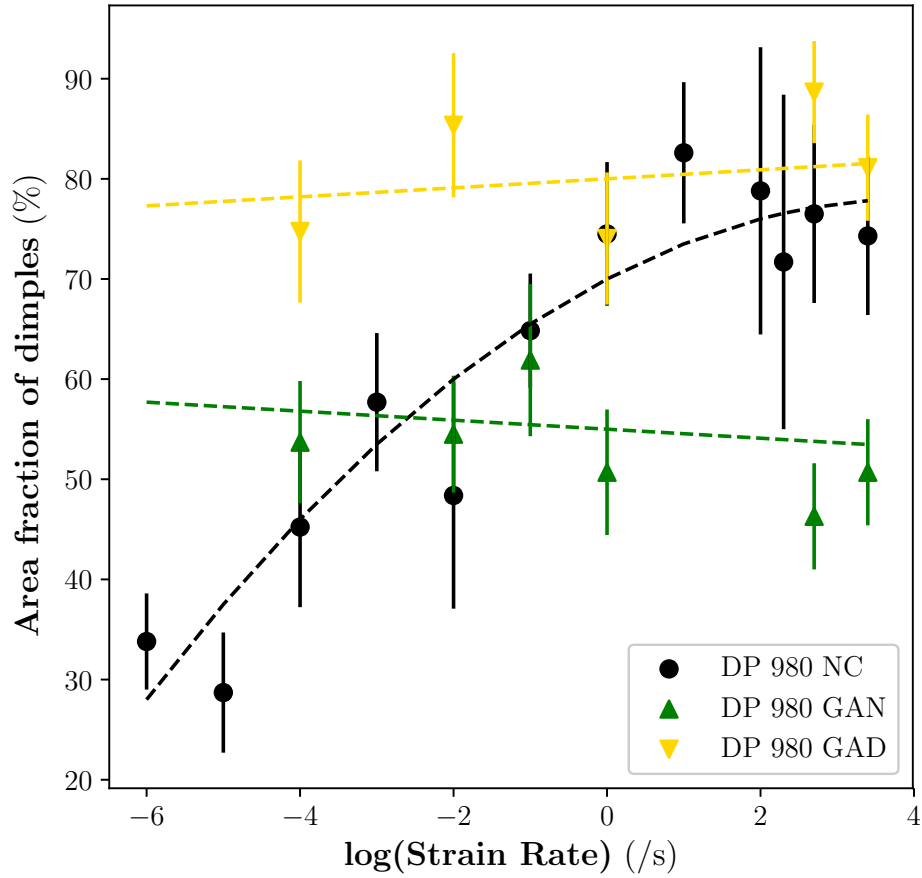


Figure 4.17: Area fraction of Dimpled regions as a function of strain rate for DP 980 steels.

Figure 4.18 shows the area fraction of facets without secondary cracks as a function of the strain rate. The formation of these facets is most favorable at low strain rates and is observed to be the highest in the DP 980 NC samples. The area fraction of these features decreases as a function of strain rate across all the three steels. Thus, the mechanism responsible for these features is strain rate sensitive in all the steels.

Further, figure 4.19 shows the area fraction of facets with secondary cracks. These features are observed at a much greater extent with GAN steels, thus confirming the qualitative observations. These estimations suggest that while the *extent* of the

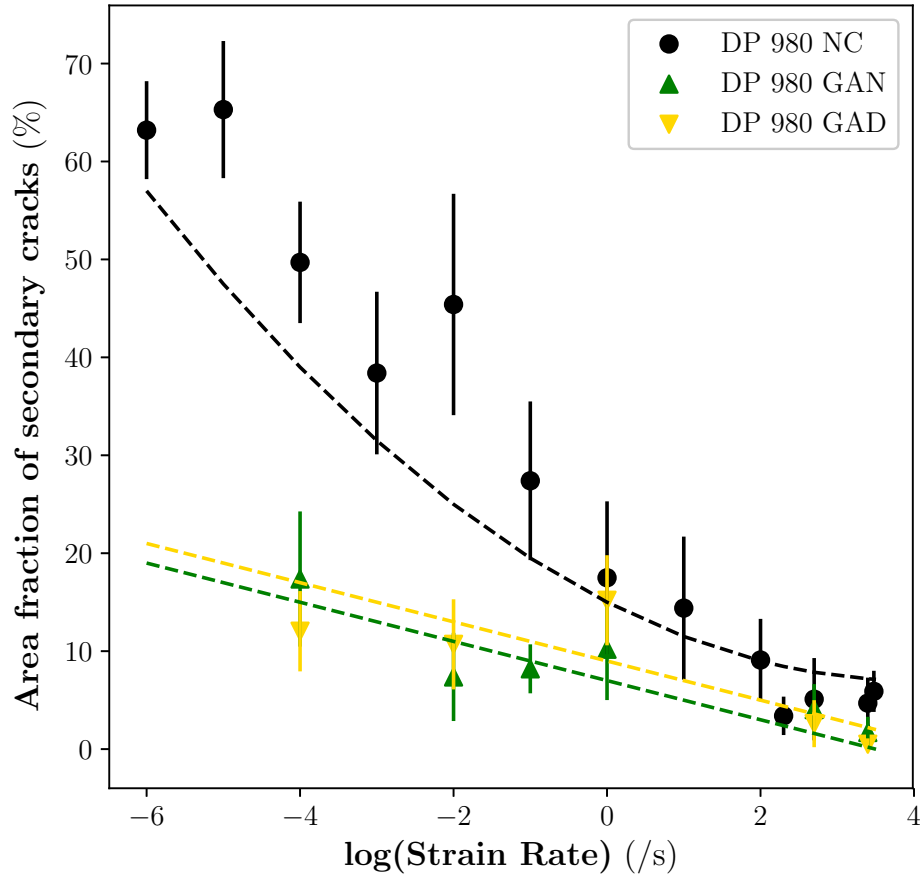


Figure 4.18: Area fraction of featureless faceted regions as a function of strain rate for DP 980 steels.

secondary cracks with facets is different in each steel and can be a function of the underlying microstructure, its *sensitivity* to strain rate is similar in all three steels. Additionally, since the area fractions of dimples in DP 980 GAN and GAD remains constant across strain rates, the increase in the secondary cracks occurs at the expense of the reduction in facets. Thus, these features are preferred at higher strain rates.

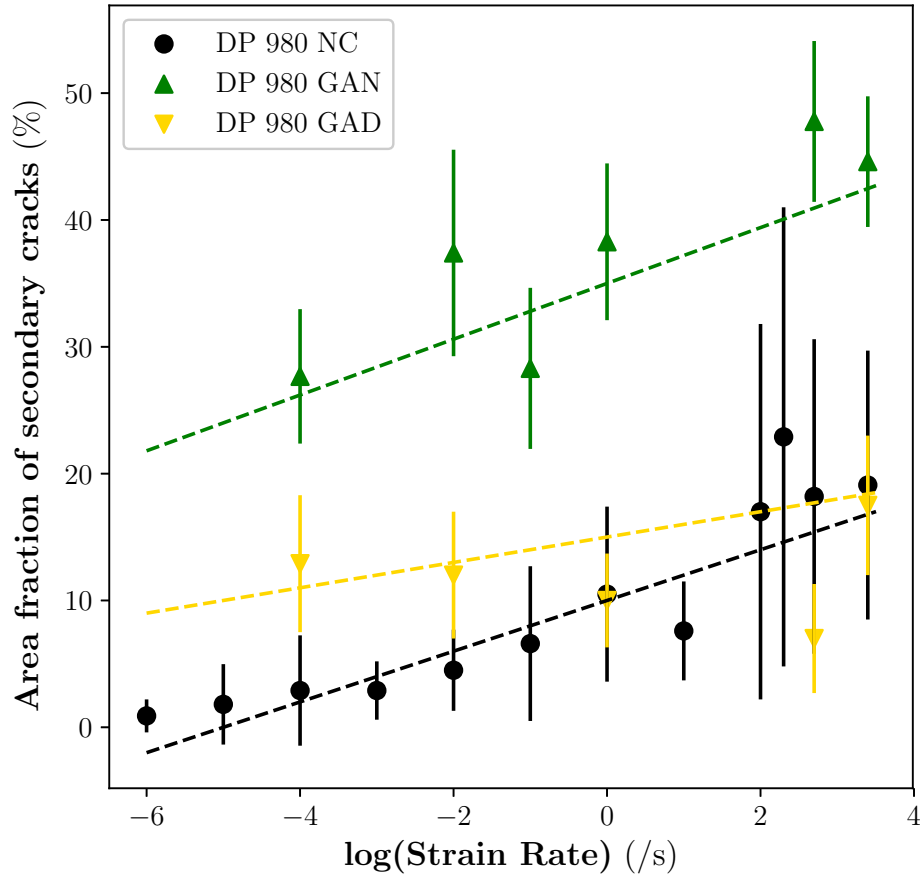


Figure 4.19: Area fraction of regions with secondary cracks as a function of strain rate for DP 980 steels.

#### 4.4 Fracture profile and deformed microstructures

The following section goes over the deformed microstructures and the fracture profiles observed at different strain rates to gain a deeper understanding of the deformation and void formation mechanisms of the DP steels.

##### 4.4.1 DP 590

Figure 4.20 shows the fracture profiles of the DP 590 steels at (a)  $10^{-4}/s$ , (b)  $1/s$ , (c)  $3 \times 10^3/s$  strain rates. Voids originating at the interface of the ferrite and martensite



interface are seen at all strain rates along with a deformed microstructure. Voids originating due to the cracking of martensite are also observed. Inter-facial elongated voids growing along the direction of loading are also observed. The deformation of the microstructure at three strain rates was quantified by estimating the aspect ratio of ferrite and martensite grains at different strain rates near the fracture surface and away from it but still in the gage section of the sample. Figure 4.21 shows the aspect ratio of the ferrite grains. Ferrite shows increased deformation at the intermediate strain rates indicating that ferrite could be taking the bulk of the total strain at these strain rates. Figure 4.21 also shows the aspect ratios of martensite. The deformation trend between ferrite and martensite is reversed near the fracture edge. The aspect ratios can also aid in understanding the strain partitioning between the two phases at different strain rates and will be discussed in the next chapter.

#### 4.4.2 DP 980 NC

Figure 4.22 shows the fracture profile of the DP 980 NC steels at strain rates of (a)  $10^{-6}/s$ , (b)  $10^{-4}/s$ , (c)  $1/s$  and (d)  $3 \times 10^3/s$ . The fracture profile at the slowest strain rate of  $10^{-6}/s$  shows largely circular voids and qualitatively fewer compared to the other strain rates. The fracture profile is also  $\sim 45^\circ$  indicating a predominately shear like fracture. Large delamination cracks can be observed at strain rates of  $10^{-4}/s$  and  $1/s$ . The fracture profile at the intermediate strain rate does not show a large crack but several elongated voids originating from delamination between the phases. Qualitatively, the microstructure at the intermediate strain rate is the most deformed indicating the substantially high strain experienced at this strain rate.

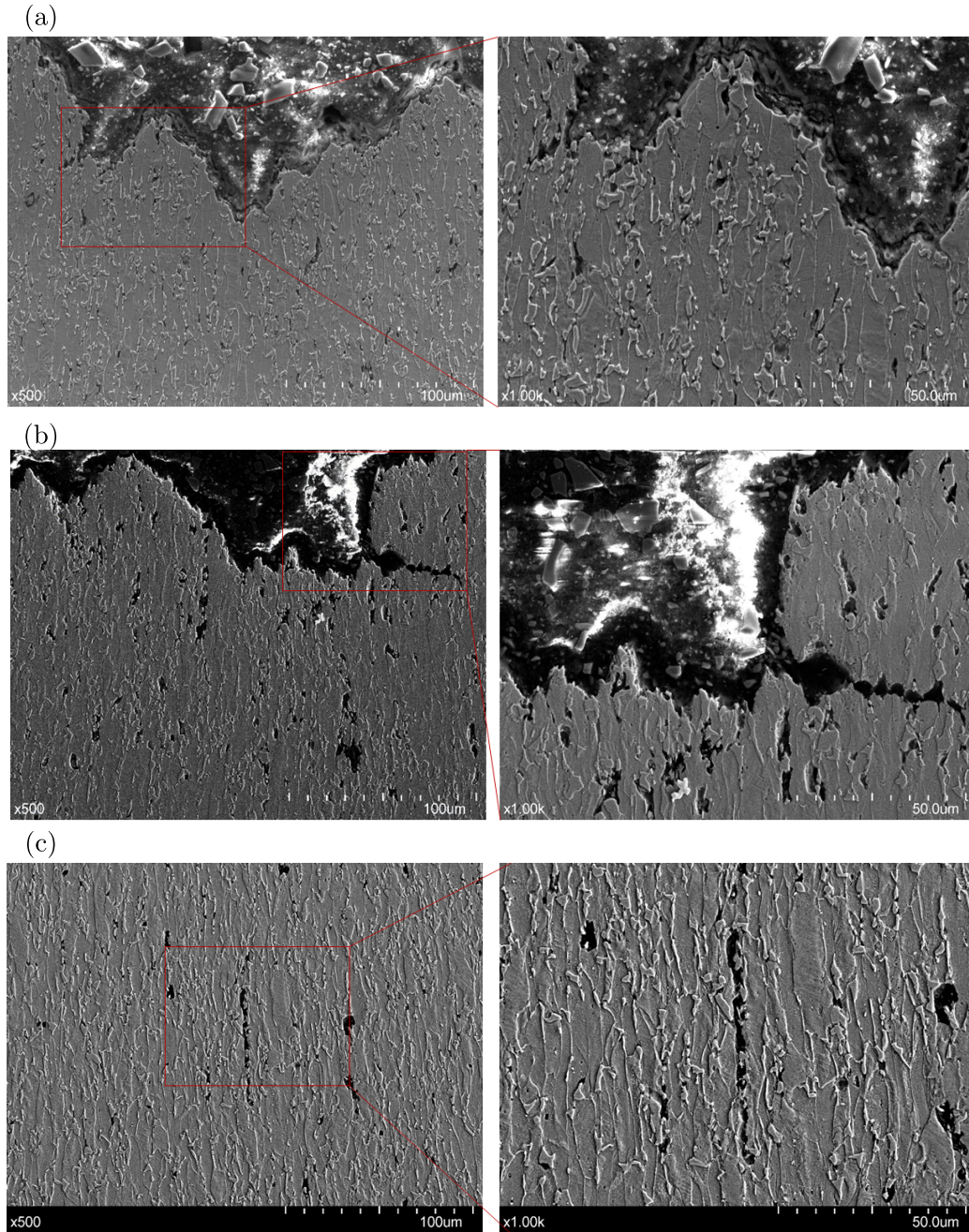


Figure 4.20: Fracture profile and deformed microstructures of DP 590 NC at (a)  $10^{-4}/s$ , (b)  $1/s$  and (c)  $3 \times 10^3/s$ . Voids generated by the cracking of martensite an inter-facial fracture can be observed at all strain rates.



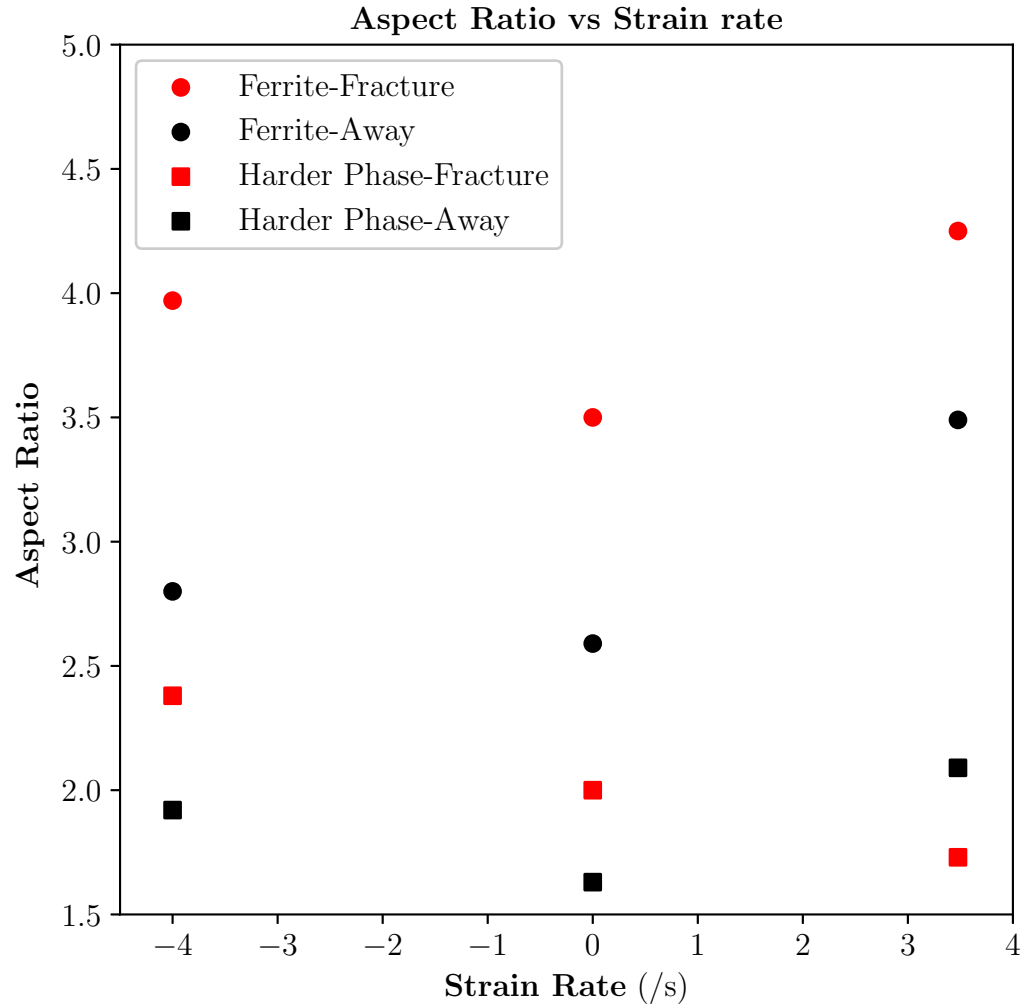
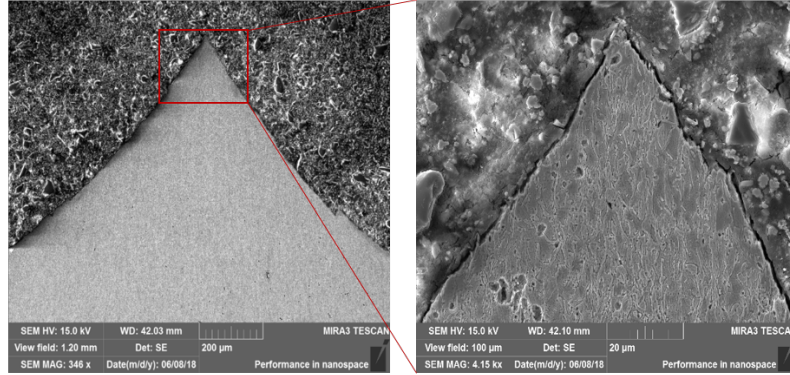
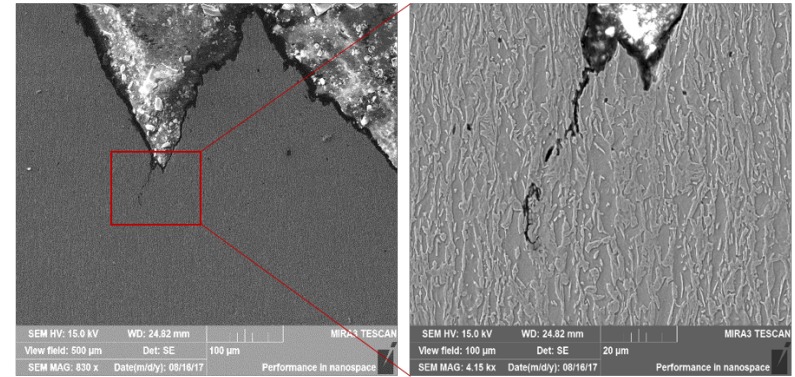


Figure 4.21: Plot showing the aspect ratio of the ferrite and martensite grains at different strain rates close to the fracture surface and away from it in the uniformly deformed region. High aspect ratio of ferrite and conversely low aspect ratio of martensite at the highest strain rate suggest a large portion of the strain was partitioned in ferrite at the highest strain rate.

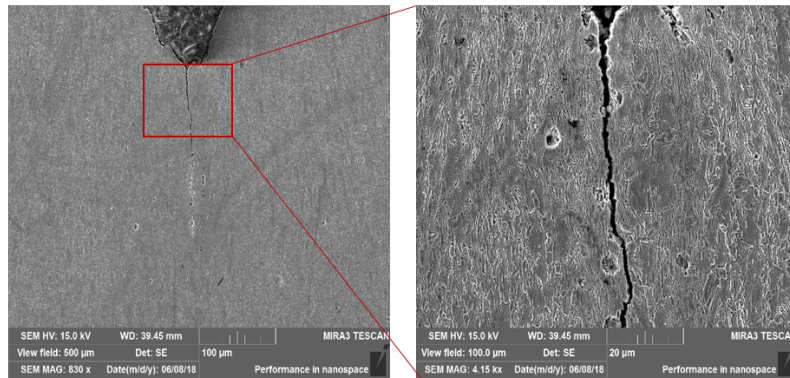
(a)



(b)



(c)



(d)

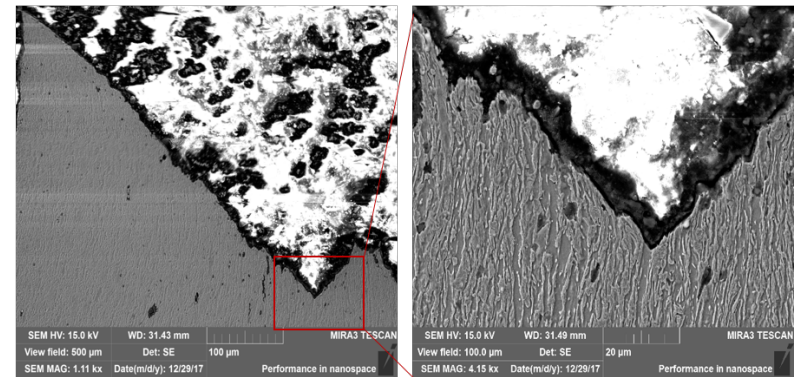


Figure 4.22: Representative low and high magnification SEM images showing the fracture profiles of DP 980 NC at different strain rates. (a) fracture profile at  $10^{-6}/s$  with a few circular voids showing delamination, (b) fracture profile at  $10^{-4}/s$  showing the formation of cracks originating by martensite cracking, (c) substantially long delamination crack observed on the fracture profile at strain rate of  $1/s$ , (d) Fracture profile at  $2 * 10^3/s$  strain rate showing a significantly deformed microstructure and scattered elongated delamination voids.

#### 4.4.3 DP 980 GAN

The fracture profile and deformed microstructures of DP 980 GAN are depicted in figure 4.23 for strain rates of (a)  $10^{-4}/s$  and (b)  $2.5 * 10^3/s$ . A deep fissure is observed at the lower strain rate and the higher magnification image shows the fissure surrounded by heavily deformed martensite bands. This micrograph captures the plasticity of martensite at this strain rate and also shows substantial blunting of the fissure formed that can also indicate plasticity. The deformed microstructure at the intermediate strain rate shows elongated voids with delamination similar to DP 980 NC. However, qualitatively a distinct difference in the extent of microstructural deformation could not be obtained between the different strain rates of the GAN steel.

#### 4.4.4 DP 980 GAD

Figure 4.24 shows the fracture profiles of DP 980 GAD at strain rates of (a)  $10^{-4}/s$  and (b)  $1/s$ . Qualitatively, GAD showed fewer voids overall when compared to NC and GAN at the same strain rates. Additionally, most voids, although showing delamination, are largely circular as opposed to the elongated voids seen in GAN and NC steels. The dispersed martensite may be responsible for the blunting of the voids. Similar to the GAN steels, a large difference in the deformation of the microstructures at the two different strain rates was not observed.

### **4.5 Plate Impact Experiments- Spall Failure**

#### 4.5.1 Overview

Plate impact experiments were carried out to understand the dynamic tensile (spall) behavior and resulting complete fracture and incipient spall in which the failure is arrested to reveal a deformed and void nucleated microstructure. During plate-on-

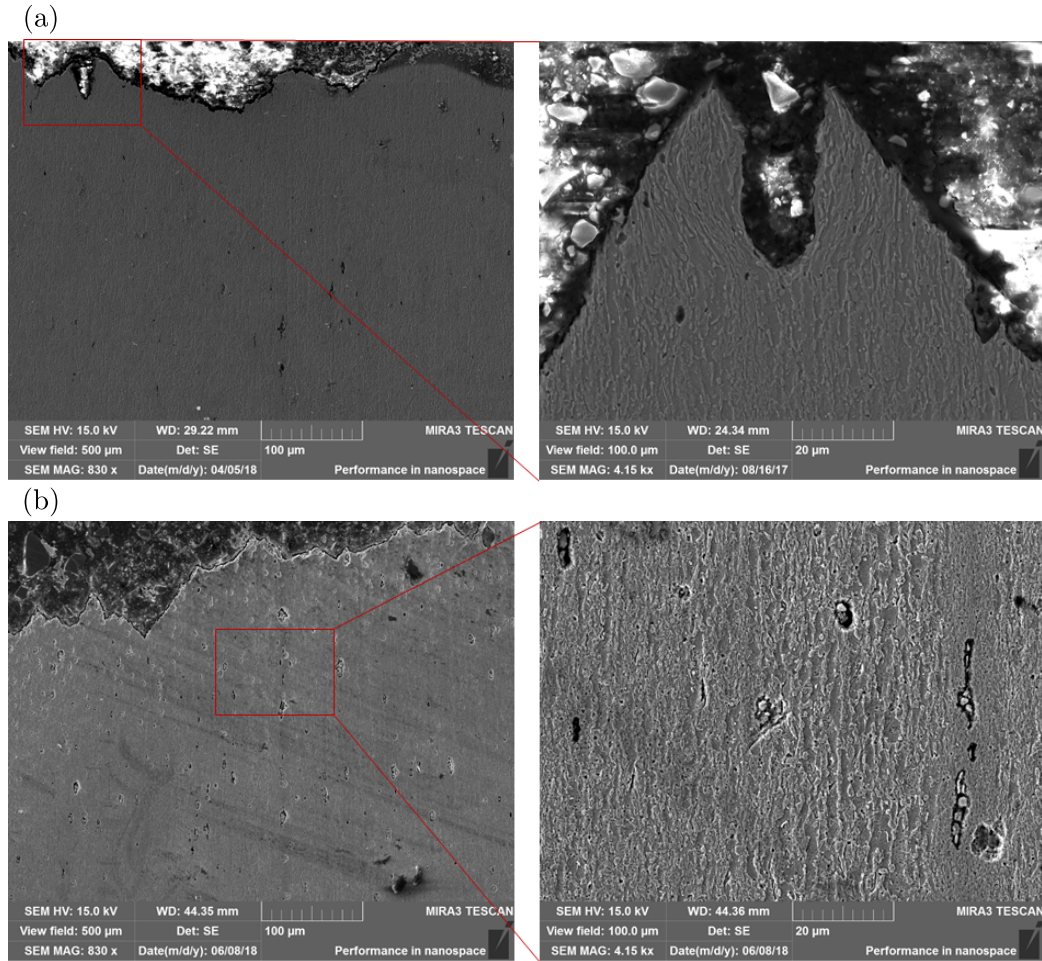


Figure 4.23: Fracture profile of DP 980 GAN at strain rates of (a)  $10^{-4}/s$ ; the profile shows the formation of a fissure and heavily deformed martensite bands indicating the plasticity of the phase, (b) fracture profile at  $2 * 10^3/s$  showing scattered elongated voids and a few delamination voids along the banded regions of martensite

plate impact experiments, compression waves are generated in the sample and in the flyer plate, which reflect off the back and free surfaces enter the sample. Interaction of the reflected compression waves from the back of the flyer and sample generate tension that results in spallation if the magnitude of tension exceeds the tensile strength. Figure 4.25 shows the (a) distance versus time and (b) free-surface velocity versus time curves for a nominal plate impact experiment resulting in spall. Since the flyer plate and the samples are made from DP steels and their sound speeds are similar, the impact can be considered to be symmetric. Figure 4.25 (b) also shows the Hugoniot



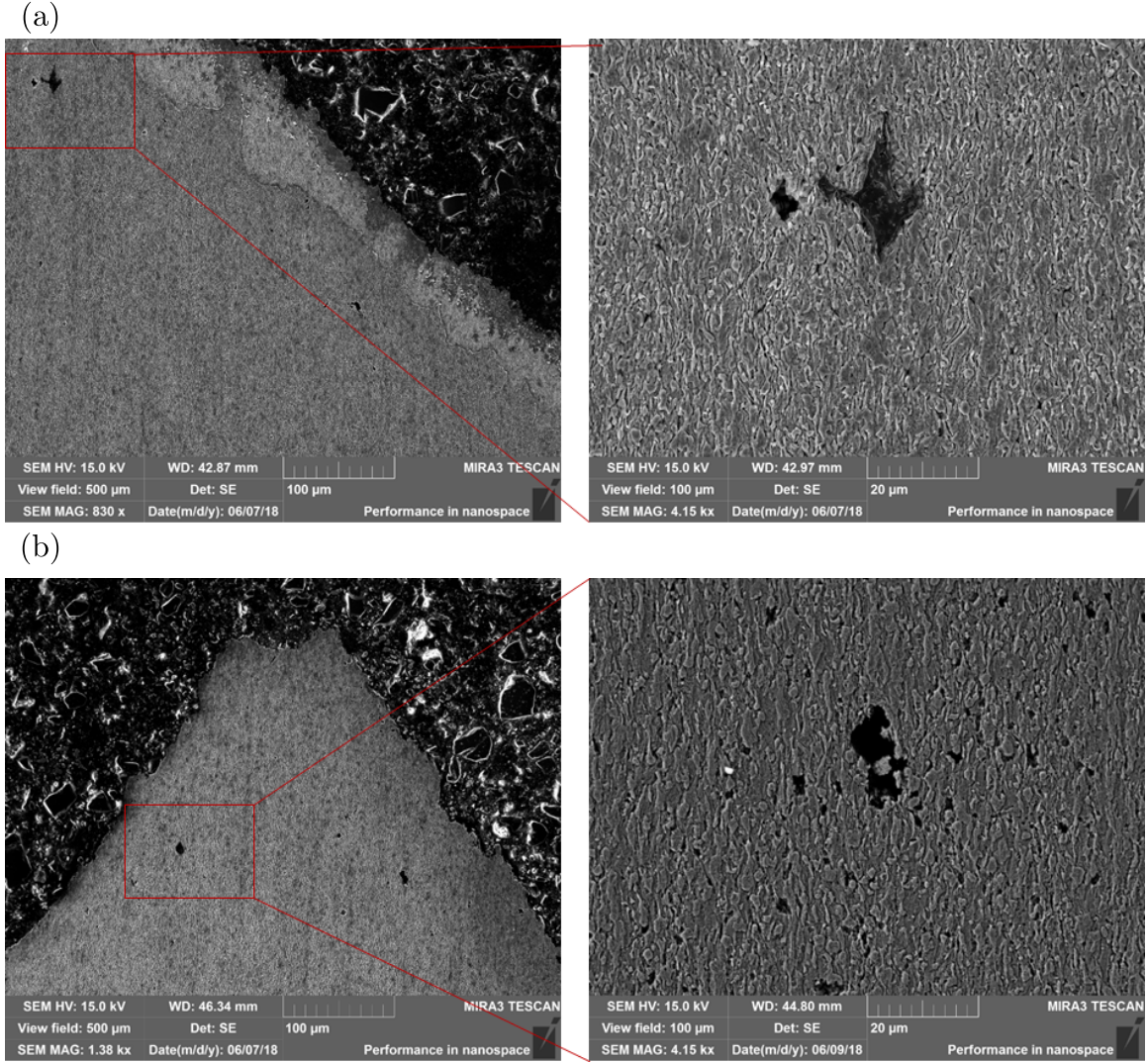


Figure 4.24: Fracture profiles of DP 980 GAD at (a)  $10^{-4}/s$  strain rate showing few circular delamination voids, (b)  $2 * 10^3/s$  strain rate also showing largely circular voids. The elongated voids observed in the NC and GAN counterparts were not observed.

Elastic Limit (HEL) at time  $t_1$  which marks the point at which the material transitions from a predominantly elastic state to an elastic-plastic state. The stress experienced at the HEL is the dynamic compressive strength and is given by equation 19.

$$\sigma_{HEL} = \frac{1}{2} \rho_0 C_L u_{HEL} \quad (32)$$

Complete spallation occurs when the magnitude of the tensile stress exceeds the

spall strength across the entire sample section and results in complete separation.

The spall strength is computed from the pull-back velocity (shown in Figure 4.24(b)), using equation (20). A correction factor is also employed and computed using equation (21).

$$\sigma_{spall} = \frac{1}{2}\rho_0 C_B(\Delta u_{fs} + \delta) \quad (33)$$

$$\delta = x_{spall}\left(\frac{1}{C_B} - \frac{1}{C_L}\right)\left(\frac{|\dot{u}_1\dot{u}_2|}{|\dot{u}_1| + \dot{u}_2}\right) \quad (34)$$

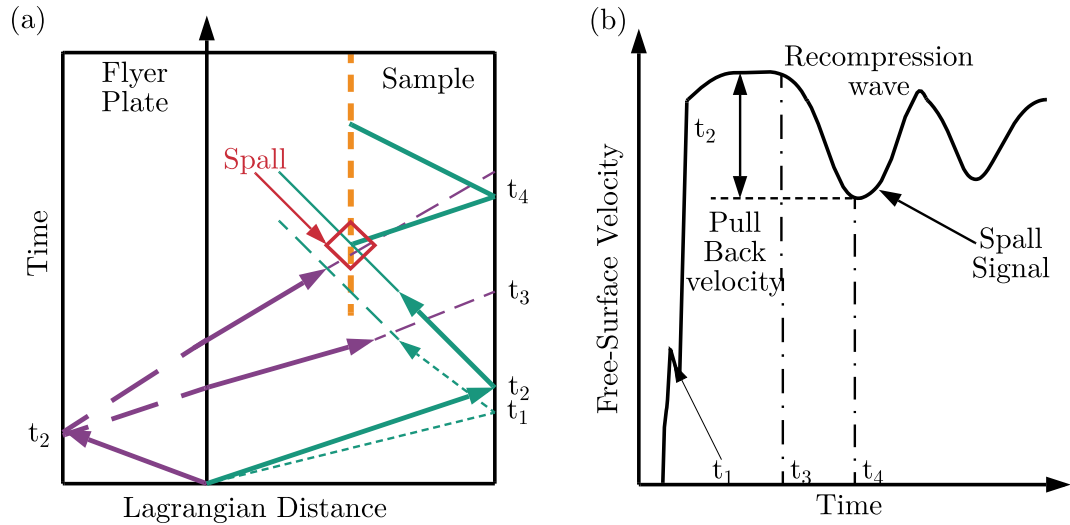


Figure 4.25: Representative schematic of (a) an x-t diagram for a symmetric impact experiment showing the interaction of the waves and the generation of the spall plane, (b) VISAR free surface velocity profile showing the HEL at  $t_1$ , the pull back velocity and the spall signal.

#### 4.5.2 Free Surface Velocity Traces

*DP 590*

The plate impact experiment conducted on this steel was at 600m/s which resulted in a complete spall. The experimental setup consisted of two samples of DP 590, with

one being probed and another being recovered. The third sample was DP 980 GAN for recovery only.

Figure 4.26 (a) shows the full free velocity VISAR profile for the probed DP 590 sample. A HEL at  $\sim 70m/s$  is clearly observed and is depicted in figure 4.26 (b). The pull back signal showing the decompression and recompression portion of the spall is shown in figure 4.26 (c). Upon closer inspection, a change in slope is observed in the recompression wave. The slopes of the recompression waves have been associated with the rates of void growth and nucleation and will be discussed in detail in the subsequent chapter. The HEL and spall strength calculated in this steel are shown in Table 4.3.

Table 4.4: HEL and Spall strength of DP 590

<b>Velocity (m/s)</b>	$\sigma_{HEL}$	$\sigma_{Spall}$
600m/s	$1.79 \pm 0.03$	$2.95 \pm 0.2$

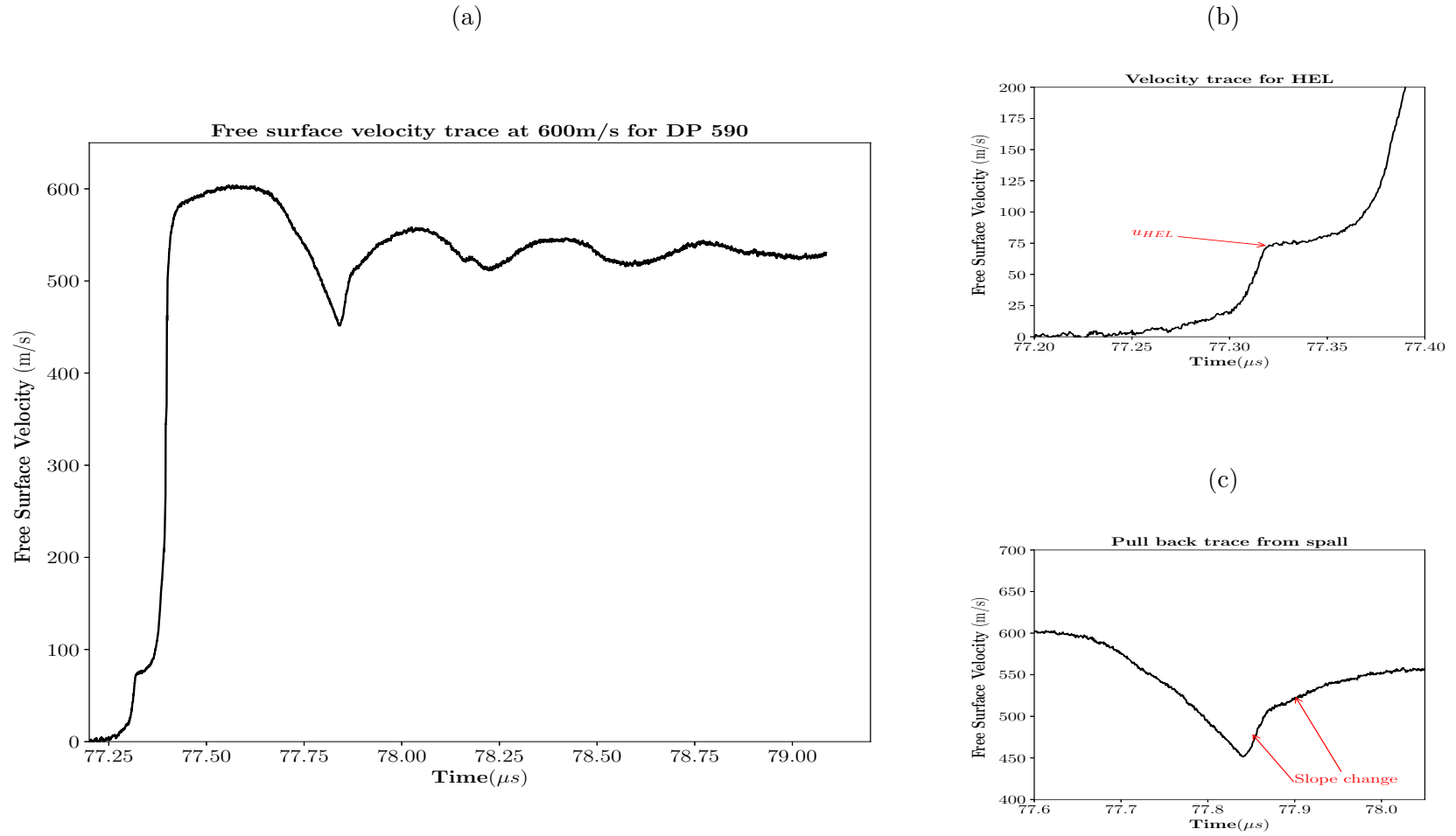


Figure 4.26: (a) Full VISAR free surface velocity of the DP 590 tested at 600 m/s, (b) zoomed in plot to show the Hugoniot Elastic Limit (HEL), (c) zoomed in plot showing the pull-back velocity and recompression wave. Two different slopes were observed in the recompression wave.



### *DP 980 NC*

Two plate-impact experiments at 600m/s and 300m/s were carried out on the DP 980 NC steels. The 600m/s velocity resulted in a complete spall and the 300m/s resulted in an incipient spall. Each experiment had three samples, where one sample was probed using VISAR interferometry and the other two samples were designed to be recovered for fractography.

Figure 4.27 (a) shows the free surface velocity VISAR profile for the 600m/s experiment. The pull-back signals indicate the spall and the subsequent ringing in the fractured sample. Figure 4.27(b) shows the step generated by the HEL at  $\sim 70m/s$ . A magnified view of the pull-back signal of the VISAR is depicted in figure 4.27(c). The recompression curves show a slope change similar to DP 590 steels indicating that there is a change in the void nucleation and growth rates under very high strain rates in these steels as well.

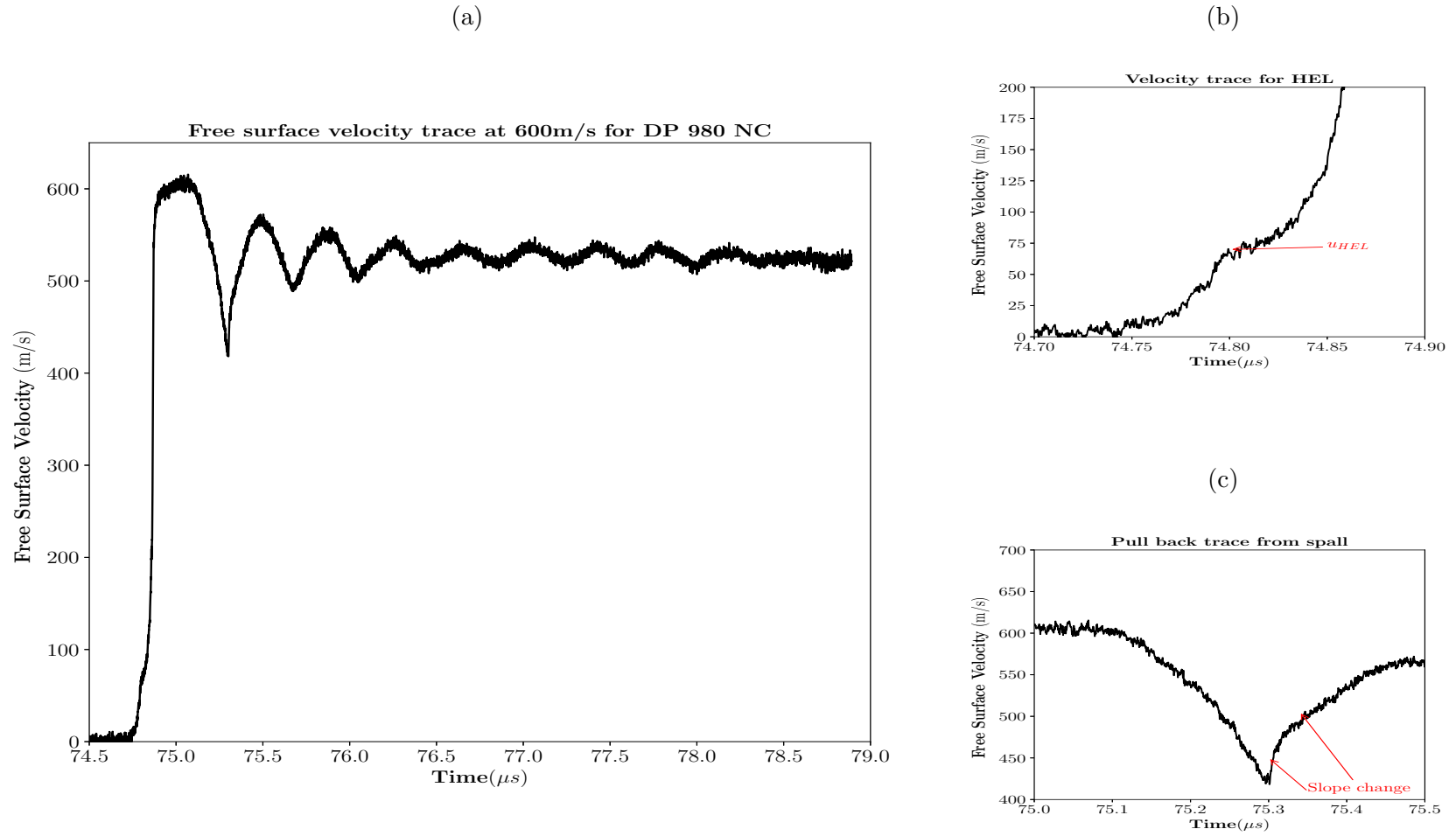


Figure 4.27: (a) Full VISAR free surface velocity of the DP 980 NC tested at 600 m/s, (b) zoomed in plot to show the Hugoniot Elastic Limit (HEL), (c) zoomed in plot showing the pull-back velocity and recompression wave. Two different slopes were observed in the recompression wave.

Figure 4.28(a) shows the full VISAR profile for the 300m/s experiment. As seen in figure 4.28(a), the pull back velocity does not reach the peak velocity indicating that the sample underwent incipient spall. Similar to the 600m/s experiment, the HEL and a magnified view of the pull back velocity are depicted in figure 4.28 (b) and (c), respectively. Additionally, a change in slope in the recompression wave is also observed. The HEL and spall strength of the two experiments are given in table 4.5. The spall strength was computed by taking an average of the two slopes in the recompression wave. The spall strength was higher than DP 590, but the HEL was observed to be slightly lower.

Table 4.5: HEL and Spall strength of DP 980 NC at different velocities

<b>Velocity(m/s)</b>	$\sigma_{\text{HEL}}$	$\sigma_{\text{Spall}}$
300 m/s	$1.71 \pm 0.2$	$4.01 \pm 0.2$
600 m/s	$1.75 \pm 0.2$	$3.94 \pm 0.2$

The recovered samples were investigated to gain a deeper understanding of the fracture generated under spall and the nucleation of voids leading to incipient spall. The fractography and deformed microstructures are presented in the next section.

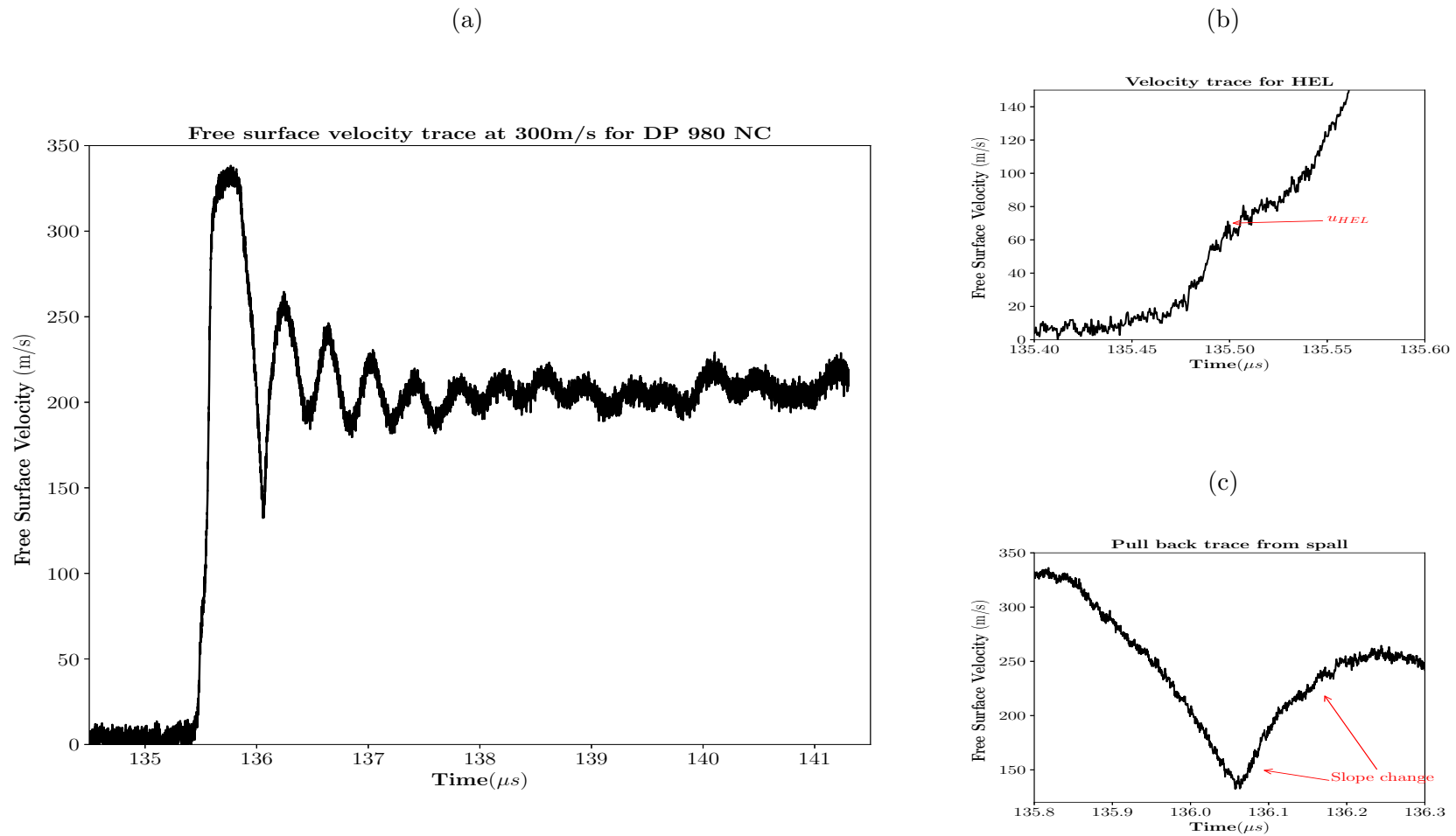


Figure 4.28: (a) Full VISAR free surface velocity trace of the DP 980 NC experiment at 300m/s, (b) zoomed in plot showing the HEL, (c) zoomed in plot showing the pull back velocity and change in slope in the recompression wave.

### *DP 980 GAD*

Figure 4.29 (a) shows the full VISAR free velocity trace for the DP 980 GAD sample shot at 600m/s. The HEL and spall response of DP 980 GAD was similar to that of DP 980 NC. The recompression curves showed a marked change in slope, similar to DP 980 NC and DP 590. Thus, the void nucleation and growth changes at these high strain rates for all three steels.

Table 4.6 shows the HEL and spall strength calculated in this steel. Although the spall strength was higher than DP 590, as expected, it was lower than DP 980 NC samples.

Table 4.6: HEL and Spall strength of DP 980 GAD

<b>Velocity (m/s)</b>	$\sigma_{HEL}$	$\sigma_{Spall}$
600m/s	$1.63 \pm 0.03$	$3.33 \pm 0.2$

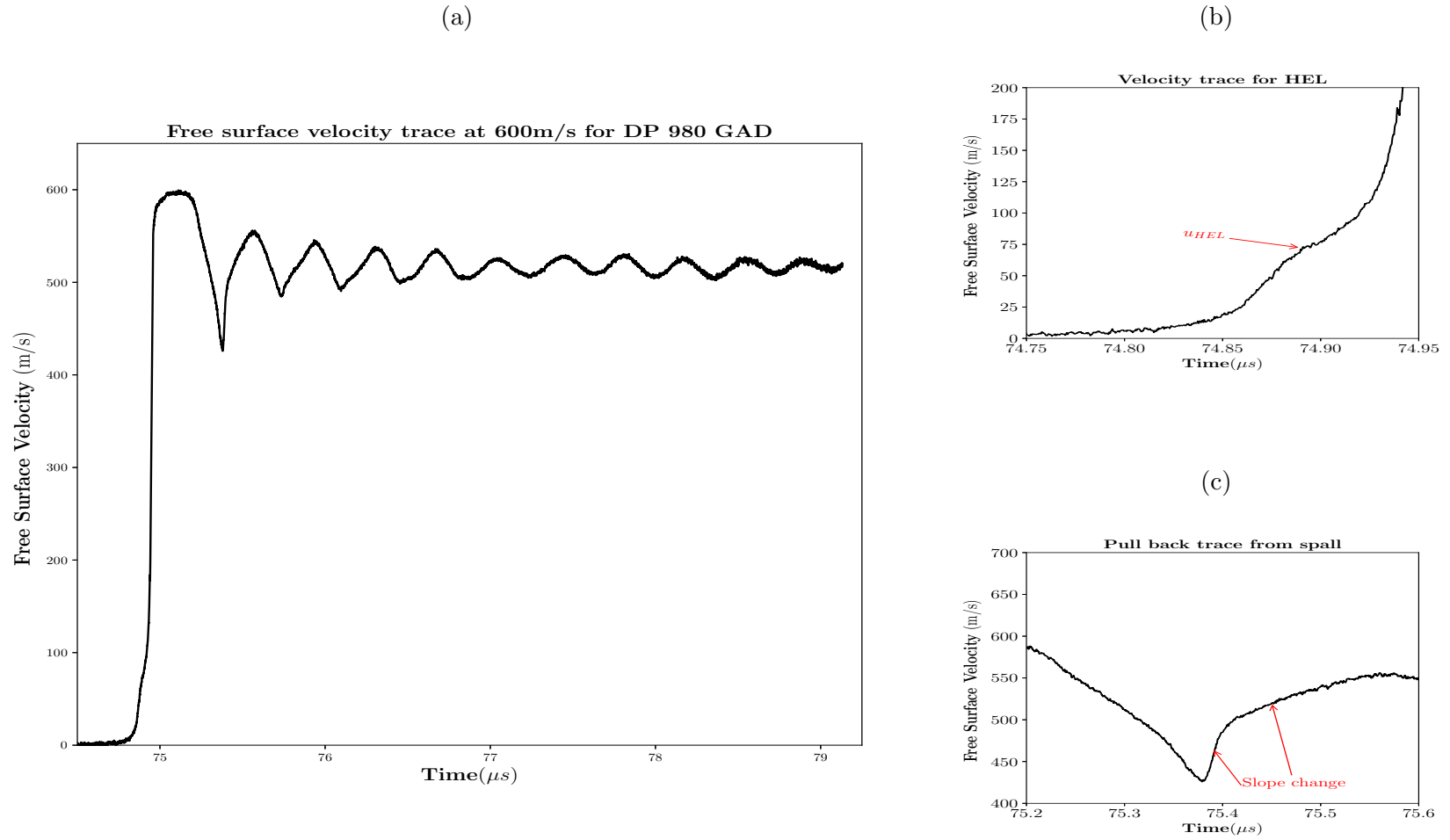


Figure 4.29: (a) Full VISAR free surface velocity of the DP 980 GAD tested at 600 m/s, (b) zoomed in plot to show the Hugoniot Elastic Limit (HEL), (c) zoomed in plot showing the pull-back velocity and recompression wave. Two different slopes were observed in the recompression wave.

### 4.5.3 Post-Mortem Fractography

#### *DP 590*

Figure 4.30 (a) shows the low magnification spall fracture surface of DP 590 NC. The fracture surface was predominantly brittle with a few long striations along the rolling direction. The brittle regions showed a quasi-cleavage response with a very few scattered voids.

SEM based fractography was conducted on unbiased images taken from the central one-third of the sample, similar to the quasi-static and intermediate strain rate samples. The observed features were classified into dimples, quasi-cleavage areas or striations. The area fraction of the brittle regions was estimated to be  $89.2 \pm 10\%$ , thus confirming the qualitative observations. Only 0.6% of the fracture was occupied by voids while the remaining 10% was occupied by the striations.

#### *DP 980 NC*

The recovered samples from the 600m/s showed complete spall. The fractured halves showed some secondary damage as shown in Figure 4.31 (a). The measured thickness of the halves were  $\sim 1mm$  indicating that the spall plane was very close to the mid-plane of the samples. Figure 4.27 (b) shows a low magnification image of the spall sample. The spall fracture surface although containing substantial heterogeneities, was predominantly brittle. Racetrack like features indicated by white arrows were also observed inter-dispersed with brittle regions as shown in figure 4.31 (c). The predominantly brittle region is depicted in figure 4.31(d).

Figure 4.32 shows the different regions within the spalled sample at higher magnifications. Figure 4.32(a) shows the racetrack like fracture features while figure 4.32 (b) shows an area of the fracture surface predominantly occupied by dimple ductile features. Higher magnification images of the racetrack like fracture features, figure

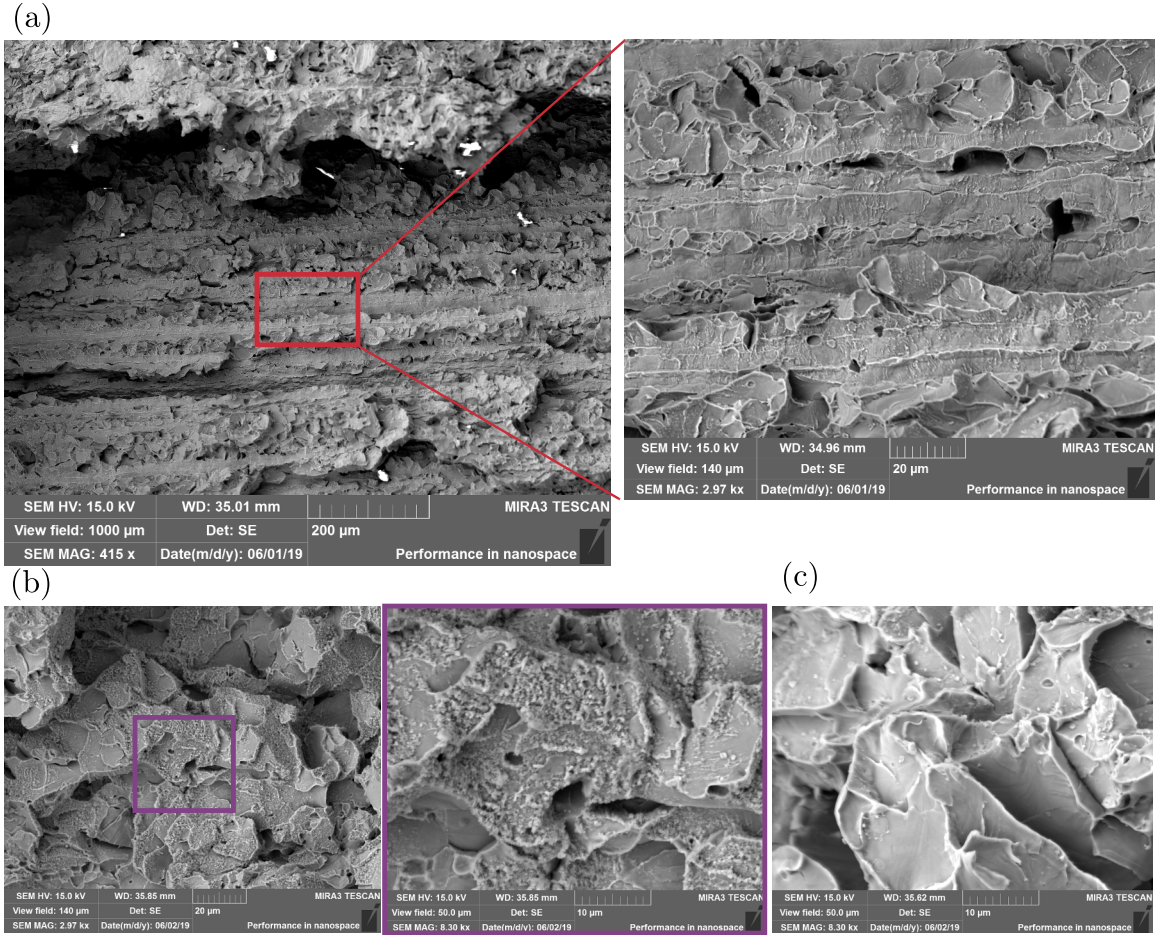


Figure 4.30: (a) Low magnification image of the spalled sample and showing the magnification at which the sample was investigated for quantitative fractography, (b) Representative SEM image of the quasi- cleavage fracture observed , (c) High magnification image of the quasi-cleavage brittle fracture in DP 590.

4.32(c) and (d) reveal thin dimpled regions which appear as ridges and long flat featureless regions. Figures 4.32 (e)-(h) show various regions of brittle fracture at different magnifications. The brittle regions composed of sharp facets with a few scattered dimples.

The area fraction of brittle regions was estimated to be  $77.4 \pm 19\%$ , thus confirming the qualitative observations.



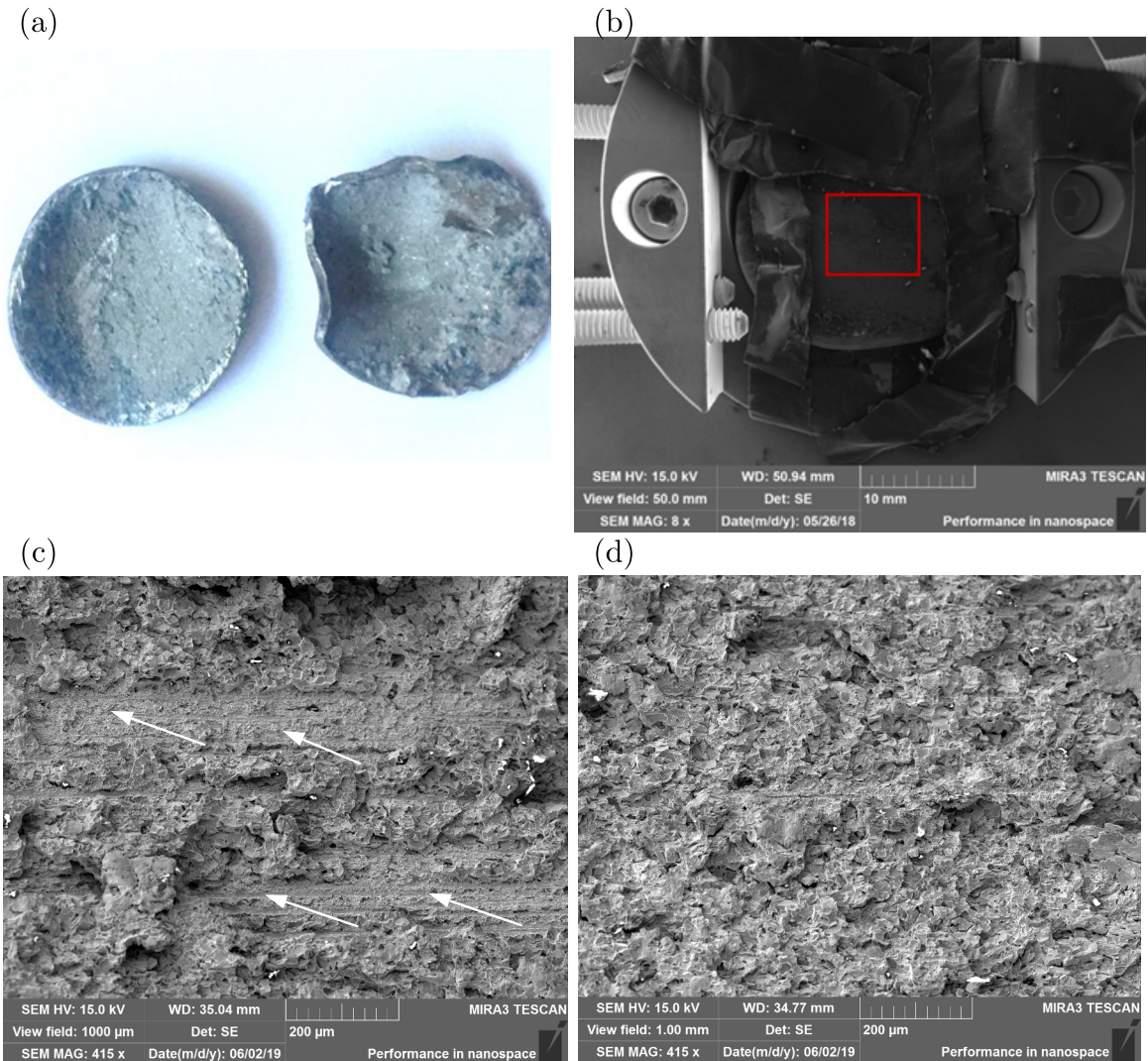


Figure 4.31: (a) Spalled sample generated from the 600m/s experiment, (b) Low magnification image of the mounted spalled sample and showing the region of the sample investigated for quantitative fractography, (c) Low magnification image of the race-track like striations seen on the fracture surface, indicated by white arrows, (d) Low magnification image of a largely brittle fracture observed.

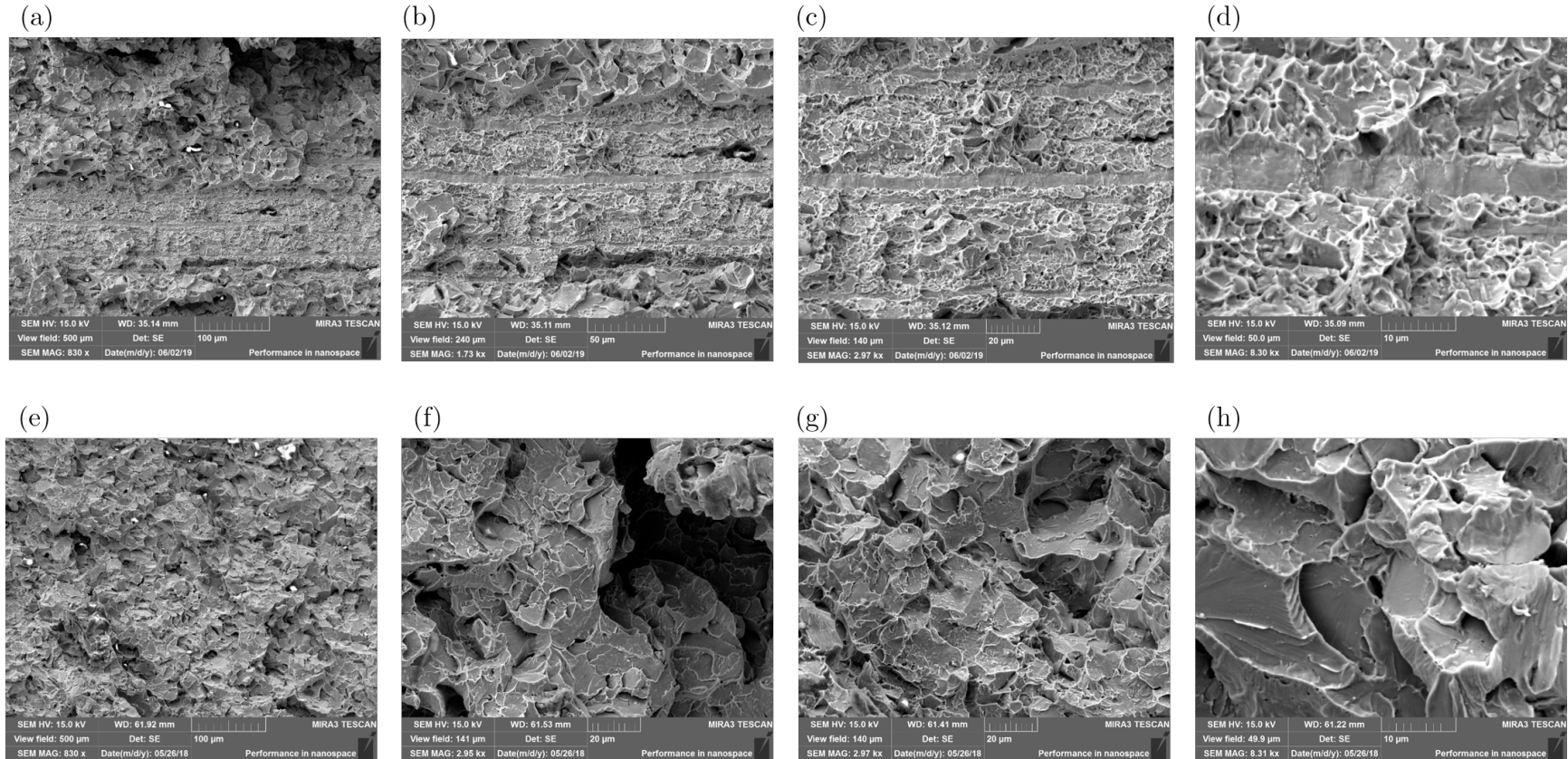


Figure 4.32: Representative SEM images of DP 980 NC showing the heterogeneities in the fracture surface by highlighting the ductile (a) to (d) and brittle fracture features (e) to (h). (a) Racetrack like striations, (b) largely dimpled region, (c) region showing a mixture of the striations, dimples and a few brittle facets, (d) high magnification image of the striations showing the presence of dimples and flat featureless areas, (e) low magnification image showing brittle fracture, (f) large void observed in a brittle region, (g) facets showing brittle fracture and (h) high magnification image of the faceted region interspersed with a few voids.

### *DP 980 GAN*

Figure 4.33 (a) shows the low magnification spall fracture of the recovered DP 980 GAN sample that was shot at 600m/s. Qualitatively, the fracture surface is distinctly different from DP 590 and DP 980 NC. A large part of the fracture surface is occupied by the long flat bands that are parallel to the rolling direction. The area fraction occupied by the bands were the largest,  $47 \pm 8\%$ , and occupied half of the fracture area. Similar to DP 980 NC, there are dimples surrounding the striations, and the area fraction was estimated to be  $31.9 \pm 5\%$ . The area fraction of brittle regions occupied by quasi-cleavage regions was  $20 \pm 6\%$ , which is considerably lower than both DP 980 NC and DP 590.

### *DP 980 GAD*

The spall fracture surface of DP 980 is shown in figure 4.34 (a) and is very similar to the that observed in DP 980 GAN steels. Long bands parallel to the rolling direction were observed in these steels as well and were surrounded by dimpled areas. The quasi-cleavage fracture was observed, however the extent of this fracture was much lower when compared to DP 590 and DP 980 NC steels.

The quantitative fractography estimated the area fraction of the bands at  $43 \pm 7\%$ , area fraction of dimples at  $31 \pm 7\%$  and area fraction of the quasi-cleavage regions is  $25 \pm 6\%$ . These estimations confirm the qualitative observation regarding the similarity between the DP 980 GAN and GAD spall fracture surfaces. The subsequent chapter will highlight a few explanations for this behavior.

#### 4.5.4 Incipient Spall-Deformed microstructure

The experiment at 300m/s resulted in incipient spallation as revealed upon observation of the cross-section of the impacted sample. Cracks were nucleated with some growth but the deformation was arrested such that the fracture did not propagate



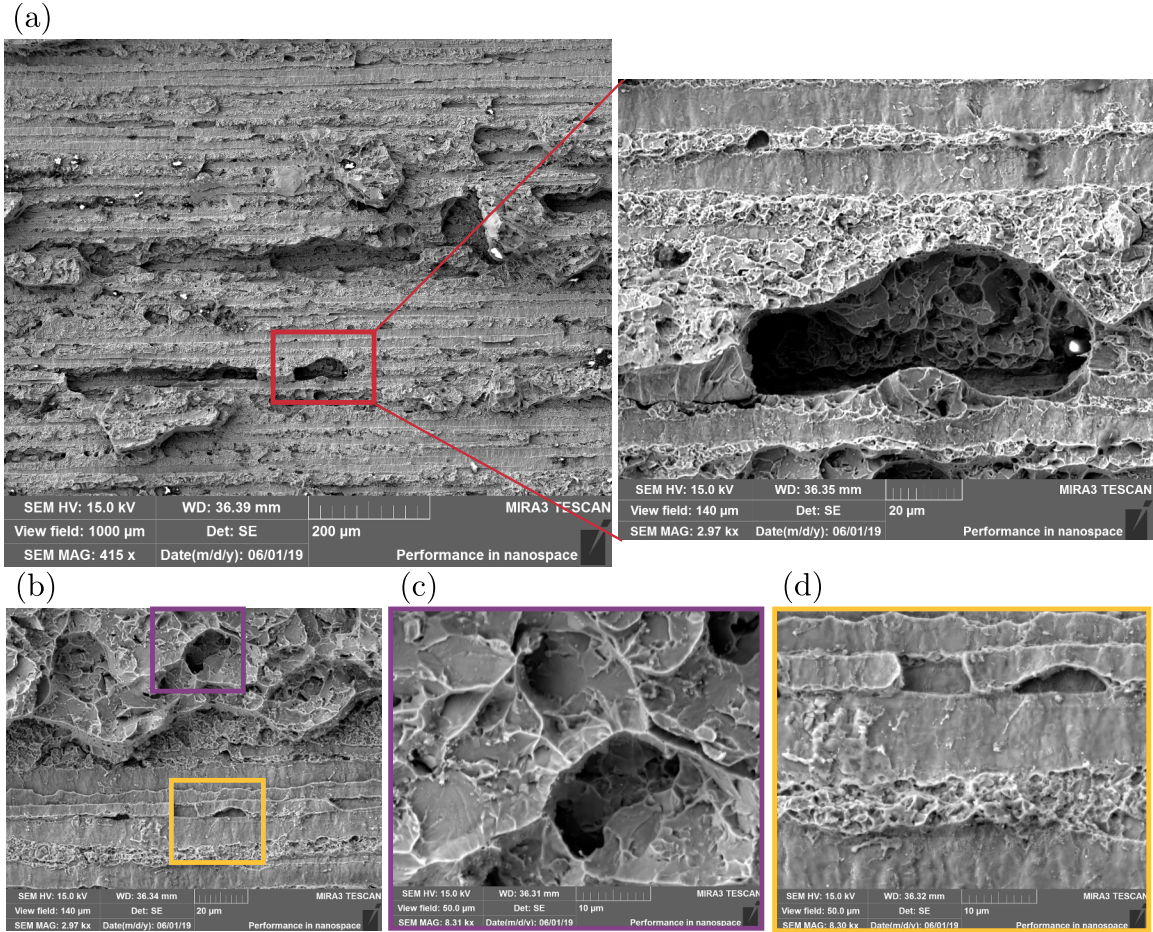


Figure 4.33: (a) Low magnification image of the spalled sample of DP 980 GAN with a large area occupied by the long bands surrounded by dimples and a zoomed in image showing the magnification at which the sample was investigated for quantitative fractography, (b) Representative SEM image of the long bands parallel to the rolling direction, (c) High magnification image of the quasi-cleavage brittle fracture and (d) High magnification image of the flat bands with dimples.

throughout the sample. Generation of incipient spall gives crucial information on the preferential area in the microstructure for void nucleation under shock loading. Figure 4.35 (a) shows a low magnification montage of incipient sample cross-section containing the longitudinal section. Large voids nucleated near the center of the sample are indicated in figures 4.35 (b),(c) and (d). The sample did not have much secondary damage and hence the damage can be attributed to be created almost entirely by the spall process.

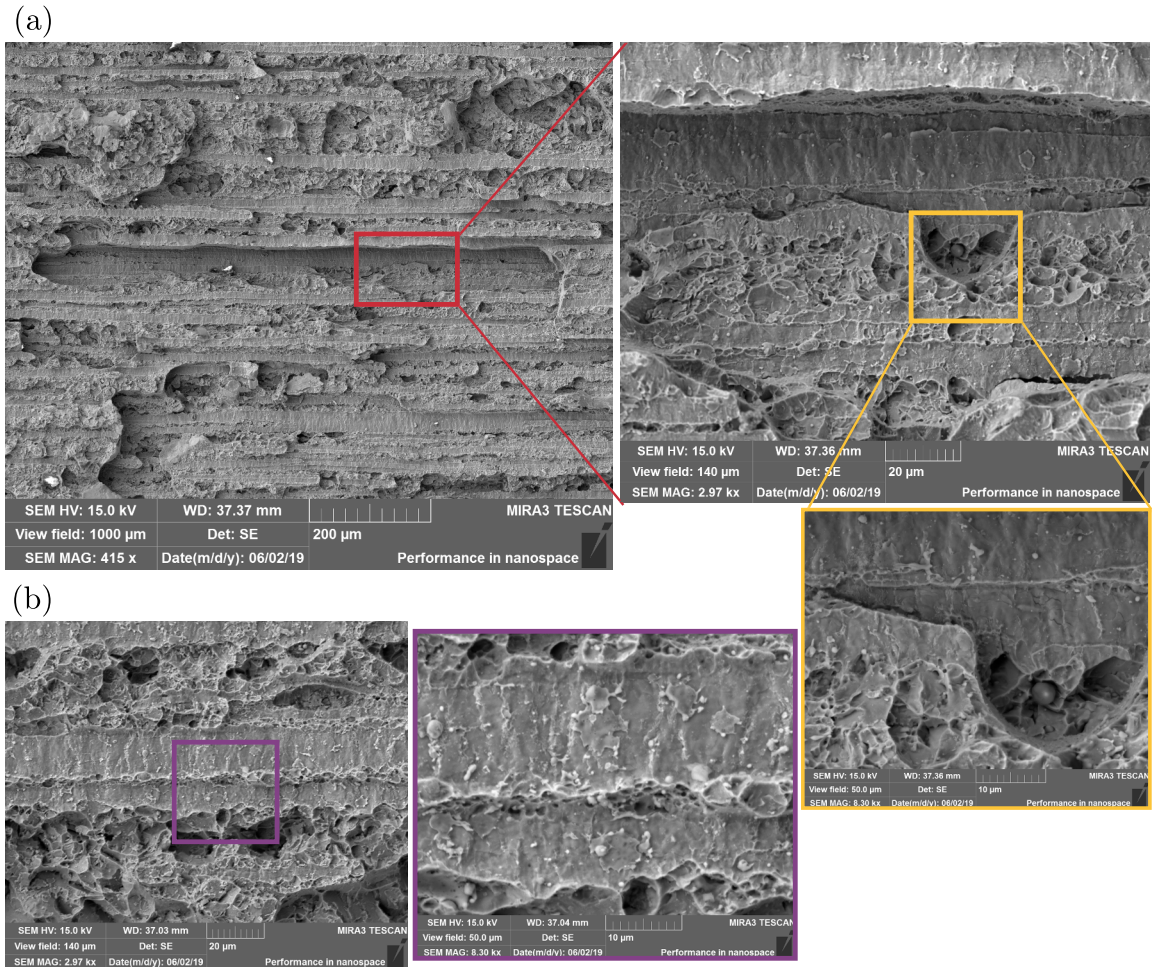


Figure 4.34: (a) Low magnification image of the spalled sample of DP 980 GAD with a large area occupied by the long bands surrounded by dimples and a zoomed in image showing the magnification at which the sample was investigated for quantitative fractography and the area containing the flat bands and dimples, (b) Representative SEM image of the long bands parallel to the rolling direction and a corresponding high magnification image of the flat bands with dimples.



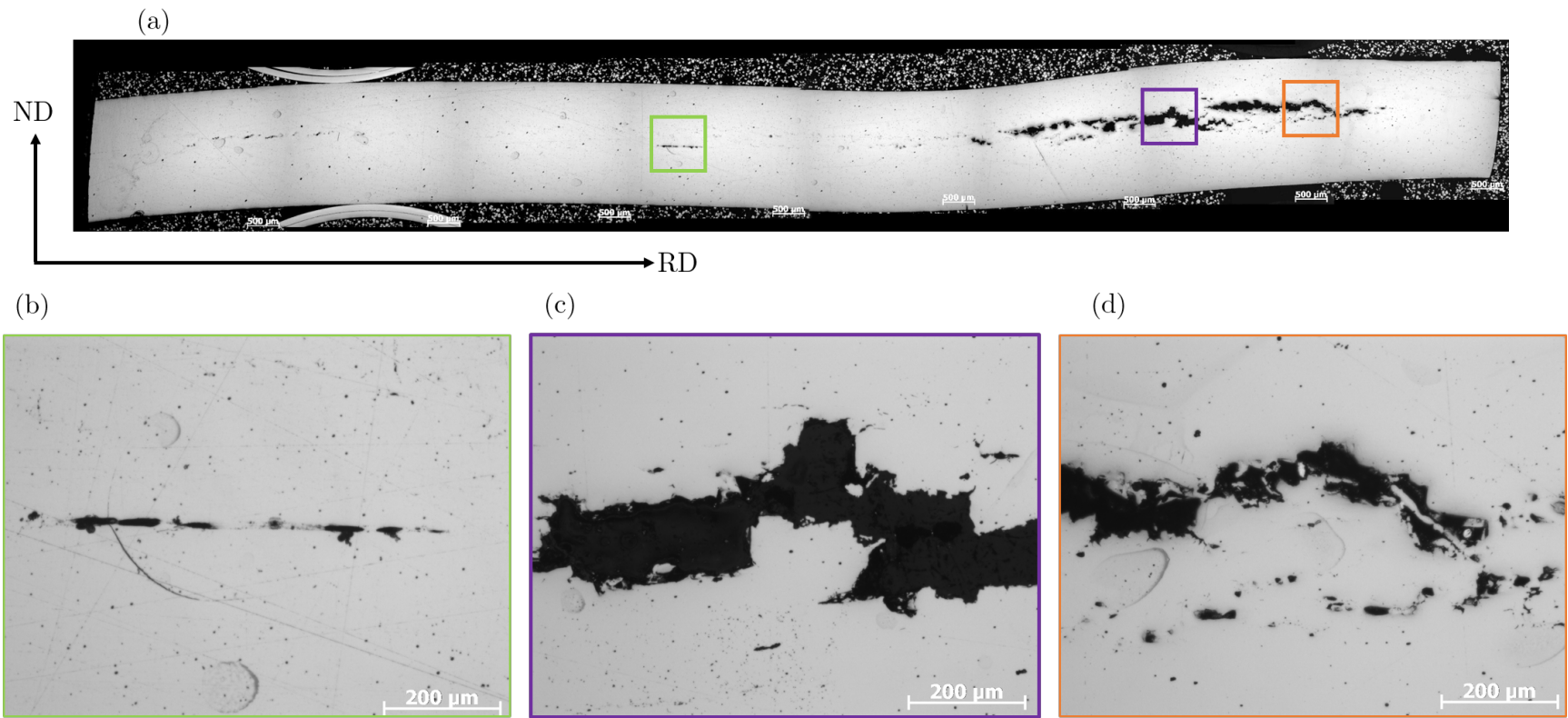


Figure 4.35: (a) Optical unetched montage of the incipient spall sample showing large voids, (b) elongated voids observed on the center of the sample, (c) large coalesced voids (d) collection of smaller connected voids

Figure 4.36 shows the etched microstructures of the incipient spall sample captured using optical and scanning electron microscopy. Distorted banded structures of martensite can be observed near the bigger voids in figure 4.36 (a). Figure 4.36 (b) and (c) show martensite bands deforming substantially and rotating to become nearly vertical in the vicinity of the large voids.

Higher magnification images confirm the extensive deformation and plasticity demonstrated by martensite. Deformation bands at  $\sim 45^\circ$  can be observed in figure 4.36 (d) indicating the possibility of shear band formation. Figure 4.36 (e) shows the extensive plasticity of martensite near a void and figure 4.36 (f) shows inter-facial cracks that were scattered throughout the sample.

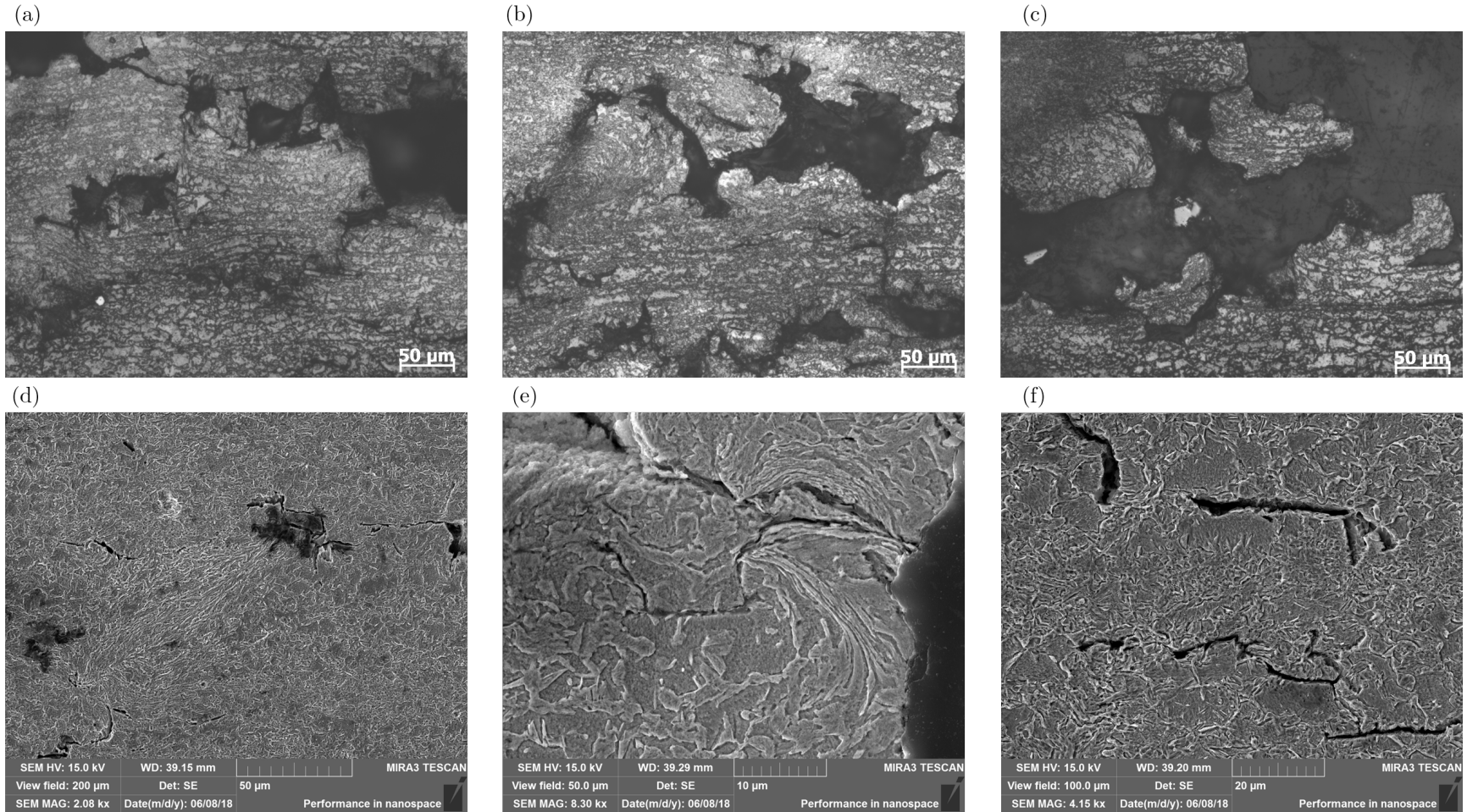


Figure 4.36: (a) optical microstructure showing the deformed martensite bands around large voids, (b) shows significant rotation of the phases near a void, (c) shows bending and rotation of the phases close to the void, (d) SEM image showing a deformation band linking two separated voids, (e) high magnification image of the heavily deformed and rotated martensite, (f) interfacial delamination cracks observed on the center of the specimen.



### *Martensite plasticity*

Figure 4.37 (a) shows the presence of a vertical deformation band connecting two different cracks in the microstructure. A similar band, although horizontal, can be seen to connect inter-facial cracks to a larger void in the microstructure. This substantial bending and plasticity of martensite could be responsible for the propagation of deformation and ultimately the creation of the spall plane during shock loading of DP 980 NC.

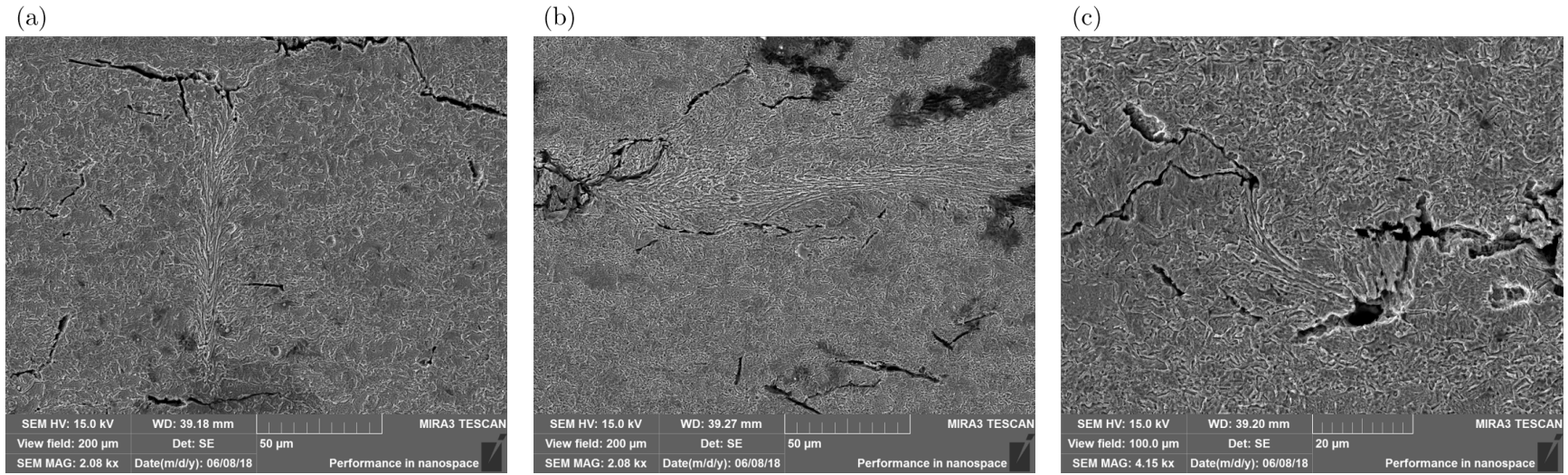


Figure 4.37: (a) Vertical deformation band connecting two cracked regions, (b) horizontal deformation band connecting cracks to a network of voids, (c) deformed and rotated martensite between two interfacial delaminated cracks.

## **CHAPTER 5**

### **DISCUSSIONS**

The current chapter will provide a deeper understanding of the operative deformation and fracture mechanisms of the four commercial DP steels investigated in this work. This will be achieved first by discussing the effect of volume fraction of martensite on the mechanical properties and fracture response. Results of a few other commercial steels reported in the literature under similar conditions will be used for the discussions. Further, the differences observed in the three DP 980 grade steels with a similar volume fraction of martensite will be discussed to understand the effects of the addition of the coating layers and the presence of a gradient microstructure on the strain rate sensitivity of the mechanical properties and fracture response. Finally, the effect of geometry on the mechanical properties and deformation of DP 590 will be discussed to illustrate the importance of maintaining a constant geometry at all strain rates.

#### **5.1 Effect of Volume fraction of martensite**

Four different commercial steels namely High Strength Low Alloyed (HSLA) 590, DP 590, DP 980 NC and USIBOR 1500 containing 0%, 29%, 68% and 100% of martensite respectively, are selected for the discussions in the current section. The data for the HSLA 590 and USIBOR 1500 steels were taken from the work conducted by Mishra et al. [84], to understand the effects of strain rate on completely ferritic and uncoated HSLA 590 steels and the effects of both strain rate and processing conditions on DUCTIBOR 590 and USIBOR 1500. DUCTIBOR and USIBOR contain an aluminum-silicon coating and were processed using hot stamping. Among the various time-temperature combinations discussed in the study by Mishra et al., the USIBOR

1500 steel, processed with a time-temperature condition of  $920^{\circ}\text{C}$  for seven minutes, were chosen for this discussion since it is considered to be the nominal condition when hot stamping these steels. The nominal tensile strengths of the steels under quasi-static strain rates were 590 MPa (HSLA and DUCTIBOR) and 1500 MPa (USIBOR). The chemistry and processing conditions of HSLA 590 and USIBOR 1500 were different from the DP steels and can also affect the mechanical properties and fracture response of these steels. However, for the following sections, only the effect of the volume fraction of martensite will be explored in detail. Additionally, all the steels discussed in Mishra et al.'s [84] work, similar to the current study, have applications in the automotive industry and can thus be exposed to high strain rate conditions that arise during sheet metal forming and crash, making their strain rate sensitivity an important aspect as well.

#### 5.1.1 Comparing microstructures

As discussed before, HSLA 590 has a completely ferritic structure. It has a fine grain size with dispersed carbides distributed within the grains and also along the grain boundaries. Figure 5.1 (a) shows the microstructure of this steel under optical and scanning electron microscopy. Figures 5.1 (b) and (c) show the microstructures of DP 590 and DP 980 NC for comparison. The USIBOR 1500 microstructure is shown in figure 5.1 (d) and is comprised entirely of martensite.

#### *Comparing the martensite in the steels*

As mentioned before, both HSLA 590 and DP 590 have similar ultimate tensile strengths of 590 MPa at quasi-static strain rates. Whereas finer grain size and dispersed carbides act as the strengthening mechanism in HSLA 590 steel, the dispersed martensite is the strengthening mechanism for DP 590. These microstructural differences, though leading to similar strength levels, can lead to differences in other

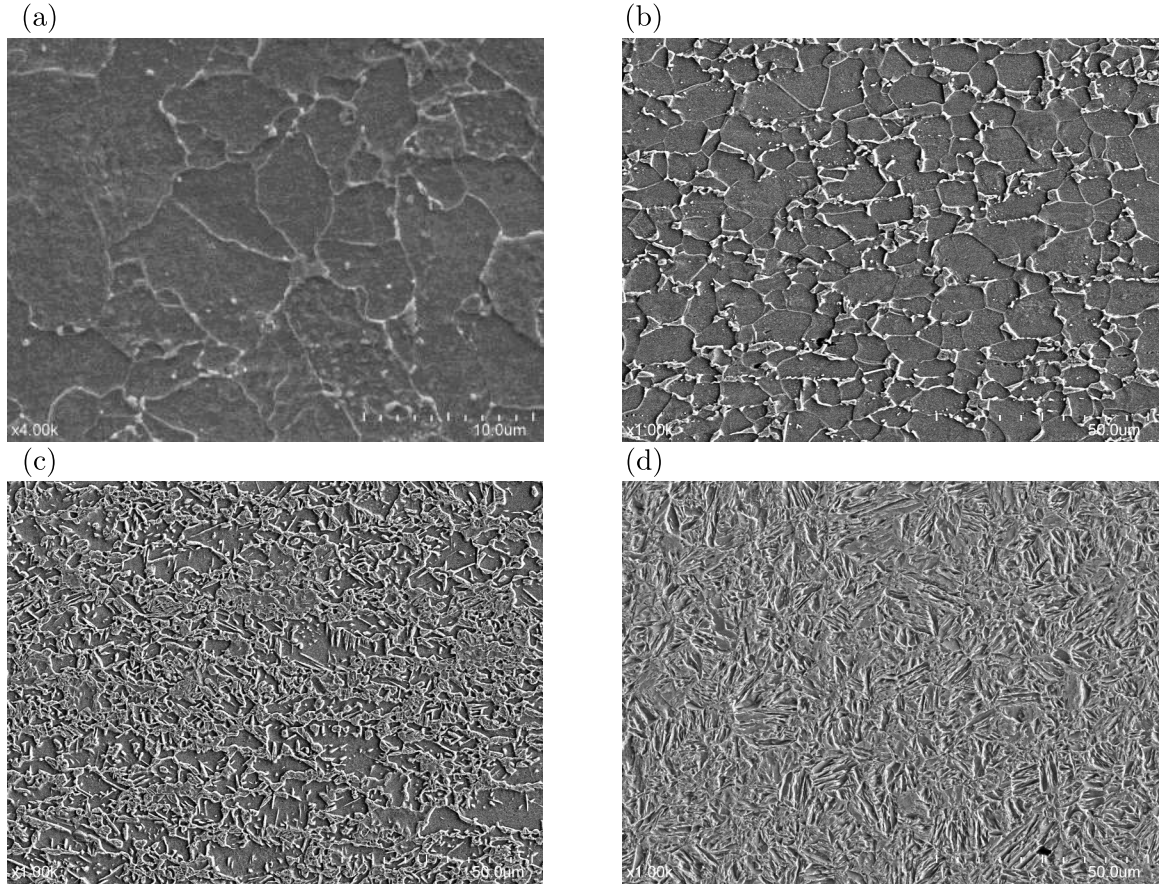


Figure 5.1: Representative SEM images of the different AHSS steels with different volume fractions of martensite. (a) HSLA-completely ferritic with dispersed carbides [85], (b) DP 590-with 30% martensite and ferrite matrix, (c) DP 980 NC-with 70% martensite and dispersed ferrite islands, (d) USIBOR-100% martensitic microstructure.

mechanical properties and fracture response, as discussed in the subsequent sections.

As shown in table 4.1, the volume fraction of martensite in DP 590 is  $\sim 30\%$  and in DP 980 is  $\sim 70\%$ . Thus, the phases in these steels are topologically reversed. Further, the mean free path in the matrix phase are also similar in both steels indicating that that the sizes of the connected ferrite phase in DP 590 and the connected martensite phase in DP 980 are of the same order. The bulk carbon content in the steels are also the same and thus martensite of DP 590, with more carbon partitioned in it compared to DP 980, would be stronger. Since USIBOR 1500 consists of only martensite, the mean free path estimations are not meaningful.

In addition to the volume fractions, the morphology of martensite was also observed to be different in all three steels with martensite. While some internal structure was observed in the martensite of both USIBOR 1500 and DP 980 NC, none were seen in DP 590.

These differences in the volume fraction and morphology of martensite manifest in different mechanical properties and are discussed next.

### 5.1.2 Quasi-static mechanical properties

Figure 5.2 shows the quasi-static engineering stress-strain curves for the four steels at a strain rate of  $10^{-2}/s$ .

Comparing HSLA 590 and DP 590, steels with a similar strength level, the influence of the introduction of a second harder phase from a single ferritic phase can be observed primarily in the work hardening differences. Where DP 590 characteristically exhibits high initial work hardening expected in DP steels [7, 8, 86], HSLA 590 shows an almost linear and horizontal behavior at low strains indicating lower work hardening. One factor which contributes to work hardening is the mobility of dislocations. While grain boundaries form the area of high dislocation density in HSLA steels, the ferrite-martensite interfaces are the areas of high dislocation density in DP 590 leading to stress localization in these areas [20, 87, 51]. Thus, HSLA can facilitate the strain across a larger volume, while the deformation in DP 590 needs to be accommodated by the generation of fresh dislocations in the ferrite grains. The generation of mobile dislocations followed by pinning can explain the higher work hardening in DP 590 compared to HSLA.

The increase in the volume fraction of martensite from DP 590 to DP 980 NC to USIBOR 1500 increases the ultimate tensile strength of the steel, as observed by several studies before [4, 52] with one explanation being the (modified) rule of mixtures [19]. In the current study, the tensile strength increases by  $\sim 50\%$  from DP

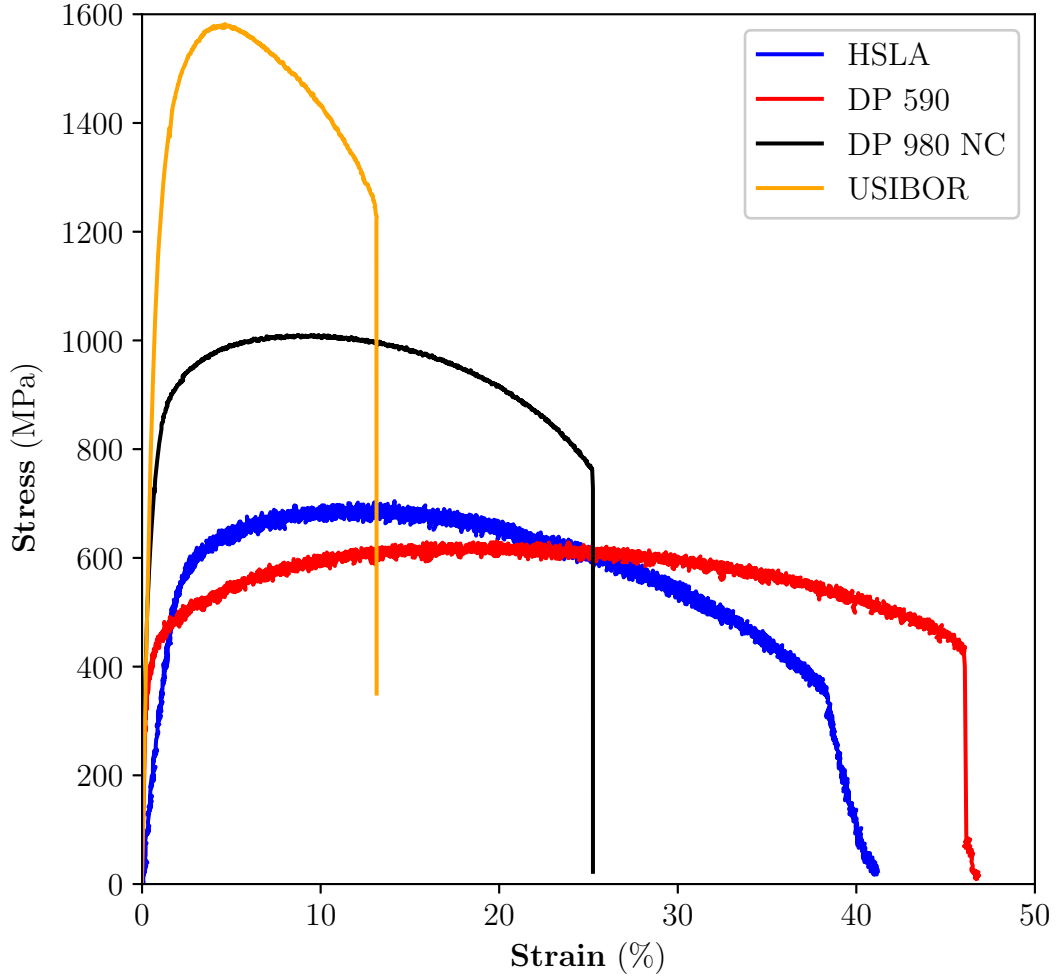


Figure 5.2: Quasi-static stress-strain response at strain rate of  $10^{-4}/s$  of HSLA (blue), DP 590 (red), DP 980 NC (black) and USIBOR (yellow). Miniature geometry used for HSLA 590 and DP 590 and REL geometry used for DP 980 NC and USIBOR 1500.

590 to 980 NC and by  $\sim 60\%$  from DP 980 NC to USIBOR 1500. This increase leads to a reduction in the total elongation of the steels.

Interestingly, although the total elongation of HSLA 590 is less than DP 590, the difference is not as substantial when compared to the difference between DP 980 NC and USIBOR. The differences in post uniform strain, however, are easily discernible.

In HSLA 590, a larger percent ( $\sim 75\%$ ) of the total strain is attributed to the post-uniform elongation compared to DP 590 ( $\sim 45\%$ ). This behavior is also observed in USIBOR 1500, also consisting of a single phase. The post uniform elongation occupied  $\sim 60\%$  of the total strain in USIBOR 1500. Thus, although the *nature* of the phase controls the strength and total elongation, the strain localization and onset of necking is influenced substantially by the *presence* of a second phase. With a single phase, the strain can be homogenized faster, leading to an earlier onset of necking, and thus, lower uniform strains, whereas in the DP steels, the strain is partitioned and localized, retarding the neck formation. This is also observed by other authors for steels containing multiple phases when compared to single phase microstructures [88, 89]. Since the fracture surface response is also a local phenomenon, the extent of the localized deformation post uniform strain can play a influential role.

### 5.1.3 Effect of strain rate on mechanical properties

The effect of the volume fraction of martensite on the strain rate sensitivity of DP steels has been studied by several authors [4, 90, 52]. The positive strain rate sensitivity of the DP steels has been attributed to the presence of ferrite, as completely martensitic steels did not show substantial sensitivity to strain rate.

Figure 5.3 shows the stress-strain curves of the four steel grades at the highest strain rate they were tested, which was in the range of  $10^3/s$ . Tensile tests on DP 980 NC were conducted on a strain rate range of  $10^{-6}/s$  to  $10^3/s$ , while the strain rates on DP 590, HSLA and USIBOR steels spanned a strain rate range of  $10^{-4}/s$  to  $10^3/s$ . The high stresses at initial strains are prevalent in all the steels and arise due to mechanical instabilities during the Hopkinson bar testing.

A positive strain rate sensitivity is associated with an increase in the stress, as the strain rate is increased. This is attributed to the increase in dislocation density with an increase in stress, leading to work hardening. However, a competing effect at



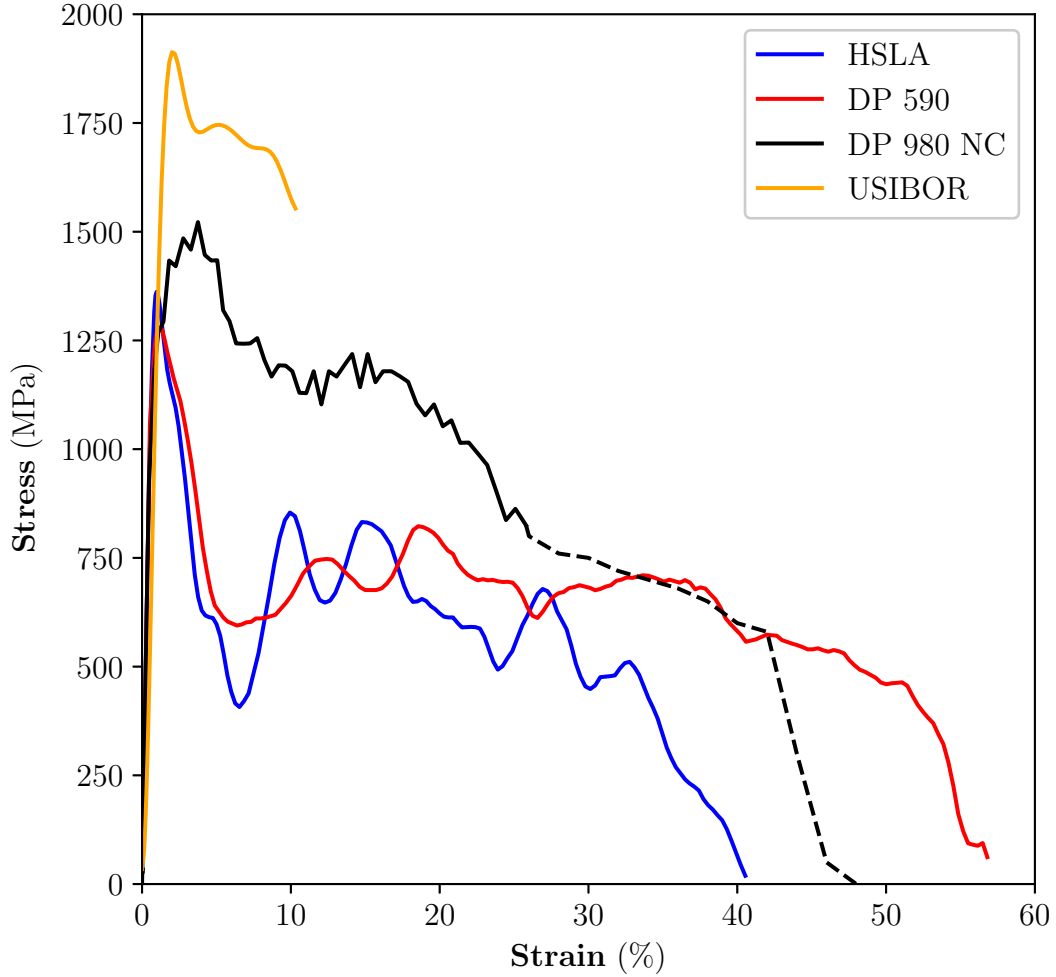


Figure 5.3: Plot showing the intermediate strain rate stress-strain response at the highest strain rates the AHSS steels were tested for. (a) HSLA and (b) DP 590, both at  $3 \times 10^3/s$ , (c) DP 980 NC at  $2.5 \times 10^3/s$  and (d) USIBOR at  $10^3/s$  strain rate. All the steels showed an initial peak in stress arising due to mechanical instabilities.

higher rates is that of thermal softening, which dictates that part of the energy at high deformation rates is converted to heat and leads to the softening of the material [4, 39, 33]. The subsequent strain rate sensitivity of the material which is dictated by the creation, interaction, and annihilation of dislocations travelling within the material is also a function of the underlying microstructure [91, 92, 93]. This is explained

by Kun et al. [93] using Orowan's equation (equation 35) which relates the plastic strain rate to the density of mobile dislocations and the average dislocation velocity. At higher strain rates, the dislocation velocity and density would increase, leading to higher stresses.

$$\dot{\epsilon}_P = \alpha b \rho_m \bar{v} \quad (35)$$

The study by Kun et al. attempts to explain the different strain rate sensitivities of different metals based on the sensitivity of dislocation movement to the stress in the given material. Thus, a distinction in the work hardening and strain rate sensitivity is made such that, while strain hardening dictates the *threshold* of dislocation movement, the strain rate sensitivity is dictated by how these dislocations move, interact, multiply, and annihilate.

The above discussions are pertinent to understanding the strain rate sensitivity of the four steels with different volume fractions of martensite. Figure 5.4 shows the variation of UTS with the log of strain rate for the four steels. All steels show some positive strain rate sensitivity of UTS. The *extent* of this sensitivity, however, varies with the underlying microstructure.

All four steels show the appearance of two different regimes in the strain rate sensitivity. One regime that operates up to a strain rate of 1/s with no substantial change in strength, and the other beyond 1/s, where the increase in strength is noticeable. These regimes are seen most clearly in DP 980 NC steels that were tested for the largest strain rate range. (The difference in the strength shown by DP 980 NC at a strain rate of  $10^2/s$  - marked by the dotted circle - can be attributed to noise created by load cell oscillations during the high strain rate tensile test.)

Figure 5.5 shows the change in the UTS from the lowest to the highest strain rate to help understand the *extent* of sensitivity that each of these steels shows to strain rate.

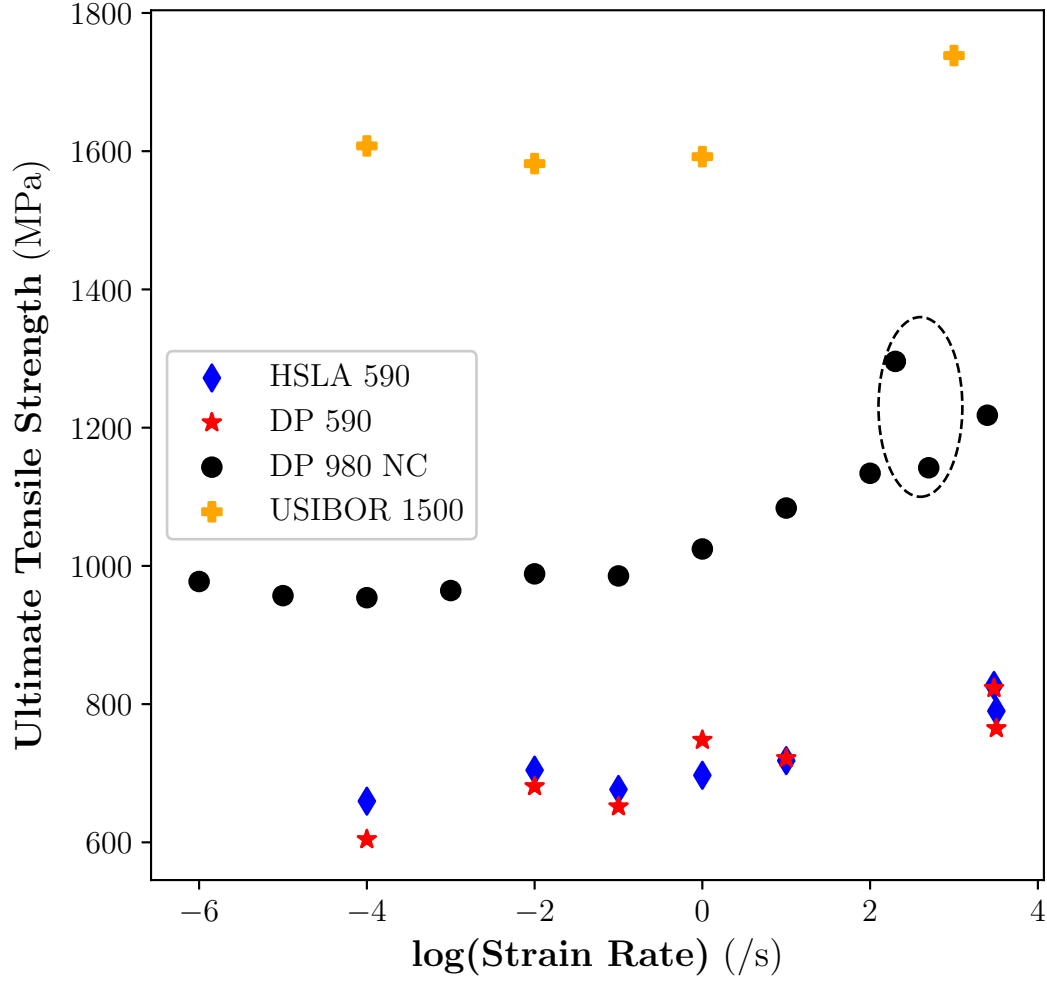


Figure 5.4: Plot showing the variation of the UTS of the AHSS steels as a function of strain rate. Two different regimes in the strain rate sensitivity were observed.

DP 590, HSLA 590 and DP 980 NC do not show a substantial difference in strain rate sensitivity of UTS. Overall, USIBOR with a completely martensitic microstructure shows the lowest strain rate sensitivity, with only a 5% increase, which is similar to that observed by other studies on completely martensitic steels [4, 94]. An interesting observation is the substantial increase (25%) in the UTS of DP 980 NC steel at the highest strain rate compared to USIBOR 1500. These observations confirm that the strain rate sensitivity of these steels is not a function of the volume fraction

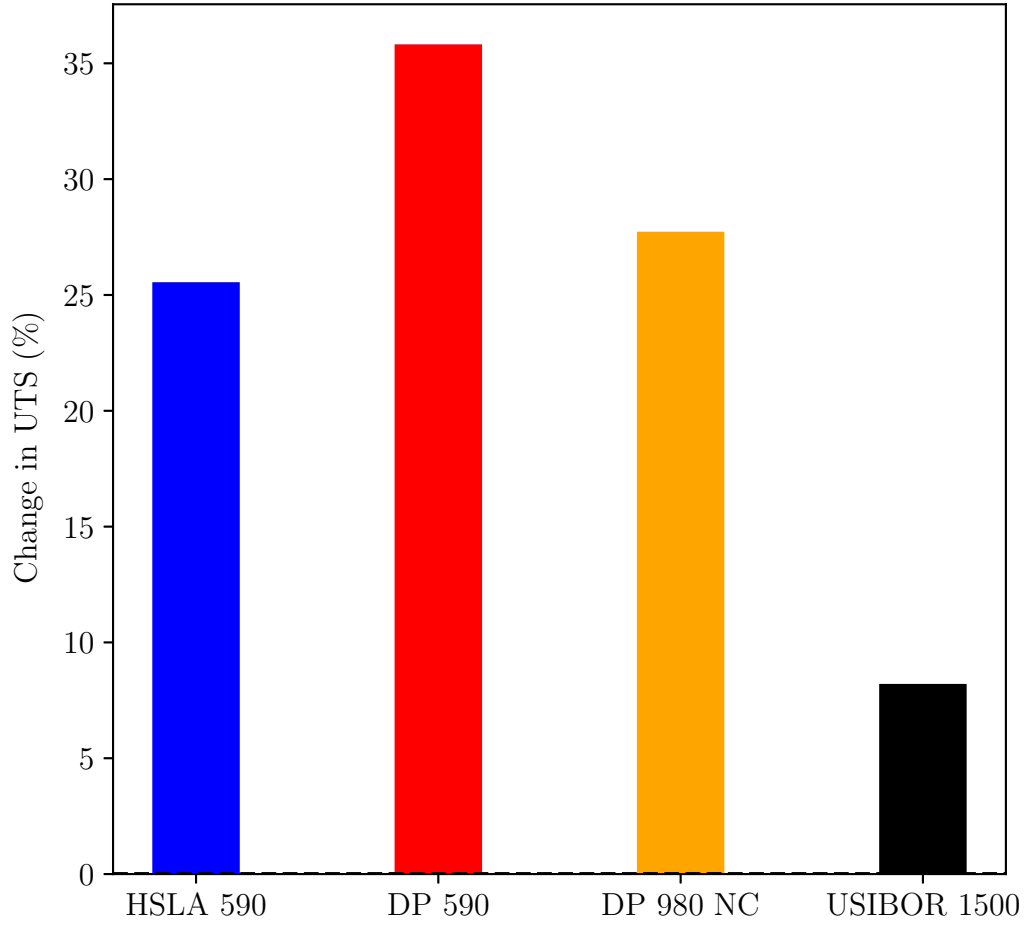


Figure 5.5: Plot showing the change in the UTS of the four steels from the lowest to the highest strain rate

of martensite alone, but dependent on other factors which control the movement of dislocations at a given strain rate.

The flow stresses of a material can be divided into three separate components to shed more light on the mechanisms controlling them [95]. The equation describing this is shown in equation 36, where  $\sigma_i$  is the athermal strain independent stress,  $\sigma^*$  is the thermal component of stress which depends on the strain rate and density of mobile dislocations, and  $\sigma_d$  is the component arising due to long range interaction of

dislocations and is a function of the total dislocation density within the material.

$$\sigma = \sigma_i + \sigma^* + \sigma_d \quad (36)$$

The differences in the strain rate sensitivity of these steels can thus be attributed to an insensitivity of the thermal stresses with strain rate, where the single phase HSLA 590 and USIBOR 1500 steels do not show marked effects of thermal stresses on strain rate. This also emphasizes the role played by the processing conditions on the strain rate sensitivity. Although both DP 980 NC and USIBOR 1500 contain a martensitic matrix, martensite in USIBOR 1500 had lower strain rate sensitivity. This can be due to a higher carbon content in martensite and varying processing conditions leading to differences in the resulting martensite properties of the two steels, which eventually control the strain rate sensitivity.

#### *Strain rate sensitivity of elongation*

Figure 5.6 shows the total elongations of the four steels as a function of strain rate. Although, no single clear trend is observed, the behavior of DP 590, 980 NC and USIBOR 1500 appears to be similar as a function of strain rate. On the contrary, HSLA 590 steels largely show an increase with an increase in strain rate.

The increase in the total elongations of the DP and USIBOR steels is also observed after a certain threshold of strain rate, similar to the stresses.

Figure 5.7 (a) shows the change in the total elongation at the highest strain rate for the four steels. DP 980 NC shows the highest strain rate sensitivity, as the elongation more than doubles at the highest strain rate, followed by USIBOR 1500, which shows a 40% increase. All four steels however, show a positive sensitivity in both stresses and elongations, indicating that under strain rates that are representative of crash, these steels show an improved behavior in both strength and elongation compared to the quasi-static strain rates. This increase in the total elongation in a large part

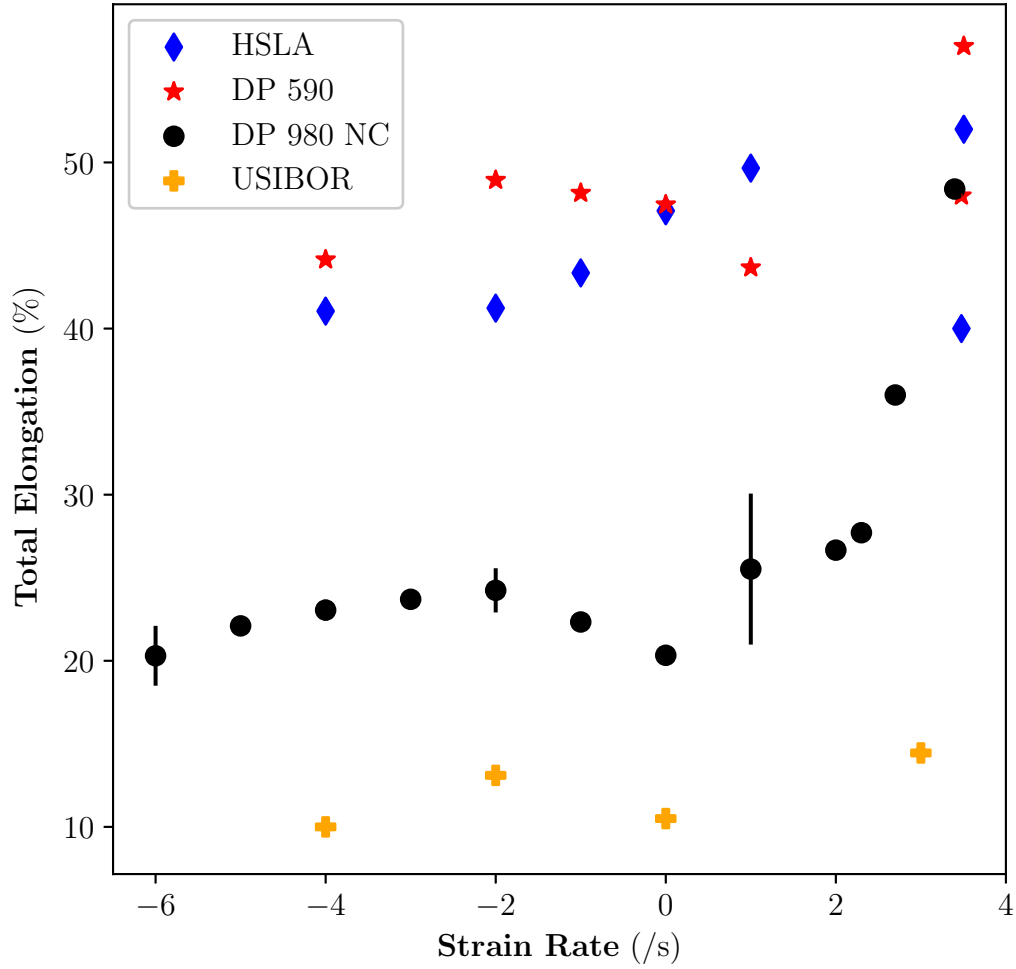


Figure 5.6: Plot showing the strain rate sensitivity of the total elongation of the AHSS steels. All steels showed an increased elongation at intermediate strain rates that could be attributed partially to adiabatic heating.

is attributed to the increase in the post-uniform elongation at higher strain rates, as shown in figure 5.7 (b).

Several studies have attributed the increase in strains at higher strain rates to thermal softening effects resulting from the adiabatic heating of the steels at high strain rates [4, 52]. Additionally, the deformation at higher strain rates is also localized [55]. Based on figure 5.7(a), steels with the higher volume fraction of martensite,

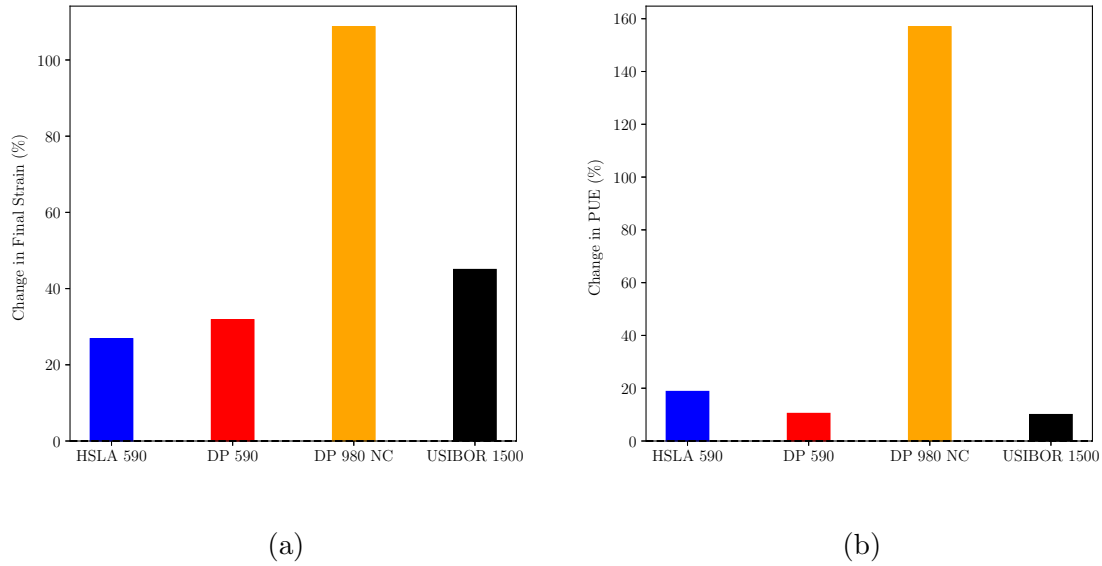


Figure 5.7: Plots showing the change in the (a)total elongation and (b) Post-Uniform Elongation(PUS) of the four steels from the lowest to the highest strain rate

namely DP 980 NC and USIBOR 1500, show a higher sensitivity to strain rate, indicating that the global plasticity of these microstructures is increased at the higher strain rates. Interestingly, DP 980 NC shows a greater sensitivity compared to DP 590 which could suggest the influence of the carbon partitioning in martensite and the connectivity of martensite in establishing the global plasticity of the DP steels at higher strain rates.

While these discussions pertain more to the global scale mechanisms, the creation of fracture surfaces are dictated by local deformation mechanisms and may be different from those operating at the global scale. These local mechanisms can be understood through a discussion on the data obtained by observing the fracture surfaces, as presented in the subsequent section.

#### 5.1.4 Fracture response

The fracture response portrays the effects of deformation and failure occurring at the local scale and provides insight on the local level mechanisms operating in the

steels. While all four steels showed large areas of the fracture surface occupied by dimples indicating the primary mechanism to be that of void nucleation and growth arising from local plasticity, other features alluding to secondary mechanisms are also observed. The prominent features, other than dimples, were pullouts, flat featureless regions and long secondary cracks that often span the width of the fractured surface. Figure 5.8 shows the representative fracture surfaces of HSLA 590, DP and USIBOR 1500 steels. The features observed are largely classified into those that have been formed due to ductile and brittle mechanisms. While dimples are associated with plasticity and are classified as ductile features; pullouts, facets and secondary cracks are associated with brittle mechanisms.



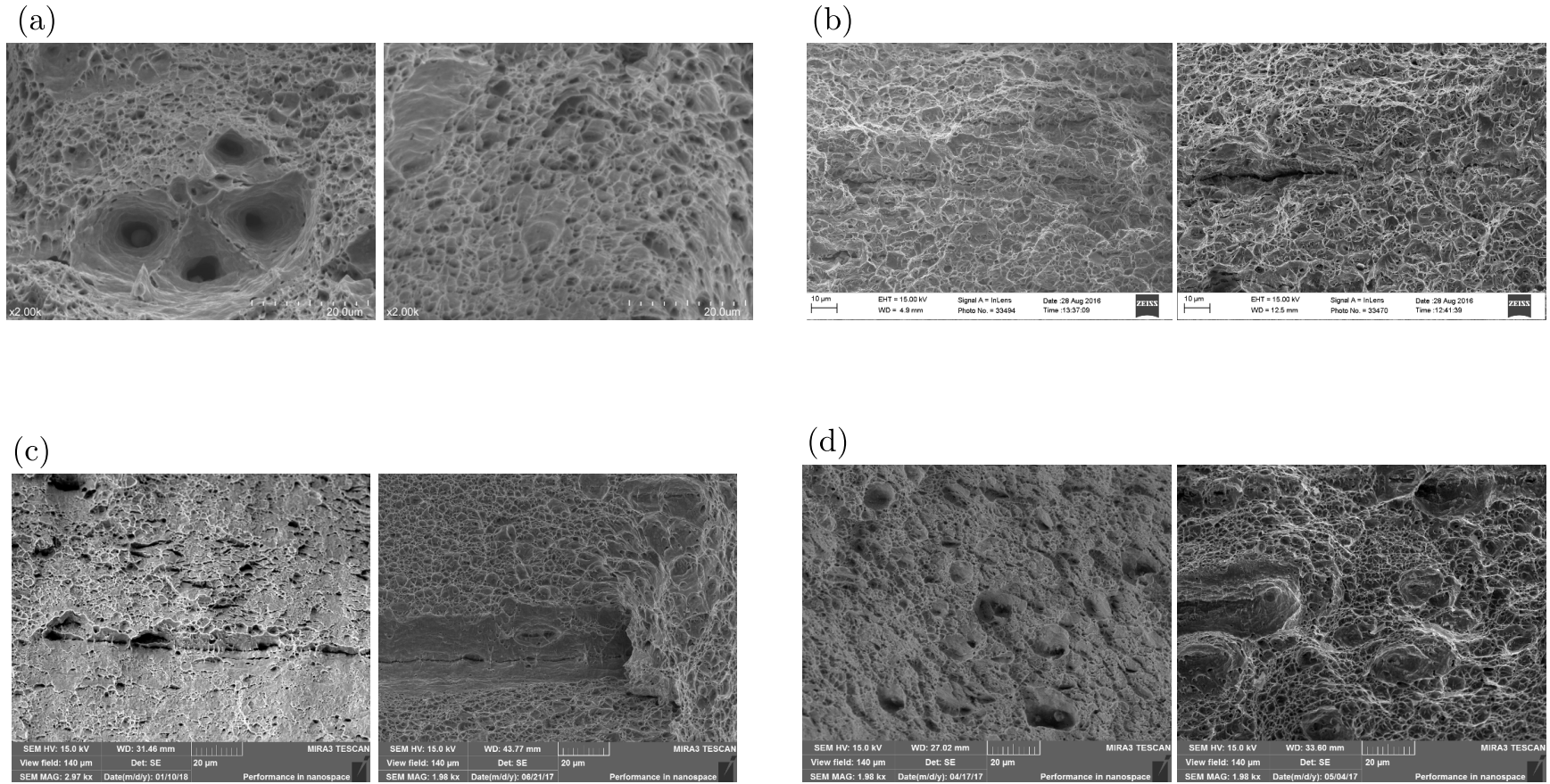


Figure 5.8: Representative SEM images of the fracture surfaces at the lowest strain rate and the highest strain rate achieved using the hopkinson bar for (a) HSLA, (b) DP 590, (c) DP 980 NC and (d) USIBOR. The secondary cracks were observed the most in the DP steels which had a connected martensitic phase.

Qualitatively comparing the fracture surfaces of DP 590 and HSLA 590 which showed similar strength and elongation behaviors, a marked difference in the fracture response, particularly in their brittle fracture mechanisms, is observed. Upon comparing the  $10^{-4}/s$  fracture surfaces at low magnifications, the distinct deformation difference observed in the form of higher post uniform elongation of HSLA 590 steels was confirmed by the smaller fracture surface area compared to DP 590, as shown in figure 5.9. Even at these low magnifications, the large pullouts in HSLA 590 and the longer secondary cracks in DP 590 which form the respective brittle mechanisms in these two steels can be easily discerned. The secondary cracks in DP 590 run parallel to the rolling direction and are present at all strain rates. Previous studies have attributed these cracks to fissures produced due to manganese sulphide inclusions [34], or shear assisted fracture [96], segregation of elements in the center of the steel [32], or cleavage like long bands that could lead to premature fracture [33]. The absence of these cracks in HSLA steels indicates that this feature is formed due to the presence of a ferrite-martensite interface.

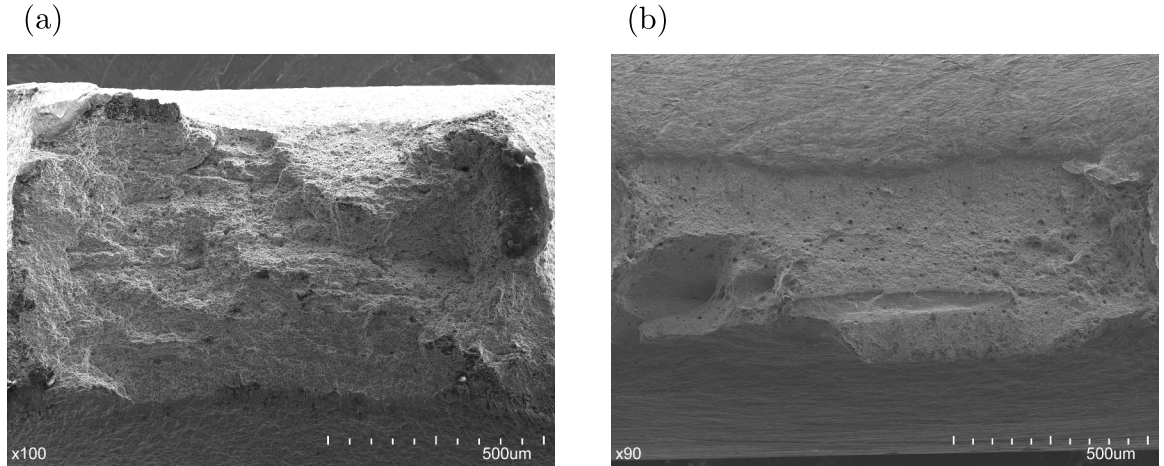


Figure 5.9: Representative low magnification SEM images of the fracture surfaces for (a) DP 590, and (b) HSLA 590. HSLA 590 shows a considerable necked region compared to DP 590

The estimated area fractions of the dimpled regions is higher in DP 590 ( $\sim 85\%$ )

steels at all strain rates compared to HSLA 590 steels with  $\sim 65\%$ . Thus, the microstructure of DP 590 with a harder phase shows a higher amount of local plasticity while retarding the neck formation at the global scale. This can be explained by trying to understand the void initiation sites in both the steels and the stresses required for the formation of a void. Equation 37 shows the model proposed by Goods and Brown [97], where  $\sigma_f$  is the flow stress that is a function of the microstructure and is impacted by the presence of inclusions or particles and mechanisms that increase the dislocation density,  $\sigma_c$  is the local stress and  $p$  is the triaxial stress.  $\sigma_I$  is the particle-matrix interface strength, which when surpassed can lead to the formation of a void.

$$\sigma_f + \sigma_c + p \geq \sigma_I \quad (37)$$

It can be assumed that both homogeneous (voids originating at regions with high dislocation density) and heterogeneous (voids nucleating in areas with inclusions, precipitates or other discontinuities) void nucleation take place in these steels [98].

Thus, the primary heterogeneous void nucleation sites in HSLA 590 and DP 590 are the inclusions in the former and interfaces between martensite and ferrite in the latter. As discussed earlier, DP 590 steels show stress/strain localization at the interfaces. This localized stress corresponds to  $\sigma_c$  which would then be substantially higher in DP 590 when compared to HSLA 590. Additionally, the presence of these interfaces and martensite, in general, increases the overall dislocation density in DP 590 compared to HSLA 590, contributing to higher stresses that exceeds the threshold for void nucleation in the former. The high area fraction of voids in HSLA 590, in general, can be attributed to the contributions made by the higher stress triaxiality factor  $p$ . DP 590 would also have a substantially higher amount of Geometrically Necessary Dislocations (GNDs) due to the presence of martensite. As observed in figure 5.2, DP 590 shows higher stresses post uniform elongation which is the regions

that is concerned with the generation of the fracture surface. Thus, the component of the flow stress concerned with the Goods and Brown model,  $\sigma_f$  for HSLA 590 is lower compared to DP 590 at higher strains. A combination of higher flow stresses and higher local stresses thus increase the tendency of DP 590 to cross the threshold for void nucleation in higher areas compared to HSLA 590, leading to higher area fractions of dimpled regions.

Since the threshold for void nucleation is crossed at lower strain rates, a further increase in strain rate does not affect the area fraction of dimples and thus, they are insensitive to strain rate.

Comparing the behavior of metals at high strain rates to that displayed at lower temperatures is a common practice since both conditions usually show an increase in strength and the tendency towards brittle fracture. At low temperatures particularly, steels display a ductile to brittle transition temperature (DBTT) which can be expected at higher strain rates as well. Looking at the current response of HSLA 590 and DP 590 steels, it can be assumed that the strain rates discussed so far are not of the magnitude to initiate brittle fracture in these steels. Or to continue the analogy, the fractures observed are those that are above the DBTT. A more detailed insight on this analogy for DP 590 and DP 980 NC steels will be provided later in this section.

The fracture surfaces of DP 980 NC and USIBOR 1500 containing a substantial amount of dimples indicated that the microstructure with a martensite matrix can also display local plasticity by void nucleation. Continuing the explanation used for DP 590 and HSLA 590, the stress required to generate voids in both DP 980 and USIBOR 1500 can be attributed to a high  $\sigma_f$  stress in both these steels due to the high dislocation density of martensite and in the case of DP 980 NC, the interfaces between the phases can increase the localized stress as well. Upon quantifying the area fractions of the dimples, it is seen that DP 980 NC contains only  $\sim 35\%$  of the

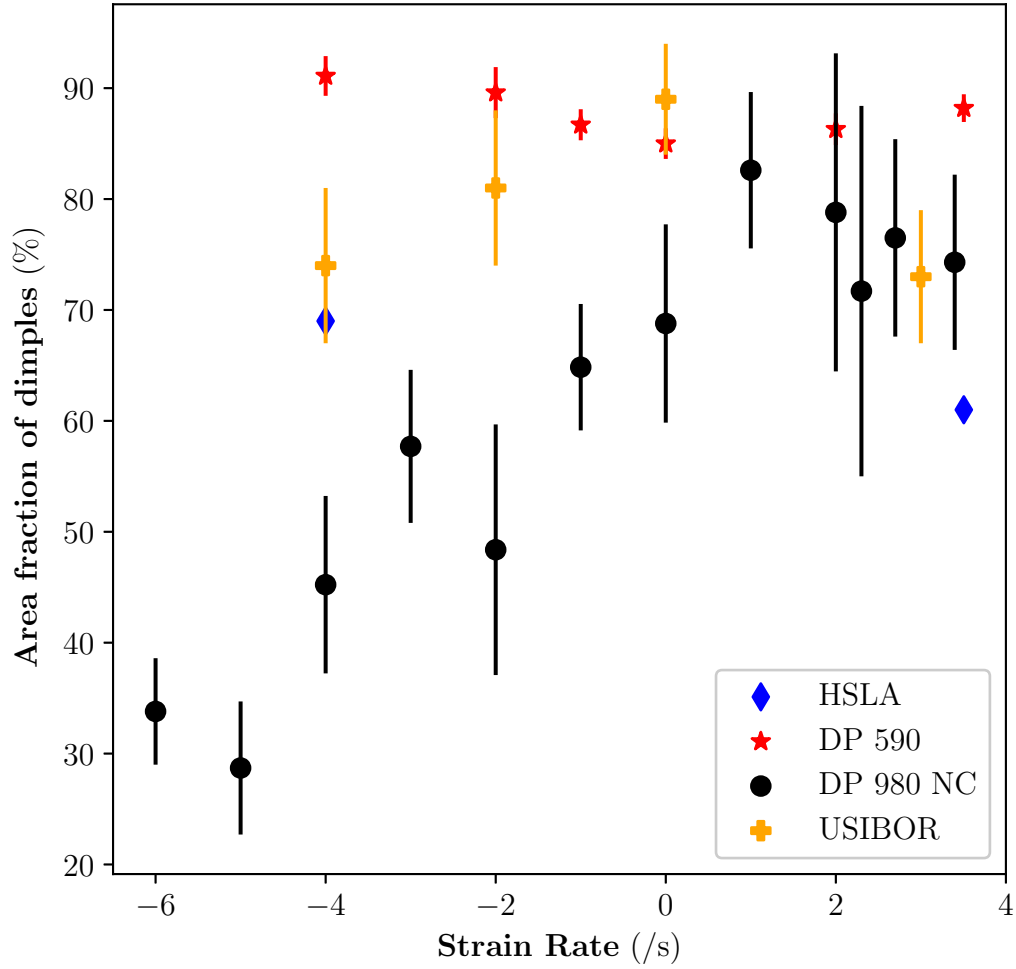


Figure 5.10: Plot showing the area fraction of dimples in the four steels as function of strain rate. DP 980 NC shows the highest sensitivity to strain rate.

area occupied by voids while USIBOR 1500 contains  $\sim 65\%$  of the area occupied by dimples. Thus, at lower strain rates, the stresses required to form voids is exceeded locally in fewer areas and as such the brittle mechanisms dominated in DP 980 NC. Additionally, the long secondary cracks observed in DP 590 are also observed in DP 980 and are largely absent from USIBOR 1500. Thus, the presence of secondary cracks formed a prominent fracture mechanism only in the steels with a continuous and connected secondary phase. Observations also indicate that these secondary cracks

are more prevalent in DP 980 NC steels when compared to DP 590, indicating that the presence of higher amounts of martensite bands in the microstructure accentuates this fracture mechanism in the DP steels. In addition to the secondary cracks, the formation of shear like facets is also observed only in DP 980 NC. Thus, as the matrix changes from ferritic to martensitic, the shear like fracture increases, indicating that these features can be formed due to a connected network of martensite in the microstructure.

Figure 5.10 shows the strain rate sensitivity of the area fraction of dimples in all the four steels. Only DP 980 NC showed a sensitivity with strain rate. With an increase in strain rate, the area fraction of voids increases. This can be explained using Goods and Brown model [97] discussed before. With an increase in strain rate, an increase in the flow stress is observed, which implies an increase in  $\sigma_f$  component. Additionally, as the strain rate increases, the deformation becomes highly local and the higher strain rates also show an increased post-uniform elongation indicating a corresponding increase in the  $\sigma_c$  and  $p$  stresses. Thus, the threshold for the formation of voids is crossed in multiple areas, leading to the high area fractions of dimples observed. Interestingly, the area fraction plateaus at the higher rates which implies that the threshold was reached and that the dependence of the component stresses discussed earlier do not have a linear dependence to the logarithm of strain rate. Another interesting observation is the heterogeneity of the fracture surface in DP 980 NC steels. This can be observed by looking at the error bars on the area fraction of dimples which is averaged over all fields of view measured. The large error bars indicate that there are some fields of view which are entirely dominated by brittle mechanisms while other consisted only of dimples. This heterogeneity increases at higher strain rates, also implying that the operative mechanisms are very local and can change from one field of view to the other, or a distance of  $100\mu m$ . Higher heterogeneity is observed in the steels dominated by martensite matrix while DP 590

and HSLA show a more homogeneous fracture response.

Continuing the analogy between high strain rate and temperature, the behavior of DP 980 NC suggests that a more ductile behavior can be expected at lower temperatures and that the steel may need to be exposed to an even higher strain rate to simulate the lower temperatures and resulting DBTT. The increase in local and global plasticity at lower temperatures in DP steels has also been observed in other studies [99]. Additionally, the elastic-plastic fracture toughness ( $J_{IC}$ ) of steels has been observed to go through a minimum with a decrease in testing temperatures [100].

A greater understanding on this difference between the strain rate sensitivities of the fracture mechanisms of the two DP steels can be understood by subjecting them to higher local strain rates and observing the fracture generated using spall tests.

#### 5.1.5 Fracture response of DP steels under dynamic tensile (spall) failure

Plate impact tests conducted on DP 590 and DP 980 NC at 600m/s, exposed the steels to strain rates of the order of  $10^6/s$ . Although, the direction of loading was different from that of the quasi-static and intermediate strain rates, the focus of the following discussion is to understand the effect of very high *local* strain rates on the fracture response of DP steels with varying volume fraction of martensite.

Just like the quasi-static and intermediate strain rate flow stresses, the spall strength of DP 590 is also lower than DP 980 NC steel as shown in the previous chapter. Figure 5.11 shows the spalled fracture surfaces of DP 590 and DP 980 NC at low magnifications. Both steels show a largely brittle fracture. DP 980 NC, however, still shows a highly heterogeneous behavior indicating that different areas of the fracture were subjected to different local fracture mechanisms. The presence of large amounts of quasi-cleavage fracture in both the steels suggests that a transition from ductile to brittle fracture occurs with a local increase in strain rates, which when

comparing to deformations at low temperatures would indicate that these strain rates simulate temperatures below the DBTT. An interesting observation is the presence of higher area fraction of voids in DP 980 NC near the long horizontal bands, whereas the fracture surface of DP 590 is almost entirely devoid of voids. This can be an effect of lesser carbon being partitioned in martensite in DP 980 NC, leading to some plasticity at these high strain rates. The plasticity in the martensitic phase is observed in the incipient spalled sample showing local bending of the martensite bands (figure 4.36).

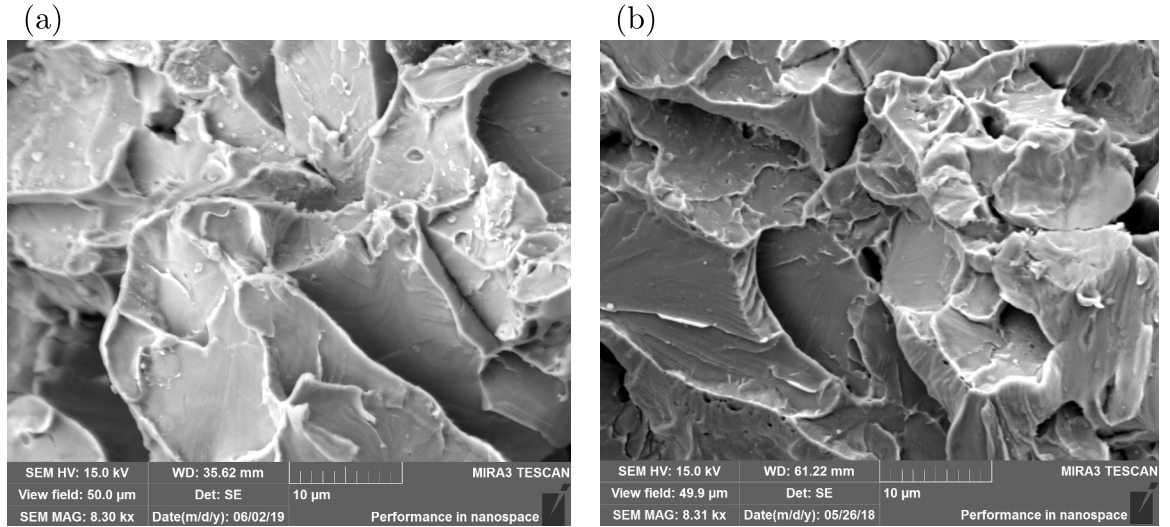


Figure 5.11: Representative SEM images showing the spalled fracture surfaces of (a) DP 590 and (b) DP 980 NC.

The recompression curves from the free velocity traces have been used by some investigators to explain the differences in fracture being dominated by nucleation or growth mechanisms [101, 67, 66]. Figure 5.12 shows the time and velocity adjusted recompression curves of DP 590 and DP 980 NC. DP 590 shows a more distinct nucleation region which is determined by the faster rise followed by slope change, leading to the growth or coalescence stage. DP 980 NC, on the other hand, shows a faster fracture compared to DP 590 after the slope change. This data does not particularly align well with the area fractions of voids observed. One possible explanation could



be that the free velocity trace is a point measurement and may be capturing a very local event compared to the quantitative fractography which covers a larger area.

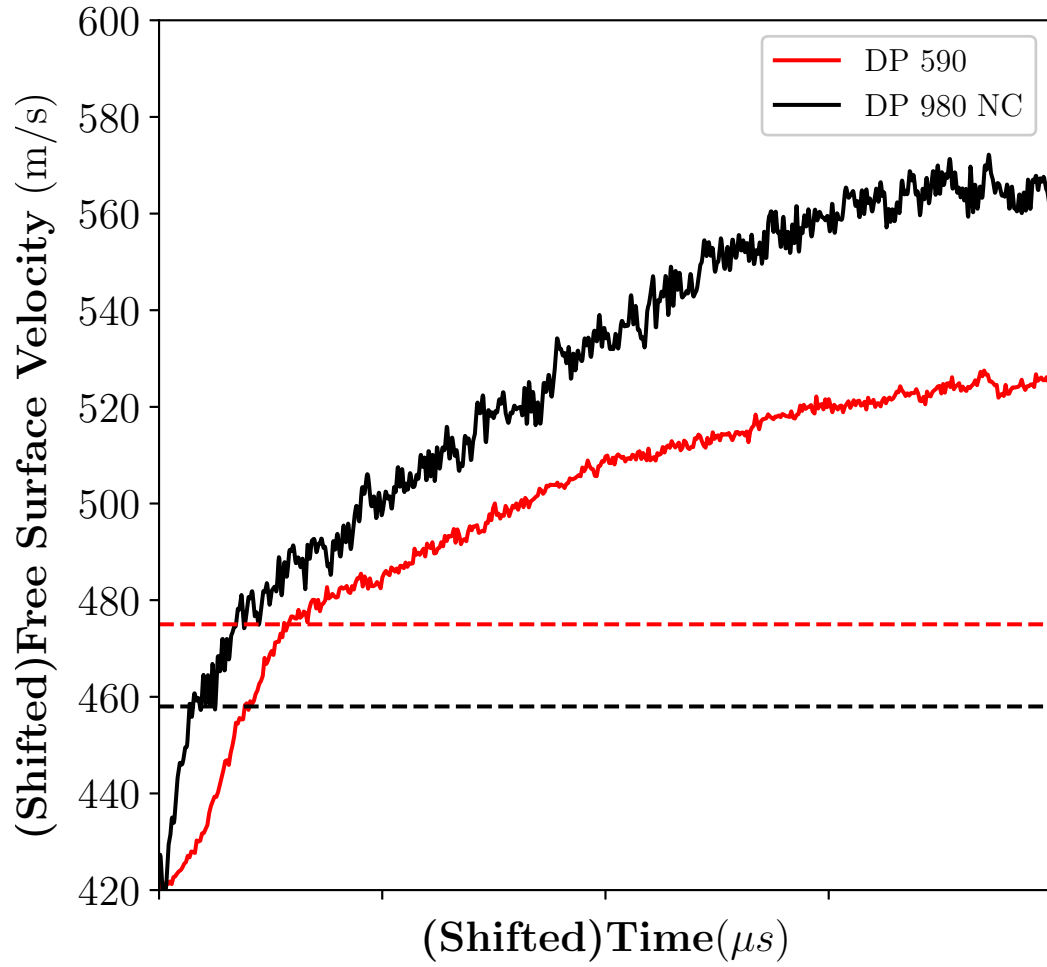


Figure 5.12: Plot showing the time and velocity adjusted recompression curves of DP 590 and DP 980 NC. DP 590 shows a longer void nucleation region.

More information of the mechanisms of fracture and deformation can be obtained by observing the fracture profiles and will be discussed next.

### *Deformation response and fracture profile*

The deformed microstructures and fracture profiles of DP 590 and DP 980 NC at different strain rates depicted in chapter 4, section 4.4 are used to understand the differences in the deformation behavior with increasing volume fraction of martensite.

As seen in figures 4.20 and 4.21, both steels consisted of voids originating due to interfacial decohesion and martensite cracking, surrounded by heavily deformed microstructures. The deformation of the individual phases in DP 590, measured by obtaining the aspect ratios, provided information on the strain partitioning between the two phases present. The aspect ratios in ferrite show a slight increase at higher strain rates suggesting that a larger fraction of the strain is partitioned in it. However, the aspect ratios of martensite also showed an increase from the undeformed state and thus underwent plastic deformation. Similar behavior was observed qualitatively in DP 980 NC steels in the form of elongated ferrite islands and harder phase bands.

Long cracks showing the cracking of martensite and subsequent interfacial decohesion are observed in the fracture profiles of DP 980 NC at quasi-static strain rates. The cracking of martensite, although seen in DP 590, was not seen to propagate far down into the deformed microstructure as in DP 980 NC, figure 4.21 (b) and (c). The presence of a ferrite matrix can lead to these cracks being arrested in DP 590, whereas in DP 980 NC, a connected harder phase led to the propagation of these cracks by interfacial decohesion. Thus, the presence of a connected martensitic phase will propagate the crack, and coalesce the voids formed, promoting interfacial decohesion.

Qualitatively, the fracture profiles of both DP 980 and 590 show a more deformed ferrite and martensite phase at the highest strain rate. This aligns well with the increased PUE observed in both the steels. The fracture profile of DP 590 is also observed to be qualitatively rougher when compared to DP 980 NC, which comprised of a few jagged valleys at  $\sim 45^\circ$ . These differences can explain the high area fraction

of dimples in DP 590 and the presence of shear like facets in DP 980 NC.

## 5.2 Effect of protective coating and decarburized layers

The addition of galvanized coatings and decarburized layer alters the microstructure of DP 980 GAN and GAD from that of DP 980 NC. These changes result from changes in both alloying chemistry and processing conditions. The discussions in this section help understand if the addition of the galvanized coating and decarburized layers change the strain rate behavior and fracture response of these steels and if so, are the changes observed beneficial under high strain rates, or not.

Although, the volume fraction of martensite (martensite, bainite, retained austenite and carbides) remains the same in all the three DP 980 steels, there are differences in both distribution and morphology of the same in the three steels. As shown chapter 4, section 4.1, the microstructure of DP 980 NC is comprised of a matrix of martensite with dispersed islands of ferrite. DP 980 GAN also comprises of a martensitic matrix, however, the extent of banding of martensite was determined to be higher in this steel. DP 980 GAD consisted of a co-continuous microstructure with martensite dispersed, save a few connected bands observed in the center of the steel. Additionally, the microstructure of the coated steels, i.e, DP 980 GAN and DP 980 GAD are finer than DP 980 NC as observed qualitatively, and confirmed by the higher  $S_V$  values. The interfaces between ferrite and martensite are also different in the uncoated and galvanized steels. These interfaces are smooth in NC, whereas in GAN, were rough and jagged. While this observation is harder to make in the DP 980 GAD steel due to highly dispersed harder phase, the regions in the center of the steel with a connected harder phase showed a rougher interface similar to that of GAN steel.

### 5.2.1 Effect on mechanical properties

#### *Quasi-static strain rates*

Figure 5.13 shows the quasi-static stress-strain response at  $10^{-2}/s$ . DP 980 GAN and GAD show higher tensile strengths of the three steels, which can be attributed partially to the presence of higher amounts of chromium and molybdenum in these steels, both of which generally aid in increasing the tensile strength. This increase in tensile strength may not have a significant contribution from the refinement of the microstructure in the coated steels since the difference in DP 980 GAN and GAD steels is negligible, even though GAD had a dispersed and finer microstructure. Furthermore, the addition of the coating layers and the decarburized layer do not seem to impact the final elongations significantly, indicating that the global elongation is insensitive to these changes at quasi-static strain rates.

### 5.2.2 Strain rate sensitivity

Figure 5.14 shows the stress-strain response of the three DP 980 steels at the highest strain rate of  $2 * 10^3/s$ . The difference in strength observed under quasi-static strain rates is absent at the intermediate strain rates. Thus, DP 980 NC shows the maximum increase in strength as a function of strain rate.

Figure 5.15 shows the UTS as a function of the logarithm of strain rate. The two different regimes in the strain rate sensitivity discussed in the previous section for the four steels can be observed in DP 980 GAN and GAD steels as well. However, the increase in the UTS of GAN and GAD steels is lesser than that of NC. Thus, the strain rate sensitivity is affected in GAN and GAD steels which consist of a more composite structure. However, the addition of a softer decarburized layer and a dispersed harder phase does not alter the strain rate sensitivity.

The differences in the sensitivities can be explained with the help of equation 36

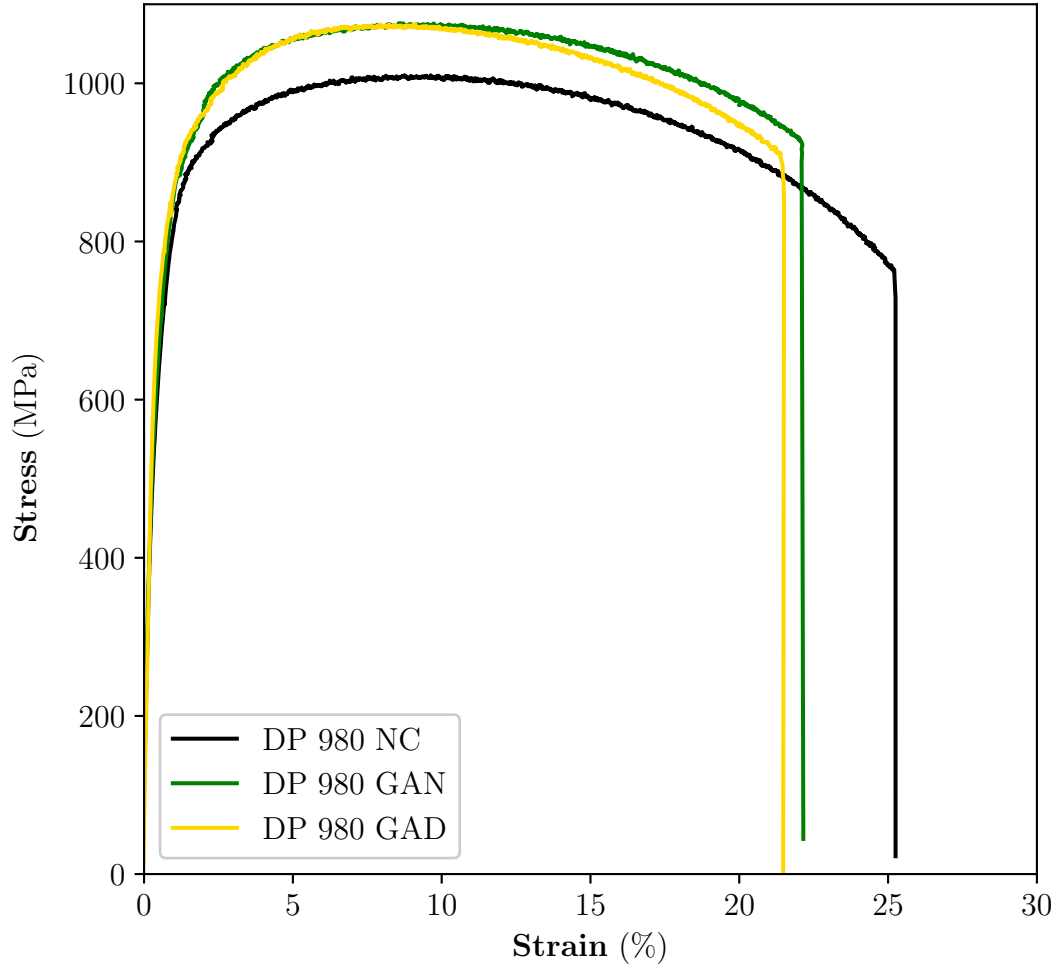


Figure 5.13: Quasi-static stress strain response of the three DP 980 grade steels. The increase in strength can be attributed to a finer microstructure in the case of DP 980 GAN and GAD. This refinement did not affect the total elongation of the steels at this strain rate.

in the previous section. Even in GAN and GAD, the thermal stress component of the flow stress,  $\sigma^*$  is less sensitive to the corresponding component in DP 980 NC. Thus,

$$\Delta\sigma_{DP980NC}^* > \Delta\sigma_{DP980GAN}^*, \Delta\sigma_{DP980GAD}^*$$

The effect of the composite microstructures is more apparent when comparing the

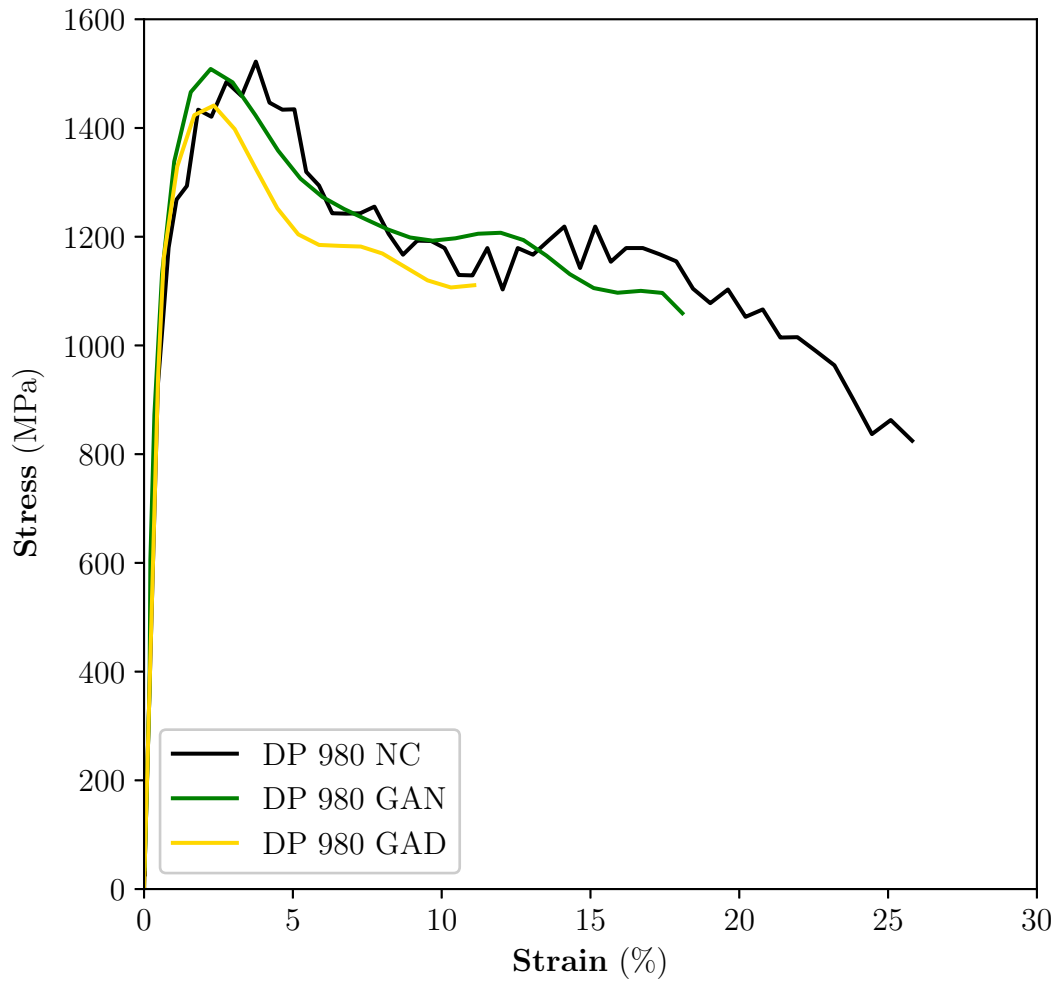


Figure 5.14: Intermediate stress strain response of the three DP 980 grade steels. No difference in strength was observed at these strain rates, however, the elongation in DP 980 NC was the highest.

total elongations at higher strain rates. Figure 5.16 shows the variation of the total elongation of the three steels as a function of the logarithm of strain rate. While DP 980 NC shows a significant increase in the final elongation, both DP 980 GAN and GAD remain largely insensitive to strain rate. Thus, the increase in the total elongation in DP 980 NC cannot be completely attributed to thermal softening due to adiabatic heating since DP 980 GAN and GAD, with similar bulk heat capacities but

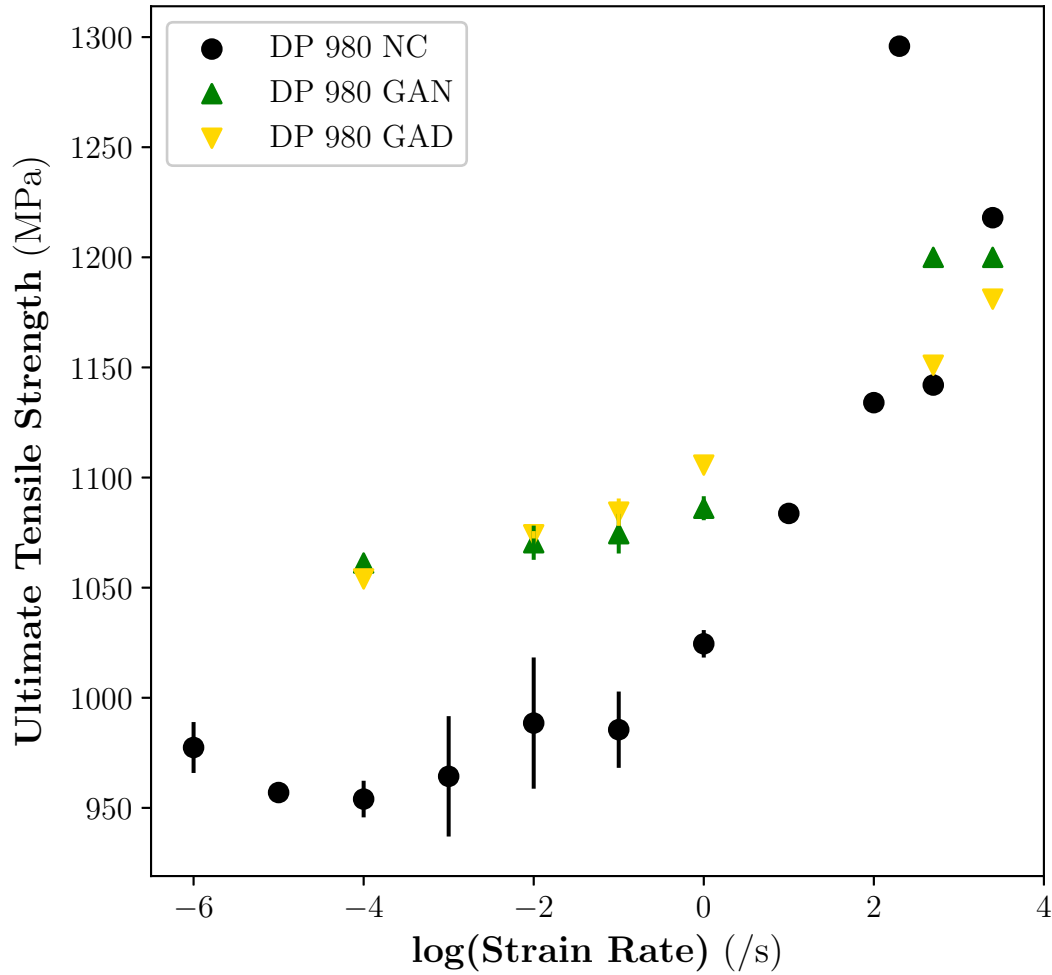


Figure 5.15: Plot showing the variation of UTS with the logarithm of strain rate for DP 980 NC, GAN and GAD. DP 980 NC shows the highest increase in strength as a function of strain rate.

with a composite microstructure, do not show global plasticity, despite being exposed to similar strain rates.

The uniform elongation and PUE behavior also showed a similar response in all three steels up to the intermediate strain rates. Interestingly, at intermediate strain rates, the uniform elongation increases for all three steels indicating a more uniform deformation at the higher strain rates. Thus, irrespective of the initial microstructure,

the plasticity and strain partitioning between the phases is improved at intermediate strain rates for all three steels.

At intermediate strain rates the PUE behavior of DP 980 NC is distinctly different and significantly larger compared to GAN and GAD steels. This indicates that the deformation in NC is highly local when compared to GAN and GAD. Where previous studies have indicated that the presence of an equiaxed harder phase or a tempered harder phase can lead to an increase in the uniform elongation at quasi-static strain rates,[3, 29], in the current study, these effects are not observed at high strain rates when comparing DP 980 NC and GAD.

An important observation is that the presence of a softer decarburized layer does not alter the behavior of coated steels significantly. Thus, the current study helps to establish that the bendability of galvanized DP 980 steels can be improved by adding the decarburized layer without any adverse affects at high strain rates.

The differences in the strain rate sensitivity of the local deformation of these steels can be better understood by observing the fracture surface and local operative mechanisms and is discussed ahead.

### 5.2.3 Fracture surface response

The fracture surface response, which gives a more local operative mechanism shows differences based on the distribution of martensite and change in strain rate. As discussed in the previous chapter, the features observed in all three DP steels are similar, but the *extent* of them varies.

The area fractions occupied by different features is expected to be dictated by the local stress conditions and the mechanism that facilitates the local deformation under the given stress and the time it is exposed to.

Figures 4.17, 4.18 and 4.19 show the area fractions of the different features as a function of the logarithm of strain rate. While the formation of voids in the coated and



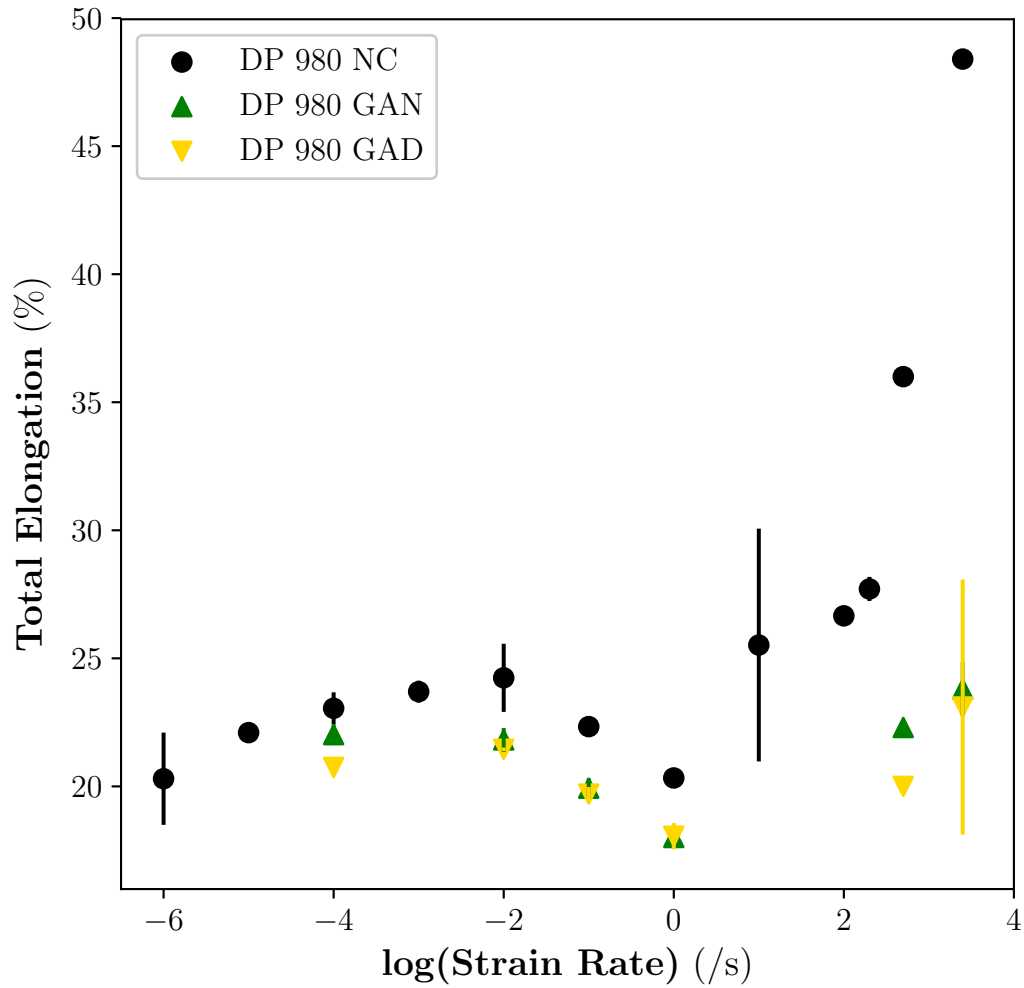


Figure 5.16: Plot showing the variation of total elongation with the logarithm of strain rate for DP 980 NC, GAN and GAD. DP 980 NC shows the highest increase in elongation as a function of strain rate, while GAN and GAD remain largely insensitive.

uncoated steels shows differences in the strain rate sensitivity, the brittle mechanisms (comprising of facets with and without secondary cracks) shows a similar strain rate sensitive behavior.

As discussed in the previous section, the formation of voids is dictated by the local stresses surpassing the interfacial strength to create voids, as per the Goods and Brown model [97]. The brittle mechanisms, however, compete against each other as

a function of strain rate, and the secondary cracks grow largely at the expense of the facets at higher strain rates. Thus, the formation of facets is favorable under low stresses and strain rates, where the material has more time to deform. As the strain rate is increased and the time for fracture is significantly reduced, facets are replaced by the formation of the secondary cracks. A hypothesis based on the stress required to initiate the local mechanisms as a function of strain rate for each of the steels based on the discussions above is presented ahead. In the following hypothesis, it has been assumed that the interfacial strength and the cleavage strength are thresholds and are not dependent on strain rate.

#### *Fracture response of DP 980 NC*

Figure 5.17 shows the hypothesis based on the Goods and Brown model [97] showing the variation of each of the stress parameters with an increase in strain rate. In the DP 980 NC steels, the total stresses reached at lower strain rates do not cross the threshold required for nucleation of voids in a majority of the fracture surface. Thus, the areas of void nucleation are *bridged* by the formation of facets under local shear.

As the strain rate increases, the dislocation density increases, leading to a local increase in stress. Larger areas of the fracture surface now cross the threshold to form voids and the area fraction of voids increase. The increase in local stresses is concentrated where the dislocation density is higher, i.e., at the interfaces between ferrite and martensite leading to decohesion voids. These voids, nucleated due to interfacial decohesion, easily grow along the interface and eventually coalesce to form secondary cracks. The formation of these secondary cracks is a faster mode of fracture since it travels along an already strained interface and is thus preferable under higher strain rates. With a combination of higher nucleation of voids, and less time for fracture, the area fraction of facets is less preferred and is reduced. At higher strain rates, DP 980 NC shows higher stress tri-axiality which also contributes to increasing

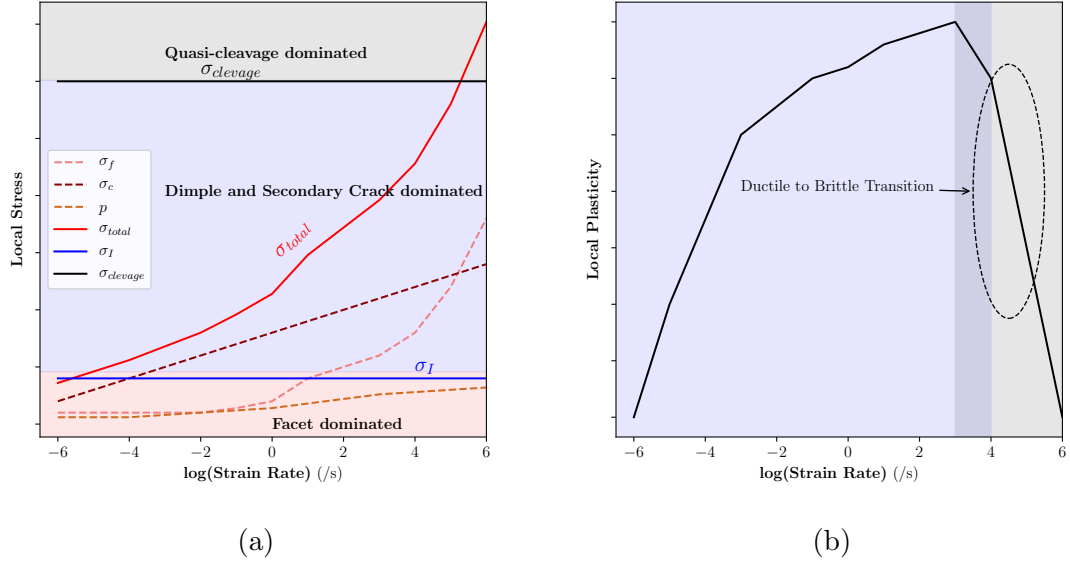


Figure 5.17: Schematic of the hypothesis for the fracture and formation of fracture surface features of DP 980 NC at different strain rates. The increase in the local stress leads to the formation of higher area fraction of voids at higher strain rates. The lowest strain rates are dominated by the presence of the facets while dimples dominate at the higher strain rates. Thus, there is a change in the dominant operative fracture mechanism with an increase in strain rate.

the local stresses, thus enabling a majority of the fracture surface to nucleates voids. Additionally, the interfaces with high dislocation density and local stresses lead to faster void formation in these areas followed by the rapid coalescence to form the secondary cracks. Thus, the density of interfacial voids that form the secondary cracks increases. Figure 5.18 shows a schematic of the nucleation of voids in different regions as a function of strain rate in DP 980 NC steels.

Under Spall conditions, the local stresses finally reach a value which exceeds that of microscopic cleavage. Since cleavage is a fast form of fracture, it is preferred under the highest strain rates where the material has very little time to fracture. Although a majority of the fracture surface is occupied by the quasi-cleavage features, some areas also show nucleation of voids indicating that the stresses in these areas are not considerably high such that nucleation of voids is preferred. Thus, to continue the

fracture hypothesis.pdf  
DP 980 NC Fracture mechanism Hypothesis

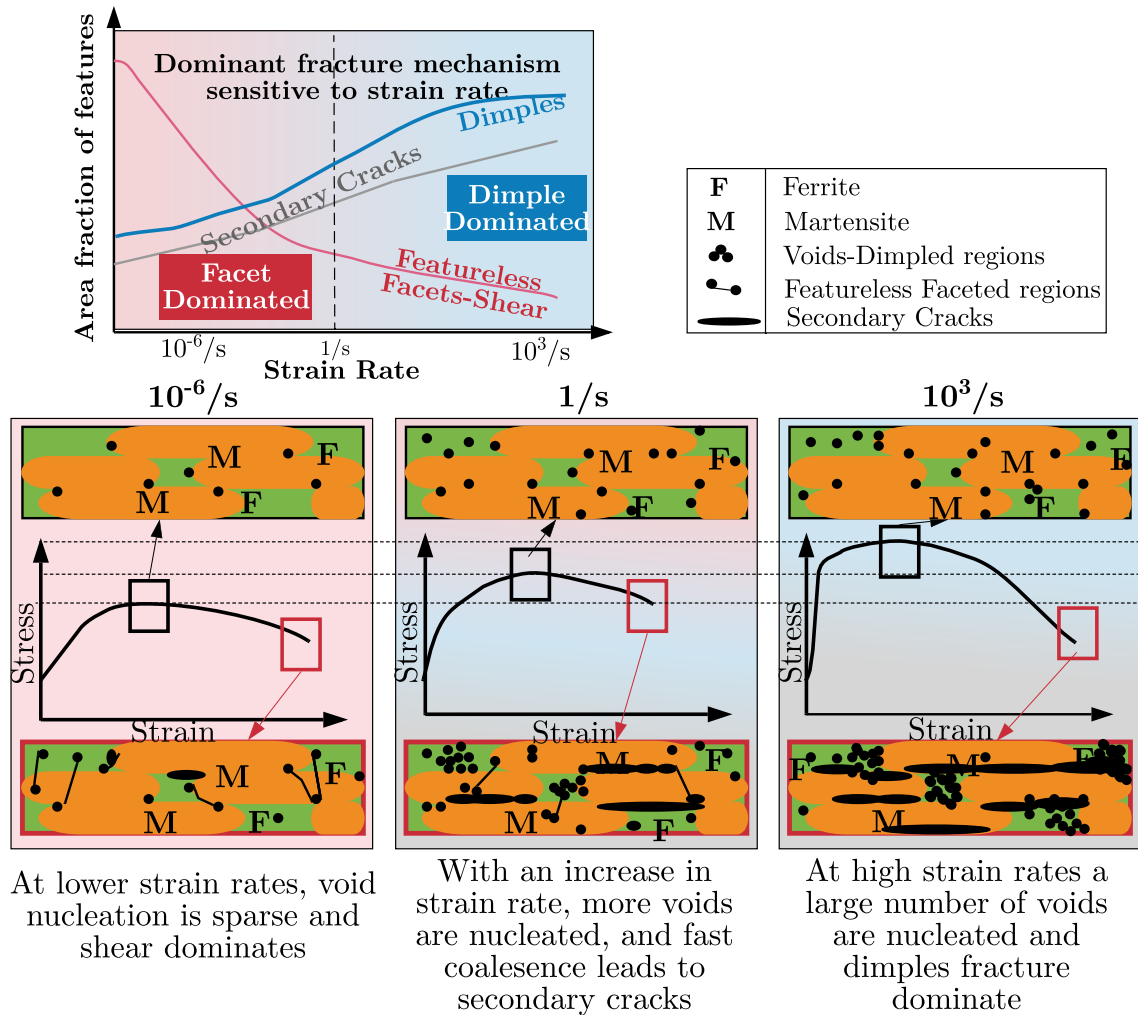


Figure 5.18: Schematic of the void formation and coalescence in DP 980 NC at different strain rates. At lower strain rates, the threshold for void nucleation is not reached at multiple locations, while at higher strain rates, a large number of voids are nucleated, especially along the interfaces.

analogy of low temperatures and high strain rates, the plate impact tests expose DP 980 NC to corresponding temperatures that are very close to DBTT.

### Fracture response of DP 980 GAN

Unlike DP 980 NC, the fracture response of DP 980 GAN was not dictated entirely by featureless facets at lower strain rates. Furthermore, the area fraction occupied

by voids in the GAN steel was higher than that of NC at lower strain rates, and was not sensitive to strain rate. The majority of the fracture surface in these steels was occupied by the secondary cracks. Figure 5.19 shows the hypothesis for the mechanism discussed.

Extending the methodology used to hypothesize the fracture mechanism of DP 980 NC, the contributions of the flow stresses ( $\sigma_f$ ) in GAN would be higher. Since these steels also have different alloying chemistry and processing conditions, the interfacial strength in the coated steels could be different from the NC steels. Further, since GAN has a finer microstructure, the contribution of the local stresses ( $\sigma_c$ ) at the interfaces is also greatly increased. Thus, even at lower strain rates, the local stresses are high enough to nucleate voids. Additionally, since the interfaces have a higher dislocation density, and GAN steels possess a greater degree of martensite banding, the interfacial decohesion voids form a majority of the nucleated voids and coalesce, leading to a large part of the fracture surface being occupied by the secondary cracks. Thus, fewer areas in the GAN steels are occupied by the featureless facets.

With an increase in the strain rate, the decohesion mechanism increases at the expense of the faceted feature formation, similar to the NC steels. Figure 5.20 shows a schematic of the different region in the microstructure where voids are nucleated in DP 980 GAN at varying strain rates. At higher strain rates, a large number of interfacial decohesion voids lead to the formation of a large area occupied by secondary cracks. Since, the area fraction of dimples remains largely unchanged, these cracks replace the facets observed at lower strain rates.

The spall fracture of these steels shows a more dimpled appearance compared to NC steels suggesting that locally the stresses are not high enough to propagate fracture by cleavage. However, the high area fraction of bands suggests that interfacial fracture still predominates at these strain rates. Thus, the equivalent DBTT temperature in these steels is lower than NC steels and is not reached with the equivalent

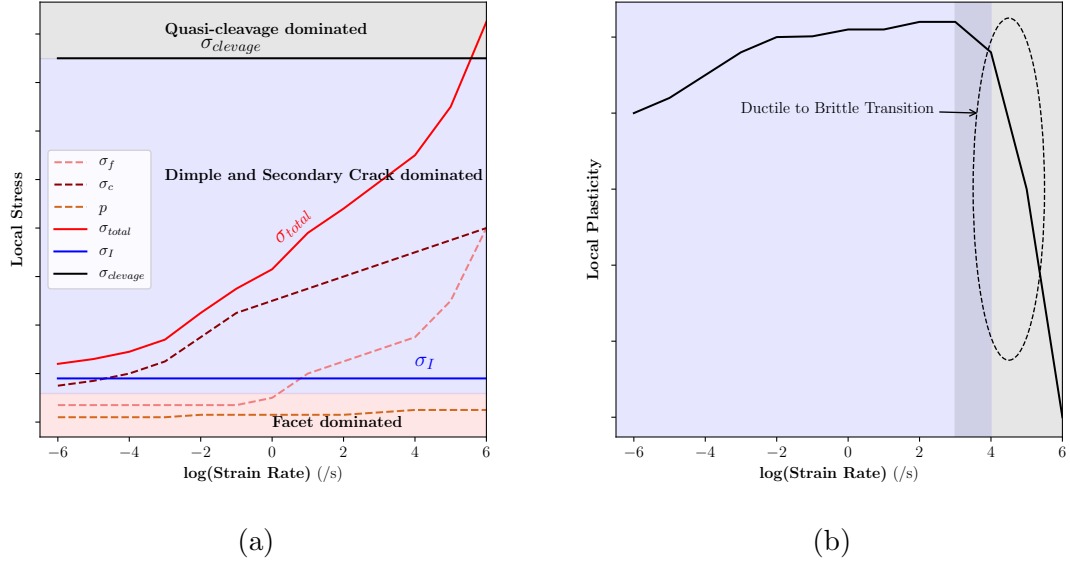


Figure 5.19: Schematic showing the fracture mechanism hypothesis for DP 980 GAN at different strain rates. The presence of a higher degree of banding along with an increase in the interfacial area leads to higher local stresses that increases the area fraction of voids. The higher area fraction of secondary cracks in the fracture surface is attributed to the higher degree of harder phase banding in these steels and increased interfacial surface area.

strain rates of the order of  $10^6/s$ .

#### *Fracture response of DP 980 GAD*

The microstructure of DP 980 GAD is different from that of DP 980 GAN and NC in that martensite is largely equiaxed and it possesses a co-continuous microstructure. With an increase in the interfacial surface area, the  $\sigma_c$  component of the Goods and Brown model [97] also increases. As it is reasonable to assume that the interfacial strength is similar in the GAN and GAD steels, larger areas in the GAD steel can cross the stress threshold required to nucleate voids, thus explaining the high area fraction of voids observed in the GAD steels at all strain rates.

With an increase in the strain rate, the local stresses around the interfaces increase, similar to that of DP 980 NC and GAN. However, since martensite is more equiaxed in

fracture hypothesis.pdf  
DP 980 GAN Fracture mechanism Hypothesis

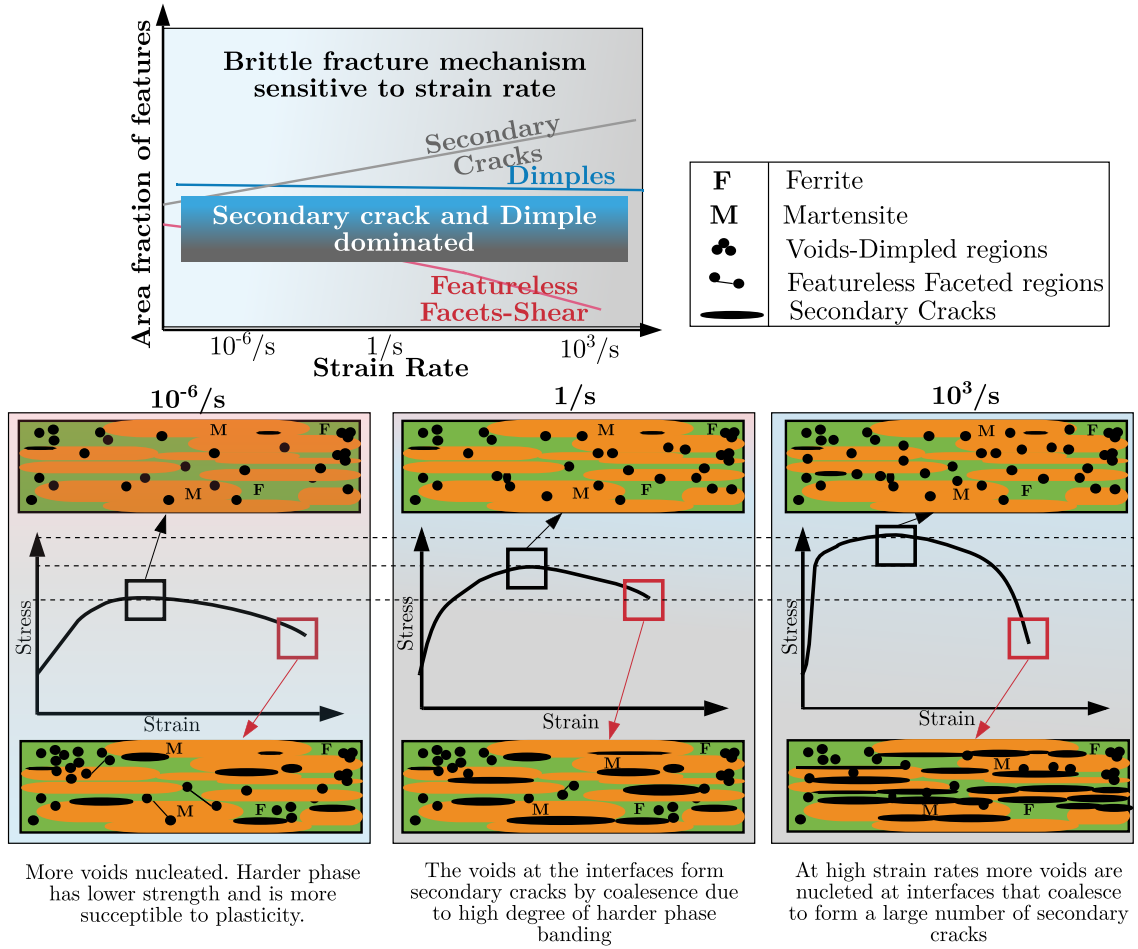


Figure 5.20: Schematic of the void formation and coalescence in DP 980 GAN at different strain rates. At lower strain rates the threshold for void nucleation is not reached at multiple locations, while at higher strain rates, a large number of voids are nucleated, especially along the interfaces.

GAD, the nucleated voids are not arranged along the rolling direction like in NC and GAN. This explanation is strengthened further with the observation of the presence of the secondary cracks present largely only in the center of the GAD steel where martensite is connected in the microstructure to form long bands. Figure 5.21 shows the schematic of the void nucleation and coalescence in DP 980 GAD at varying strain rates.

An interesting observation is the striking similarity in the spall behavior between

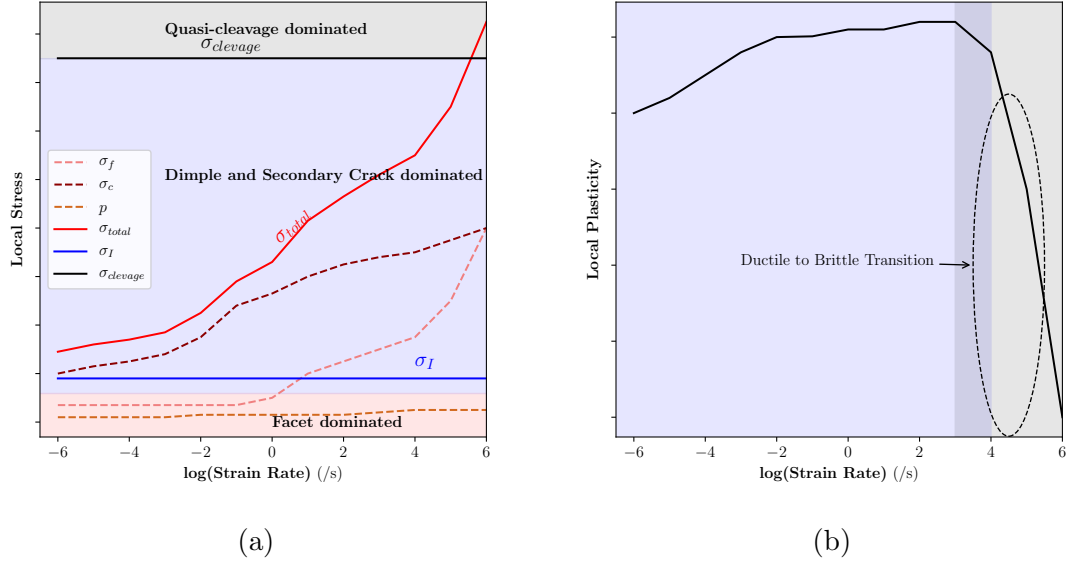


Figure 5.21: Schematic showing the fracture mechanism for DP 980 GAD steels at different strain rates. With a highly dispersed harder phase (compared to GAN), the void initiation sites in GAD steels is increased, leading to the high area fraction of dimples in this steel. The presence of secondary cracks and a connected harder phase only in the center of steel also indicates that these cracks are formed due to decohesion.

GAN and GAD steels. The GAD steels also show large areas occupied by voids indicating that the local stress required to generate quasi-cleavage fracture in these steels is also not reached. Figure 5.23 shows the velocity and time shifted recompression curves of DP 980 NC and DP 980 GAD. The time for the nucleation of voids in DP 980 GAD is observably longer than DP 980 NC.

The appearance of a large area of these steels occupied by the long flat bands in GAN, are observed in the GAD steels as well. One explanation for this is that the spall plane in all the steels is along the central mid-plane of the thickness of the steel. The GAD steels are observed to show a connected martensite along the central mid-plane. This leads to an important conclusion, that when the fracture is preferentially nucleated at the center of the steel where martensite contains maximum anisotropy, the spall fracture nucleation is similar in the coated steels with and without a decar-



fracture hypothesis.pdf  
DP 980 GAD Fracture mechanism Hypothesis

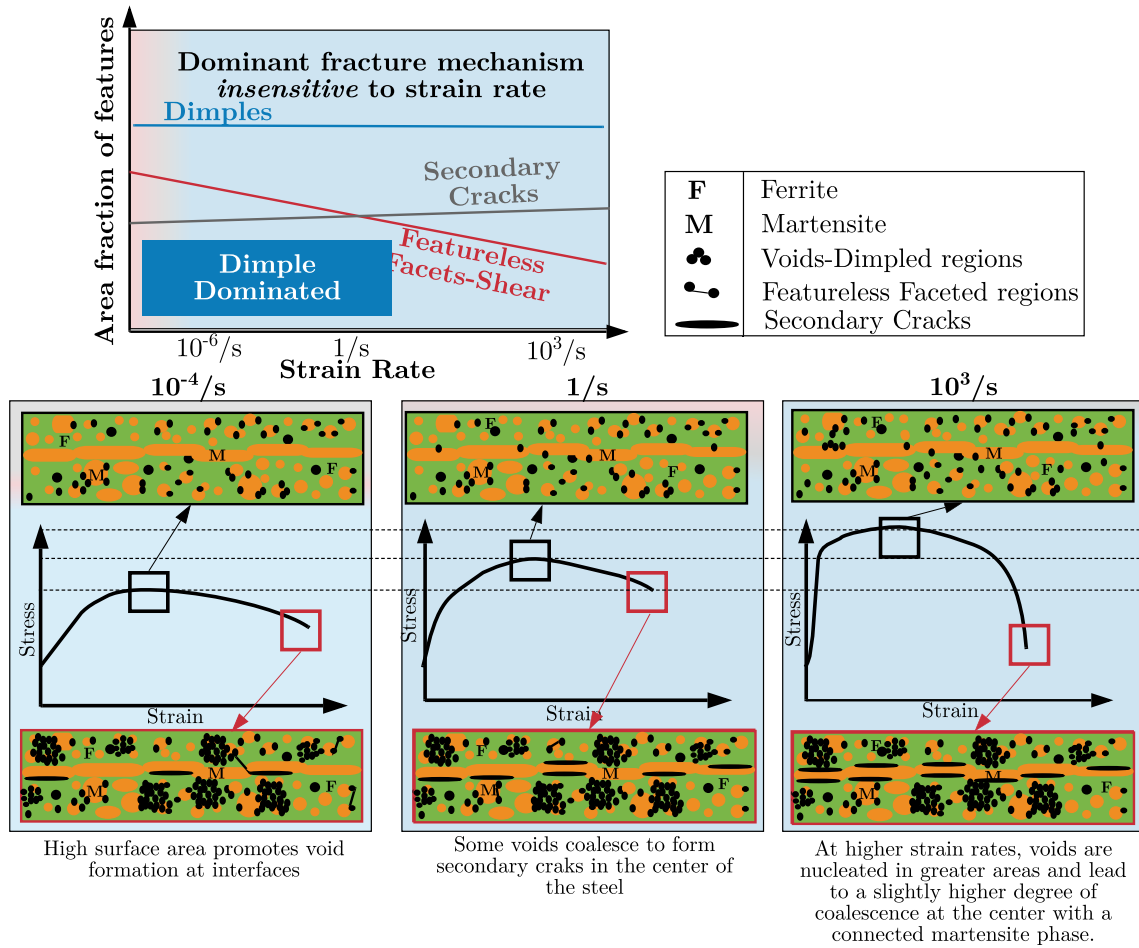


Figure 5.22: Schematic of the void formation and coalescence in DP 980 GAD at different strain rates. At lower strain rates the threshold for void nucleation is not reached at multiple locations, while at higher strain rates, a large number of voids are nucleated, especially along the interfaces.

burized layer. A high magnification image of the microstructure of DP 980 GAN and GAD at center of the short-transverse direction (same plane as the fracture observed under spall) also reveals the striking similarity in the microstructure.

#### 5.2.4 Comparing fracture mechanisms

The discussions above show the contribution of the coating layer added to create a composite structure and its effects on the local stresses and fracture mechanisms in

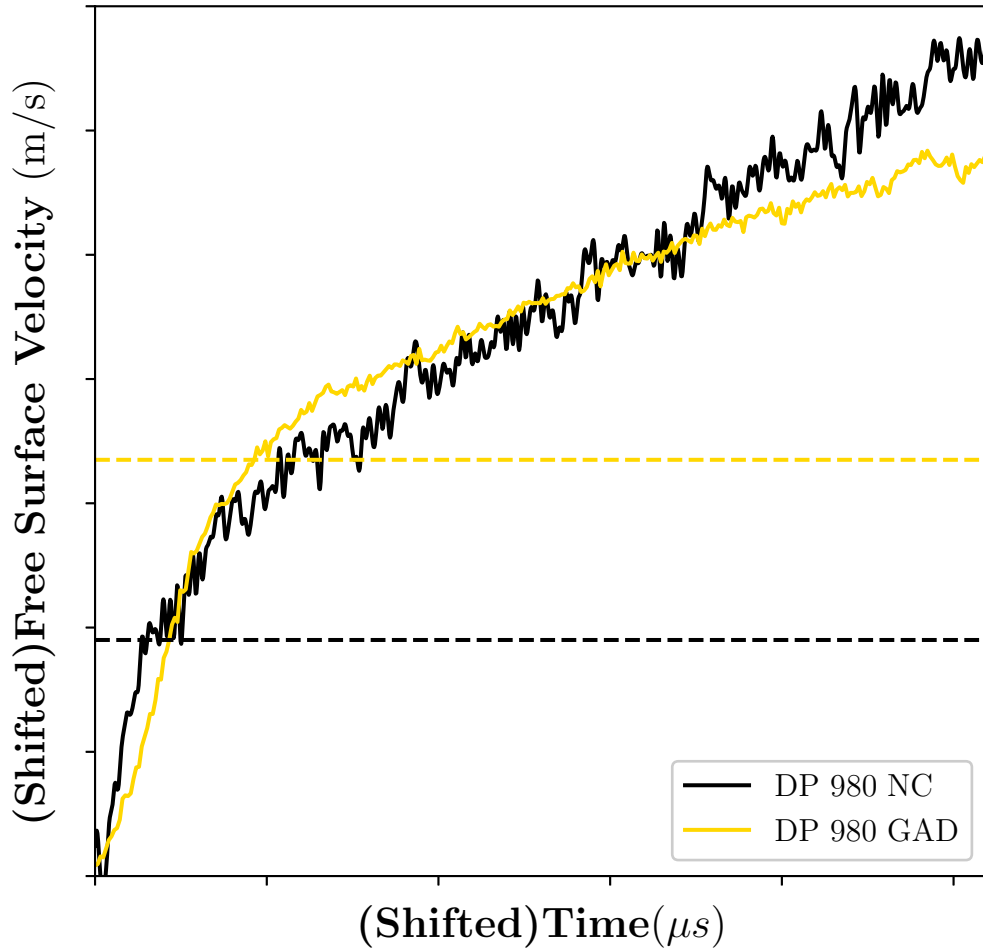


Figure 5.23: Plot showing the time and velocity adjusted recompression curves of DP 980 NC and DP 980 GAD. DP 980 GAD shows a longer void nucleation region.

DP 980 grade steels. The formation of facets is favored under a more heterogeneous local stress distribution and the formation of secondary cracks is due to interfacial decohesion along the banded martensite. The estimated dimple sizes do not vary with strain rate and are similar in all the DP steels investigated, indicating that the fracture was driven more by nucleation than by growth. The constant dimple sizes as a function of strain rate and an increase in interfacial decohesion fracture at higher strain rates has also been observed by Das et al. [51].

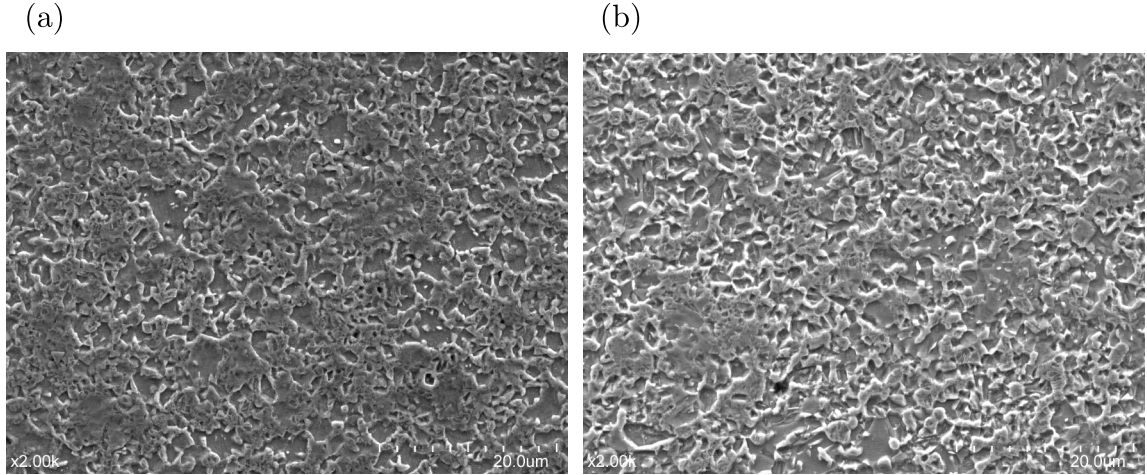


Figure 5.24: High magnification SEM images from the center of the short transverse direction of (a) GAN and (b) GAD steel.

The Goods and Brown model is largely used for materials with elastic particles in a plastically deforming matrix. In the case of DP 980 steels, the matrix is that of martensite which also deforms plastically, thus, the applicability of the model in these steels is very limited. However, the use of the flow stress and local stresses in the model make the *comparison* of different void nucleation mechanisms in the DP 980 steels easier.

#### *Effect of volume fraction of martensite*

In the HSLA 590 and DP 590 steels, the addition of the martensitic phase increased the post uniform elongation flow stress and local stresses such that the area fraction of dimpled regions in DP 590 was higher. Additionally, the area fraction of dimpled regions were also insensitive to strain rate.

With a further increase in the volume fraction of martensite and the presence of a martensitic matrix, such as DP 980 NC, inhibits the formation of voids at lower strain rates, or in other words, the threshold required for void nucleation in DP 980 NC is higher compared to DP 590 with a predominantly ferritic matrix. Thus, for DP 980 NC steels, the increase in strain rate and subsequent increase in flow stress,

then crosses the threshold required for void nucleation and results in the increase in area fraction of dimpled regions at higher strain rates.

There are also differences in the brittle mechanisms where the DP 590 steels with a ferritic matrix, show fewer secondary cracks compared to DP 980 NC, since there are fewer ferrite-martensite interfaces in these steels.

#### *Addition of surface layers*

With the addition of surface galvanized and decarburized layers, the subsequent microstructure is also altered, such that DP 980 GAN steels with a higher degree of total interfacial area and anisotropy of martensitic phase and DP 980 GAD with a more dispersed martensitic phase with some connectivity in the center of the steel, show different fracture surface response.

Both GAN and GAD steels surpassed the threshold stress required for void nucleation at lower strain rates. Since the threshold stresses were higher than the interfacial strength for void nucleation even at lower strain rates, the area fractions of dimples were higher than the NC steel and was also insensitive to strain rate.

Additionally, GAN steels with higher anisotropy of martensite also shows higher secondary cracks since the voids are preferentially nucleated at the interface and coalesce along it to form the cracks. GAD steels with a dispersed martensite phase, have a lower extent of secondary crack formation.

To gain a deeper understanding of the presence of these secondary cracks, the fracture surface of the GAN steel at 1/s strain rate, showing a high number density of secondary cracks, was polished such that the fracture features and the underlying microstructure could be observed simultaneously. The polished surfaces showed that the secondary cracks were caused by interface decohesion and void formation along the interfaces. Figure 5.25 shows the partial fractography images of GAN steel.

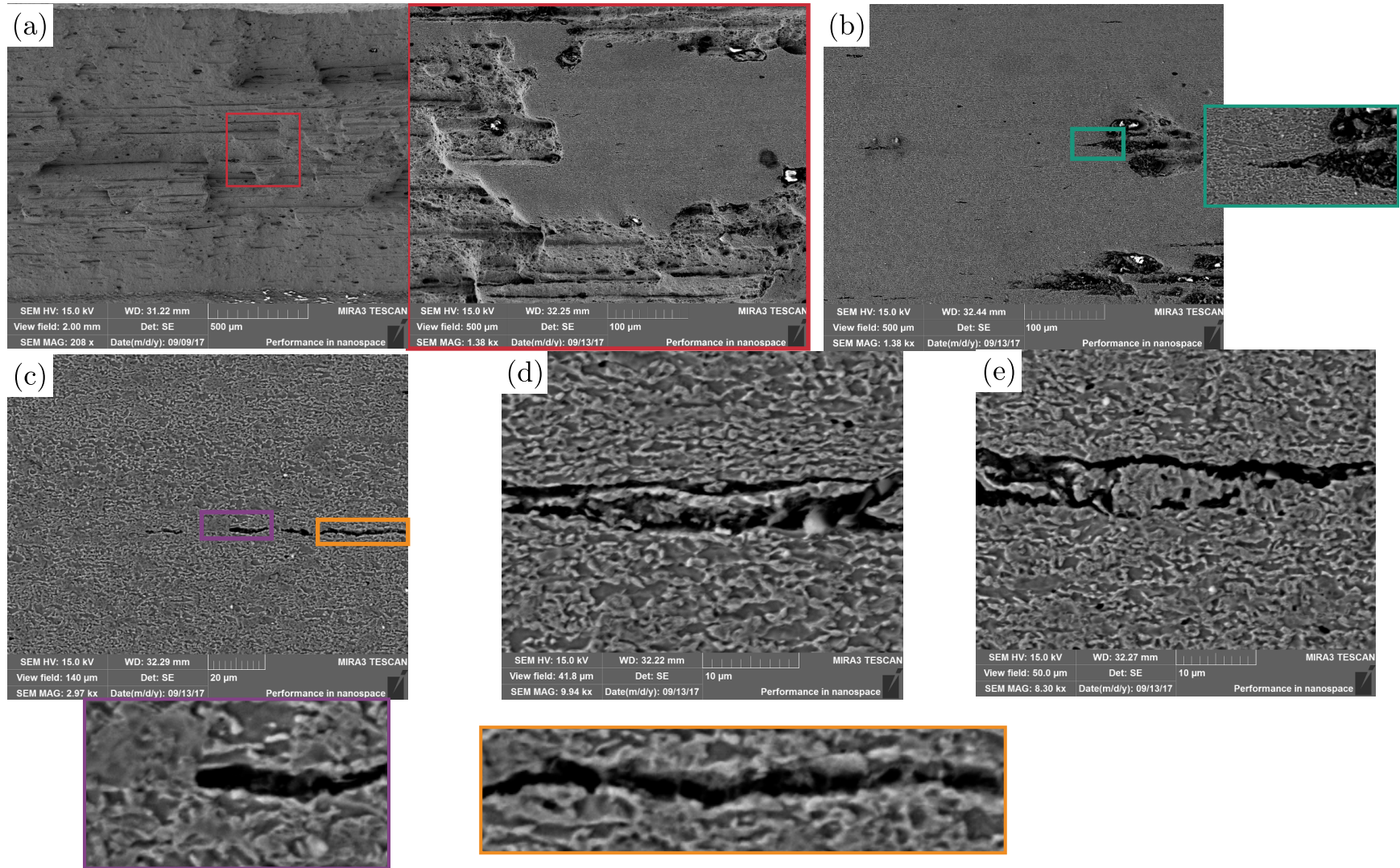


Figure 5.25: (a) Low magnification SEM image of the fracture surface before and after the partial polishing to reveal the deformed microstructure that participated in the fracture, (b) formation of a secondary crack by the linking of voids and decohesion of the ferrite and harder phase, (c) image showing the blunting of a cracks by a large harder phase island and interfacial decohesion along a long crack, (d) and (e) high magnification images of the microstructure consisting of the secondary cracks showing interfacial decohesion between the ferrite and harder phase.

When observing the fracture profiles and deformed microstructure, long cracks from cracking of martensite and subsequent decohesion are observed in DP 980 NC at lower strain rates. The macroscopic fracture profiles at these strain rates also contain flatter regions at  $\sim 45^\circ$  angles indicating fracture by local shear. At higher strain rates, a qualitative increase in the plasticity of martensite was observed.

The fracture profile of GAN steels shows considerable plasticity of martensite as indicated by deflection of cracks leading to the formation of a fissure as seen in figure 4.22. Additionally, both DP 980 NC and GAN shows elongated voids near the fracture formed due to interfacial decohesion. On the contrary, most voids observed in DP 980 GAD are circular and may not have not been elongated largely due the blunting effect of a co-continuous ferrite structure in these steels.

### 5.3 Effect of geometry on the stress-strain and fracture response

The background and experimental work chapters capture the need for different geometries during dynamic testing and the different geometries used in the current work for the various DP steels. The effect of geometry in the current work has been elucidated by testing DP 590 and using JIS and miniature geometries, as discussed before. This was done to capture the differences in the mechanical properties and deformation and fracture response of the two different geometries. Figure 5.17 shows the stress-strain response of the JIS and miniature geometry at two strain rates.

Table 5.1 shows the measured mechanical properties of the two geometries at the slowest and fastest strain rate the JIS specimens could be tested under,  $10^{-4}/s$  and  $1/s$  respectively. As expected, the yield and ultimate tensile strengths do not show a strong dependence on geometry. However, the final elongation, as expected, is observed to be sensitive to the gage length. The miniature geometry with gage length just 5% of the JIS geometry gage length displayed forced elongation and, thus, a much higher elongation compared to the JIS geometry. An interesting result is

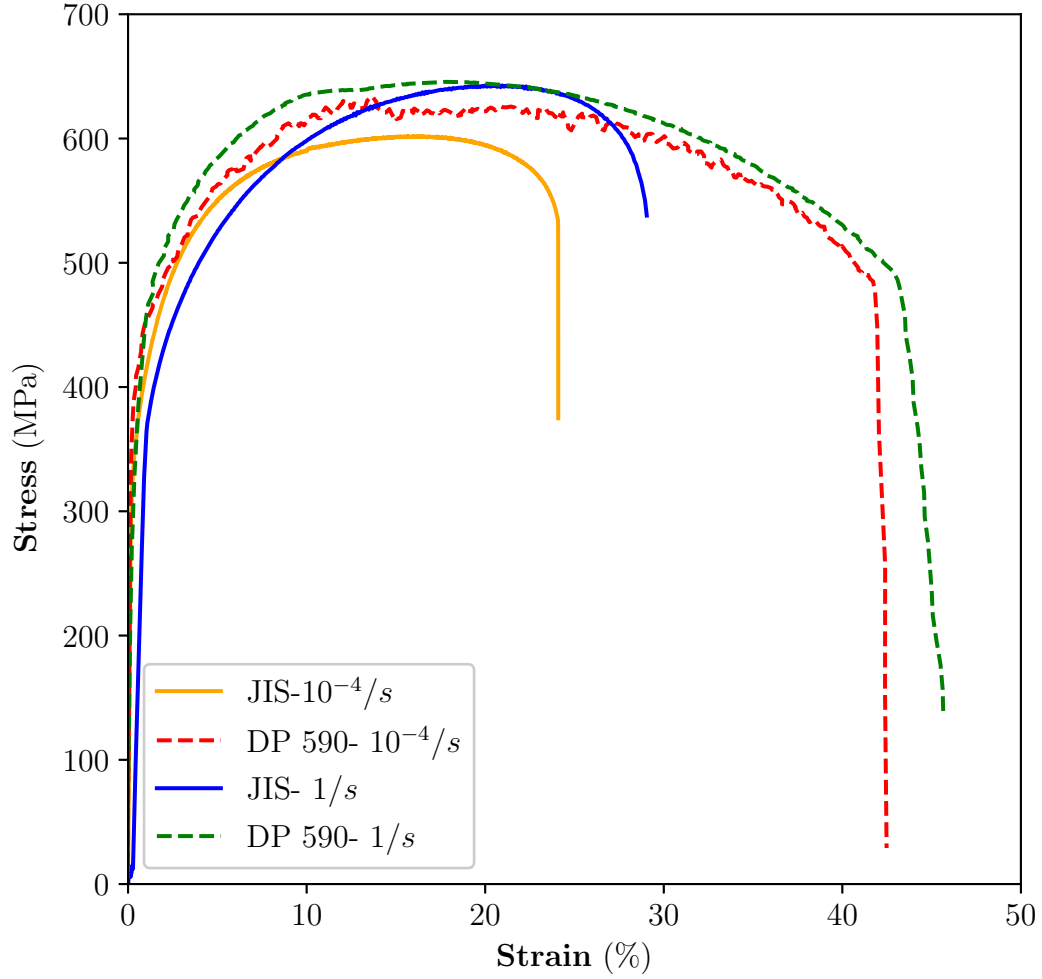


Figure 5.26: Stress-Strain response of the JIS and miniature tensile geometry at strain rates of  $10^{-4}/s$  and  $1/s$ . The effect of forced elongated on the miniature samples is observed clearly at both strain rates.

the difference in the uniform strain values, which indicates that the geometry also impacts the advent of stress tri-axiality in the sample, and thus, controls the uniform strain and in turn the global deformation.

The difference in the deformation was captured by computing the aspect ratio of the ferrite and martensite phases in both the geometries at increasing distances from the fractured edge. Table 5.2 shows the aspect ratios of ferrite and martensite



Table 5.1: Comparing mechanical properties of JIS and Miniature geometries

Property	JIS Geometry		Miniature Geometry	
Strain rate	0.0001/s	1/s	0.0001/s	1/s
Ultimate Tensile Strength (MPa)	642	674	657	657
Yield Stress (MPa)	400	438	350	370
Total elongation (%)	29	31	44	48
Uniform elongation (%)	20	25	13	18

Table 5.2: Comparing aspect ratios of ferrite and martensite in the JIS and Miniature geometries

Geometry Type		JIS geometry		Miniature geometry	
Strain rate		0.0001/s	1/s	0.0001/s	1/s
Aspect ratio of ferrite	Near Fracture	2.3	2.7	3.9	4.3
	In uniformly deformed region	1.6	2.8	2.8	3.5
Aspect Ratio of martensite	Near Fracture	1.7	1.7	2.4	1.7
	In uniformly deformed region	1.6	1.8	1.9	2

of the two geometries. The forced elongation in the miniature geometry explains the increased aspect ratios of ferrite and martensite at all strain rates compared to the JIS geometry. Additionally, a lower aspect ratio of ferrite and martensite in the uniformly deformed regions of the JIS specimens may also explain the higher uniform elongation values. Thus, from these observations, the geometry does seem to affect the global deformation of DP 590 steels. The local fracture mechanism, however, did not seem to be largely affected at the strain rates observed, since the area fraction of dimpled regions remained similar in both the geometries. These observations highlight the importance of maintaining a uniform geometry for a holistic comparison of the mechanical and deformation response of materials as a function of strain rate.



## CHAPTER 6

### CONCLUSIONS AND PROPOSED FUTURE WORK

This study focused on obtaining the strain rate dependence of the mechanical properties and fracture response of four commercial Dual Phase steels. The objective of this work was to determine microstructure driven fracture mechanisms of the DP steels by employing quantitative fractography. Quasi-static and dynamic strain rate tensile tests were performed on all steels. Plate impact tests to determine the dynamic tensile spall strength were conducted to investigate the fracture mechanisms at strain rates of  $10^6/s$ .

#### 6.1 Research Outcomes

##### Microstructure characterization

Stereology based quantitative characterization was performed on all four DP steels to determine the volume fraction, connectivity and distribution of the ferrite and martensite. DP 590 comprised of a ferritic matrix with  $\sim 29\%$  martensite in the form of dispersed islands located along the ferrite grain boundaries and triple points. Some connectivity of the martensite phase was observed in the form of bands. All three DP 980 grade steels contained  $\sim 70\%$  martensite. While martensite formed the matrix of DP 980 NC and GAN, DP 980 GAD possessed a co-continuous microstructure with dispersed martensite islands which showed connectivity only in the center of the steel's thickness. DP 980 GAN had a higher degree of martensite banding compared to DP 980 NC.

The decarburized layer thickness in DP 980 GAD was determined by obtaining the hardness using micro-hardness indents from the surface to the center of the steel.

The interfacial surface area per unit volume was determined to be a better parameter for validating the decarburized layer thickness as opposed to the volume fraction of martensite.

#### Mechanical properties at quasi-static and intermediate strain rates

The four DP steels were tested under strain rates spanning twelve orders of magnitude. All DP 980 grade steels with a higher volume fraction of martensite showed a higher strength and lower total elongation when compared to DP 590 steel. The role of alloying chemistry and processing was responsible for the slight increase in the strength of DP 980 GAN and GAD at quasi-static strain rates compared to DP 980 NC. No differences in the total elongation were observed at low strain rates.

All four steels showed positive strain rate sensitivity with higher stresses at higher strain rates. The extent of this increase however was different. The strain rate sensitivity of DP 590, predominantly comprised of ferrite, was higher than DP 980 NC. The total elongations did not show a distinct trend, however the elongation of both DP 590 and DP 980 NC was higher at intermediate strain rates. With the addition of the coating layers, the strain rate sensitivity of the 980 grade steels reduced in both strength and total elongation. At intermediate strain rates, there was no substantial difference in the strength of the steels, however, DP 980 NC was the only steel which showed an increase in total elongation. The total elongation of DP 980 GAN and GAD was insensitive to strain rate. Thus, under crash conditions, DP 980 NC is expected to show a better mechanical response when compared to the coated counterparts. The addition of the decarburized layer did not alter the strain rate sensitivity of the mechanical properties in the coated steels.

### Fracture response at quasi-static and intermediate strain rates

The fracture surface of all the steels showed a largely ductile dimple response. Similar fracture features were observed in all DP steels, however the area fractions differed as a function of the underlying microstructure. The fracture surface of DP 590 comprised of dimples predominantly, and its area fraction was insensitive to strain rate. The brittle features were essentially long secondary cracks arising primarily due to interfacial decohesion. With an increase in the volume fraction of martensite (DP 980 Steels), a second brittle feature in the form of featureless facets with a few asymmetric dimples was observed. While all DP 980 steels showed a strain rate sensitivity of the brittle features, only DP 980 NC showed a strain rate sensitivity of the area fraction of dimples. The area fraction of dimples doubled from the lowest to intermediate strain rates in DP 980 NC. The brittle features competed against each other, with facets being preferred at lower strain rates and secondary cracks preferred at higher strain rates.

### Plate Impact tests- Spall

Complete spallation of DP 590 and all three DP 980 steels was obtained at an impact velocity of 600m/s. DP 980 NC had the highest HEL and spall strength followed by DP 980 GAD and then DP 590. All three steels showed a change in the recompression curve indicating a shift from the void nucleation to the void and growth and coalescence regime.

Post-mortem fractography showed DP 590 to possess a completely brittle fracture along with a few long flat bands. DP 980 NC showed a highly heterogeneous fracture surface with quasi-cleavage features and long bands surrounded by dimples. The spall fracture surfaces of DP 980 GAN and GAD were very similar and comprised largely of the long flat bands surrounded by ductile dimples. Overall, the spall fracture surfaces of the DP 980 GAN and GAD steels were more ductile compared to DP 980 NC and

DP 590.

### Fracture mechanism hypotheses

A fracture mechanism hypotheses based on the Goods and Brown model is suggested to explain the area fraction of the features observed in the different DP steels at increasing strain rates. The model is used to estimate the differences in the local stresses leading to the threshold required for void formation in the steels.

The hypotheses help explain the strain rate sensitivity of different local stresses as a function of the underlying microstructure, leading to the formation of varying amounts of dimples in the different steels as a function of strain rate.

The formation of secondary cracks is attributed to interfacial decohesion between the ferrite and martensite phases. The decohesion is seen to be maximum in DP 980 GAN steels with the highest degree of martensite banding in the microstructure. The partial fractography conducted on DP 980 GAN confirms this observation.

### Effect of sample geometry

DP 590 was subjected to tensile tests using two sample geometries, one was a standard JIS geometry and the other was a miniature tensile geometry compatible with the intermediate strain rate tests conducted using the Hopkinson bar.

Although no substantial differences in the UTS was observed, the total elongation was significantly higher in the miniature samples, due to forced elongation that occurs at smaller gage lengths. The post-uniform elongation occupied a larger part of the total strain in the miniature samples, showing that the sample geometry also affects the global plasticity and neck formation in these steels.

Finally, differences observed in the aspect ratios of ferrite and martensite in the JIS and miniature geometries at the same strain rates indicated that the local deformation and strain partitioning mechanisms are also impacted by the sample geometry.

Thus, the current study helps illustrate the importance of using similar geometries when comparing mechanical properties across strain rates to capture a geometry independent material behavior.

## **6.2 Recommendations for future work**

The current study aimed to provide a comprehensive assessment of the quasi-static and dynamic mechanical properties and the operative fracture mechanisms of four commercial DP steels. Further studies to expand the data-set of DP 980 GAN and GAD steels at lower strain rates can help shed light on some of the behavior observed in NC steels and aid in improving the current hypothesis as to the origin of featureless facets.

Subsequent studies focusing on interrupted tensile tests at different strain rates can help explain and capture some of the void nucleation mechanisms in the steels. A stereological approach to quantifying the strain partitioned in the ferrite and martensite phases in the DP 980 grade steels will help shed more light on the local deformation mechanisms of these steels and how the processing conditions influence the local damage mechanisms. Incipient spall tests on all steels under similar conditions will be helpful in comparing the plasticity of martensite as a function of the carbon partitioned in it and the differences arising from the processing conditions the steels are exposed to.

Further, a microstructure based simulation of the tests performed experimentally in this study will help establish the influence of the behavior of individual phases and their distribution on the strain rate sensitivity of the damage and failure nucleation and growth.

Finally, the approach and hypotheses developed in the current study need to be tested and extended to other DP steel grades without coatings, and with coatings other than galvanized, and gradient microstructures and also to multi- and complex

phase steels to test the robustness of the results obtained in the study.

# Appendices

## APPENDIX A

### EFFECT OF GALVANNEALED AND DECARBURIZED LAYERS

To establish the influence of the coating layers and decarburized layers on the mechanical properties and fracture response of DP GAN and GAD steels, the steels were tested under different strain rates after removing these layers.

Both DP 980 GAN and GAD were carefully ground to remove the surface layers. About  $50\mu m$  of material was removed from either side the DP 980 GAN steel and about  $100\mu m$  was removed from either side of the GAD steels to ensure that both the coating and decarburized coating layers were removed.

Figure shows the stress-strain response of the GAN and GAD steels after the coating was removed. No substantial effect on the strength and total elongation was observed at these strain rates, indicating that the behavior is independent of the composite structure at these strain rates.

The fracture response of the samples with the coating removed also did not show any difference in the area fraction of features observed in the central one-third of the samples. However, upon observing the edge of the fracture of the as-received DP 980 GAD steel and the edge after removing the coating and decarburized layer, a difference in the fracture features was observed. Figure A.2 shows the fracture edge of (a) as-received steel and (b) after removing the coating and decarburized layers. The red box denoted the fracture expected to be caused by the decarburized layer.



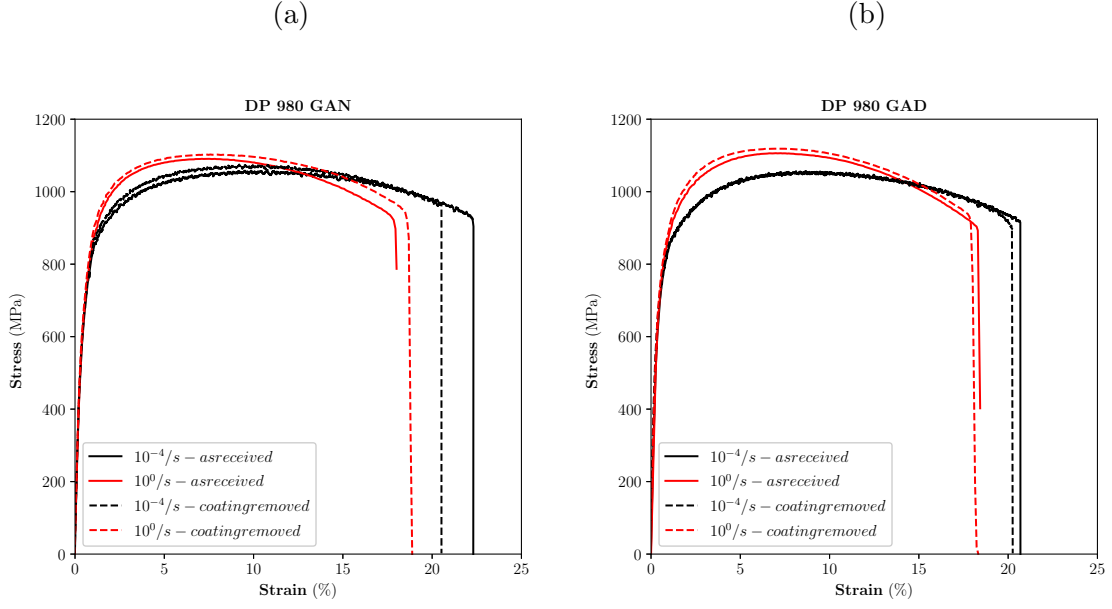


Figure A.1: Schematic showing the fracture mechanism for DP 980 GAD steels at different strain rates. With a highly dispersed harder phase (compared to GAN), the void initiation sites in GAD steels is increased leading to the high area fraction of dimples in this steel. The presence of secondary cracks and a connected harder phase only in the center of steel also indicates that these cracks are formed due to decohesion.

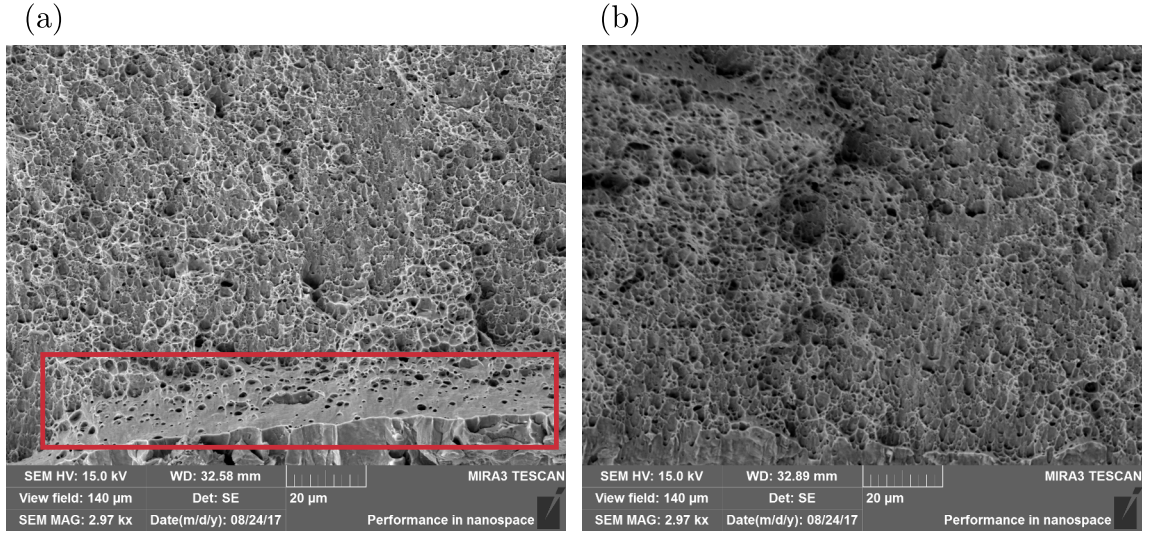


Figure A.2: Schematic of the void formation and coalescence in DP 980 GAD at different strain rates. At lower strain rates the threshold for void nucleation is not reached at multiple locations, while at higher strain rates, a large number of voids are nucleated, especially along the interfaces.

## APPENDIX B

### PLATE-IMPACT TEST CONFIGURATIONS

The table below lists the samples used in each plate-impact test and the configuration for each test.

Expt #	$v_{\text{impact}}$ (m/s)	Sample	Measurement	Experiment Type
1803	600 m/s	DP 980 NC-A	VISAR	Complete Spall
		DP 980 NC-B	Recovery	
		DP 980 NC -C	Recovery	
1807	300m/s	DP 980 NC-D	VISAR	Incipient Spall
		DP 980 NC- E	Recovery	
		DP 980 NC-F	Recovery	
1910	600m/s	DP 980 GAD-A	VISAR	Complete Spall
		DP 980 GAD-B	Recovery	
		DP 980 GAN-A	Recovery	
1911	600m/s	DP 590 -A	VISAR	Complete Spall
		DP 590-B	Recovery	
		DP 980 GAN-B	Recovery	

## ”REFERENCES”

- [1] A. Bag, K. Ray, and E. Dwarakadasa, “Influence of martensite content and morphology on tensile and impact properties of high-martensite dual-phase steels,” *Metallurgical and Materials Transactions A*, vol. 30, no. 5, pp. 1193–1202, 1999.
- [2] G Avramovic-Cingara, Y Ososkov, M. Jain, and D. Wilkinson, “Effect of martensite distribution on damage behaviour in dp600 dual phase steels,” *Materials Science and Engineering: A*, vol. 516, no. 1, pp. 7–16, 2009.
- [3] A Ramazani, Z Ebrahimi, and U Prahl, “Study the effect of martensite banding on the failure initiation in dual-phase steel,” *Computational Materials Science*, vol. 87, pp. 241–247, 2014.
- [4] W. Wang, M. Li, C. He, X. Wei, D. Wang, and H. Du, “Experimental study on high strain rate behavior of high strength 600–1000 MPa dual phase steels and 1200 MPa fully martensitic steels,” *Materials & Design*, vol. 47, pp. 510–521, May 2013.
- [5] H. Huh, S.-B. Kim, J.-H. Song, and J.-H. Lim, “Dynamic tensile characteristics of TRIP-type and DP-type steel sheets for an auto-body,” *International Journal of Mechanical Sciences*, 8th Asia-Pacific Symposium on Advances in Engineering Plasticity and its Applications (AEPA 2006), vol. 50, no. 5, pp. 918–931, May 2008.
- [6] M. S. Rashid, “Dual phase steels,” *Annual Review of Materials Research*, vol. 11, no. 1, pp. 245–266, 1981.
- [7] C. Tasan, M. Diehl, D. Yan, M. Bechtold, F. Roters, L. Schemmann, C. Zheng, N. Peranio, D. Ponge, M. Koyama, K. Tsuzaki, and D. Raabe, “An overview of dual-phase steels: Advances in microstructure-oriented processing and micromechanically guided design,” *Annual Review of Materials Research*, vol. 45, no. 1, pp. 391–431, 2015.
- [8] Y. Granbom, “Structure and mechanical properties of dual phase steels: An experimental and theoretical analysis,” 2010.
- [9] B. C. De Cooman and J. G. Speer, *Fundamentals of steel product physical metallurgy*. AIST, Association for Iron & Steel Technology, 2011.

- [10] S. Chatterjee, S. Koley, R. B. Sarkar, N. Behera, M. Manna, S. Mukherjee, and S. Kundu, "Design and development of galvanized dual-phase steel: Microstructure, mechanical properties and weldability," *Journal of Materials Engineering and Performance*, vol. 28, no. 1, pp. 231–241, 2019.
- [11] Y. Tobiyama, K. Osawa, and M. Hirata, "Development of 590 mpa grade galvanized sheet steels with dual phase structure," *Kawasaki Steel Giho(Japan)*, vol. 31, no. 3, pp. 181–184, 1999.
- [12] S. Hironaka, H. Tanaka, and T. Matsumoto, "Effect of si on mechanical property of galvanized dual phase steel," in *Materials Science Forum*, Trans Tech Publ, vol. 638, 2010, pp. 3260–3265.
- [13] H. A. Moslehabadi, "Galvannealing of dual phase steels by," 2012.
- [14] J. Rege, T. Inazumi, T. Urabe, and Y. Nagataki, *Cold rolled and galvanized or galvanized dual phase high strength steel and method of its production*, US Patent App. 10/235,535, 2004.
- [15] *Galvanized zinc-iron alloy coated steels*, [https://automotive.arcelormittal.com/products/global\\_offering/coatings/galvanized](https://automotive.arcelormittal.com/products/global_offering/coatings/galvanized).
- [16] J. Y. Koo, M. J. Young, and G. Thomas, "On the law of mixtures in dual-phase steels," *Metallurgical Transactions A*, vol. 11, no. 5, pp. 852–854, 1980.
- [17] R. G. Davies, "Influence of martensite composition and content on the properties of dual phase steels," *Metallurgical Transactions A*, vol. 9, no. 5, pp. 671–679, 1978.
- [18] E. N. Birgani and M. Pouranvari, "Effect of martensite volume fraction on the work hardening behavior of dual phase steels," *Metal 2009*, pp. 19–21, 2009.
- [19] N. Fonstein, "Advanced high strength sheet steels," *Physical Metallurgy, Design, Processing, and Properties*, Springer, 2015.
- [20] M. Calcagnotto, Y. Adachi, D. Ponge, and D. Raabe, "Deformation and fracture mechanisms in fine-and ultrafine-grained ferrite/martensite dual-phase steels and the effect of aging," *Acta Materialia*, vol. 59, no. 2, pp. 658–670, 2011.
- [21] V Colla, M De Sanctis, A Dimatteo, G Lovicu, A Solina, and R Valentini, "Strain hardening behavior of dual-phase steels," *Metallurgical and Materials Transactions A*, vol. 40, no. 11, pp. 2557–2567, 2009.

- [22] F. Pickering, “The effect of composition and microstructure on ductility and toughness (high strength low alloy type ferrite pearlite steel microstructural and compositional variations effect on work hardening, ductility and impact toughness),” *Toward improved ductility and toughness*, pp. 9–34, 1971.
- [23] Y. Bergström, Y. Granbom, and D. Sterkenburg, “A dislocation-based theory for the deformation hardening behavior of dp steels: Impact of martensite content and ferrite grain size,” *Journal of Metallurgy*, vol. 2010, 2010.
- [24] J. Zhang, H. Di, Y. Deng, and R. Misra, “Effect of martensite morphology and volume fraction on strain hardening and fracture behavior of martensite–ferrite dual phase steel,” *Materials Science and Engineering: A*, vol. 627, pp. 230–240, 2015.
- [25] T. S. Byun and I. S. Kim, “Tensile properties and inhomogeneous deformation of ferrite-martensite dual-phase steels,” *Journal of Materials Science*, vol. 28, no. 11, pp. 2923–2932, 1993.
- [26] K. Park, M. Nishiyama, N. Nakada, T. Tsuchiyama, and S. Takaki, “Effect of the martensite distribution on the strain hardening and ductile fracture behaviors in dual-phase steel,” *Materials Science and Engineering: A*, vol. 604, pp. 135–141, 2014.
- [27] Q. Lai, O. Bouaziz, M. Gouné, L. Brassart, M. Verdier, G. Parry, A. Perlade, Y. Bréchet, and T. Pardoen, “Damage and fracture of dual-phase steels: Influence of martensite volume fraction,” *Materials Science and Engineering: A*, vol. 646, pp. 322–331, 2015.
- [28] E. Maire, O. Bouaziz, M. Di Michiel, and C. Verdu, “Initiation and growth of damage in a dual-phase steel observed by x-ray microtomography,” *Acta Materialia*, vol. 56, no. 18, pp. 4954–4964, 2008.
- [29] M. Mazinani, “Deformation and fracture behaviour of a low-carbon dual-phase steel,” PhD thesis, University of British Columbia, 2006.
- [30] E. Aşık, E. Perdahcıoğlu, and A. van den Boogaard, “Microscopic investigation of damage mechanisms and anisotropic evolution of damage in dp600,” *Materials Science and Engineering: A*, vol. 739, pp. 348–356, 2019.
- [31] G. Avramovic-Cingara, C. A. Saleh, M. Jain, and D. Wilkinson, “Void nucleation and growth in dual-phase steel 600 during uniaxial tensile testing,” *Metallurgical and materials transactions A*, vol. 40, no. 13, pp. 3117–3127, 2009.

- [32] T. Depover, F. Vercruysse, A. Elmahdy, P. Verleysen, and K. Verbeken, "Evaluation of the hydrogen embrittlement susceptibility in dp steel under static and dynamic tensile conditions," *International Journal of Impact Engineering*, vol. 123, pp. 118–125, 2019.
- [33] J.-H. Kim, D. Kim, H. N. Han, F. Barlat, and M.-G. Lee, "Strain rate dependent tensile behavior of advanced high strength steels: Experiment and constitutive modeling," *Materials Science and Engineering: A*, vol. 559, pp. 222–231, 2013.
- [34] S Celotto, H Ghadbeigi, C Pinna, B. Shollock, and P Efthymiadis, "Deformation-induced microstructural banding in trip steels," *Metallurgical and Materials Transactions A*, vol. 49, no. 7, pp. 2893–2906, 2018.
- [35] C Zener and J. Hollomon, "Effect of strain rate upon plastic flow of steel," *Journal of applied physics*, vol. 15, no. 1, pp. 22–32, 1944.
- [36] N. Mott, "A theory of work-hardening of metals ii: Flow without slip-lines, recovery and creep," *The London, Edinburgh, and Dublin Philosophical Magazine and Journal of Science*, vol. 44, no. 354, pp. 742–765, 1953.
- [37] L. Clarebrough and M. Hargreaves, "Work hardening of metals," *Progress in Metal Physics*, vol. 8, 1IN141IN349IN557–40IN248IN456103, 1959.
- [38] I Gupta and J. Li, "Stress relaxation, internal stress, and work hardening in some bcc metals and alloys," *Metallurgical Transactions*, vol. 1, no. 8, pp. 2323–2330, 1970.
- [39] J. Mason, A. Rosakis, and G Ravichandran, "On the strain and strain rate dependence of the fraction of plastic work converted to heat: An experimental study using high speed infrared detectors and the kolsky bar," *Mechanics of Materials*, vol. 17, no. 2, pp. 135–145, 1994.
- [40] B. Hopkinson, "A method of measuring the pressure produced in the detonation of high explosives or by the impact of bullets," *Philosophical Transactions of the Royal Society of London. Series A, Containing Papers of a Mathematical or Physical Character*, vol. 213, pp. 437–456, 1914.
- [41] H Kolsky, "An investigation of the mechanical properties of materials at very high rates of loading," *Proceedings of the Physical Society. Section B*, vol. 62, no. 11, p. 676, 1949.
- [42] R. Davies, "A critical study of the hopkinson pressure bar," *Philosophical Transactions of the Royal Society of London A: Mathematical, Physical and Engineering Sciences*, vol. 240, no. 821, pp. 375–457, 1948.

- [43] J. Lifshitz and H Leber, "Data processing in the split hopkinson pressure bar tests," *International Journal of Impact Engineering*, vol. 15, no. 6, pp. 723–733, 1994.
- [44] H. Huh, W. J. Kang, and S. S. Han, "A tension split hopkinson bar for investigating the dynamic behavior of sheet metals," *Experimental Mechanics*, vol. 42, no. 1, pp. 8–17,
- [45] *Split-hopkinson pressure bar testing*, <http://hrdg.matse.illinois.edu/hopbar.html>.
- [46] B. A. Gama, S. L. Lopatnikov, and J. W. Gillespie, "Hopkinson bar experimental technique: A critical review," *Applied Mechanics Reviews*, vol. 57, no. 4, pp. 223–250, 2004.
- [47] P. Verleysen, J. Degrieck, T. Verstraete, and J. Van Slycken, "Influence of specimen geometry on split hopkinson tensile bar tests on sheet materials," *Experimental Mechanics*, vol. 48, no. 5, pp. 587–598, 2008.
- [48] S Winkler, A Thompson, C Salisbury, M Worswick, I Van Riemsdijk, and R Mayer, "Strain rate and temperature effects on the formability and damage of advanced high-strength steels," *Metallurgical and Materials Transactions A*, vol. 39, no. 6, pp. 1350–1358, 2008.
- [49] P. Verleysen, J. Peirs, J. Van Slycken, K. Faes, and L. Duchene, "Effect of strain rate on the forming behaviour of sheet metals," *Journal of Materials Processing Technology*, vol. 211, no. 8, pp. 1457–1464, 2011.
- [50] H. Yu, Y. Guo, and X. Lai, "Rate-dependent behavior and constitutive model of dp600 steel at strain rate from  $10^{-4}$  to  $10^3$  s $^{-1}$ ," *Materials & Design*, vol. 30, no. 7, pp. 2501–2505, 2009.
- [51] A. Das, M. Ghosh, S. Tarafder, S Sivaprasad, and D. Chakrabarti, "Micromechanisms of deformation in dual phase steels at high strain rates," *Materials Science and Engineering: A*, vol. 680, pp. 249–258, 2017.
- [52] S Curtze, V.-T. Kuokkala, M Hokka, and P Peura, "Deformation behavior of trip and dp steels in tension at different temperatures over a wide range of strain rates," *Materials Science and Engineering: A*, vol. 507, no. 1, pp. 124–131, 2009.
- [53] D. Dong, Y. Liu, Y. Yang, J. Li, M. Ma, and T. Jiang, "Microstructure and dynamic tensile behavior of dp600 dual phase steel joint by laser welding," *Materials Science and Engineering: A*, vol. 594, pp. 17–25, 2014.

- [54] J. Hutchinson and K. Neale, “Influence of strain-rate sensitivity on necking under uniaxial tension,” *Acta Metallurgica*, vol. 25, no. 8, pp. 839–846, 1977.
- [55] ———, “Sheet necking-iii. strain-rate effects,” in *Mechanics of sheet metal forming*, Springer, 1978, pp. 269–285.
- [56] A. Ghosh, “The influence of strain hardening and strain-rate sensitivity on sheet metal forming,” *Journal of Engineering Materials and Technology*, vol. 99, no. 3, pp. 264–274, 1977.
- [57] M. Seth, V. J. Vohnout, and G. S. Daehn, “Formability of steel sheet in high velocity impact,” *Journal of Materials Processing Technology*, vol. 168, no. 3, pp. 390–400, 2005.
- [58] M. Singh, A. Das, T Venugopalan, K. Mukherjee, M. Walunj, T. Nanda, and B. R. Kumar, “Impact of martensite spatial distribution on quasi-static and dynamic deformation behavior of dual-phase steel,” *Metallurgical and Materials Transactions A*, vol. 49, no. 2, pp. 463–475, 2018.
- [59] M. A. Meyers, *Dynamic behavior of materials*. John wiley & sons, 1994.
- [60] W. J. M. Rankine, “Xv. on the thermodynamic theory of waves of finite longitudinal disturbance,” *Philosophical Transactions of the Royal Society of London*, no. 160, pp. 277–288, 1870.
- [61] W. Wang, H. Zhang, M. Yang, P. Jiang, F. Yuan, and X. Wu, “Shock and spall behaviors of a high specific strength steel: Effects of impact stress and microstructure,” *Journal of Applied Physics*, vol. 121, no. 13, p. 135 901, 2017.
- [62] C Li, B Li, J. Huang, H. Ma, M. Zhu, J Zhu, and S. Luo, “Spall damage of a mild carbon steel: Effects of peak stress, strain rate and pulse duration,” *Materials Science and Engineering: A*, vol. 660, pp. 139–147, 2016.
- [63] M. A. Meyers and C. T. Aimone, “Dynamic fracture (spalling) of metals,” *Progress in Materials Science*, vol. 28, no. 1, pp. 1–96, 1983.
- [64] S Christy, H. Pak, and M. Meyers, “Metallurgical applications of shock-wave and high-strain-rate phenomena,” *New York and Basel*, 1986.
- [65] T. Antoun, D. R. Curran, L. Seaman, G. I. Kanel, S. V. Razorenov, and A. V. Utkin, *Spall fracture*. Springer Science & Business Media, 2003.
- [66] D. Dennis-Koller, J. P. Escobedo-Diaz, E. Cerreta, C. A. Bronkhorst, B. Hansen, R. Lebensohn, H. Mourad, B. Patterson, and D. Tonks, “Controlled shock load-



- ing conditions for microstructural correlation of dynamic damage behavior,” in *AIP Conference Proceedings*, AIP, vol. 1426, 2012, pp. 1325–1330.
- [67] J. Escobedo, D. Dennis-Koller, E. Cerreta, B. Patterson, C. Bronkhorst, B. Hansen, D Tonks, and R. Lebensohn, “Effects of grain size and boundary structure on the dynamic tensile response of copper,” *Journal of Applied Physics*, vol. 110, no. 3, p. 033 513, 2011.
  - [68] S. Fensin, E. Walker, E. Cerreta, and G. Gray III, “When do interfaces become important for failure?” In *EPJ Web of Conferences*, EDP Sciences, vol. 94, 2015, p. 02 010.
  - [69] A. Marder, “The metallurgy of zinc-coated steel,” *Progress in materials science*, vol. 45, no. 3, pp. 191–271, 2000.
  - [70] Y. Nunomura and T. Takasugi, “Plastic deformation and fracture behavior of galvanized coating,” *ISIJ international*, vol. 43, no. 3, pp. 454–460, 2003.
  - [71] G. Song, T Vystavel, N Van der Pers, J. T. M. De Hosson, and W. Sloof, “Relation between microstructure and adhesion of hot dip galvanized zinc coatings on dual phase steel,” *Acta Materialia*, vol. 60, no. 6, pp. 2973–2981, 2012.
  - [72] P. R. Mouton, *Principles and practices of unbiased stereology: an introduction for bioscientists*. JHU Press, 2002.
  - [73] R. T. DeHoff and F. N. Rhines, “Quantitative microscopy,” 1968.
  - [74] A. M. Gokhale and N. U. Deshpande, “Application of stereology in materials science and engineering,” *Acta Stereologica*, vol. 13, pp. 253–268, 1994.
  - [75] A. Gokhale and G. Patel, “Origins of variability in the fracture-related mechanical properties of a tilt-pour-permanent-mold cast al-alloy,” *Scripta materialia*, vol. 52, no. 3, pp. 237–241, 2005.
  - [76] A. M. Gokhale, “Quantitative characterization and representation of global microstructural geometry,” *Materials Park, OH: ASM International, 2004.*, pp. 428–447, 2004.
  - [77] H. J. G. Gundersen, “Notes on the estimation of the numerical density of arbitrary profiles: The edge effect,” *Journal of microscopy*, vol. 111, no. 2, pp. 219–223, 1977.
  - [78] E. Underwood, Q. Stereology, and R. Addison-Wesley, *Massachusetts*, 1970.

- [79] E. E. Underwood and K. Banerji, “Quantitative fractography,” *ASM Handbook*, vol. 12, pp. 193–210, 1987.
- [80] A. Gokhale and E. Underwood, “A general method for estimation of fracture surface roughness: Part i. theoretical aspects,” *Metallurgical Transactions A*, vol. 21, no. 5, pp. 1193–1199, 1990.
- [81] A. Gokhale and W. Drury, “A general method for estimation of fracture surface roughness: Part ii. practical considerations,” *Metallurgical Transactions A*, vol. 21, no. 4, pp. 1201–1207, 1990.
- [82] R. Jamwal, A. Gokhale, and S. Bhat, “Quantitative fractographic analysis of variability in the tensile ductility of a high strength dual-phase steel,” *Metallography, Microstructure, and Analysis*, vol. 2, no. 1, pp. 30–34, 2013.
- [83] X. Sun, K. S. Choi, A. Souلامي, W. N. Liu, and M. A. Khaleel, “On key factors influencing ductile fractures of dual phase (dp) steels,” *Materials Science and Engineering: A*, vol. 526, no. 1, pp. 140–149, 2009.
- [84] K. Mishra, “Effects of microstructure and strain rate on deformation behavior in advanced high strength steels,” PhD thesis, Georgia Institute of technology, 2017.
- [85] A. Godha, “Microstructural effects on fatigue damage evolution in advanced high strength sheet (ahss) steels,” PhD thesis, Georgia Institute of Technology, 2015.
- [86] D. Bhattacharya, “Developments in advanced high strength steels,” in *The Joint International Conference of HSLA Steels*, 2005, pp. 70–73.
- [87] J Kadkhodapour, A Butz, S Ziaei-Rad, and S Schmauder, “A micro mechanical study on failure initiation of dual phase steels under tension using single crystal plasticity model,” *International Journal of Plasticity*, vol. 27, no. 7, pp. 1103–1125, 2011.
- [88] M. Rashid and E. Cprek, “Relationship between microstructure and formability in two high-strength, low-alloy steels,” in *Formability Topics—Metallic Materials*, ASTM International, 1978.
- [89] F Ozturk, A Polat, S Toros, and R. Picu, “Strain hardening and strain rate sensitivity behaviors of advanced high strength steels,” *Journal of Iron and Steel Research International*, vol. 20, no. 6, pp. 68–74, 2013.

- [90] E Cadoni, F D’Aiuto, and C Albertini, “Dynamic behaviour of advanced high strength steels used in the automobile structures,” *DYMAT*, vol. 1, pp. 135–141, 2009.
- [91] K Yasunaga, M Iseki, and M Kiritani, “Dislocation structures introduced by high-speed deformation in bcc metals,” *Materials Science and Engineering: A*, vol. 350, no. 1-2, pp. 76–80, 2003.
- [92] U. Lindholm, “Some experiments with the split hopkinson pressure bar,” *Journal of the Mechanics and Physics of Solids*, vol. 12, no. 5, pp. 317–335, 1964.
- [93] Q. Kun, Y. Li-Ming, and H. Shi-Sheng, “Mechanism of strain rate effect based on dislocation theory,” *Chinese Physics Letters*, vol. 26, no. 3, p. 036 103, 2009.
- [94] E Cadoni, N. Singh, D Forni, M. Singha, and N. Gupta, “Strain rate effects on the mechanical behavior of two dual phase steels in tension,” *The European Physical Journal Special Topics*, vol. 225, no. 2, pp. 409–421, 2016.
- [95] Y Bergström, “A dislocation model for the stress-strain behaviour of polycrystalline  $\alpha$ -fe with special emphasis on the variation of the densities of mobile and immobile dislocations,” *Materials Science and Engineering*, vol. 5, no. 4, pp. 193–200, 1970.
- [96] J. Samei, D. E. Green, J. Cheng, and M. S. de Carvalho Lima, “Influence of strain path on nucleation and growth of voids in dual phase steel sheets,” *Materials & Design*, vol. 92, pp. 1028–1037, 2016.
- [97] S. Goods and L. Brown, “Overview no. 1: The nucleation of cavities by plastic deformation,” *Acta Metallurgica*, vol. 27, no. 1, pp. 1–15, 1979.
- [98] O. Furukimi, C. Kiattisaksri, Y. Takeda, M. Aramaki, S. Oue, S. Munetoh, and M. Tanaka, “Void nucleation behavior of single-crystal high-purity iron specimens subjected to tensile deformation,” *Materials Science and Engineering: A*, vol. 701, pp. 221–225, 2017.
- [99] Y. Cao, J. Ahlström, and B. Karlsson, “The influence of temperatures and strain rates on the mechanical behavior of dual phase steel in different conditions,” *Journal of Materials Research and Technology*, vol. 4, no. 1, pp. 68–74, 2015.
- [100] E Amar and A Pineau, “Interpretation of ductile fracture toughness temperature dependence of a low strength steel in terms of a local approach,” *Engineering Fracture Mechanics*, vol. 22, no. 6, pp. 1061–1071, 1985.

- [101] R. O. Diaz, “Dynamic deformation of titanium-based bulk metallic glass composites,” PhD thesis, Georgia Institute of Technology, 2016.